ASD-TDR-62-578

SUPPRESSION OF JET NOISE WITH EMPHASIS ON THE NEAR FIELD

TECHNICAL DOCUMENTARY REPORT ASD-TDR-62-578

February 1963

Flight Dynamics Laboratory
Aeronautical Systems Division
Air Force Systems Command
Wright-Patterson Air Force Base, Ohio

Project No. 1370, Task No. 137005

**(Prepared under Contract No. AF33(616)-7772
by Western Electro-Acoustic Laboratory, Los Angeles, California.
Authors, Kenneth M. Eldred, Robert W. White, Myron A. Mann
and Miltiades G. Cottis**

NOTICES

FOREWORD

The research work in this report was performed by Western Electro-Acoustic Laboratory, Inc., Los Angeles, California, for the Flight Dynamics Laboratory, Directorate of Aeromechanics, Deputy for Technology, Aeronautical Systems Division, Wright-Patterson Air Force Base, Ohio, under AF Contract Nr AF33(616)-7772. This research is part of a continuing effort to obtain more accurate prediction methods for noise suppression in jet flow for flight vehicles which is part of the Air Force Systems Command's Applied Research Program 750A, the Mechanics of Flight. The Project Nr is 1370 "Dynamic Problems in Flight Vehicles" and the Task Nr is 137005 "Methods of Noise Prediction, Control and Measurement". David Smith and later Phillip Hermes of the Flight Dynamics Laboratory were the Project Engineers, and their helpful comments have been appreciated by the authors. The research was conducted from December 1960 to January 1962.

The individual participants in this report include: R. Kosin of Norair, who acted as a consultant to the program and contributed the major part of Section V entitled "Performance Aspects of Noise Suppression Nozzles and Turbofan Engines"; R. White, who wrote Appendix B entitled "Derivation of Modified Acoustic Equation for Turbulent Jet Exhausts"; M. Cottis, who wrote Appendix C entitled "Sound Propagation in a Cylindrically Symmetrical Temperature Distribution"; M. Mann, who derived the near field prediction model in Section III; and K. Eldred, who is primarily responsible for the remainder, including Appendix A.

ABSTRACT

This report gives methods for computing the acoustic power spectra generated by jets from coaxial turbofans, generalized mixing nozzles and ejectors, and compares the aerodynamic performance gains or penalties associated with these various devices. The results give the limits of acoustic power reduction which can be achieved by mixing nozzles. Further, the results show that major new reduction in jet noise can be obtained only with the development of new turbofan engines which have the maximum practical bypass ratios.

These prediction methods for noise suppression in jet flows are based in part on derivations of the flow from axisymmetric and slot jets contained in the report. These flow derivations are based on the Prandtl mixing length concept and include an analysis of the mixing length determined from measured jet turbulence, and the interrelationship between flow Mach number, mixing length, and the resultant jet core length.

The report also derives a new model of the angular distribution of the radiation of noise from a 1000°F Mach 1 jet as a function of both frequency and axial position from empirical data. This derivation sheds considerable new light on the radiation properties and generation of noise in the jet. These results are found consistent with a new basic differential equation governing the radiation and generation of sound within the jet, which is derived in this report. In addition, theoretical consideration is given to the radiation of sound in a cylindrical temperature gradient and to the acoustic power generation of the jet as a function of axial position.

PUBLICATION REVIEW

This report has been reviewed and is approved.

FOR THE COMMANDER

Walter J. Mykytow

WALTER J. MYKYTOW
Chief, Dynamics Branch
Flight Dynamics Laboratory

TABLE OF CONTENTS

TABLE OF CONTENTS
(continued)

LIST OF ILLUSTRATIONS

Figure No.		Page No.
14	Variation in core length for constant density axisymmetric jet as a function of Mach number	16
15	Calculated flow contours for constant density axisymmetric jet with exit Mach number of 1.0, and zero external velocity	18
16	Comparison of relative axial velocity and relative maximum longitudinal turbulence for constant density axisymmetric jet at Mach .3 from Laurence, with calculated axial velocity	18
17	Calculated flow contours for constant density axisymmetric jet with external velocity $U_o = .5\ U_e$, $M_e = 1$, and using c based on relative Mach number	19
18	Calculated variation in the core length as a function of the ratio of external velocity (U_o) to jet exit velocity (U_e) (not including variation of c with Mach number)	19
19	Calculated flow contours for a constant density slot jet with exit Mach number of 1.0 and zero external velocity	20
20	Axial decay of velocity computed for Mach .3 slot jet using ($k\ c^2$) from axisymmetric jet. Data cre for 3.14 x 1 in. nozzles with two spacings from Laurence, NACA TN 4029	21
21	Contours of overall sound pressure level (rms) in db re .0002 dyne/cm^2 for J57 engine at military power, from unpublished data by Bioacoustics Branch ASD, and from Howes et al	27
22	Contours of sound pressure level in db re .0002 dyne/cm^2 in one-third octave bandwidths for J57 engine at military power, data from Howes, et al	28
23	Overall sound pressure level along 10° boundary line, data from Howes, et al	29
24	Sound pressure level in one-third octave bands measured along 10° boundary line, data from Howes, et al	30
25	Location of maximum sound pressure level in one-third octave frequency bands as a function of a modified Strouhal number and axial distance. Data from Howes, et al	31

Figure No.		Page No.
26	Comparison of octave band power spectra first estimated from 10° boundary maximum sound pressure level and area between minus 3 db points with generalized spectra computed from far field measurements	33
27	Ray diagram for radiation from simple source located at the center of the jet velocity and temperature gradient, for exit velocity of 1850 ft/sec. and exit temperature of 1000°F	34
28	Example of relation between zero crossing of correlation coefficient, wavelength and direction of propagation	36
29	Contours of equal sound pressure level in 5 db increments for one-third octave band centered at 400 cps, together with axial variation in level along 10° measurement boundary and primary direction from spacial pressure correlations. Data from Howes, et al	37
30	Variation of the predominant propagation angle for various frequencies from measurements along the 10° boundary as a function of a non-dimensional axial frequency parameter	39
31	Generalized far field directivity in the 37.5 - 75 and 75 - 150 cps octave bands for various turbojet engines operating at military power	41
32	Generalized far field directivity in the 150 - 300 and 300 - 600 cps octave bands for various turbojet engines operating at military power	42
33	Generalized far field directivity in the 600 - 1200 and 1200 - 2400 cps octave bands for various turbojet engines operating at military power	43
34	Generalized far field directivity in the 2400 - 4800 and 4800 - 9600 cps octave bands for various turbojet engines operating at military power	44
35	Sound pressure level in octave bands along the 10° boundary, from the one-third octave band data by Howes, et al	46
36	Illustration of effect of ground plane for the 600 - 1200 cps octave band	47

Figure No. Page No.

Figure No.		Page No.

Figure No. Page No.

SECTION I

INTRODUCTION

The work described in this report represents a continuation of efforts by this and other organizations toward practical understanding and reduction of jet noise.

The primary purpose of the present study is the evaluation of methods to reduce jet noise in the near field where it is responsible for the sonic fatigue of aircraft structure. The validity and practicality of these evaluations presuppose an adequate understanding of the noise generating and radiating characteristics of arbitrary jet flows. In turn, this understanding depends upon a satisfactory definition of the jet flow itself, and upon the relationships between flow parameters and noise generation.

Unfortunately, these interrelationships are not well documented. Therefore, considerable emphasis in this study was directed toward the development of similarity parameters for jet flow, near field noise generation, and refraction of noise within the jet. These efforts assisted in the semi-empirical determination of the spacial and directional distribution of noise along the outer boundary of a conventional jet at military power. In addition, they provided a basis for an evaluation of the effect of flow alteration on jet noise generation, supplemented with a discussion of the aerodynamic considerations implicit in multiple nozzles and bypass engines.

These topics are developed throughout the report as follows: Section II relates jet flow and turbulence similarity parameters. Section III documents the near noise field of the 1000°F, Mach 1, axisymmetric jet and derives an empirical model for the angular distribution of noise as a function of frequency and axial position. The performance of various noise control devices is treated in Section IV comparing measured results with those expected on the basis of prediction techniques developed in Sections II, III and IV. Finally, the aerodynamic performance penalties or gains of noise suppression nozzles and turbofan engines are discussed in Section V. Three appendixes follow the text. Appendix A derives solutions for several representative jet flows. A theory of generation and radiation of sound is discussed in Appendix B and a new equation is derived which removes some of the restrictions of earlier theory. The properties of sound radiating from the axis of a cylindrically symmetric temperature distribution are developed in Appendix C.

Manuscript released by the authors September 1962 for publication as an ASD Technical Documentary Report.

SECTION II

TURBULENCE AND FLOW SIMILARITY

The noise generated by a jet flow results from the turbulent fluctuations within the flow. The magnitude of this noise is dependent upon the intensity and frequency of the turbulent fluctuations and the size of fluctuating eddies. Further, the magnitude of the radiated noise is dependent upon the mean flow parameters and their gradients. Thus, alteration of one or more of the basic flow characteristics may be expected to alter the characteristics of the noise radiated from the flow. This is the basic premise of the in-flight noise suppressor.

The first step toward the evaluation of the noise radiated from a modified jet flow is the estimation of the characteristics of the flow itself. Since no purely analytical theory or method is known which can predict the noise radiated from a jet flow, the evaluation of the noise radiation of a modified flow is heavily dependent upon analogy to the noise radiation of well-documented flows. In this latter category, the majority of available data applies to the axisymmetric jet, and therefore it provides a primary basis for evaluation of the effects of flow modification.

Figures 1 to 3 illustrate the gross flow parameters for an axisymmetric jet. As shown in figure 1, the jet core extends for several nozzle diameters from the nozzle. This essentially laminar core is surrounded by a mixing region which grows linearly with axial distance. The maximum turbulent intensity occurs in the portion of the mixing region where the velocity gradient is steepest, as shown in figure 2. Since the noise generated in the flow is directly dependent upon a power of the turbulent intensity, the region wherein the mean square turbulence $(u')^2$ exceeds one-half of its maximum value affords a conceptual definition of the actual noise source region. Thus, the region of primary noise generation in an axisymmetric jet is an annular volume which grows in thickness with increased axial distance, as illustrated in figure 3.

Downstream of the core tip the axial velocity decreases and the jet continues to spread. This decrease in velocity reduces the velocity gradients and the intensity of turbulence generated in the downstream region. Here, as pointed out by Ribner (Ref. 1), the intensity of the noise generated downstream of the core should decrease with a relatively high power of the axial distance. Therefore, as will be shown later in a more conclusive fashion, the mixing region external to the core is the major source of the noise generated by the jet flow.

This conceptual model of the relationships between turbulence and gross flow parameters is continued in the following subsections to provide a practical definition of the similarity parameters required for later consideration of the noise generation of modified flows.

Note: The references are numbered consecutively in each section and are listed at the end of each section together with a list of symbols.

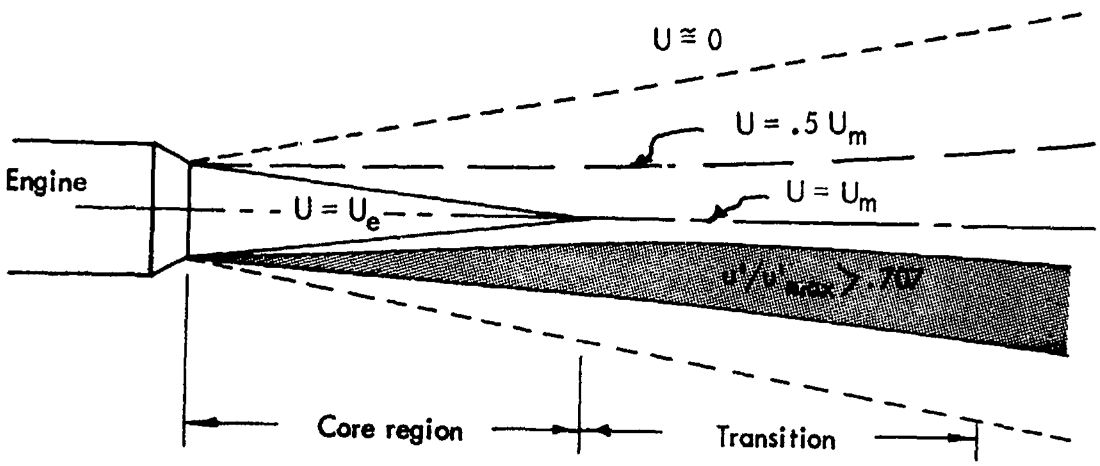

Figure 1. Mean flow for constant density axisymmetric jet at Mach .7 from Laurence.

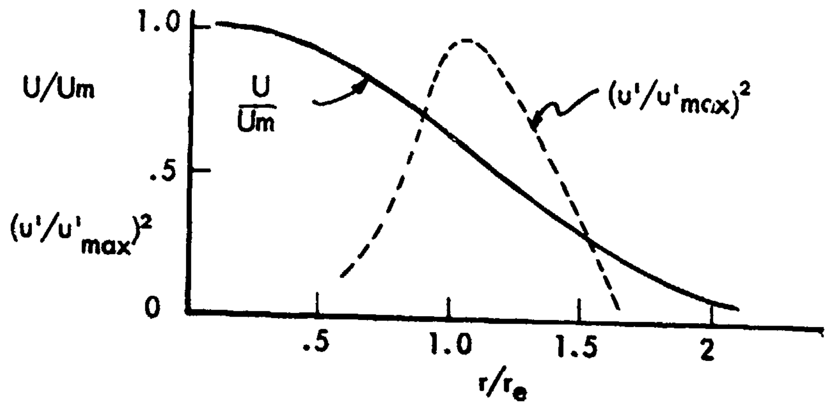

Figure 2. Relative velocity and turbulence profiles at 8 radii downstream of nozzle for constant density axisymmetric jet data, from Laurence.

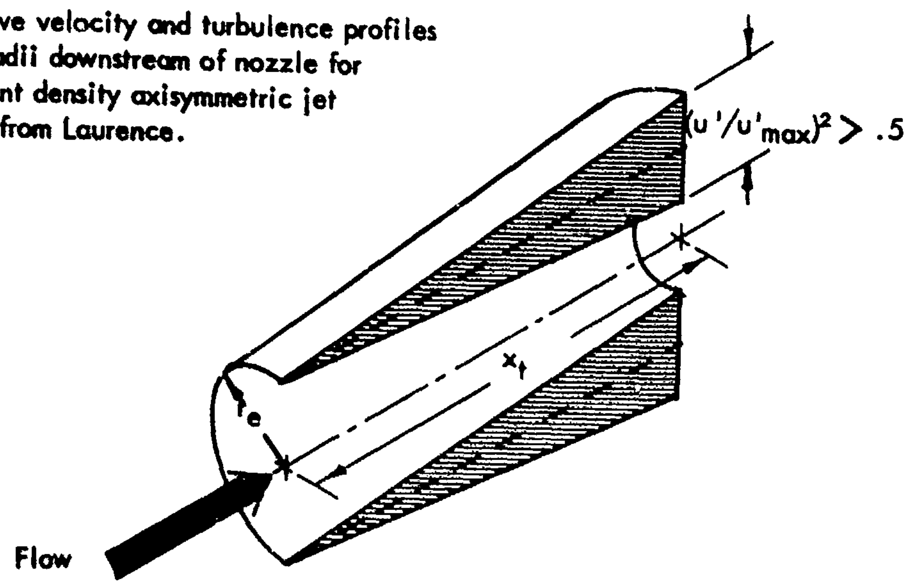

Figure 3. Schematic volume of maximum noise generation where $(u'/u'_{max})^2 > .5$

Jet Turbulence

Although turbulent phenomena have been observed in both wind and sea throughout history, a great deal remains to be understood about the basic mechanisms of turbulence, particularly for shear flows. Therefore, it is necessary to rely primarily on experimental results with only general theoretical guidance. Fortunately, considerable turbulence data have been obtained in jet flows by Corrsin (Refs. 2, 3, 4), Liepman (Ref. 5), Laurence (Refs. 6, 7, 8) and others. Since Laurence's data were taken with primary regard to noise generation, the major emphasis in his experiments was placed on the mixing region surrounding the core. The resulting data form the most complete set of flow and turbulence data available for the study of jet noise.

The longitudinal velocity spectra for an axisymmetric constant density jet of 1.75 in. radius and exit Mach number of .4 measured by Laurence (Ref. 6) are given in figure 4,

where
$$\mathcal{F}(f) = \frac{1}{\overline{U^2_{oa}}} \lim_{\Delta f \to 0} \frac{\overline{U^2}}{\Delta f}$$

$\overline{u^2}$ is the mean square turbulence velocity measured in a bandwidth of Δf(cps)

$\overline{u^2_{oa}}$ is the total mean square turbulence over the total bandwidth

and
$$\int_0^\infty \mathcal{F}(f)\,df = 1$$

The spectra for the non-dimensional axial distances (x/r_e) between 2.29 and 16 have been normalized by U_e/x and are given as a function of a Strouhal number fx/U_e in figure 5. Despite the unique low frequency characteristic of the spectra at x/r_e of 2.29 and 4.58 with respect to the spectra farther downstream, there is an apparent gross similarity of the normalized spectra throughout the entire mixing region.

The lateral turbulence spectra (Ref. 6), measured at two stations, have been normalized by U_e/x and are compared to the longitudinal spectra in figure 6. These data indicate that the lateral velocity spectra are probably also similar; however, they appear shifted in frequency by a factor of two above the longitudinal spectra.

Although the data shown in figures 4 to 6 offer evidence of gross similarity for the turbulence spectra as a function of axial distance, they do not test similarity as a function of velocity because U_e was not varied in the experiment. Furthermore, these turbulence spectra do not give the actual frequency spectra of the turbulent fluctuations themselves, when viewed by an observer moving at the mean flow velocity. For, as Taylor pointed out, (Ref. 9) and Laurence (Ref. 6) proved for the majority of these data, these turbulent power spectra density curves are simply the Fourier transforms of the longitudinal spacial velocity correlation coefficient (R_x). Therefore, the turbulent spectra measured with the hot wire are exactly a measure of the mean square fluctuating velocities associated with eddies of varying size (λ), which are convected past the measuring device with velocity U_c. Thus,

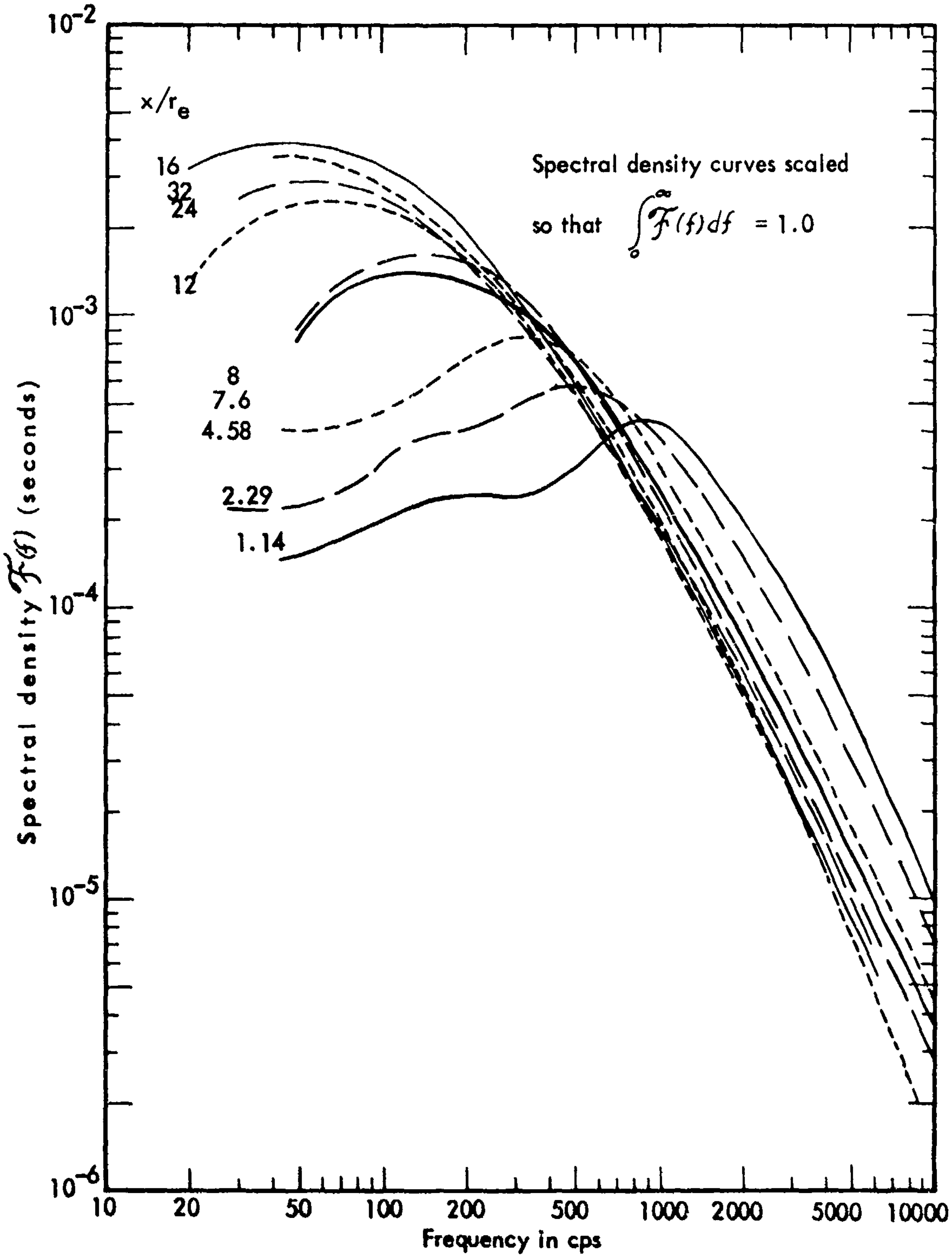

Figure 4. Longitudinal turbulent spectra at various axial distances, at approximately one radius from the centerline, data for 1.75 in. radius nozzle at Mach .3, from Laurence.

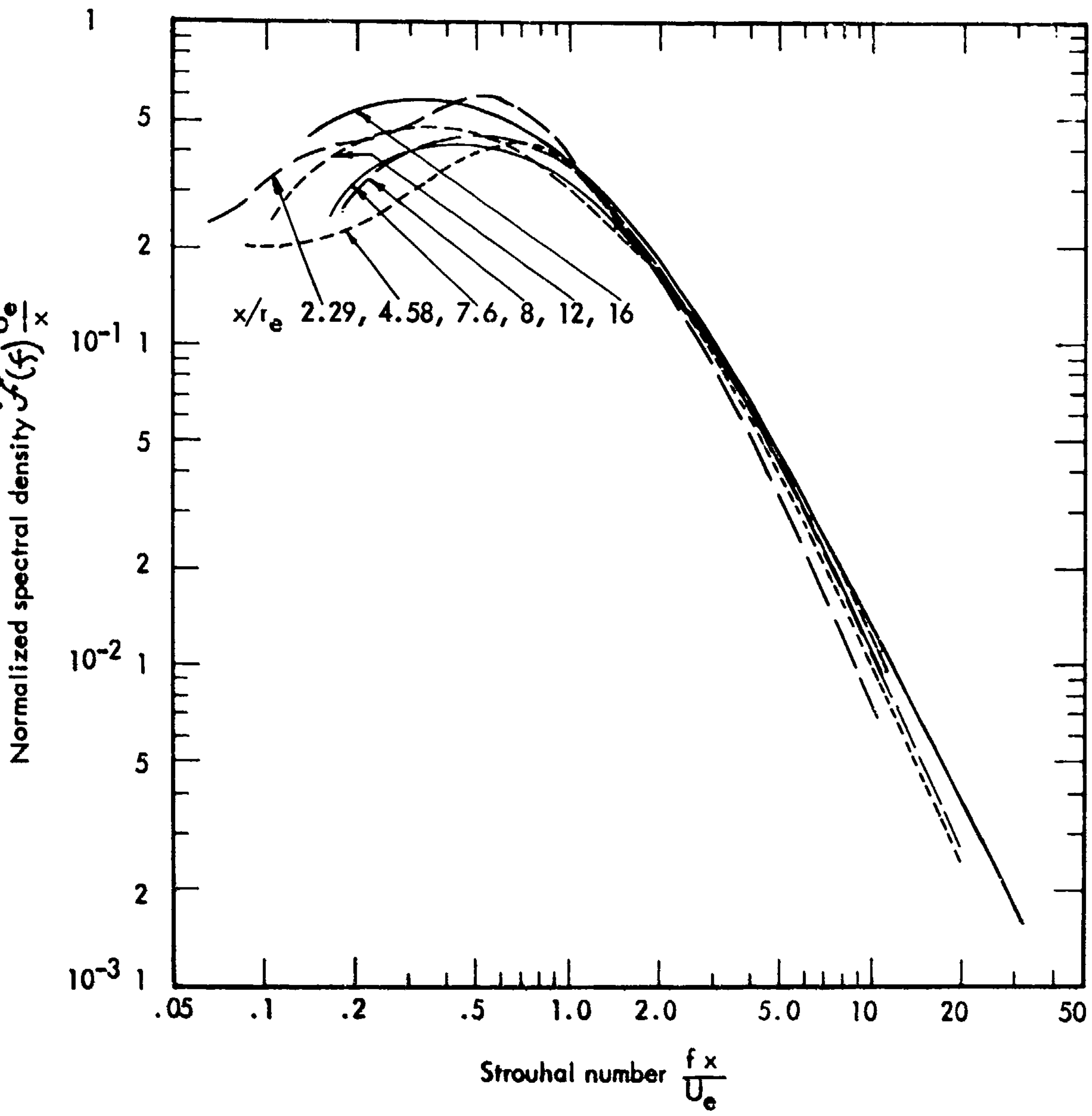

Figure 5. Longitudinal turbulent spectra from previous figure normalized by a Strouhal number based on axial distance.

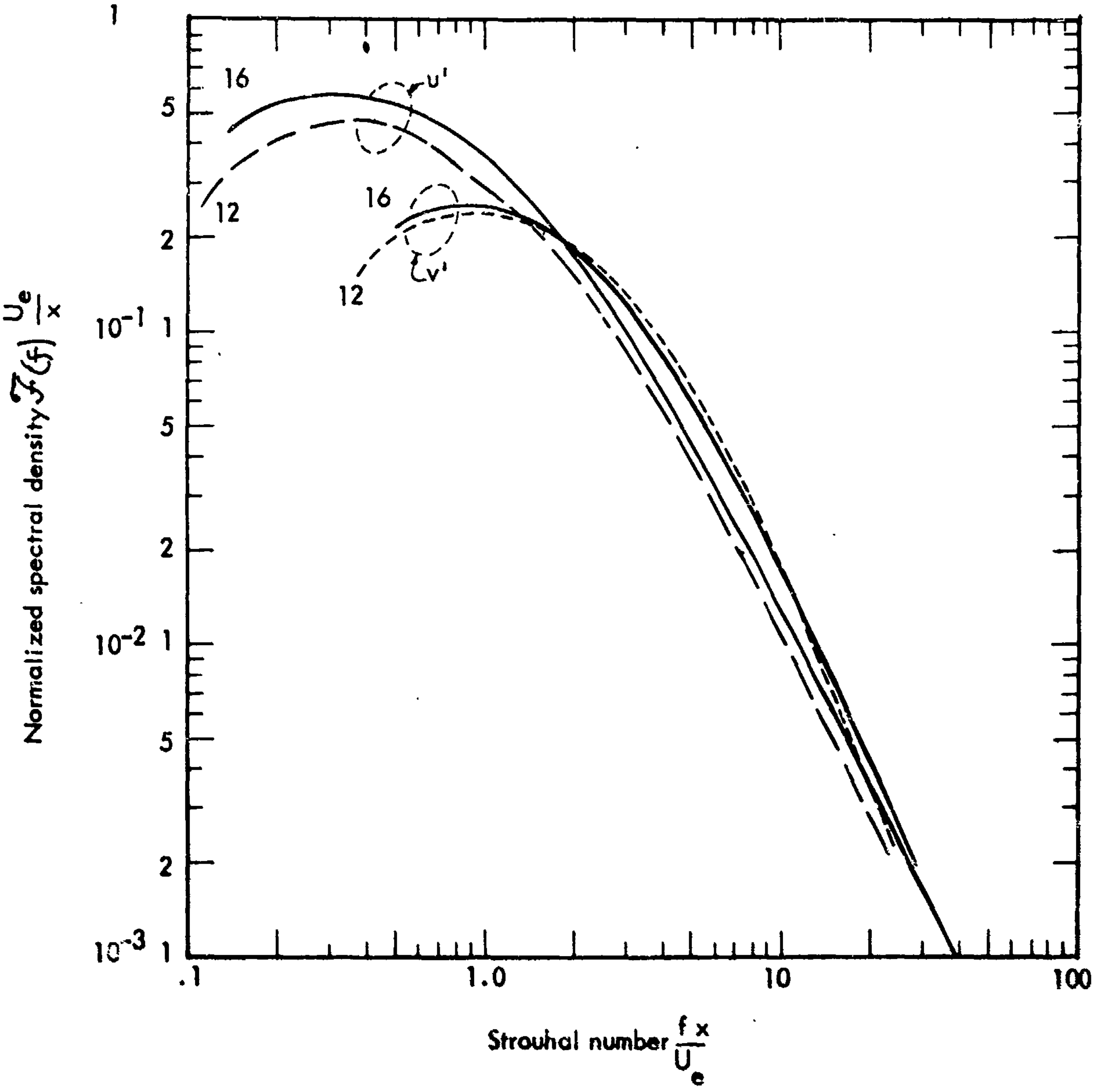

Figure 6. Turbulent spectra at x/r = 12, 16 in both axial (u') and radial (v') directions, normalized by a Strouhal number based on axial distance, data from Laurence.

the frequency scale in figure 4 is equivalent to U_c/λ, and the similarity found in figures 5 and 6 really applies to the distribution of turbulent energy with respect to eddy size, rather than with respect to actual turbulent frequencies.

The rate of the spread of the mixing region in the flow is governed by the turbulent shear stress (τ) which, for an axisymmetric flow, is given primarily by $\rho \overline{uv}$ where u and v are the instantaneous velocity fluctuations in the longitudinal and lateral directions, respectively. There is considerable evidence in Anderson and Johns' work (Ref. 10) that the length of the core of an axially symmetric jet increases significantly at higher Mach numbers, implying a reduction τ with an increase of Mach number. The relationship between τ and M is also significant for noise generation since the primary noise source term is the second time derivative of τ. Unfortunately, no measurements of τ itself could be found for flows with nozzle Mach numbers greater than approximately .2. However, Laurence (Ref. 6) gives profiles of the longitudinal velocity fluctuations over a Mach range from .2 to .7 which show a decrease in the ratio of rms turbulent velocity to exit velocity (u'/U_e) as Mach number is increased. These data afford an opportunity to determine the approximation variation τ with Mach number.

Several investigators, including Prandtl, Taylor and vonKarmen, have proposed expressions which relate the turbulent shear stress to the gross flow parameters (Ref. 11). Of these expressions, the concept of a constant exchange coefficient E across the mixing region, such that $\tau = \rho E \frac{dU}{dy}$, and the original Prandtl mixing length hypotheses, are most readily applied to jet flows.

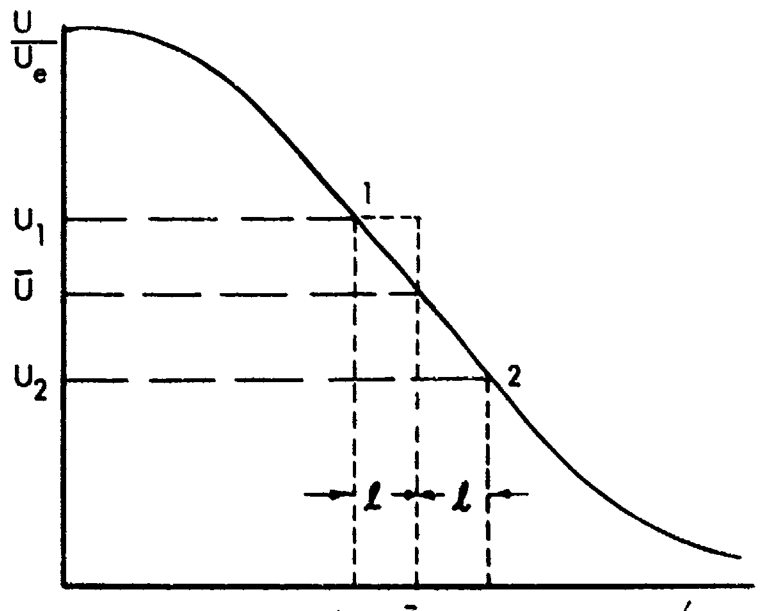

Figure 7. Illustration of Prandtl mixing length hypothesis.

The mixture length (ℓ) in Prandtl's hypothesis is analogous to the mean free path in the kinetic theory of gasses. If a small mass of fluid initially at radius r_1, and velocity U_1, as illustrated in figure 7, is displaced radially outward to $\bar{r}$, it gives rise to an increase of velocity at $\bar{r}$, the magnitude of the increase Δu being equal to $U_1 - \bar{U}$.. Similarly, a small mass of fluid at r_2 displaced inward to $\bar{r}$ results in a decrease in the velocity at $\bar{r}$ of magnitude $\bar{U} - U_2$. With this assumption, the rms fluctuating longitudinal velocity component u' at $\bar{r}$ is:

$$u' \sim 1/2 \left(|\Delta U_1| + |\Delta U_2| \right) \sim \ell \left| \frac{dU}{dr} \right|$$

where $\Delta U_1 = U_1 - \bar{U} = \mathcal{U}(\bar{r} - \ell) - \mathcal{U}(\bar{r}) = \ell \frac{dU}{dr}$ + higher order terms.

Taking the lateral velocity component proportional to the longitudinal component, the shear stress becomes:

$$\tau \sim \rho \ell^2 \left| \frac{dU}{dr} \right| \frac{dU}{dr} = k \rho \ell^2 \left| \frac{dU}{dr} \right| \frac{dU}{dr}$$

where the absolute value of $\frac{dU}{dr}$ is utilized to insure that τ has the same sign as $\frac{dU}{dr}$

Defining a non-dimensional mixing length parameter δ, where

$$\delta = \frac{\ell}{r_e} = \frac{u'}{r_e \frac{dU}{dr}} = f(r/r_e, x/r_e, M, Re)$$

the Laurence data were examined to determine the functional dependence of δ on radial and axial position, Mach number and Reynolds number.

Figure 8 gives δ/δ_{av} as a function of radial position and at various axial distances where δ_{av} is the average value of δ across the central mixing zone at each station and for each Mach number. Superimposed on the scatter of approximately ±10% appears to be a systematic variation in the mean line with the value of δ at the center of the mixing zone approximately 4% above its average value.

The variation of δ_{av} with axial position is given in figure 9. The data clearly show that δ_{av} is a linear function of axial distance and a function of Mach and/or Reynolds number. Although it is not possible to separate the latter effects in the present data because only one size jet was utilized, the Reynolds number, which was above 192,000 for the various experiments, is sufficiently high to expect that fully turbulent flow develops in the mixing region in a relatively short distance downstream from the nozzle. Therefore, it is probable that the major factor is Mach number. The magnitude of the dependence of δ_{av} on Mach number is shown in figure 10, where $\left(k_1 = \frac{\delta_{av}}{x/r_e}\right)$ is given as a function of Mach number. The relationship between the lateral scale of turbulence found by

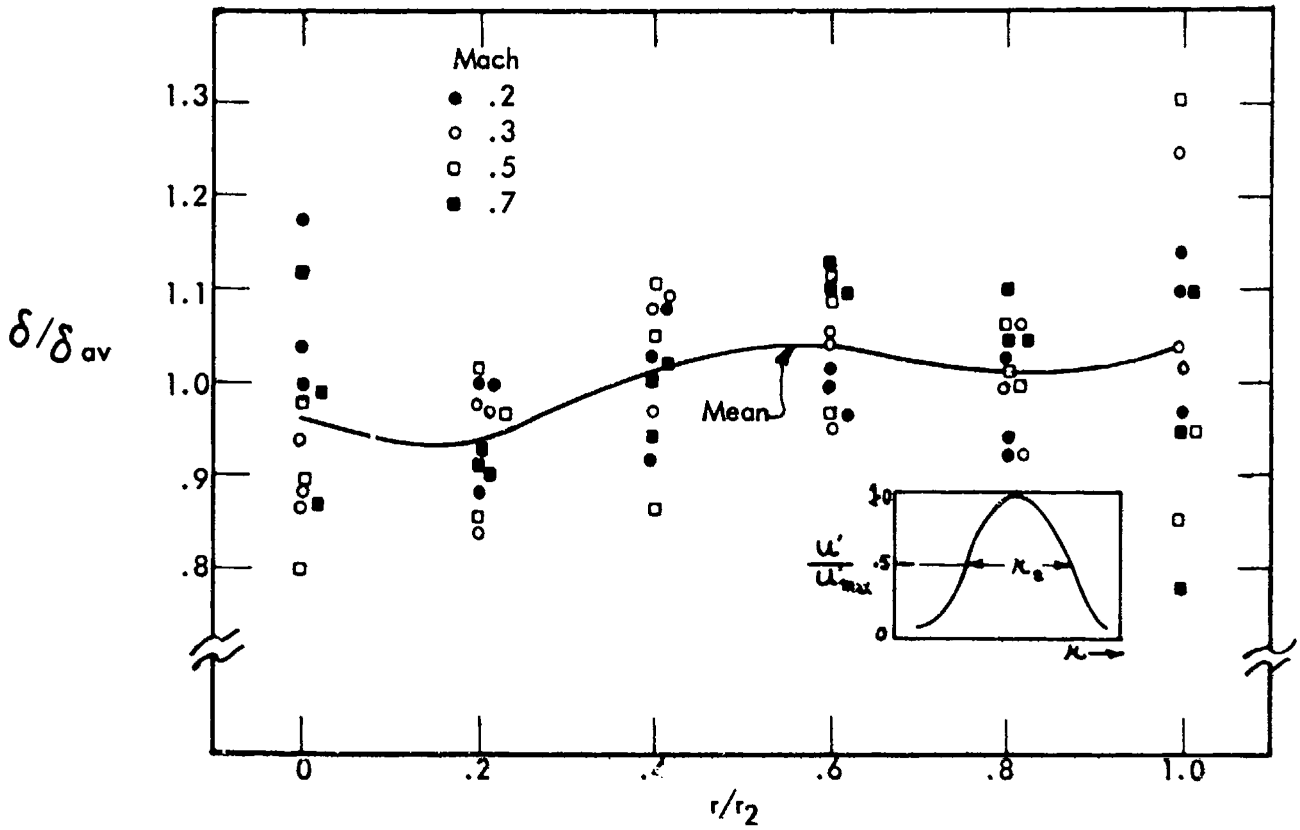

Figure 8. Variation of δ/δ_{av} with r/r_2 where r_2 is the width of the central mixing zone defined as the distance between the points where $u'/u'_{max} = 1/2$ for $x/r_e = 2.29$, 4.58 and 7.6. Data from Laurence.

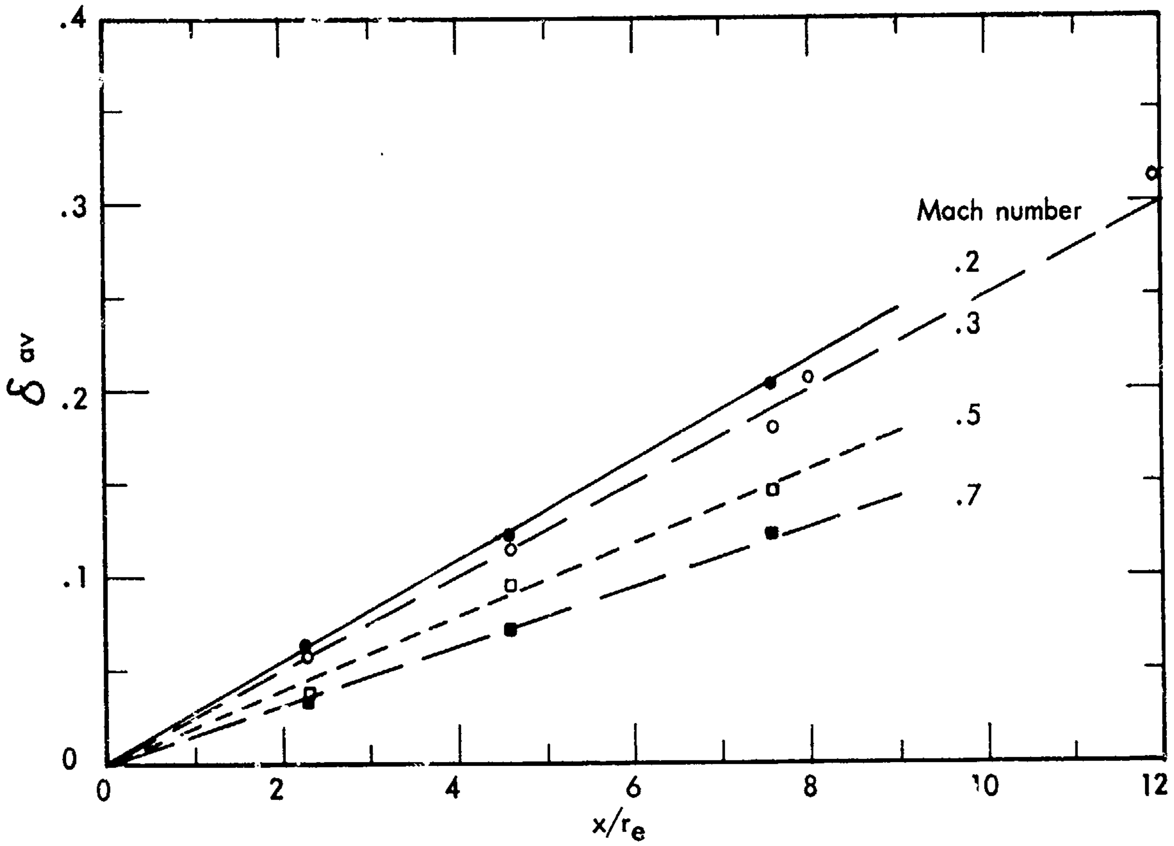

Figure 9. Variation of δ_{av} with axial distance for various Mach numbers, data from Laurence.

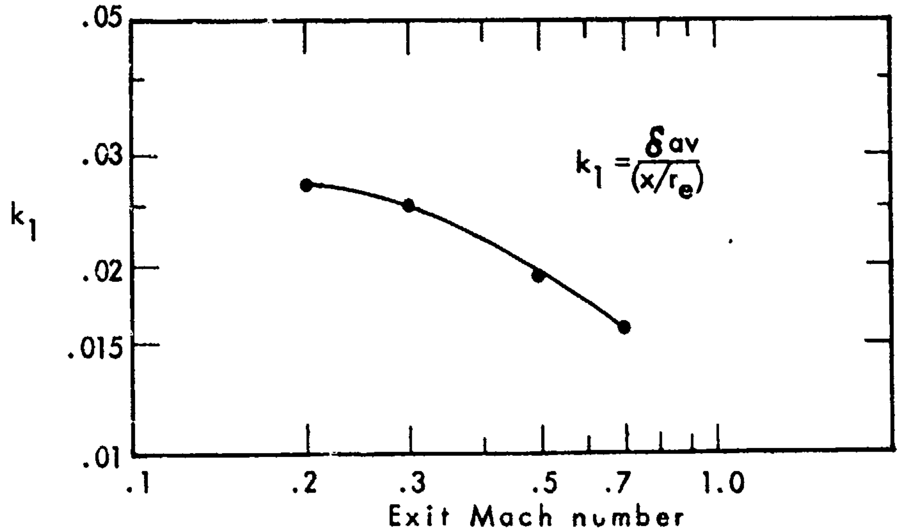

Figure 10. Variation of k_1 with Mach number, data from Laurence.

Laurence in his spacial correlations and the ℓ defined by the mixing length hypothesis is shown in figure 11. At Mach .3, ℓ is approximately 2/3 of the conventional lateral scale of turbulence $\mathcal{L}_y$ where

$$\mathcal{L}_y = \int_0^\infty R_y \, dy$$

and R_y is the correlation of longitudinal velocity fluctuations as a function of lateral distance (y) between the measurement points.

To the extent that the mixing length hypothesis represents the gross turbulent mixing process in the region of maximum jet shear, the frequency of the turbulence (f) in the coordinate system moving at the mean eddy convection velocity is of the order of

$$f \sim \frac{u'}{2\ell} = \frac{1}{2}\frac{dU}{dr}$$

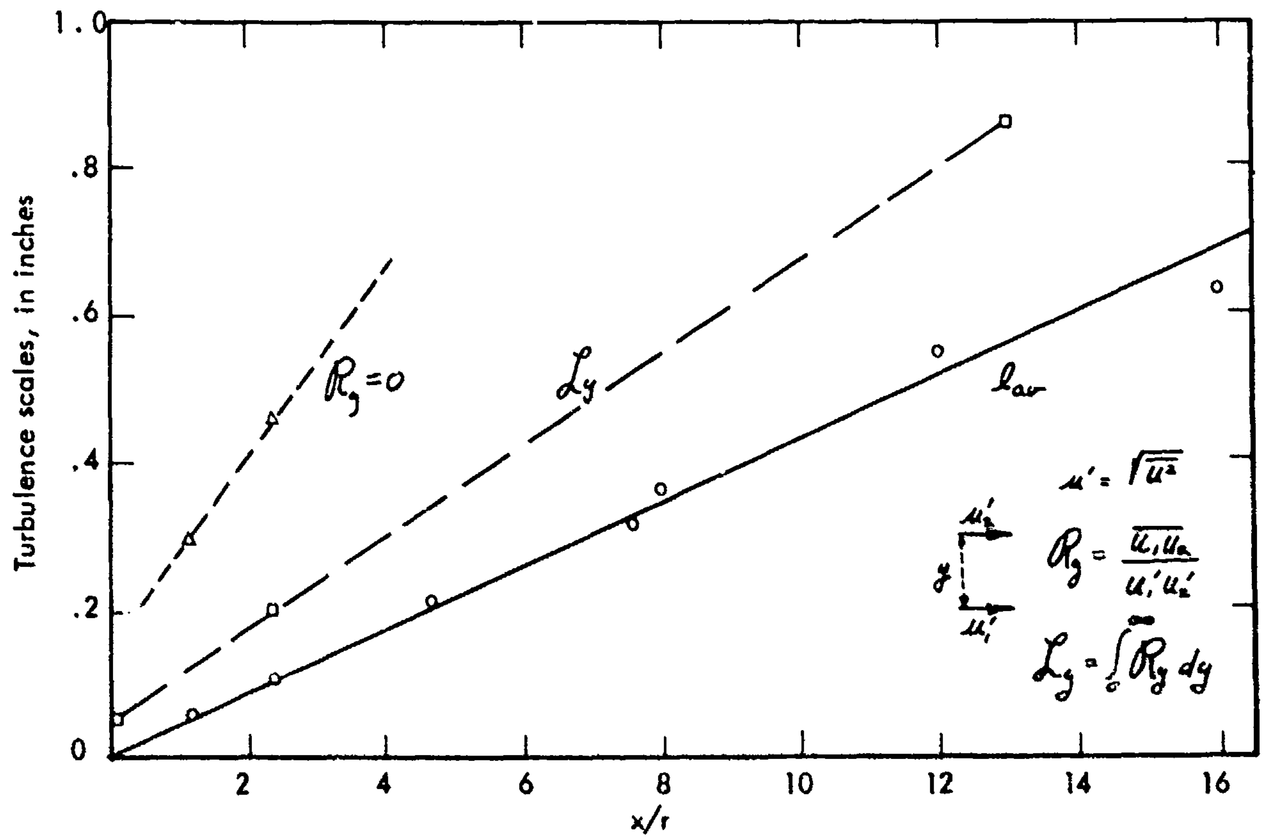

Figure 11. Comparison of lateral scale of turbulence at Mach .3 with mixing length as a function of axial distance, data from Laurence.

As will be shown later, the maximum velocity gradient at the tip of the core is equal to $1.2 \frac{U_e}{d}$ where d is the jet exit diameter. Hence, with these assumptions, the predicted center frequency of the turbulence at the core tip would be of the order of $.6 \frac{U_e}{d}$, or equivalently, the Strouhal number based on exit diameter and velocity would be approximately .6 at the core tip.

Jet Flow Similarity

The flow of a fully turbulent axisymmetric and a two-dimensional slot jet with zero external velocity ($U_o = 0$), and constant density has been investigated theoretically by several individuals (Refs. 11, 12). More recently, Szablewski (Ref. 13) undertook solution of the downstream fully developed flow for variable jet density and $U_o > 0$.

The flow in the mixing region adjacent to the core was first solved by Kuethe (Ref. 14) for a constant density jet with $U_o = 0$. His solution contained an asymptotic velocity profile obtained through an iterative procedure. Later, Squire and Trouncer (Ref. 15) obtained solutions for the complete constant density jet with variable external velocity utilizing a (1 - cosine) velocity profile. For the purposes of this study, it was desirable to have a uniform set of flow solutions which included both axisymmetric and slot jets, and which allows extension to high Mach number and/or variable density flows. It was also desirable that the solutions utilize an asymptotic profile which could be readily adapted to concentric and more complicated jet flows. Further, the profile should match the mean flow data and, where possible, agree with the profile of turbulent fluctuations so that it would have general utility in describing the turbulence in the mixing region in terms of noise generation.

An examination of the mean flow profiles in the region adjacent to the core shows that they can be represented by an exponential of the form $e^{-\eta^2/2}$, where η is a non-dimensional shape parameter. The maximum error occurs at the outermost boundary of the flow and is of the order of 4%. Since the low value of shear at the outermost boundary is not important to the overall mixing process, this error is acceptable. This profile function has been previously utilized in the fully developed downstream region by Reichardt (Ref. 16) and others, so that its use enables a simple approximate extension from the core region to the entire flow.

The flow for a constant density axisymmetric jet with variable external velocity, and a constant density slot jet has been derived in Appendix A. The derivations utilize the integral form of the momentum equations described by Goldstein (Ref. 17) and follow the general approach of Squire and Trouncer (Ref. 15). In the derivations the velocity profile was assumed to be $U = U_o + (U_m - U_o)e^{-\eta^2/2}$

where U_o is the external velocity,

U_m is the centerline velocity, and equal to U_e adjacent to the core region

and $\eta = \frac{r - a}{b}$ where a is the distance from the centerline to the outer boundary of the core and b is a width parameter which controls the magnitude of the velocity gradient.

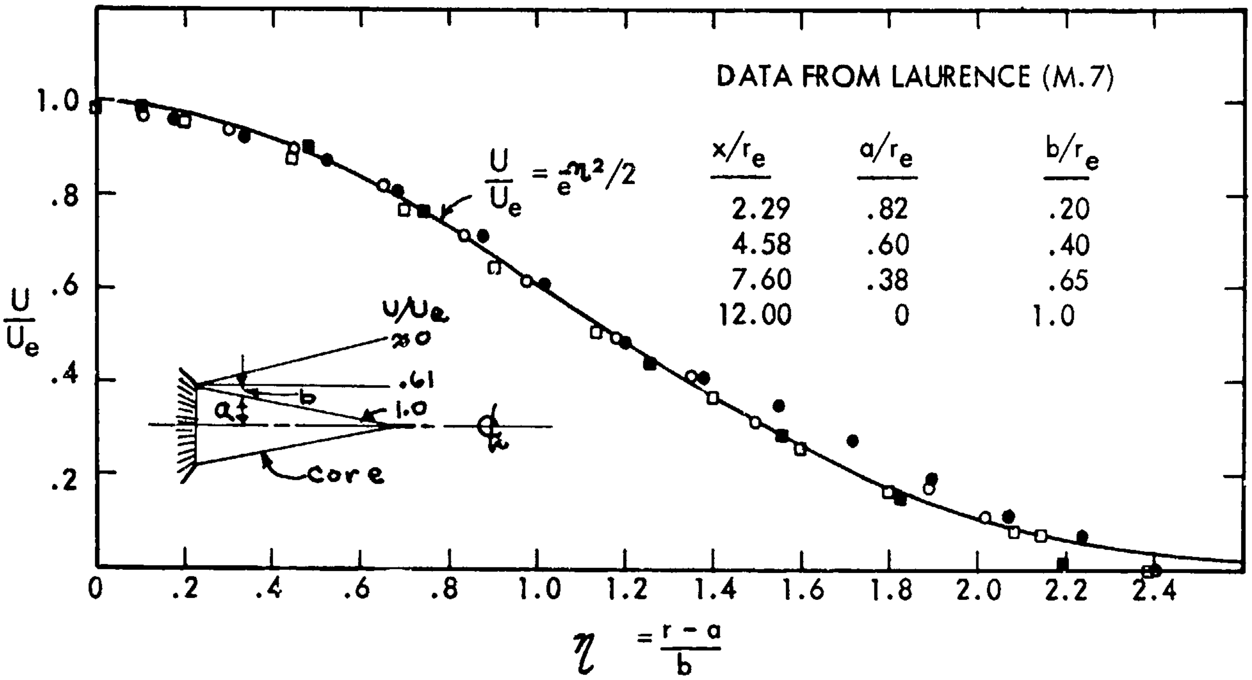

Figure 12. Comparison of assumed velocity profile for axisymmetric constant density jet with Mach .7 data from Laurence.

This profile is compared with Laurence's (Ref. 6) Mach .7 data at various axial stations in figure 12. Note that when $r - a = b$, $\eta = 1$, and $U/(U_m - U_o) = .606$.

The Appendix A solution for relative length of the core $\left(\frac{x_t}{r_e}\right)$ of the axisymmetric jet is

$$\frac{x_t}{r_e} = \frac{.32}{k\,c^2}$$

where $c = \frac{\ell}{b}$ and k is a constant = .88.

It was noted previously that the mixing length ℓ varied as a function of Mach number in the range of M = .2 to .7. Further, the data of Anderson and Johns (Ref. 10) have demonstrated that the relative core length becomes much longer as the exit Mach number is increased. These results have been combined in figure 13 to give the variation of c with Mach number (from Refs. 3, 10, 18, 19). Figure 14 shows the equivalent variation in relative core length with exit Mach number. Perhaps the most interesting feature of these two curves is the small effect which large changes in temperature have on the core length, relative to the significant role of Mach number. In general, the hot, low density, jet core appears to be no more than 20% shorter than the core of a jet of the same exit Mach number which has a total temperature equal to ambient.

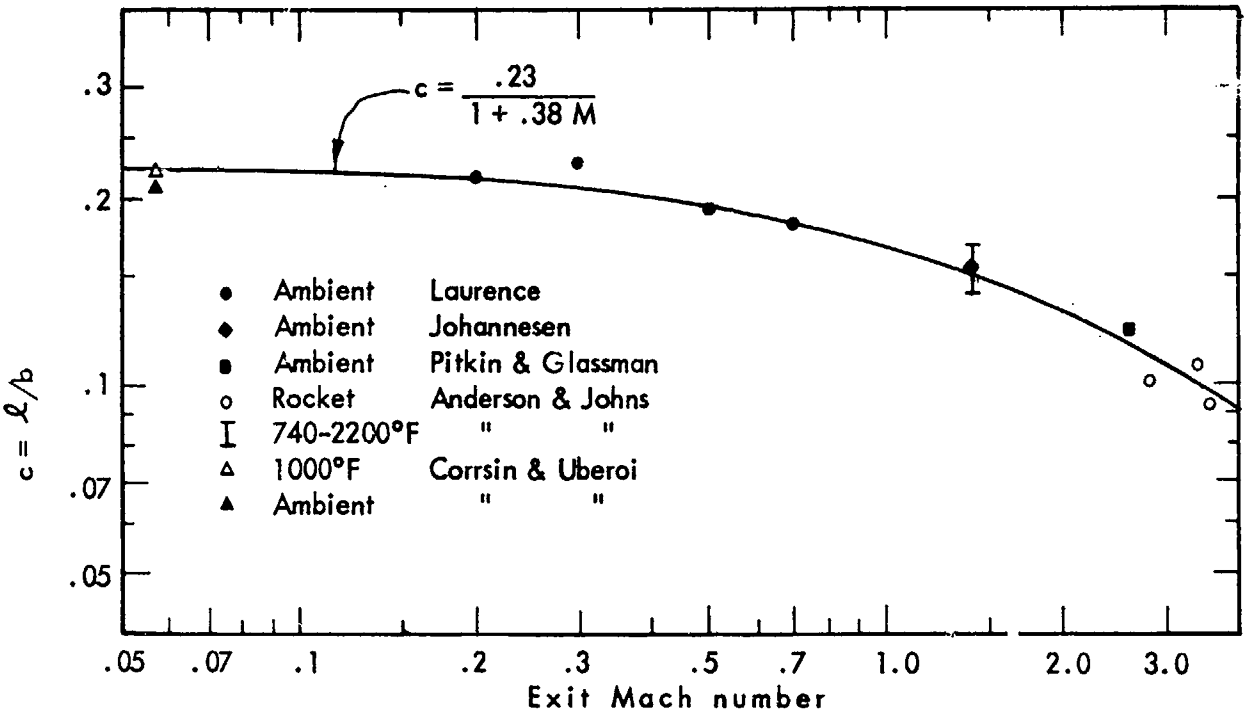

Figure 13. Variation of the constant c with Mach number. c was computed from Laurence turbulence data, and from core length for other data.

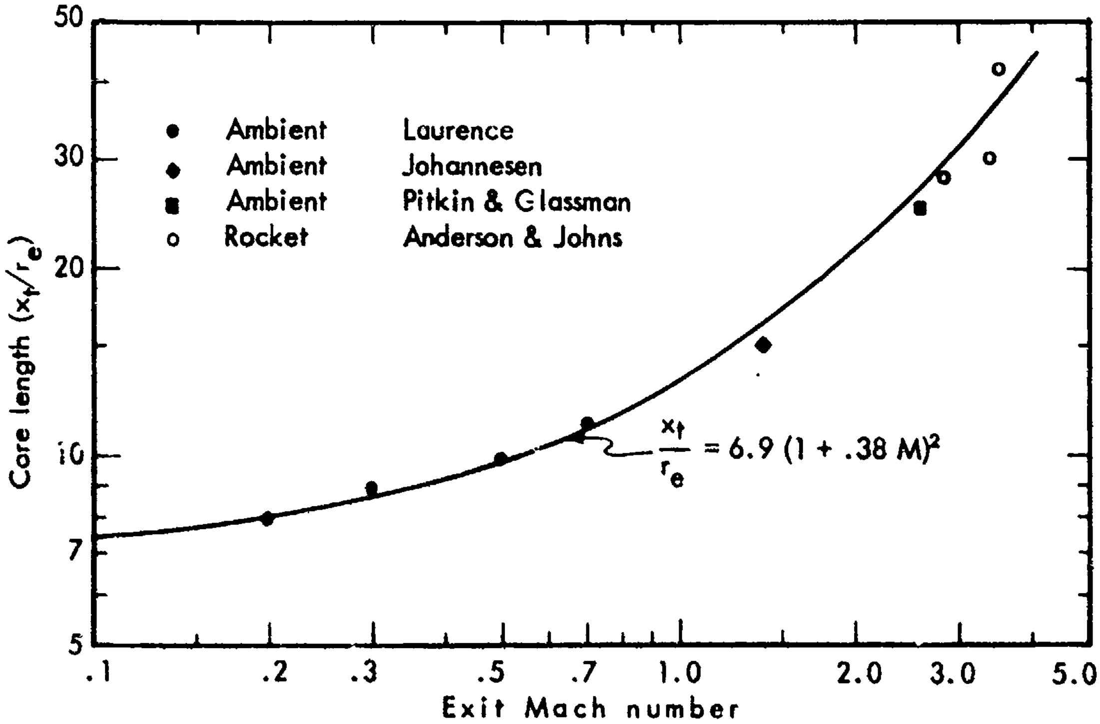

Figure 14. Variation in core length for constant density axisymmetric jet as a function of Mach number.

Several types of theoretical derivations of the variable density jet were conducted under this program. However, the results were inconclusive in that they were excessively dependent upon initial assumptions, particularly in regard to the ratio of heat to momentum transfer which has been variously reported (Ref. 11) through a range of 1.3 - 2.0. These values result from previous theoretical and experimental efforts which were restricted to temperature ratios (jet to ambient) of approximately 2 and in general are limited to low Mach number. From the present investigation it appears that the theoretical solution of the effects of density on jet flow in the primary range of interest requires additional experimental effort to gain a better definition of the relationship between heat and momentum transfer at high Mach number. However, for the present, the indication that a hot jet core length is reduced no more than 20% compared with the ambient jet, is sufficient.

The flow contours calculated from the Appendix A solution for an axisymmetric jet with an exit Mach number of 1 are given in figure 15. The solid contours give the ratio of $\frac{U}{U_e}$ and the dashed contours downstream of the core give the ratio of $\frac{U}{U_m}$, where U_m is the centerline velocity. These contours can be extended to any other Mach number by revising the axial scale by the ratio of $\frac{x_t}{13}$ where x_t is obtained for the new Mach number from figure 14.

Figure 16 shows that the calculated axial decay of the mean velocity in the axisymmetric jet downstream of the nozzle agrees with the data from Laurence (Ref. 6). In addition, figure 16 shows the relative turbulent velocities $\frac{u'_m}{u'_{fm}}$ from Laurence as a function of axial position. Here u'_m is the maximum value of rms turbulent velocity at each axial station and u'_{fm} is the maximum value of u'_m in the entire flow. From the simple flow theory, the axial variation of $\frac{u'_m}{u'_{fm}}$ should be similar to the variation of centerline velocity. This relationship appears to hold to $\frac{x}{r_e}$ of 24. However, farther downstream the turbulence is somewhat greater than would be expected from the local value of the flow gradients. These higher values of $\frac{u'_m}{u'_{fm}}$ probably result from the convection of the more intense turbulence generated upstream past the downstream positions.

Figure 17 gives the calculated flow contours for an axisymmetric jet at Mach 1, with an external velocity U_o equal to one-half of the nozzle exit velocity. The value of c utilized in the equation was chosen at Mach .5, the relative Mach number for the two flows. It is interesting to note that the external flow has lengthened the core to twice the axial distance for zero external velocity.

This result is generalized in figure 18 where the ratio of $x_t/(x_t$ for $U_o = 0)$ is given as a function of U_o. Since this curve depends upon Mach number, through the dependence of c on Mach number, actual computations of core length should be based directly upon the

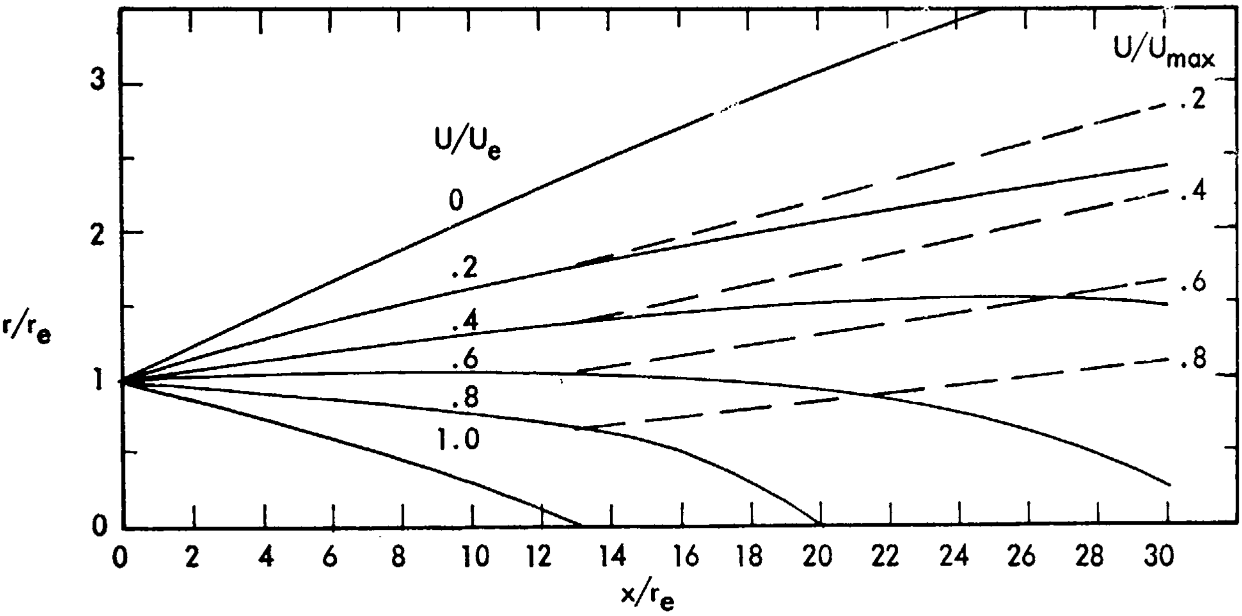

Figure 15. Calculated flow contours for constant density axisymmetric jet with exit Mach number of 1.0, and zero external velocity.

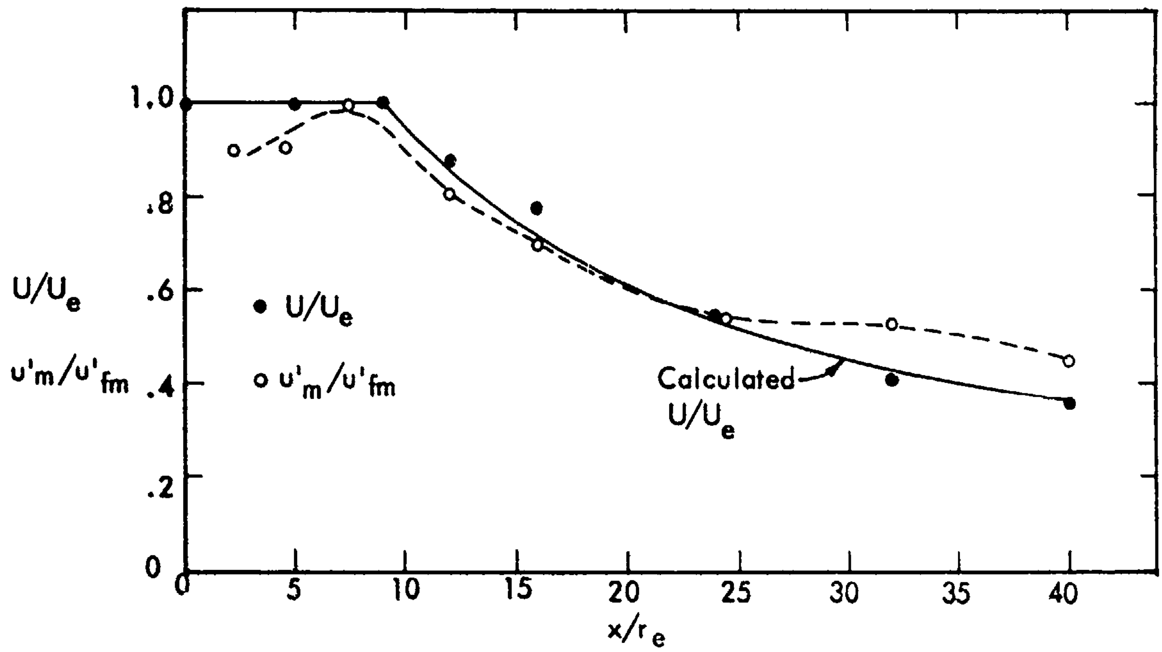

Figure 16. Comparison of relative axial velocity and relative maximum longitudinal turbulence for constant density axisymmetric jet at Mach .3 from Laurence, with calculated axial velocity.

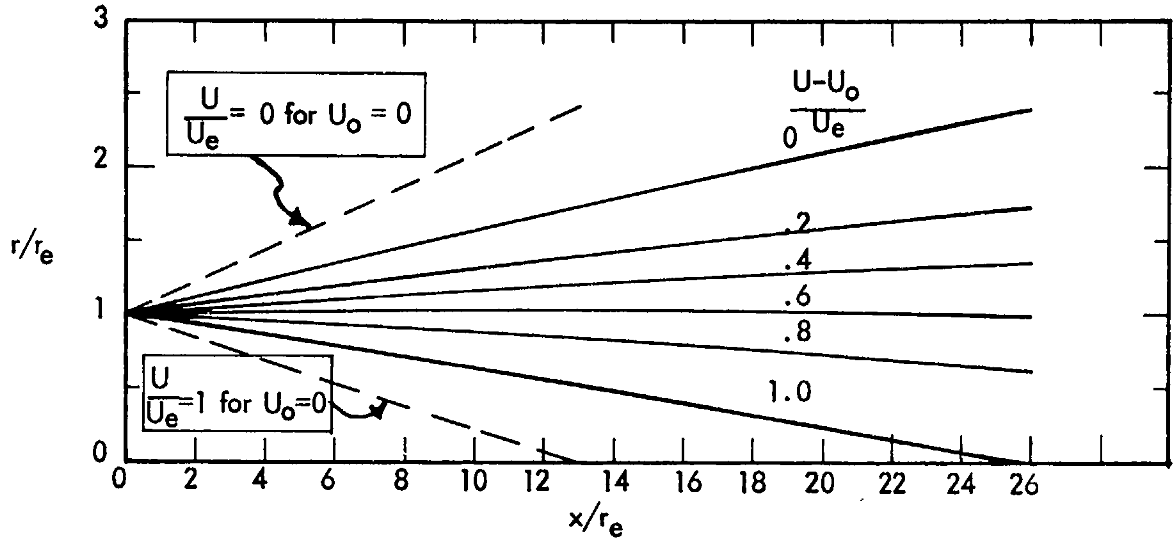

Figure 17. Calculated flow contours for constant density axisymmetric jet with external velocity $U_o = .5\ U_e$, $M_e = 1$, and using c based on relative Mach number.

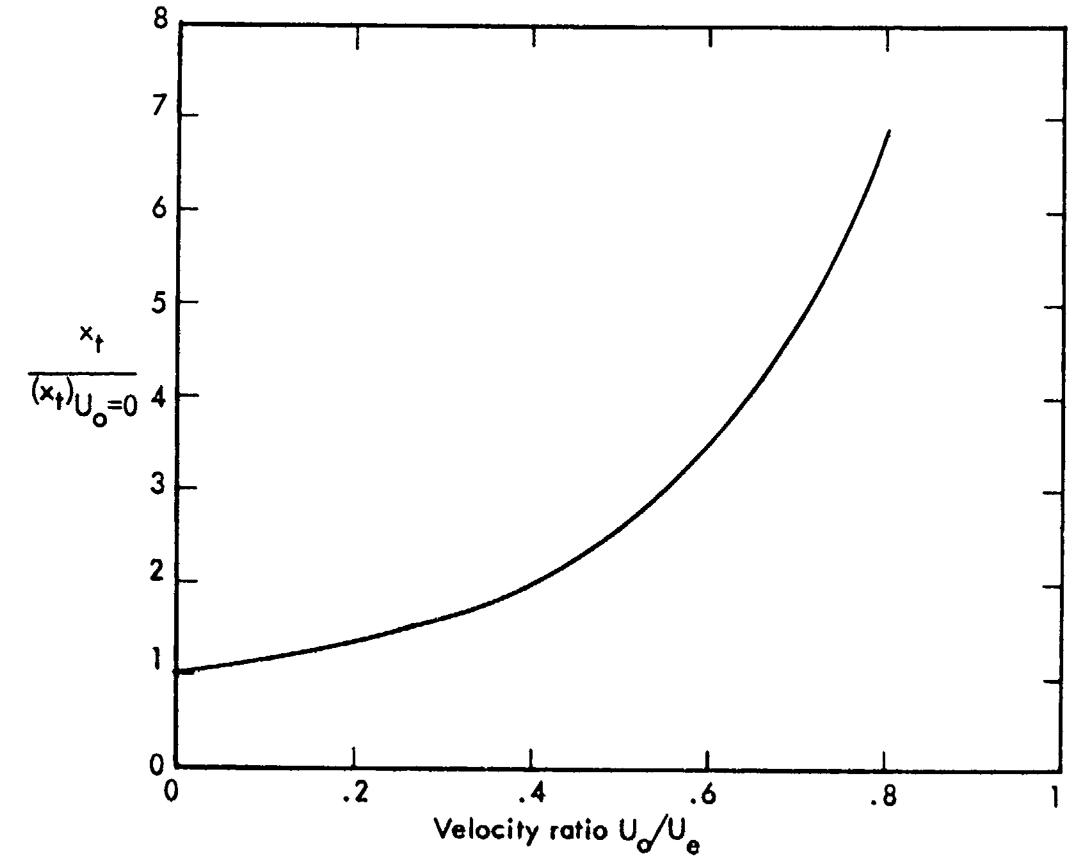

Figure 18. Calculated variation in the core length as a function of the ratio of external velocity (U_o) to jet exit velocity (U_e)(not including variation of c with Mach number.)

Appendix A solution with an appropriate choice of c. However, the qualitative feature of this curve is correct, and illustrates that large increases in core length result when the external velocity becomes appreciable. Therefore, for aircraft in flight, the core mixing region becomes considerably extended and, hence, the near field noise contours are similarly extended downstream.

Figure 19 gives the calculated flow contours for a two-dimensional constant density slot jet utilizing the value of c obtained from the axisymmetric jet. The spread of the slot jet is about 12% greater than that of the axisymmetric jet at similar positions in the mixing region adjacent to the core. However, downstream of the core the slot jet spreads much more slowly than does the axisymmetric jet, because the slot jet's centerline velocity falls off proportional to $(x)^{-1/2}$, rather than proportional to x^{-1} as found for the axisymmetric jet. This difference is illustrated in figure 20 where U/U_{max} on the centerline for a 3.14 x 1 inch rectangular jet is compared with the computed value for the slot jet. It is believed that the aspect ratio of 3.14 is probably not quite sufficient to approximate a true two-dimensional jet and, hence, the solid symbols which represent the flow of the inner nozzles are probably more representative. Therefore, the computed core is somewhat too short, indicating that the correct value of c is slightly lower for the slot jet than for the axisymmetric jet.

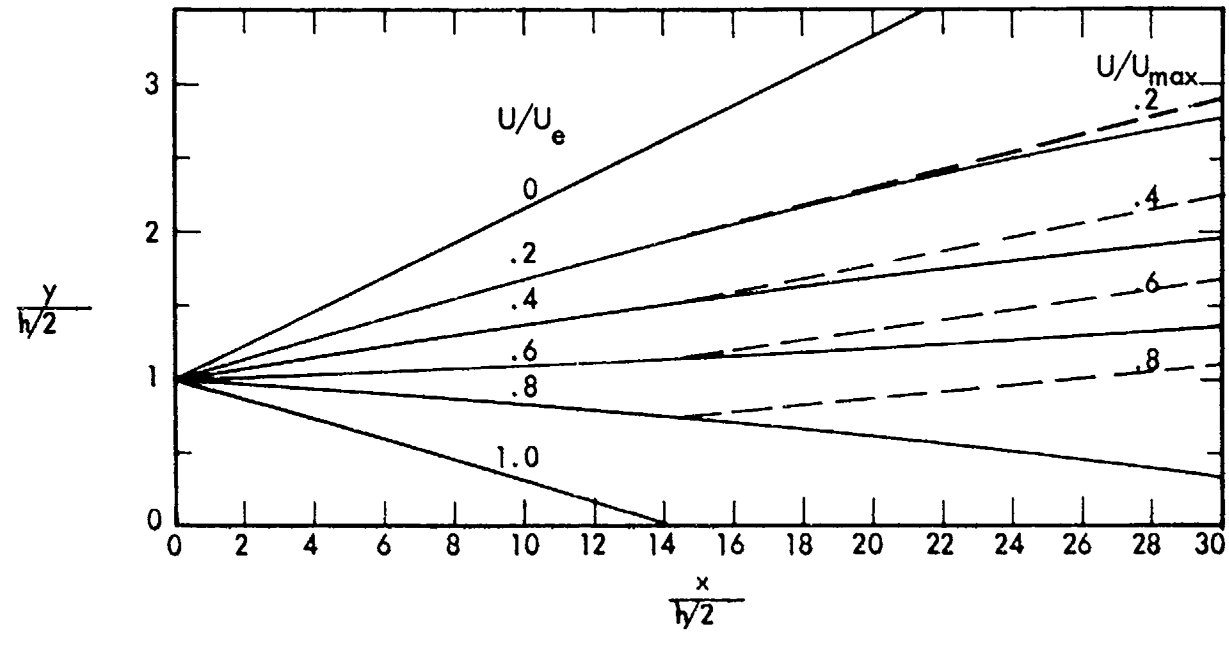

Figure 19. Calculated flow contours for a constant density slot jet with exit Mach number of 1.0 and zero external velocity

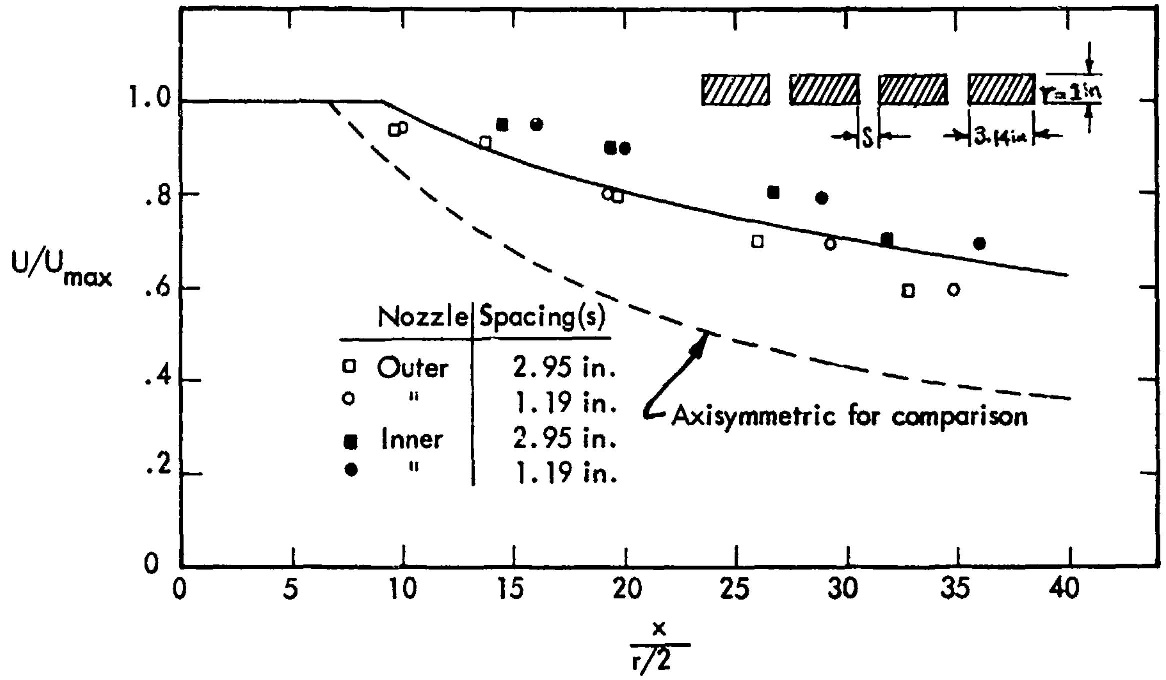

Figure 20. Axial decay of velocity computed for Mach .3 slot jet using ($k\ c^2$) from axisymmetric jet. Data are for 3.14 x 1 in. nozzles with two spacings from Laurence, NACA TN 4029.

LIST OF SYMBOLS USED IN SECTION II

Roman

a	Distance from centerline to boundary of core
b	Velocity gradient width parameter
c	ℓ/b
d	Diameter
E	Momentum exchange coefficient
$\mathcal{F}(f)$	Normalized longitudinal velocity spectral density
f	Frequency
h	Thickness of slot jet flow
k	Proportionality coefficient
ℓ	Prandtl mixing length
$\mathcal{L}_y$	Lateral scale of turbulence
M	Mach number
$\mathcal{R}$	Correlation of longitudinal velocity fluctuations
Re	Reynolds number
r	Radius
U	Flow velocity
u	Instantaneous longitudinal velocity fluctuations
v	Instantaneous lateral velocity fluctuations
x	Axial distance from exit plane
y	Lateral distance from centerline

Greek

δ	Non-dimensional mixing length
λ	Characteristic eddy size
η	Non-dimensional shape parameter
ρ	Density
τ	Turbulent shear stress

Subscripts

c	Characteristic
e	Exit
f	Flow
m	Maximum at a given axial station
o	Ambient
oa	Overall level
t	Core tip
x	As a function of longitudinal distance between measurement points
y	As a function of lateral distance between measurement points

Superscripts

$\overline{}$	Mean
'	Root mean square

Section II

References

1. Ribner, H. S., "On the Strength Distribution of Noise Sources Along a Jet" ASTIA AD 154264 April 1958. Institute of Aerophysics, University of Toronto.

2. Corrsin, Stanley, "Investigation of Flow in an Axially Symmetrical Heated Jet of Air," NACA ACR No. 3L23, December 1943.

3. Corrsin, C., Uberoi, M., "Furthe Experiments on the Flow and Heat Transfer in a Heated Turbulent Air Jet." NACA Report 998, 1950.

4. Corrsin, C., Uberoi, M., "Spectra and Diffusion in a Round Turbulent Jet." NACA Report 1040, 1951.

5. Liepmann, H. W., Laufer, J., "Investigations of Free Turbulent Mixing," NACA Report 1257, 1947.

6. Laurence, J. C., "Intensity, Scale and Spectra of Turbulence in Mixing Region of Free Subsonic Jet." NACA Report 1292, 1956.

7. Laurence, J. C., Benninghoff, J. M., "Turbulence Measurements in Multiple Interfering Air Jets," NACA TN 4029, 1957.

8. Laurence, J. C., "Turbulence Studies of a Rectangular Slotted Noise Suppressor Nozzle," NASA TN D-294, 1960.

9. Taylor, G. I., "Statistical Theory of Turbulence. Parts I - IV," Proceedings of the Royal Society, A-151, pp 421-478, 1935.

10. Anderson, Arthur, Johns, Frank, "Non-dimensional Characteristics of Free and Deflected Supersonic Jets Exhausting into Quiescent Air," WADC-ED-5401, March 1954.

11. Schlichting, Hermann, "Boundary Layer Theory," Pergamon Press, 1955.

12. Pai, S., "Fluid Dynamics of Jets," van Norstand Co., 1954.

13. Szablewski, W., "The Diffusion of a Hot Air Jet in Air in Motion," NACA TM 1288, 1960.

14. Kuethe, A. M., "Investigation of the Turbulent Mixing Regions Formed by Jets," Journal of Applied Mechanics, pp A87 - A95, 1935.

(continued)

Section II References (continued)

15. Squire, H. B., Trouncer, J., "Round Jets in a General Stream," RAE Report No. Aero 1904, January 1944.

16. Reichardt, H., "On a New Theory of Free Turbulence," Zamm, Vol. 21, No. 5, October 1941.

17. Goldstein, S., "Modern Developments in Fluid Dynamics," Vol. I, Oxford at the Clarendon Press, 1938.

18. Pitkin, E. T., Glassman, "Experimental Mixing Profiles of a Mach 2.6 Free Jet," ASTIA AD-202294, August 1958.

19. Johannesen, N. H., "The Mixing of Free Axially Symmetrical Jets of Mach Number 1.40," ASTIA AD-203564, January 1957.

SECTION III

THE NEAR NOISE FIELD

The near noise field of a jet is very complex in comparison to the far noise field, since the spacial distribution of the noise sources in the jet and other possible near field effects must be considered. Furthermore, since the measurements required for definition of the near noise field are extensive, only a few relatively complete investigations of a full scale jet engine have been undertaken (Refs. 1, 2, 3). Similar detailed measurements were undertaken for small rockets (Ref. 4) and model cold jets (Refs. 5, 6), but the major volume of other data comes from more limited measurements on a variety of types of jets.

Several efforts (Refs. 2, 6, 7, 8) have been made to generalize some of the existing near field data for use as a prediction model. References 7 and 8 presented simplified empirical models for the noise radiated forward from rocket flows. In addition, Ref. 7 presented a method for rotating the generalized noise contours for a sonic 1000°F jet, to account for higher jet temperatures and to predict aircraft noise environments. Wolfe (Ref. 2) presented the spacial variation of the exponent (n), from assuming sound pressure at a point in the near field proportional to U^n where U is the velocity, for a series of hot jet velocities ranging from 790 - 1800 ft/sec. Howes (Ref. 6) applied and extended similar concepts, which he ascribes to Greatrex (Ref. 9), in the analysis of detailed subsonic cold jet flows.

All of the above efforts to determine useful prediction models are predicated on the similarity of the near noise field from an axisymmetric jet. In this manner, it is unnecessary to postulate the mechanism of noise generation, radiation, and source distribution. All that is required is a demonstration of similarity of the noise field itself. Since various investigators, including Morgan, et al, (Ref. 10), have shown that the near noise field of a jet scales directly with jet size, as long as the flow parameters are held constant, it is only necessary to determine the change in the noise field resulting from density, temperature, and velocity changes in the jet. For the majority of practical applications to aircraft, the jet exit velocity (U_e) is sonic; hence, the temperature, density and velocity are specifically related, and the variation of a single velocity exponent is sufficient to give a practical result. For the more general case, when the exit velocity is subsonic, the variation of the noise field with temperature and velocity must be considered separately.

In the present study, the objective is the prediction of the noise generation and the resulting near field for modified jet flows. Here, the flow is a variable, violating the basic postulate of the foregoing near noise field models. Therefore, it is necessary to determine the relationships between the local jet flow parameters and the characteristics of the local generation and radiation of noise. In the following subsection the noise radiation from a axisymmetric sonic jet will be reviewed, and a generalized model of source generation will be developed.

Characteristics of the Near Noise Field of a 1000°F Axisymmetric Sonic Jet

The most intensive measurements close to a full scale jet were made by NACA (Ref. 1) in a region extending from the jet boundary to approximately 10 feet from the axis at the nozzle end to approximately 30 feet from the axis at a distance of 60 feet downstream from the nozzle. These measurements were made on an engine with 9600 lb. thrust, 1000°F exit temperature, 1850 ft/sec. exit velocity and 1.85 ft. diameter. Because these data are the most complete documentation of the near noise field of any jet known to the author, they have been utilized extensively in this discussion, supplemented, when necessary, by additional data.

Smoothed contours of equal overall noise level for the 1000°F sonic jet are given in figure 21, based on data from Refs. 1* and 3. The figure shows the steep noise gradient forward and to the side of the nozzle, an extended source region along the flow, and a low noise gradient in the direction of the maximum noise generation. Figure 22 gives the spacial distribution (Ref. 1) for three frequencies illustrating the gross shift in the angle of maximum noise generation as function of frequency. As can be seen, noise at 100 cps is directed at a small angle relative to the jet boundary and appears to originate over an extended region of the jet. In contrast, the noise at 2000 cps appears to originate close to the nozzle and is primarily radiated at a large angle from the jet boundary.

The overall noise levels measured (Ref. 1) along a line extending from the nozzle at an angle of 10° to the jet axis are given in figure 23. The third octave spectra for these data are given in figure 24 and the locations of maximum sound pressure levels for these spectra are presented in figure 25. From figure 23 it is clear that the overall noise level along the 10° boundary is constant as a function of axial distance until a short distance beyond the tip of the core, and from there on downstream the noise level decreases rapidly. In figure 24, the one-third octave band spectra all tend to exhibit sharp cutoffs beyond the core tip, and a gross overall similarity. This gross similarity of the noise spectra in the core region would be expected from the similarities previously seen for the turbulence and flow in the same region. From these considerations it would be expected that the axial location of the maximum level for each frequency band would vary inversely with axial distance as shown in figure 25. The departure from the $1/x$ relationship exhibited at the low frequencies in figure 25 results from the general decrease in level and change in similarity downstream of the core.

It would be convenient to utilize the concept of figure 25 to describe the most probable axial locations for the sources at the various frequencies. However, the extended axial distribution of noise in each frequency band shown in figure 24 indicates that this procedure would fail at positions close to the jet, where the length of the source distribution is within an order of magnitude of the distance from the position to the jet. Therefore,

*All data from Ref. 1 have been corrected to rms from original quasi peak Bruel & Kjaer readings by subtracting 2.5 db.

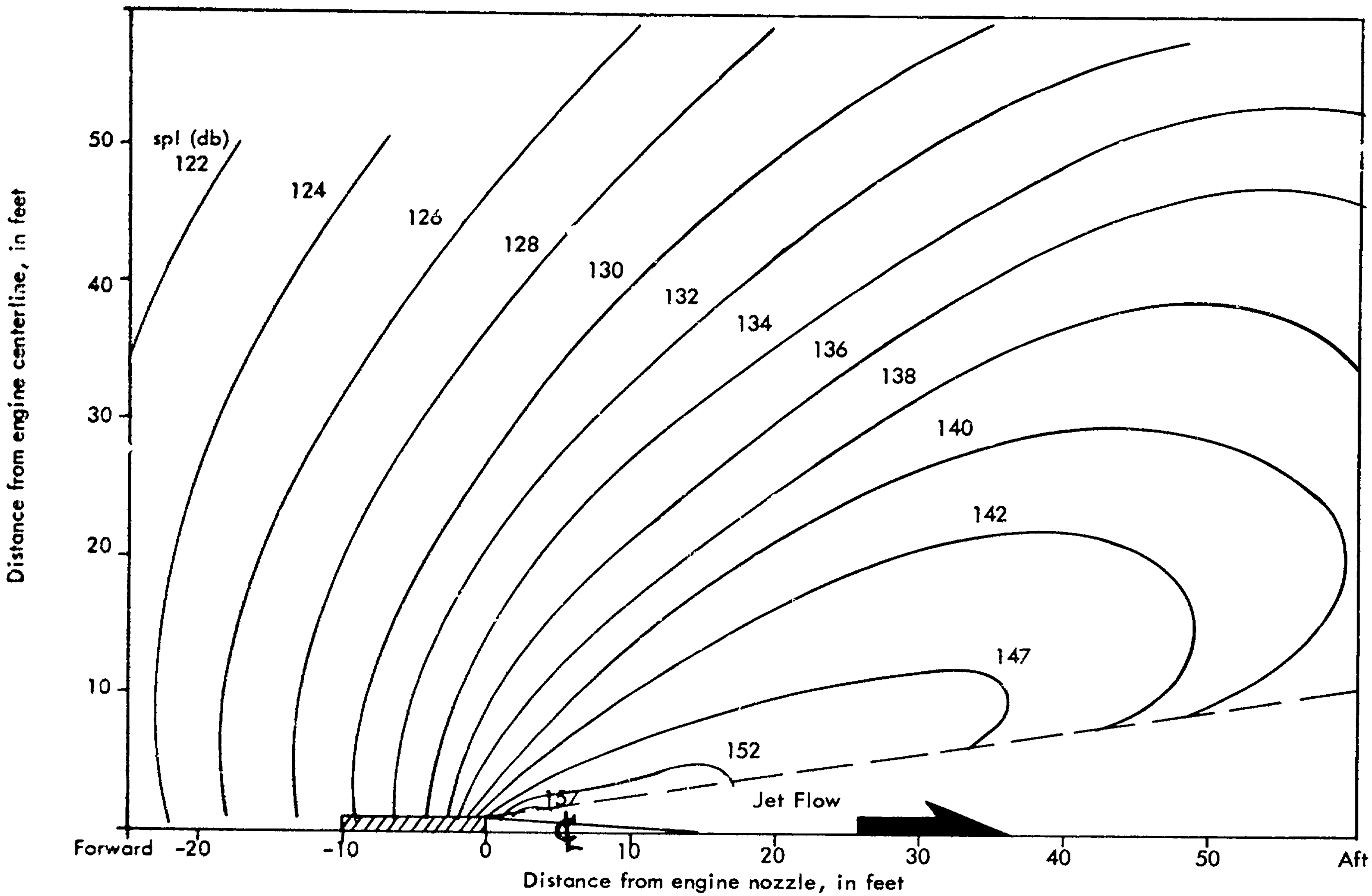

Figure 21. Contours of overall sound pressure level (rms) in db re .0002 dyne/cm² fo J57 engine at military power, from unpublished data by Bioacoustics Branch ASD, and from Howes et al.

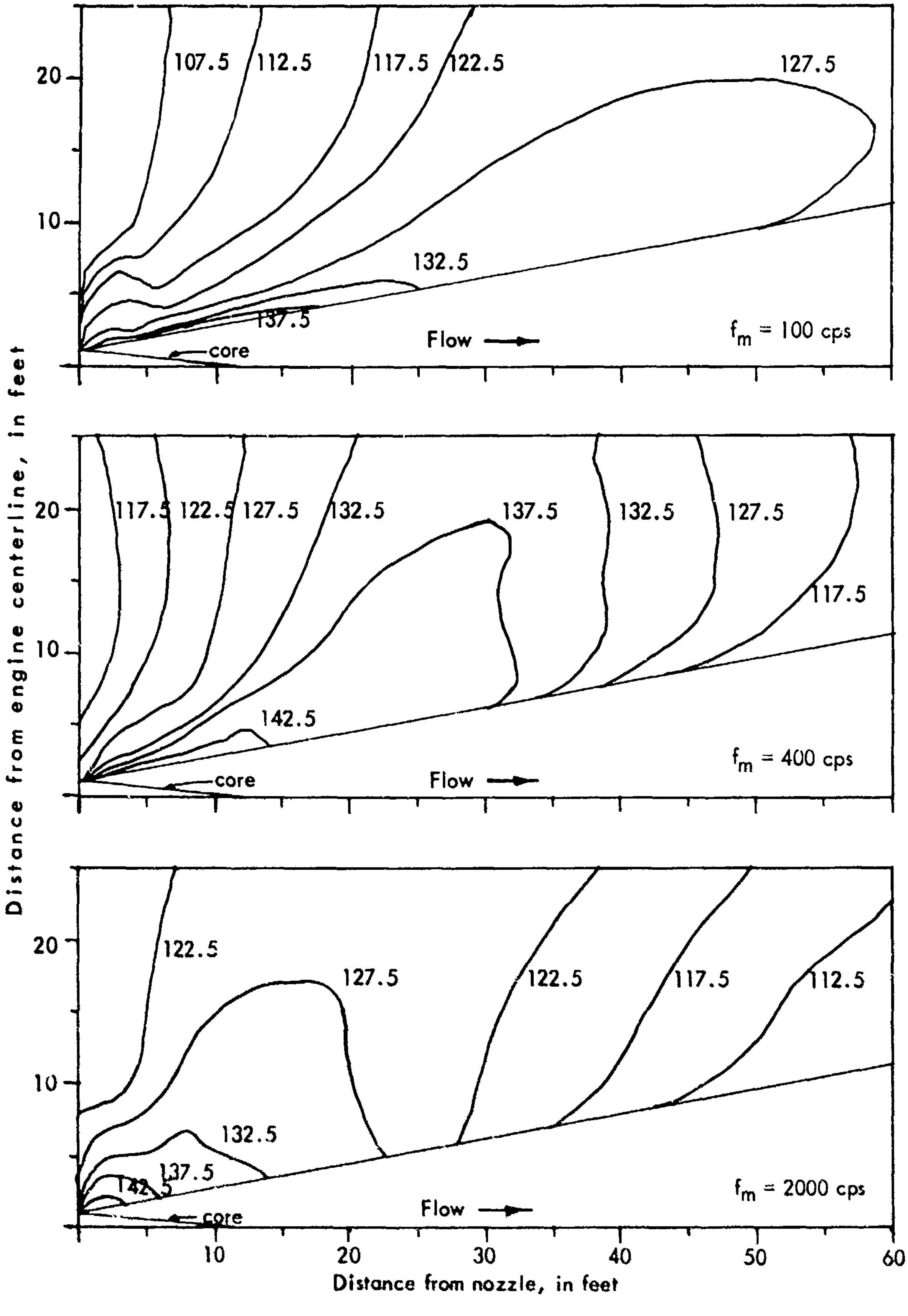

Figure 22. Contours of sound pressure level in db re .0002 dyne/cm^2 in one-third octave bandwidths for J57 engine at military power, data from Howes, et al.

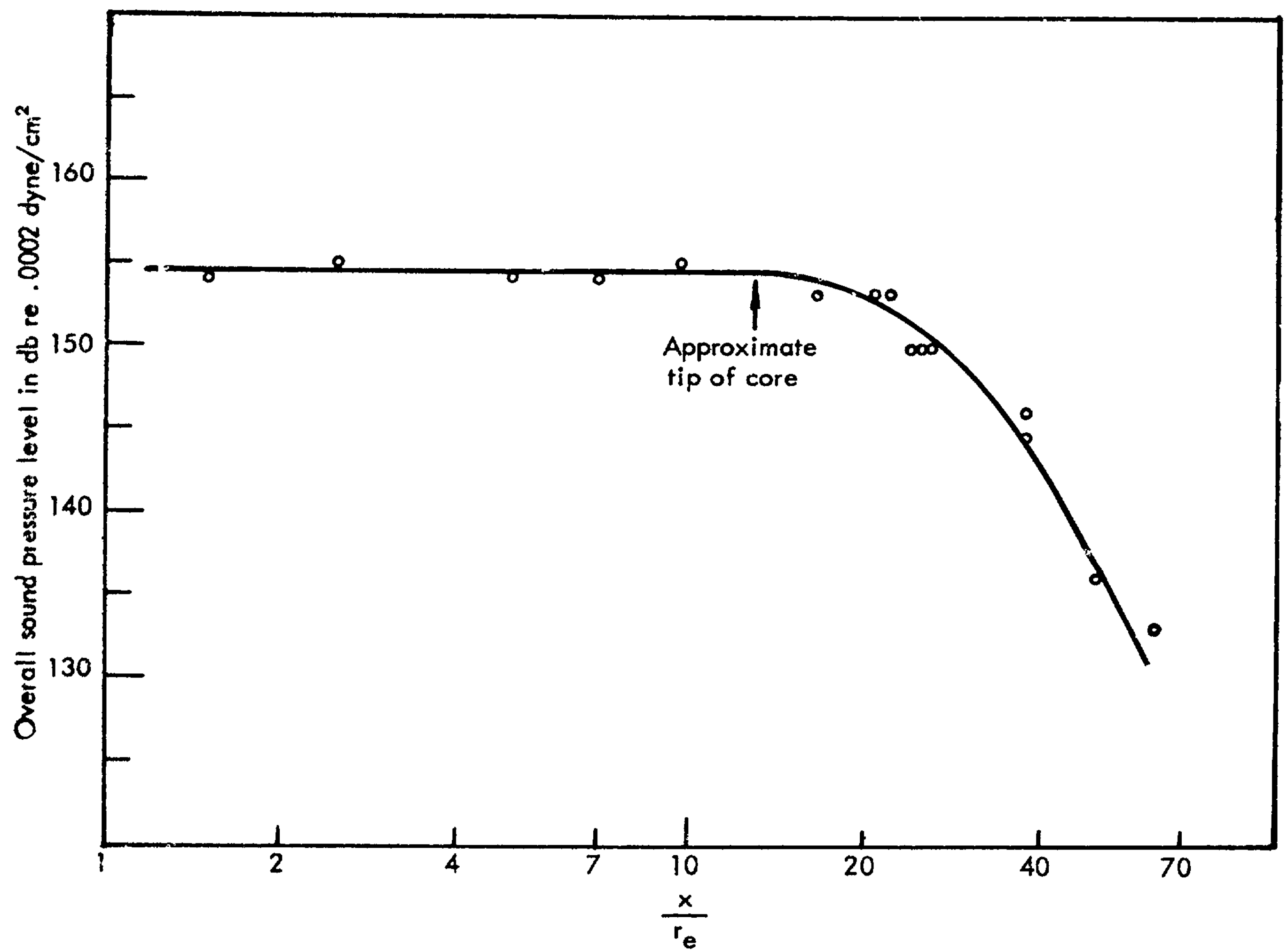

Figure 23. Overall sound pressure level along 10° boundary line, data from Howes, et al

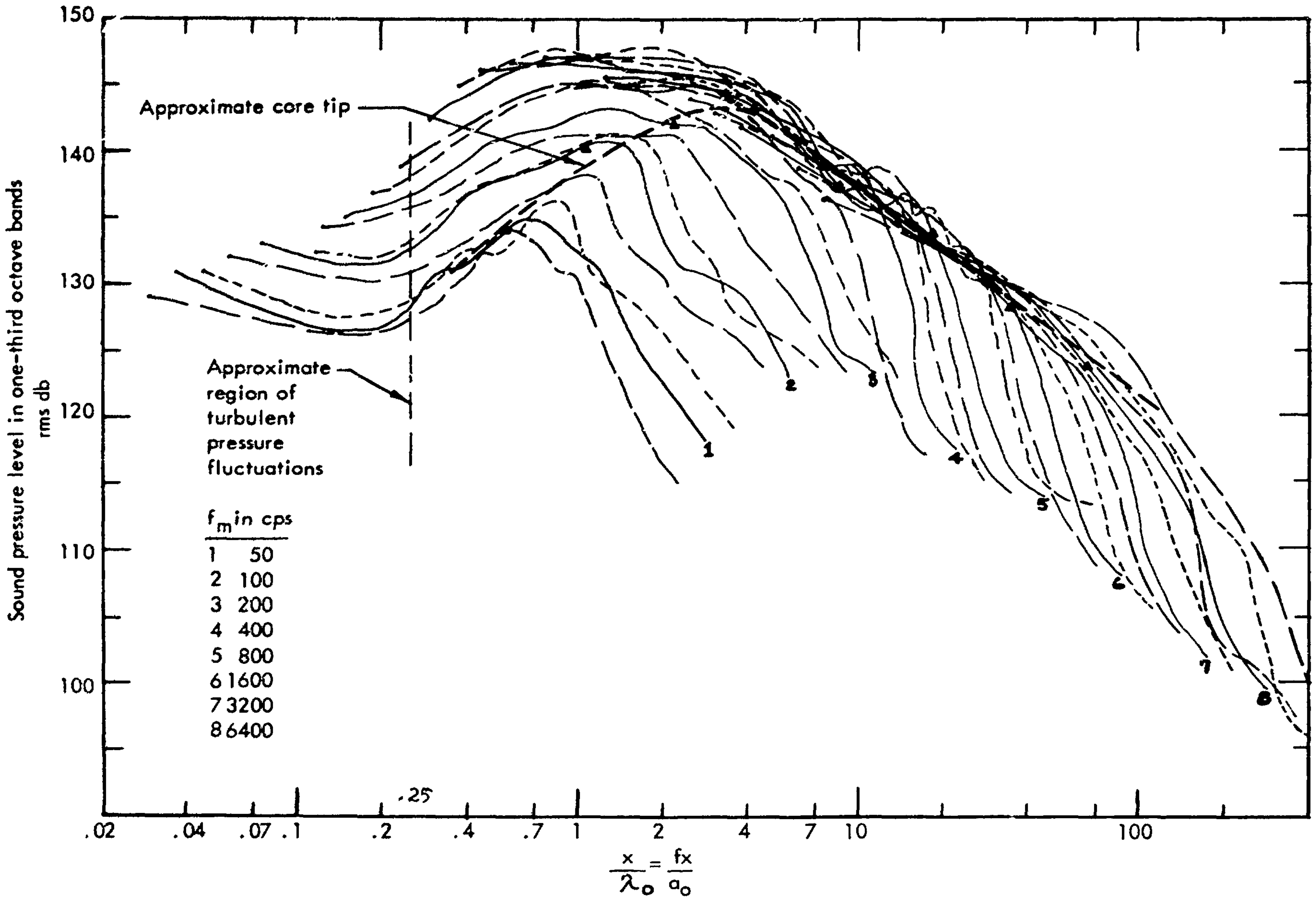

Figure 24. Sound pressure level in one-third octave bands measured along 10° boundary line, data from Howes, et al.

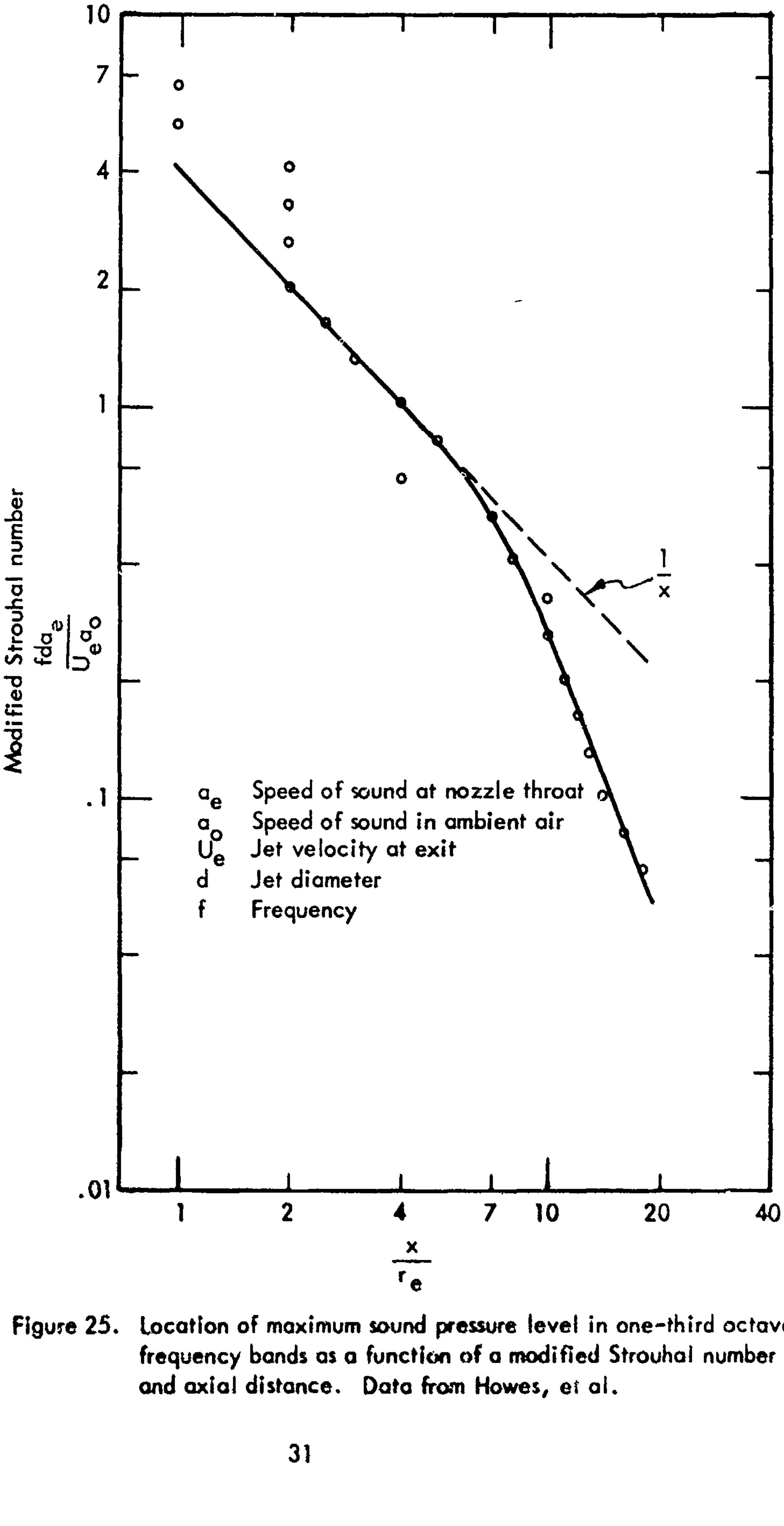

Figure 25. Location of maximum sound pressure level in one-third octave frequency bands as a function of a modified Strouhal number and axial distance. Data from Howes, et al.

it is necessary to include this axial distribution in a prediction method and to determine the directional properties of the radiation for each frequency as a function of axial position.

It was anticipated that the axial distribution of source power would be exceedingly difficult to obtain from boundary measurements because of acoustic near field effects superimposed on the geometrical near field. From consideration of probable acoustic near field effects it was expected that the sound pressures along the jet boundary would include not only the pressures associated with the radiated acoustic power, but additional pressures associated with the non-radiating inductive near field, discussed in detail by Franz (Ref. 12). Furthermore, it was expected that the low frequency pressures very close to the actual jet boundary would contain components of convected large scale eddies as found by Franklin and Foxwell (Ref. 13). These latter pressures from convected turbulence have been identified approximately on figure 24.

In order to obtain a first estimate of the magnitude of the near inductive field effect on the boundary pressure measurements, the approximate acoustic power was computed in each octave frequency band, based on the maximum pressures along the 10° boundary and the area of the truncated 10° boundary cone bounded by the axial stations where the measured pressure was 3 db below maximum. The result of this crude approximation is compared in figure 26 to the generalized J57 far field power spectrum (Ref. 14).

The most striking feature of this comparison is the agreement at low frequencies, since it was expected (Ref. 12) that the low frequency power computed from the near field would be 10 to 15 db above the far field result, with agreement obtained only for the high frequencies. This result indicates that a measure of the true acoustic power can be obtained from the 10° boundary measurements of this jet if proper attention is given to the actual boundary area normal to the direction of radiation as determined by the correlation measurements for the various frequencies and axial locations.

A qualitative estimate of the exit angle for noise radiated from a source located in the mixing region at the point of maximum shear (figures 1, 2, 3) is seen in figure 27. This ray diagram is one of several constructed to observe the qualitative effects of the refraction of sound within the flow by temperature and velocity gradients. The rays were constructed for radiation from a simple point source in a plane containing the jet axis, and are based on the ray velocity (Ref. 15) given by the vector sum of the local flow velocity and speed of sound along the normal to the phase front. As is clear from the figure, a very pronounced refraction occurs, with the result that a significant portion of the sound is directed at an angle of 110° to 115° from the forward axis. It is noted that this refraction is sufficiently severe so as to dominate the directional characteristic of the radiated sound for a relatively wide variety of assumed source directivities.

Of course, refraction estimated from a ray diagram of this type is accurate only at high frequencies, or more generally when the value of kb is large in comparison with unity, where $k = 2\pi f/a$ and b is the gradient width parameter utilized in Section II. Further, the

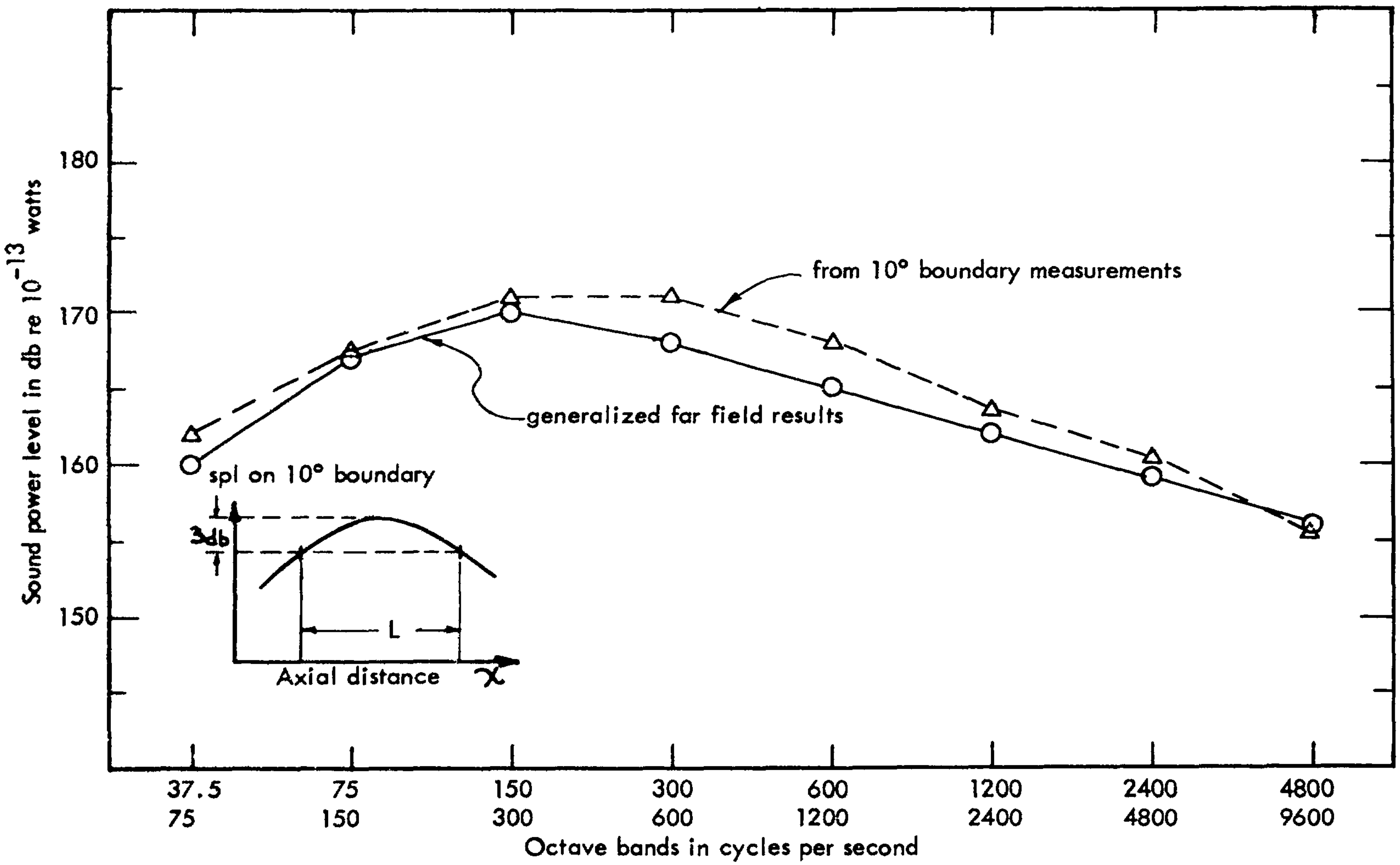

Figure 26. Comparison of octave band power spectra first estimated from 10° boundary maximum sound pressure level and area between minus 3 db points with generalized spectra computed from far field measurements.

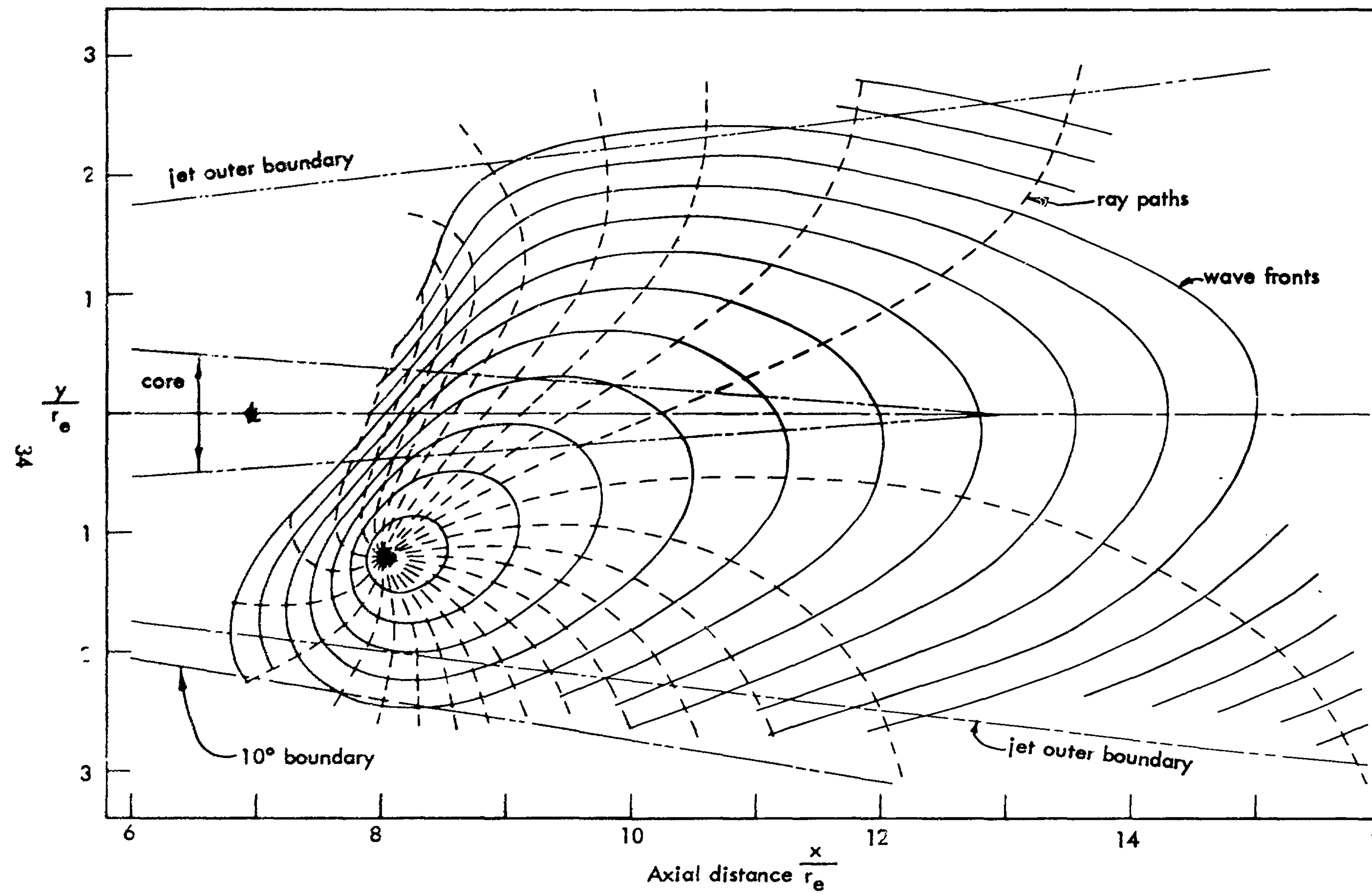

Figure 27. Ray diagram for radiation from simple source located at the center of the jet velocity and temperature gradient, for exit velocity of 1850 ft/sec. and exit temperature of 1000°F.

diagram assumes a simple point source located in the center of the mixing zone, rather than a finite quadrupole source. Clearly, the exit angle would shift further forward for sources located toward the center since the overall temperature change is greater and, conversely, the exit angle would shift aft for sources located nearer the outer boundary where the overall temperature change is less. Thus, in the region of high kb when the gross effects from ray considerations might actually apply to the associated small sources ($\lambda/b \ll 1$), the angular distribution of radiated noise should be relatively broad.

With this qualitative ray diagram as background, it is pertinent to review the spacial correlation measurements (Ref. 1) made along the 10° boundary. The spacial correlation coefficient (σ) was determined from the time average product of the pressure at a fixed point (a) and the pressure at a moving point (b) divided by the product of the rms pressures at the two points. Thus,

$$\sigma = \frac{\overline{p_a \, p_b}}{\left(\overline{p_a^2}\right)^{\frac{1}{2}} \left(\overline{p_b^2}\right)^{\frac{1}{2}}}$$

For a sound wave in free space, the angle of propagation, relative to the base line for the spacial correlations, can be determined by the distance between the origin and the first zero crossing as shown in figure 28.

This technique was applied to the correlation presented in Ref. 1. Typical results are shown in figure 29 for the one-third octave frequency band centered at 400 cps. The primary direction of propagation determined from the correlations are shown as arrows from each measurement position along the 10° boundary. As can be seen, the apparent primary direction of propagation at the location near the nozzle makes only a small acute angle with the jet boundary, whereas the primary direction for downstream locations makes a considerably greater angle with the jet. It should be noted that these interpretations of the near field pressures differ from those of Franklin and Foxwell (Ref. 13), where it was shown that the correlations close to the jet boundary indicated the convection of eddies past the measurement microphone, rather than the radiation of sound energy. However, their measurement locations were close to the core boundary of a model cold jet and a full scale engine, both of which had exit velocities of 710 ft/sec. This exit velocity is only 38% of the velocity of the present jet. If the mean square radiated sound pressure is assumed to vary as the eighth power of velocity, whereas the direct fluctuating turbulent mean square pressures (pseudo sound) vary as only the fourth power of velocity, this increase of a factor of 2.6 in exit velocity would result in an increase in the ratio of mean square sound pressure to pseudo sound pressure of approximately 46. This large potential increase in the ratio could easily account for measurement of true radiated sound along the 10° boundary of the high speed jet, whereas measurements on the lower speed jets represented convected turbulence. It should also be noted that these correlations do not include the data below x/λ values of .25 where pseudo sound is suspected, as indicated in figure 24.

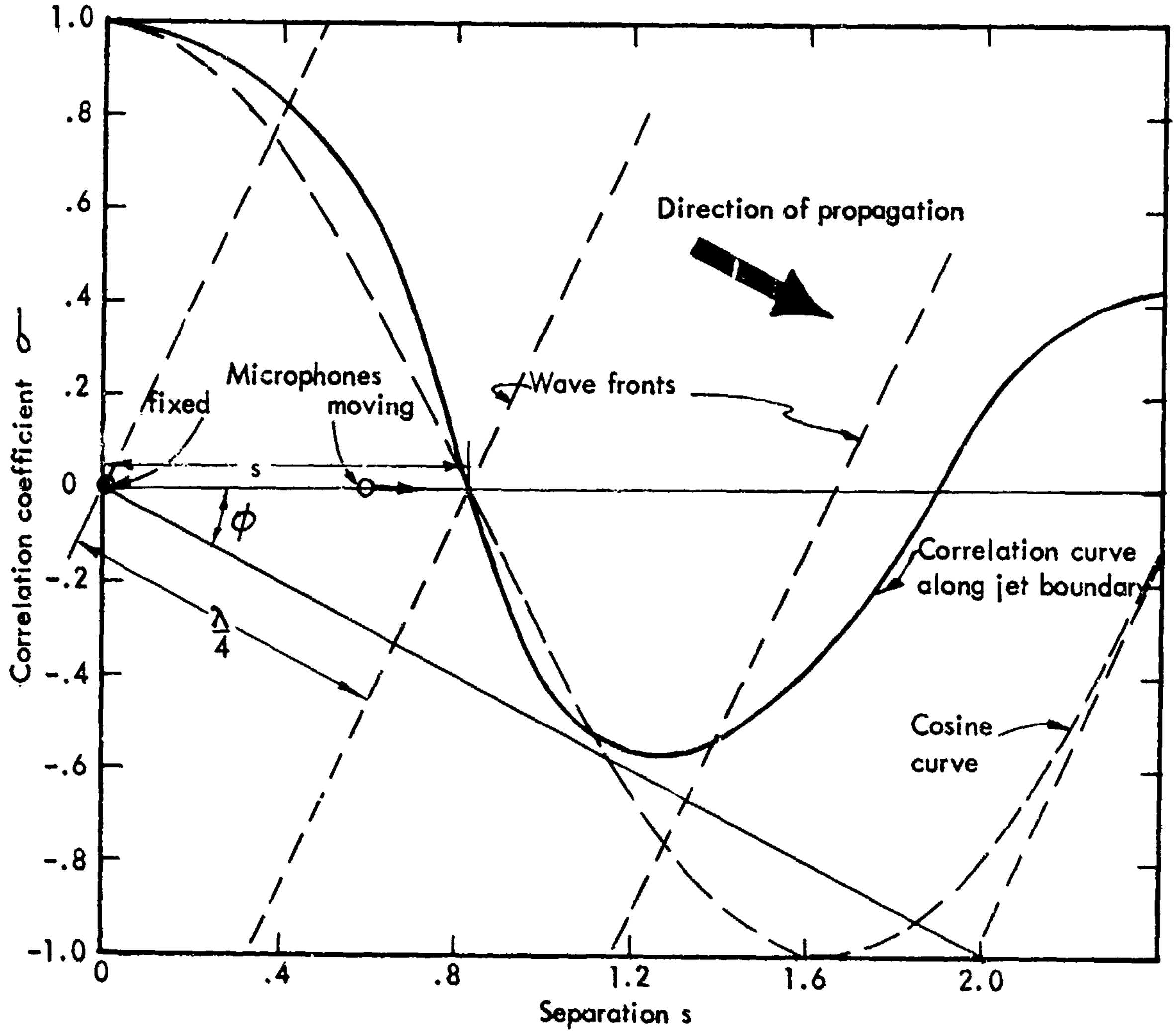

Figure 28. Example of relation between zero crossing of correlation coefficient, wavelength and direction of propagation .

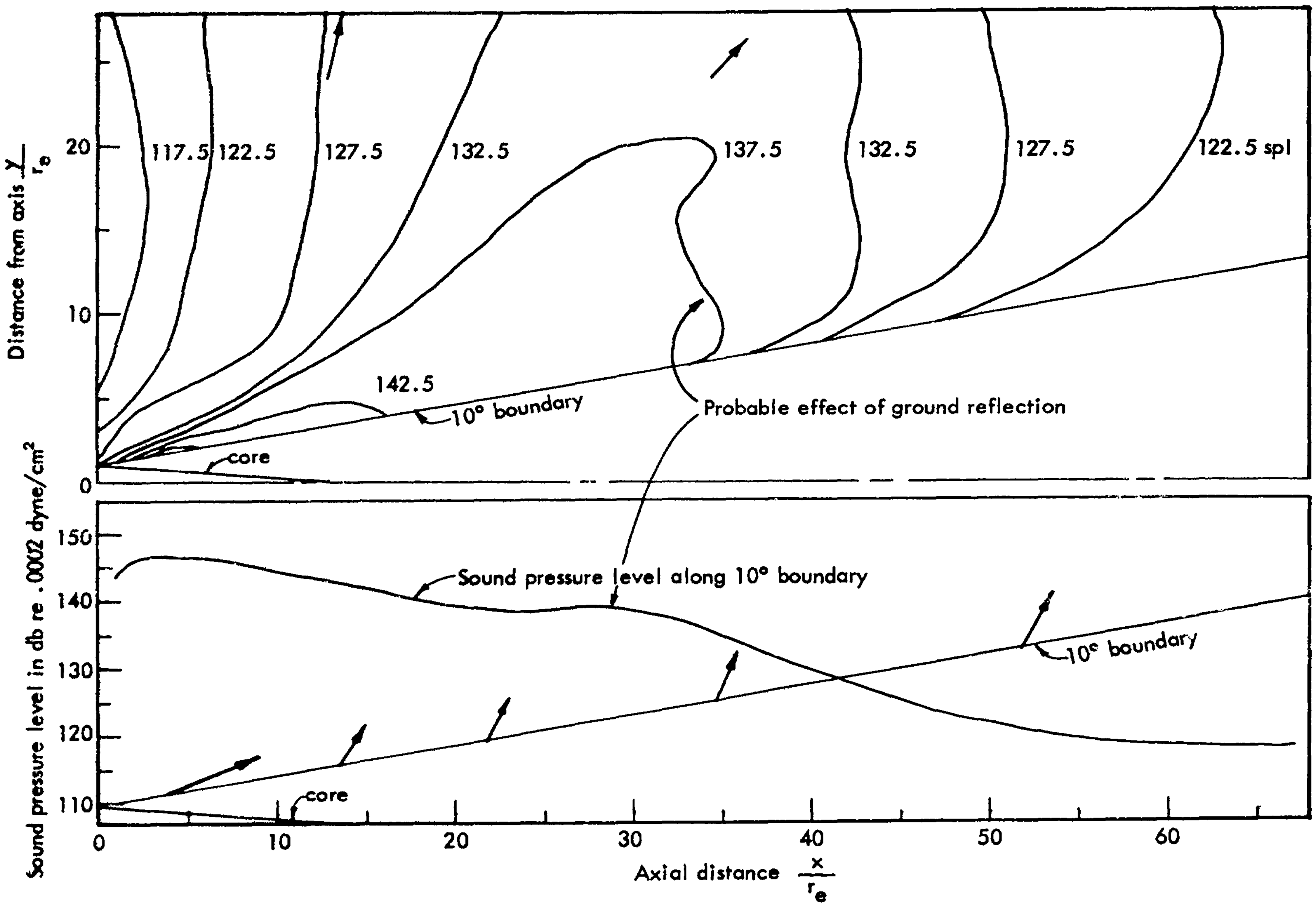

Figure 29. Contours of equal sound pressure level in 5 db increments for one-third octave band centered at 400 cps, together with axial variation in level along 10° measurement boundary and primary direction from spacial pressure correlations. Data from Howes, et al.

The apparent primary propagation angles for various frequencies and axial locations are summarized in figure 30. Although these data have some scatter, a direct relationship emerges between the primary angle and the non-dimensional axial frequency parameter ($fx/a_o = x/\lambda_o$). Furthermore, for values of $x/\lambda_o > 5$ the primary angle is identical to that predicted from the refraction of the rays in figure 27. This value of x/λ_o corresponds to a kb value of approximately 2.5.

This determination of the variation of the apparent primary radiation angle leads immediately to a qualitative interpretation of the near noise field of the jet shown in the example of figure 29. The maximum sound pressures along the measurement boundary and at a center frequency of 400 cps, occur adjacent to the core, and have a primary angle of radiation which varies between approximately 160° to 120°. Near the nozzle the radiation is primarily toward 150 to 160°, i.e. along the jet boundary; hence, the apparent steep gradient of noise level at 90° in this region. Further downstream, the primary radiation angle approaches the ray angle of 113°, contributing significantly to the broadening of the far field directivity pattern, and to radiation toward the 0° - 90° far field region.

In order to utilize and validate these concepts, it is necessary to know the angular distribution of sound energy about the primary direction as a function of x/λ_o. Once this distribution is obtained, the total power radiated through the 10° measurement boundary may be calculated more properly and compared to the power computed from far field measurements. Furthermore, the contributions to the noise at any point in the near field from various axial distances can be summed and compared to measured noise levels.

Angular Distribution of Power Along Jet

The determination of the angular distribution of radiated acoustic power as a function of both axial position along the jet and frequency is necessary if a correspondence between acoustic power generated in the jet and the sound field external to the flow is to be found. Unfortunately, the correlations which were so useful in the previous determination of primary radiation direction as a function of x/λ_o are of no further assistance, since they already represent an average of the desired information. However, the variation of primary angle with x/λ_o does enable a better estimate of the acoustic power radiated through the 10° boundary in comparison to the crude approximation of figure 26.

It is clear that a one-to-one correspondence exists between the actual power radiated through the 10° boundary and that radiated through any other surface in the noise field, neglecting ground absorption and atmospheric attenuation. Furthermore, a direct correspondence must exist between the noise level at any point in the noise field, and the noise radiated to the point from all sources along the jet. The determination of this latter correspondence, developed in the following paragraphs, is predicated on two fundamental assumptions. First, it is assumed that the axial distribution of acoustic power computed from the 10° boundary pressure and correlation measurements approximates the actual axial distribution of acoustic power. Secondly, it is assumed that the angular distribution of acoustic power is a function of x/λ_o. This latter assumption is not unreasonable since the parameter ($x/\lambda_o = fx/a_o$) is later shown to be the general similiarity parameter for axial

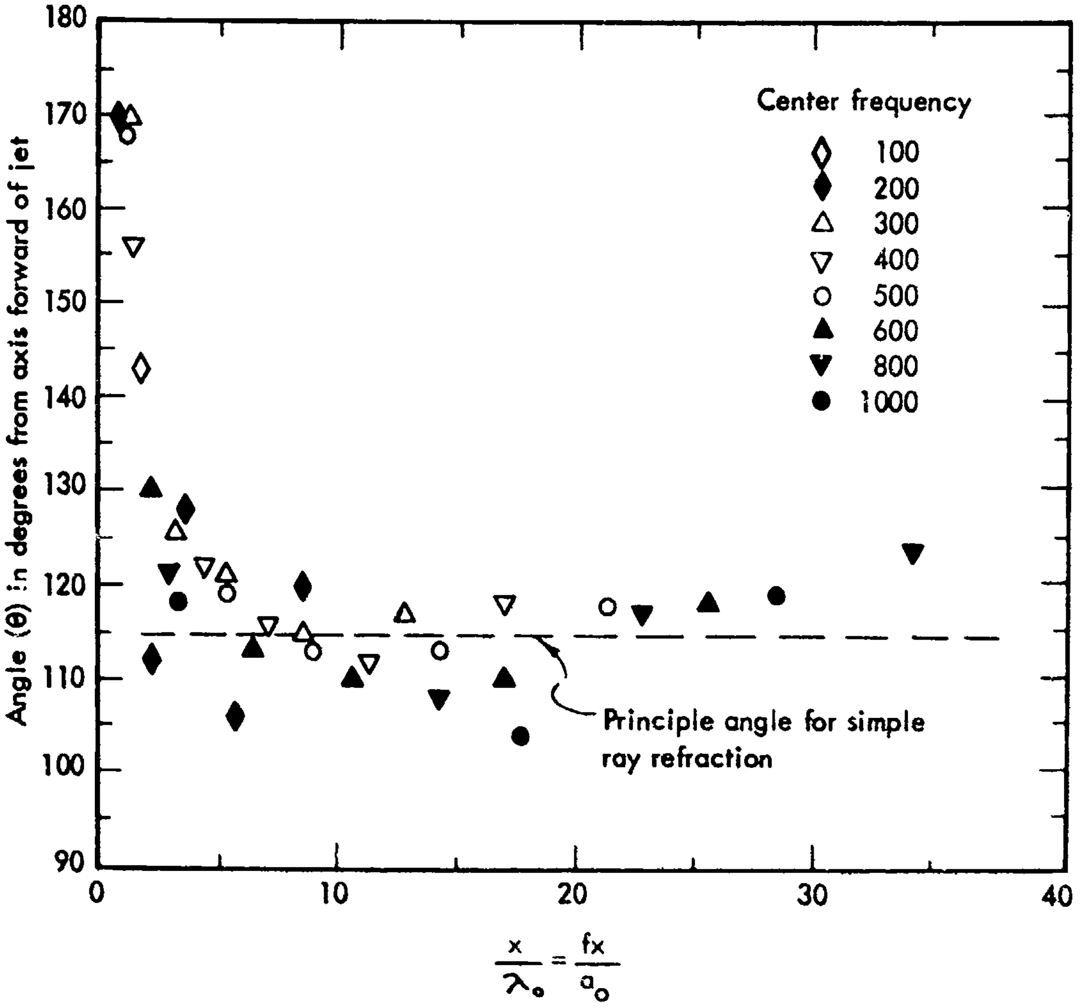

Figure 30. Variation of the predominant propagation angle for various frequencies from measurements along the 10° boundary as a function of a non-dimensional axial frequency parameter

distribution of the power spectrum. Furthermore, the angle of maximum radiation in the far field and breadth of the associated directivity pattern are dependent on frequency (Ref. 16), with the angle of maximum radiation varying, as shown in figures 31 to 34 from Ref. 16, between approximately 150° and 115° for center frequencies between 53 and 6800 cps, respectively. Note that these far field directivities were obtained at distances of 100 and 250 feet from the jet nozzle, so that the jet is assumed to approximate a point source. The far field variation in maximum angle is consistent with the angular variation of the primary directions along the 10° boundary, since the major portion of the low frequency power is radiated from regions of low x/λ_0 and the majority of the high frequency power is radiated from regions extending to high values of x/λ_0 where the primary angle becomes 110° to 115°. These generalized directivities, originally derived from a composite of hot jet measurements, were utilized directly through an iterative procedure in the derivation of angular distribution of sound radiation along the jet.

For convenience in the iteration, the jet was divided into several segments by transverse cuts, and the power from each segment was calculated from a flux formula, as follows: for the i^{th} segment the power level in db re 10^{-13} watts is given by

$$PWL_i = \overline{SPL_i} + 10 \log (A_i \cos\phi_i) \tag{III-1}$$

where $\overline{SPL_i}$ is the average sound pressure level,
A_i the radiating surface area, and
ϕ_i the direction of the sound pressure maximum relative to the normal of A_i at its mean lengthwise coordinate.

To obtain a correspondence between the far field directivity and the angular distribution of power radiated from the jet, it is necessary that the directivity obtained by summing the relative directivities of each segment in each frequency band (k) equal the far field directivity in figures 31 to 34. Hence:

$$L\sum_{i=1}^{n}\left[PWL_i^{(k)} + 10 \log f_i(\theta)\right] - L\sum_{i=1}^{n} PWL^{(k)} = 10 \log F^{(k)}(\theta) \tag{III-2}$$

where $f_i(\theta)$ is the angular distribution function for power radiated from the i^{th} segment in frequency band (k). $F^{(k)}(\theta)$ is the far field directivity function in the frequency band (k),
and the summation, $L\sum$ is logarithmic.

Note that this equation assumes that the far field directivity functions were determined at a sufficient distance so that the jet approximated a point source. Hence, no correction was made for the effect of axial displacement of the segment on the definition of the angle θ.

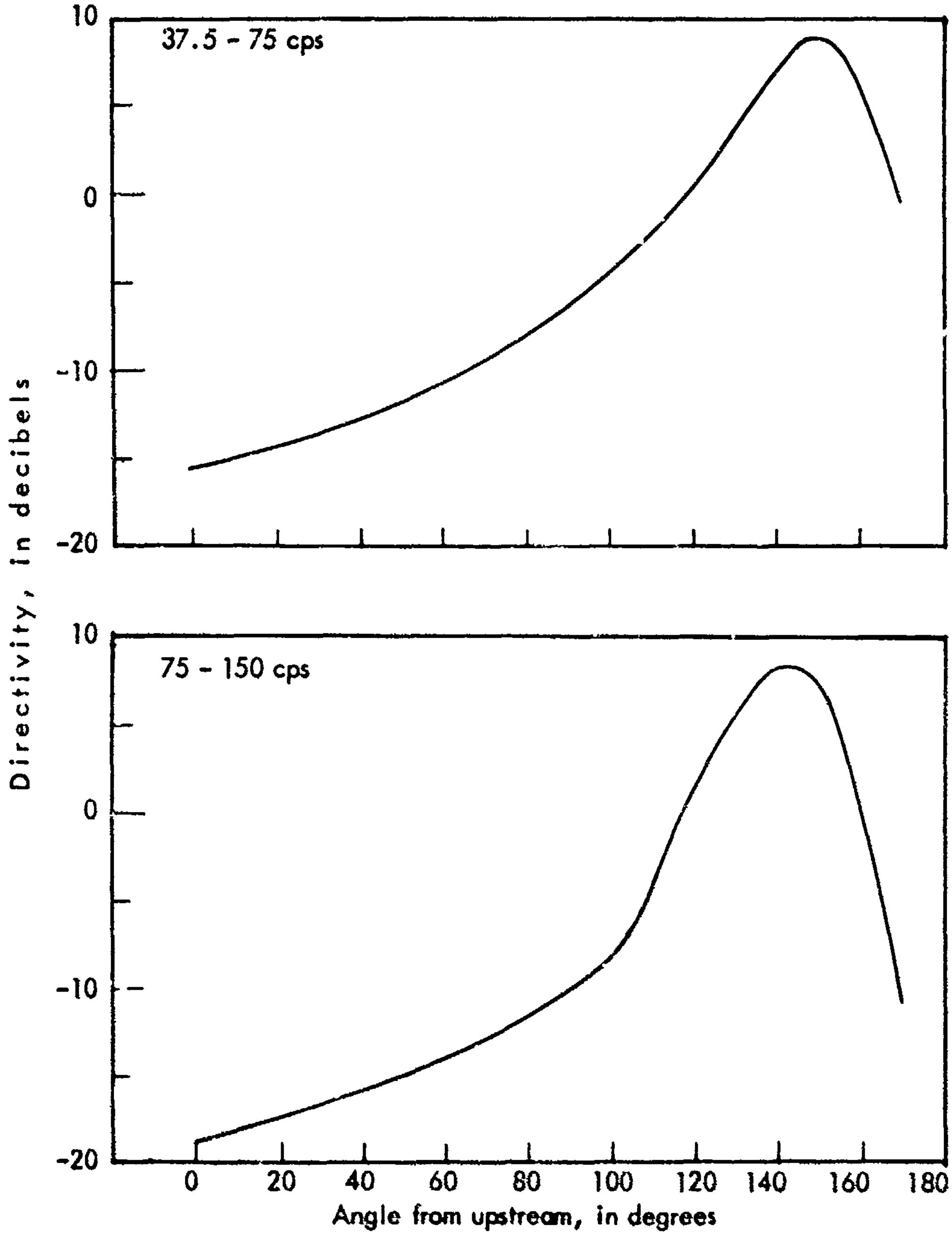

Figure 31. Generalized far field directivity in the 37.5 - 75 and 75 - 150 cps octave bands for various turbojet engines operating at military power.

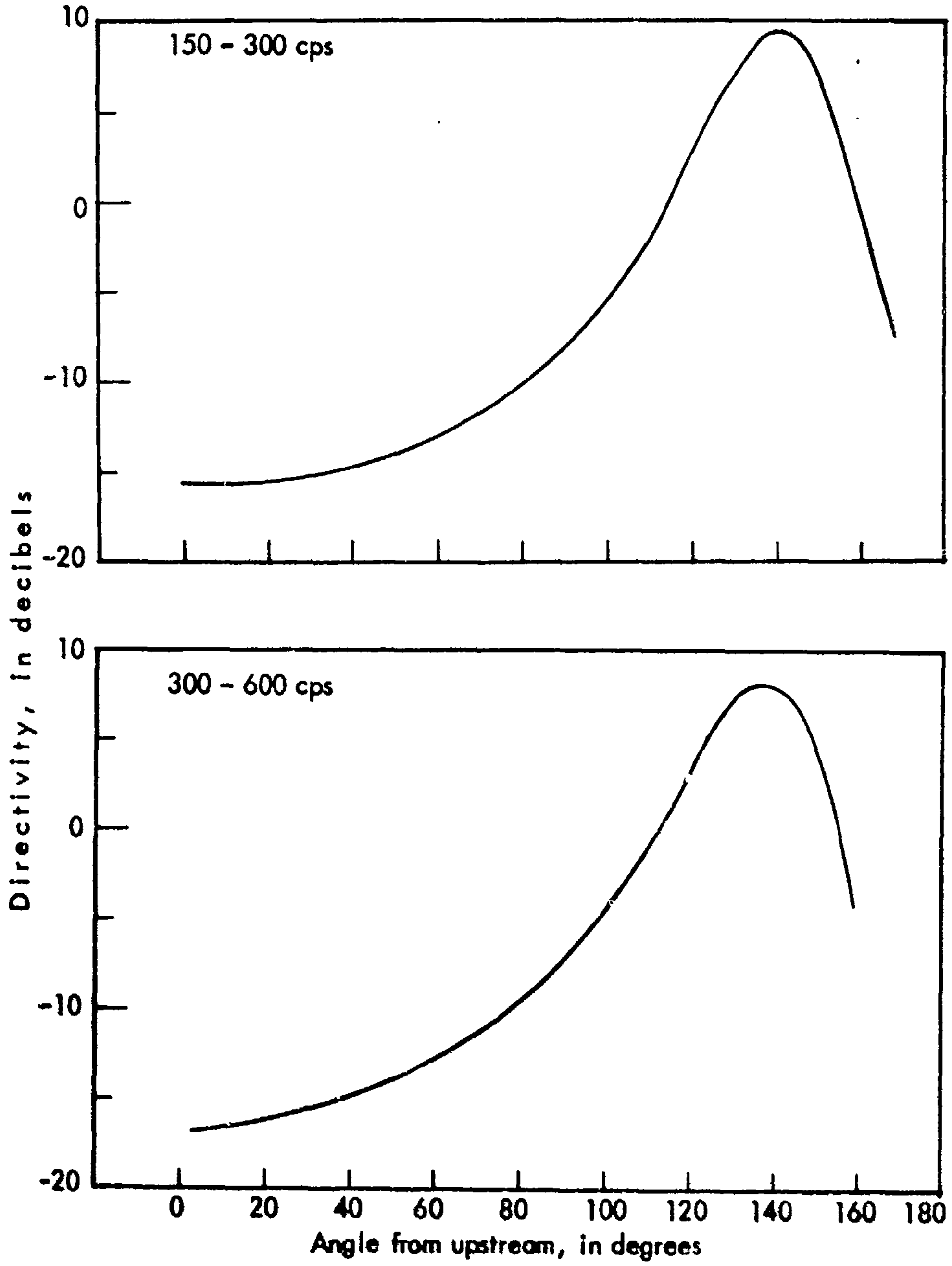

Figure 32. Generalized far field directivity in the 150 - 300 and 300 - 600 cps octave bands for various turbojet engines operating at military power.

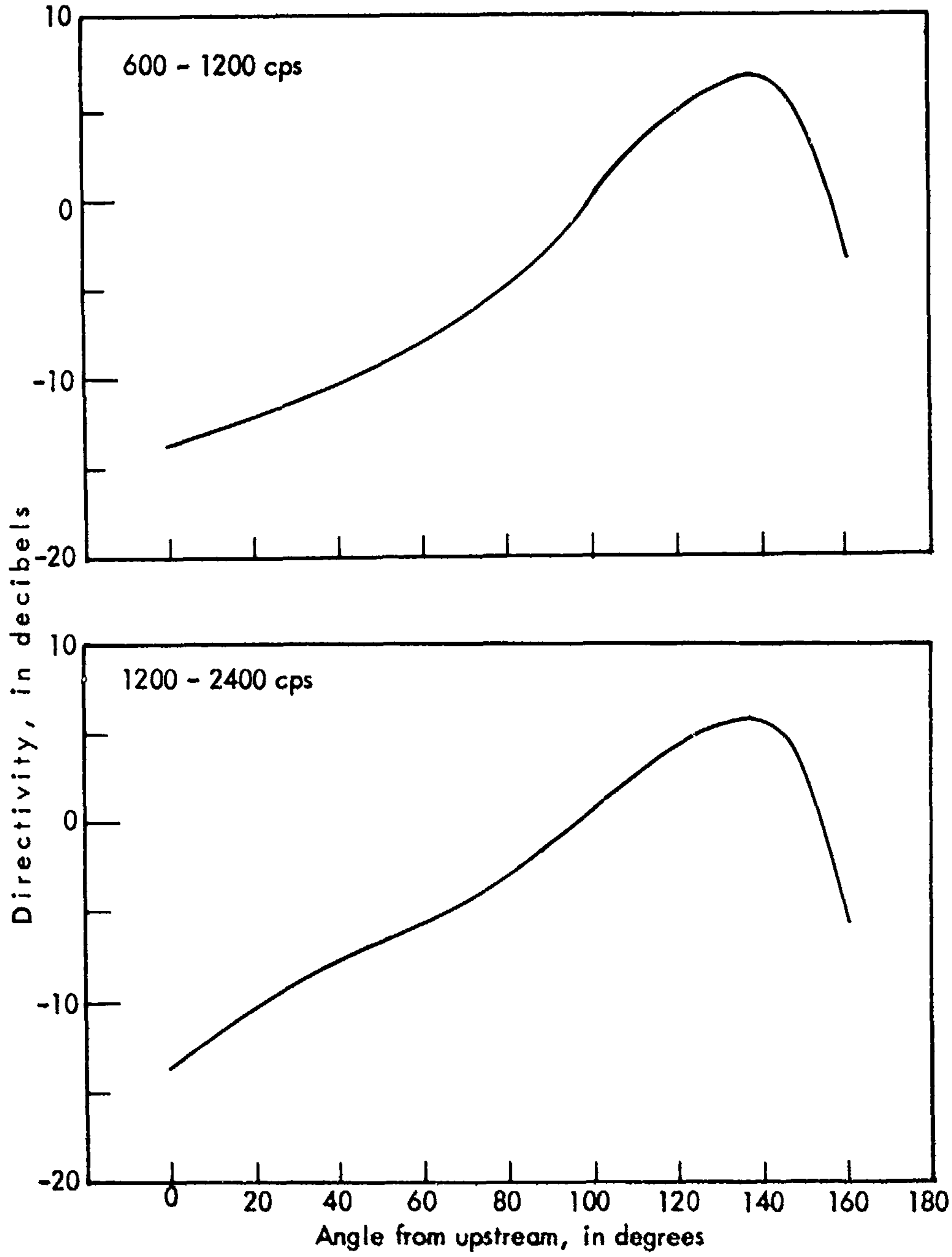

Figure 33. Generalized far field directivity in the 600 - 1200 and 1200 - 2400 cps octave bands for various turbojet engines operating at military power.

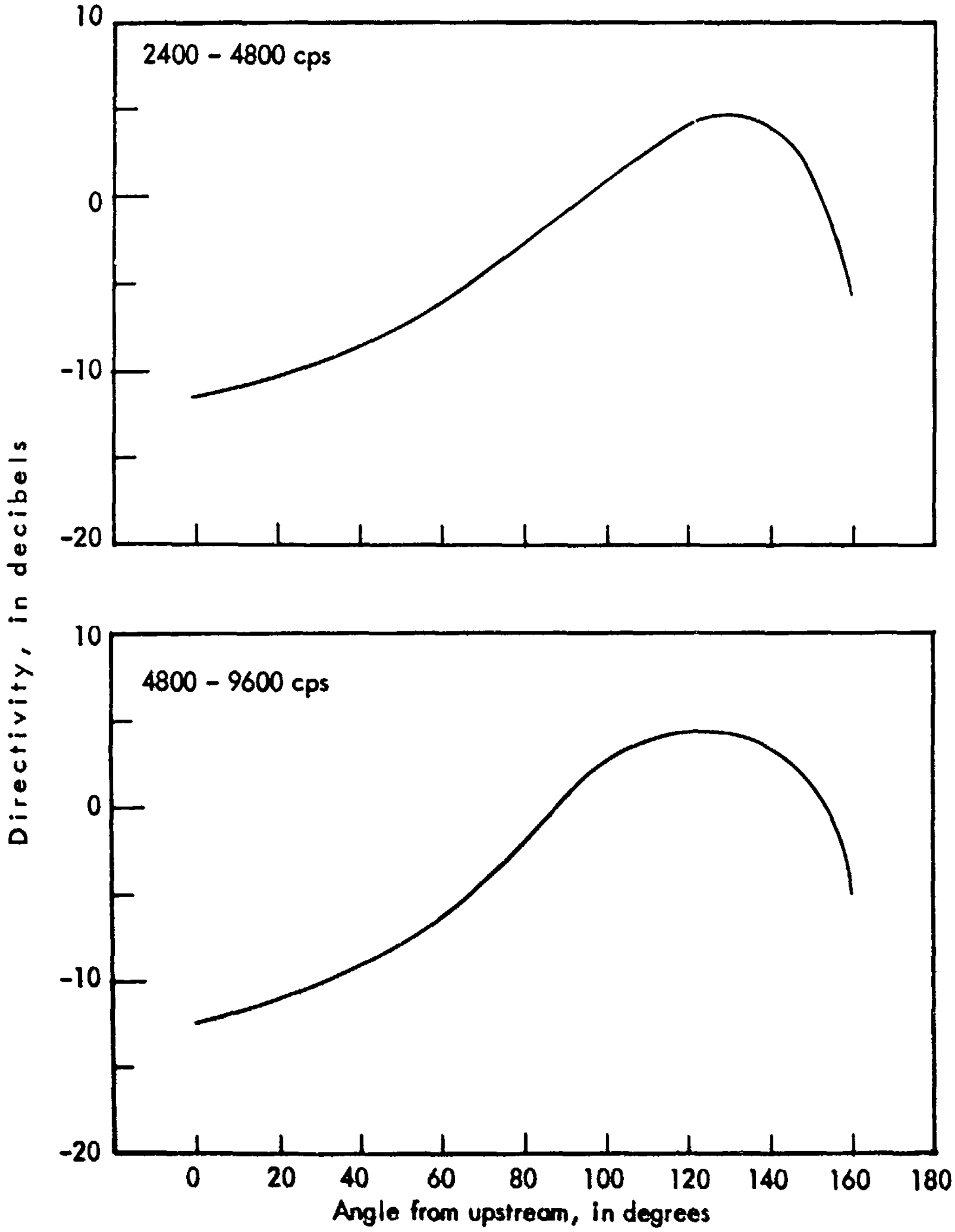

Figure 34. Generalized far field directivity in the 2400 - 4800 and 4800 - 9600 cps octave bands for various turbojet engines operating at military power.

The one-third octave band sound pressure level measurements (Ref. 1) given in figure 24 were converted to full octave band sound pressure levels as shown in figure 35. The three highest frequency bands have been extrapolated toward smaller x/λ_o to account for the power radiated in the 1 ft. distance between the first measurement position and the nozzle. Also, some smoothing has been done in the 300 to 1200 cps range to avoid what is believed to be ground-reflected noise. The onset of significant reflection appears to occur between 15 and 20 ft. downstream and continues from there on to approximately 40 to 45 ft., as can be seen in figure 29. These reflections can be qualitatively evaluated from inspection of figure 36 where the effect of the ground on the sound pressure maxima is indicated. The directions associated with the sound pressures in each segment are derived from the longitudinal correlation studies (Ref. 1) which are summarized in figure 30.

In order to solve equation (III-2) it was assumed that the near field directivity $f_i(\theta)$ would vary smoothly with x/λ_o. It was further assumed that for a sufficiently low frequency (below 37.5 cps in these computations), the whole jet could be characterized by one value of x/λ_o, i.e., that the whole jet would radiate similarly. With this latter assumption, it was possible to obtain an initial series of points on the $f_i(\theta)$ versus x/λ_o curves, utilizing unpublished far field data for a 1/8 scale J57 jet engine (Ref. 17) for an octave frequency band centered on a modified Strouhal number (fd/a_o) of .041. For the first (37.5 - 75 cps) octave band of the full scale data, the jet was divided into two segments and the power calculated for each. Applying the above condition:

$$10 \log F^{(1)}(\theta) = L\sum_{i=1}^{2}\left[PWL_i^{(1)} + 10\log f_i(\theta)\right] - L\sum_{i=1}^{2} PWL_i^{(1)}$$

where $f_1(\theta)$ is the initial series of points at 10° intervals and $f_2(\theta)$ is unknown.

Solving for $f_2(\theta)$ yields a second series of points on the $f_i(\theta)$ versus x/λ_o curves. The procedure for the second octave band (75 - 150 cps) was similar, except that the jet was divided into three segments. Now

$$F^{(2)}(\theta) = L\sum_{i=1}^{3}\left[PWL_i^{(2)} + f_i(\theta)\right] - L\sum_{i=1}^{3} PWL_i^{(2)}$$

where $f_1(\theta)$ and $f_2(\theta)$ are known and $f_3(\theta)$ is unknown.

This iteration continued throughout the eight octave bands with the subscripts maintaining their identity with x/λ_o, as the distance of the center of the segment from the nozzle in wavelengths.

During the course of the iteration it often became apparent that a value of $f_i(\theta)$ would not apply to other octave bands or would not produce a smoothly varying function. In such cases other values were estimated and tested so that the condition, Eq. (III-2) would be satisfied to within one decibel. Figure 37 shows the initial stages of this "trial and error" iterative approach, together with the initial points for two values of θ. When the first iteration was completed for the whole range of θ, as well as x/λ_o, $f_i(\theta)$ was

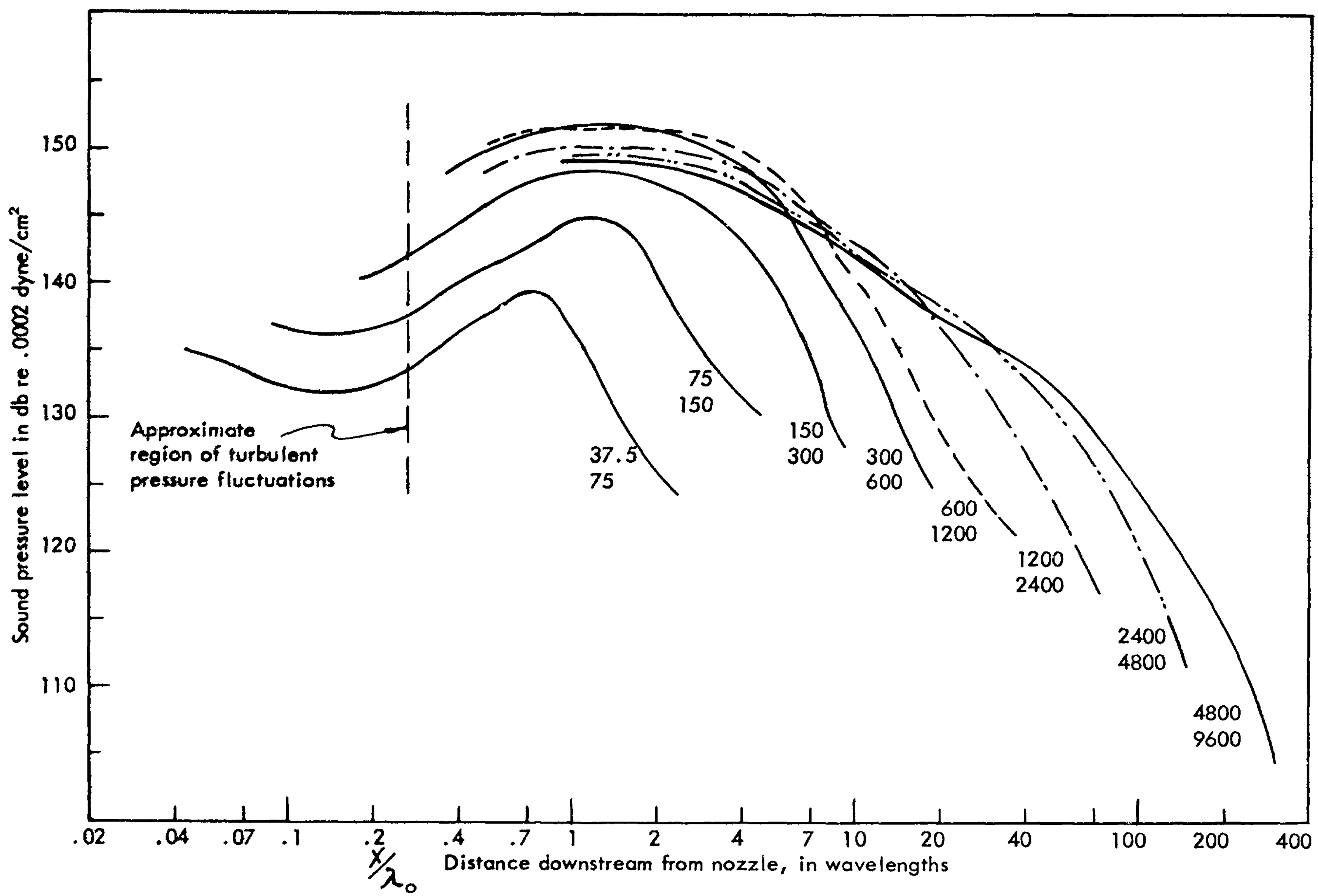

Figure 35. Sound pressure level in octave bands along the 10° boundary, from the one-third octave band data by Howes, et al.

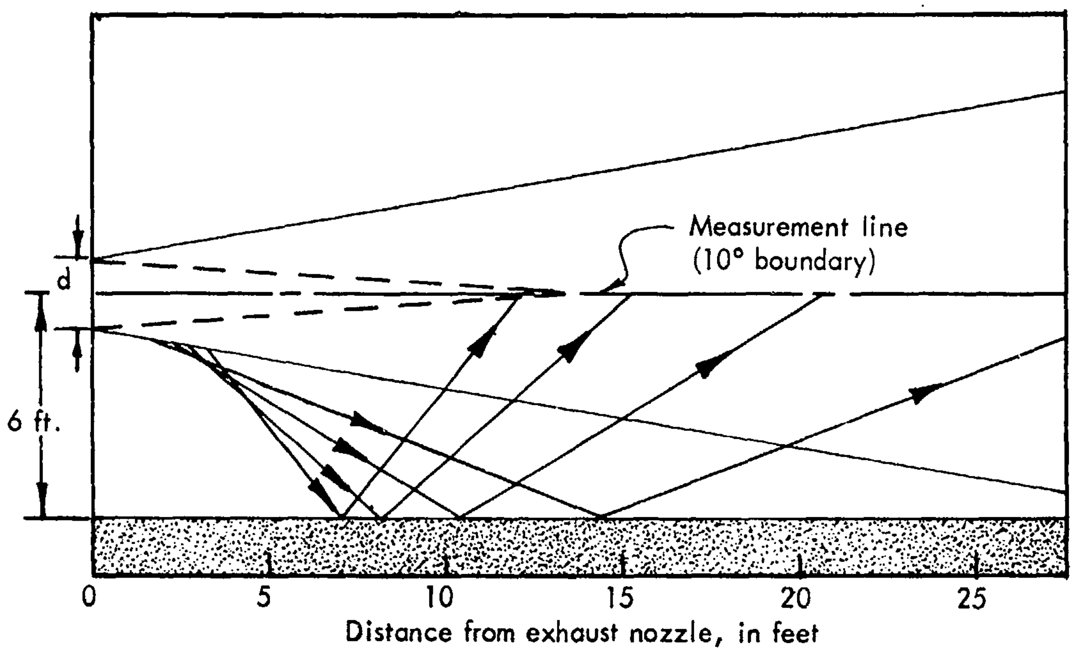

Figure 36. Illustration of effect of ground plane for the 600 - 1200 cps octave band.

plotted versus θ with x/λ_o as a parameter. These curves were then checked to insure that the integral of $.5f_i(\theta)\sin\theta$ between 0 and π was unity, as it should be. The final $f_i(\theta)$ is plotted in figure 38 as a function of θ and cross-plotted in figure 39 as a function of x/λ_o.

It would be desirable to confirm $f_i(\theta)$ through experiment, but the correlations which are required are one order of magnitude more laborious than any attempted to date. However, lacking direct experimental verification, the best estimate of the uniqueness of the $f_i(\theta)$ given in figures 38 and 39 is the strong tendency toward convergence which was noted during the iteration procedure. Therefore, with the exception of the function for $x/\lambda_o = .375$, it is believed that these functions represent a relatively unique solution to Eq. (III-2), and are thus primarily limited in accuracy by the accuracy of the generalized far field directivities from Ref. 16 in figures 31 to 34 and the near field data from Ref. 1 in figure 35. The ability of these functions to assist in the prediction of acoustic power will be discussed in the next subsection and the prediction of near field noise will be considered in the following subsection.

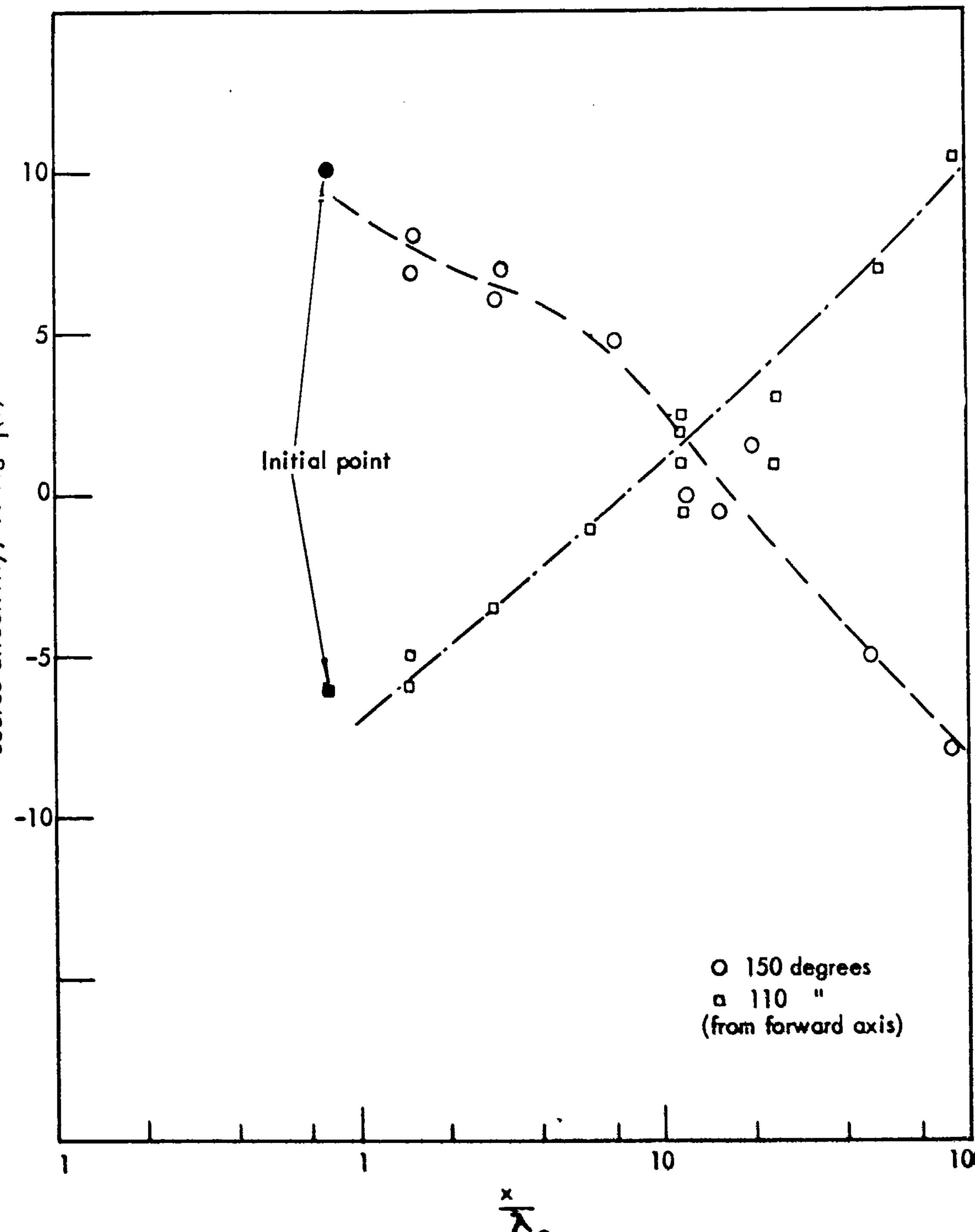

Figure 37, Preliminary results of iterative method used to obtain the directivity function $f_i(\theta)$.

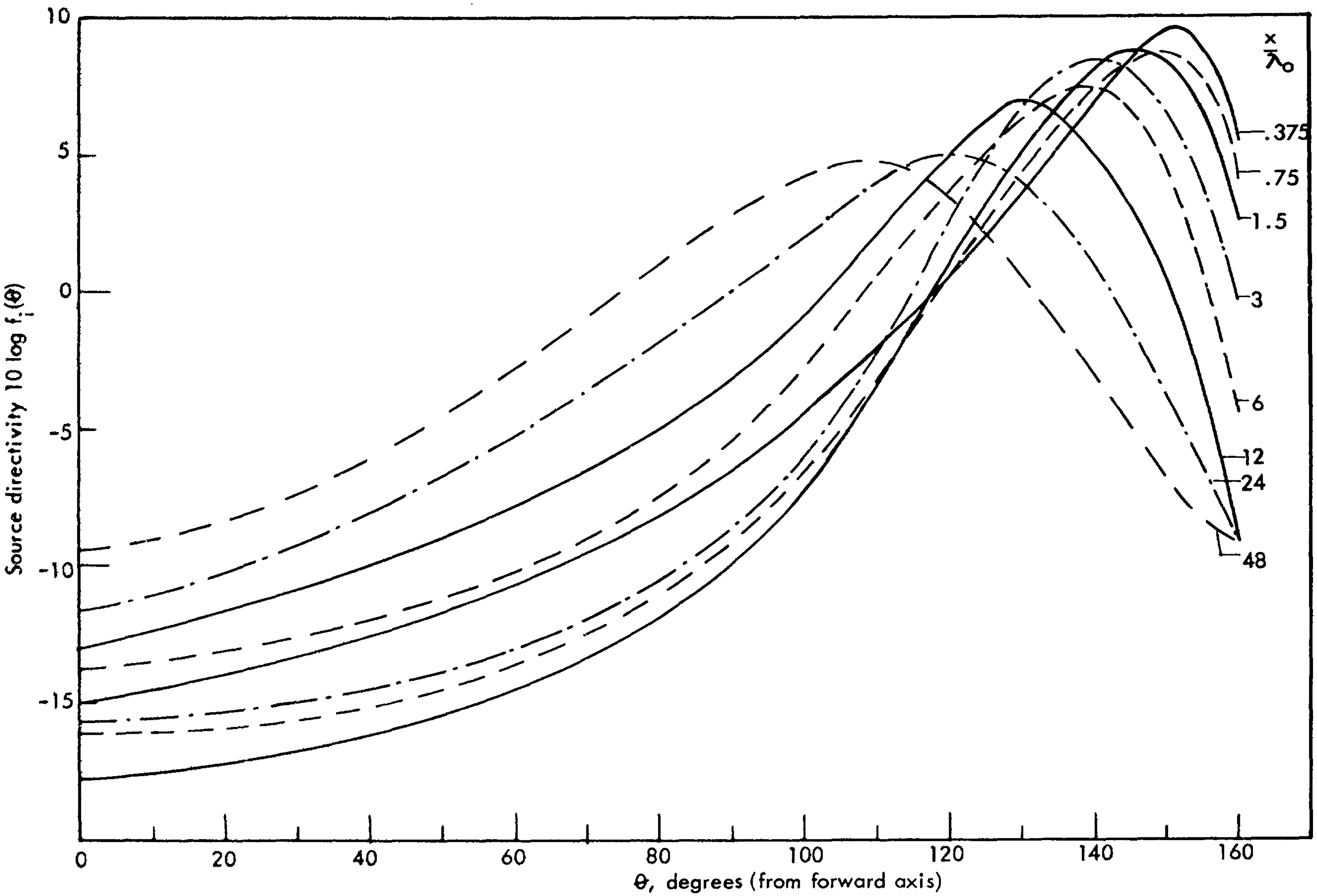

Figure 38. Calculated directivity of jet noise sources as a function of angle with $\frac{x}{\lambda_o}$, number of wavelengths downstream from the nozzle, as a parameter

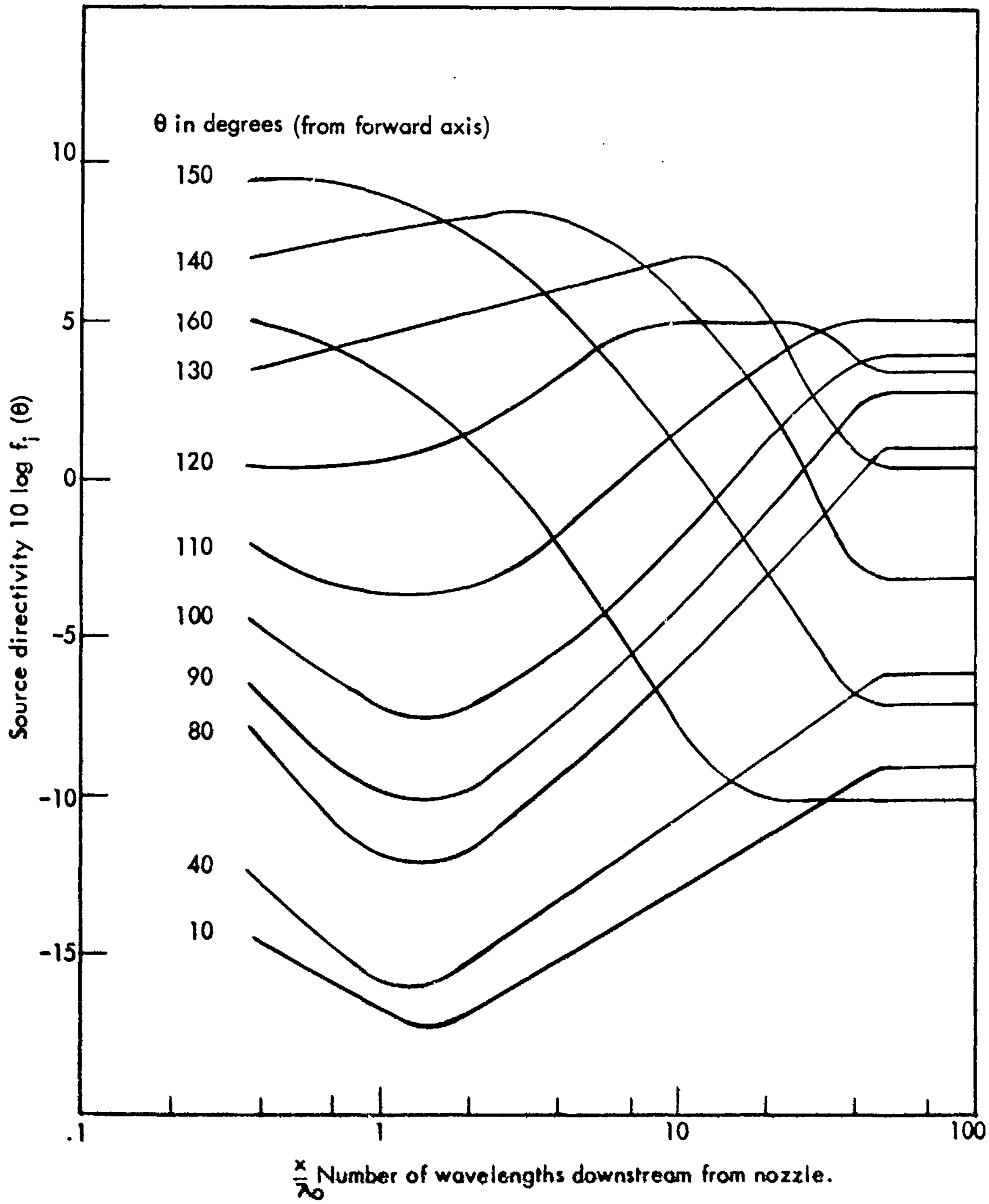

Figure 39. Calculated directivity as a function of position in the jet with θ, the angle from upstream, as a parameter.

Power Distribution Throughout the Jet

In the derivation of the angular distribution functions, $f_i(\theta)$, for the power radiated at various values of x/λ_e, there was no requirement that the total power computed from the near field equal the power computed from far field data. Hence, a comparison of these powers affords a gross test of the model.

For the first iteration for $f_i(\theta)$, the powers were computed using Eq. (III-1) for each segment based on the primary angle of radiation along the boundary (figure 30). However, for the final iteration, the angular distribution of power for each segment was considered, together with the requirement that the mean square pressure at any point on the 10° boundary must equal the sum of the mean square pressures computed from the directed powers flowing through the boundary.

The results of the final power computations from the 10° boundary measurements are presented in figure 40. The agreement between the power computed from the boundary and that computed from many far field measurements (Ref. 14) is almost exact below 300 cps. However, above 300 cps the far field generalized power is 1.5 to 2.5 db less than that computed from the near field. There are many possible reasons for this difference, in addition to the assumptions inherent in the basic jet radiation concept. These reasons include: the ground attenuation which lowers the far field sound pressure at frequencies above 300 cps, and hence the computed power; atmospheric attenuation which lowers many of the far field sound pressure levels at frequencies above 1200 cps; and the assumption of uniform radiation over the entire hemisphere which is common to all far field powers computed from ground measurement of horizontal jets.

With these additional considerations, it is clear that no further fundamental conclusion can be reached in regard to the correctness of either measure of power. To obtain a more precise conclusion would require an extremely careful experiment in free spherical space, under ideal atmospheric conditions, correlating both near and far field measurements. Therefore, it is felt that the agreement shown in figure 40 indicates that both measures of power are equally valid, and that the gross distribution of power radiated from the jet, predicted by the previous concepts, is valid.

For the purpose of predicting the power radiated from an arbitrary flow, it is necessary to examine the acoustic power generation as a function of axial distance and frequency in relation to the actual flow parameters. The power per unit axial length along the jet $(W_x)_{OB}$ where OB signifies summation over each octave frequency band is given in figure 41. The maximum values of $(W_x)_{OB}$ occur at values of x/r_e less than 1 for frequencies above 2400 cps, between 1 and 2 for 1200 and 2400 cps, and consistently further downstream for each successively lower frequency band. It should be noted that the slope of $(W_x)_{OB}$ with respect to axial distance for the highest frequency band is approximately $(x/r_e)^{-1}$, indicating that significant contributions to the total radiated power in these frequency bands results from all axial locations in the mixing region adjacent to the core. In contrast, the major contribution to the power radiated in the lowest frequency bands crosses the 10° boundary downstream of the core.

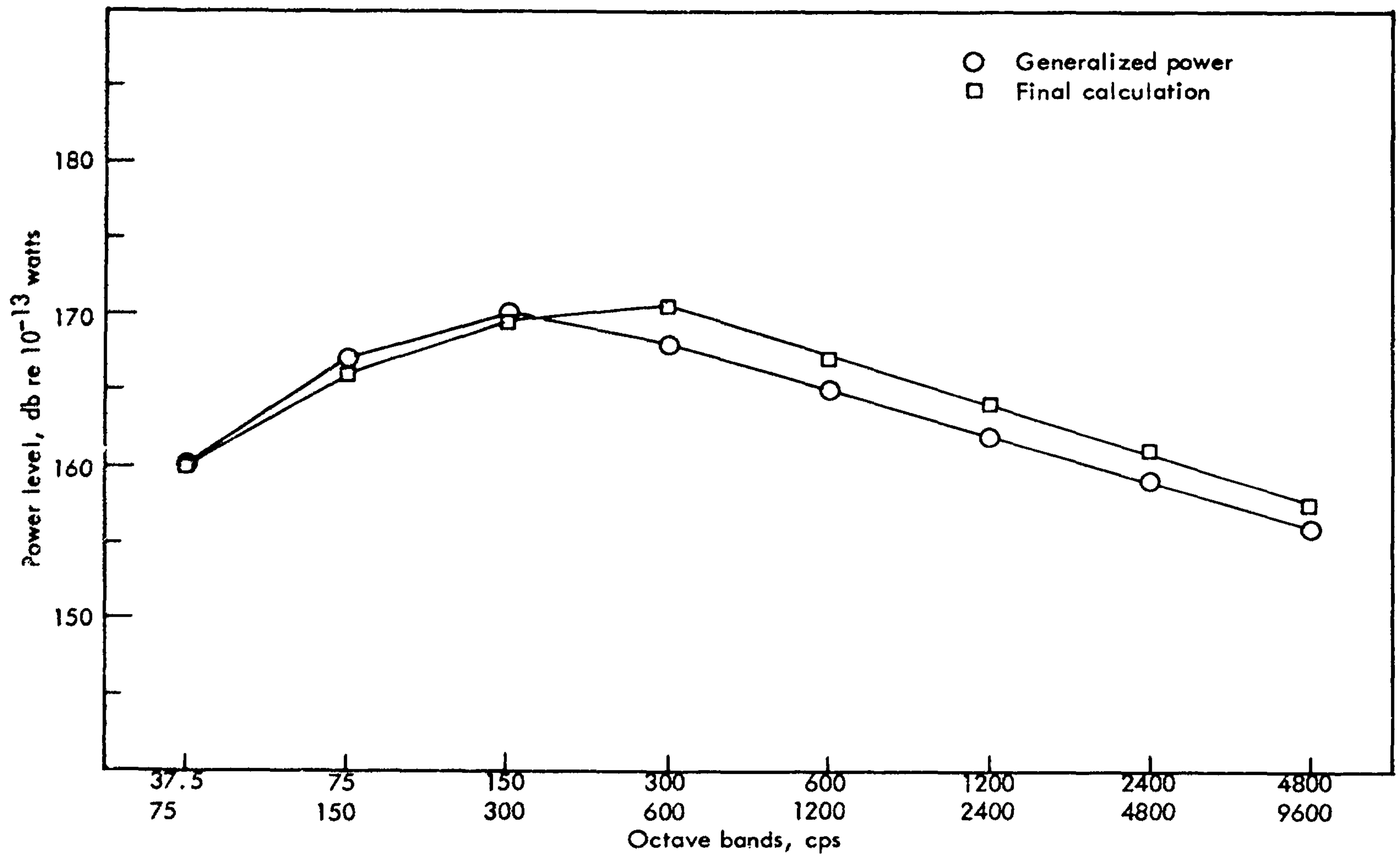

Figure 40. Comparison of the final calculation of power from the 10° boundary data with the generalized power curve based on far field measurements.

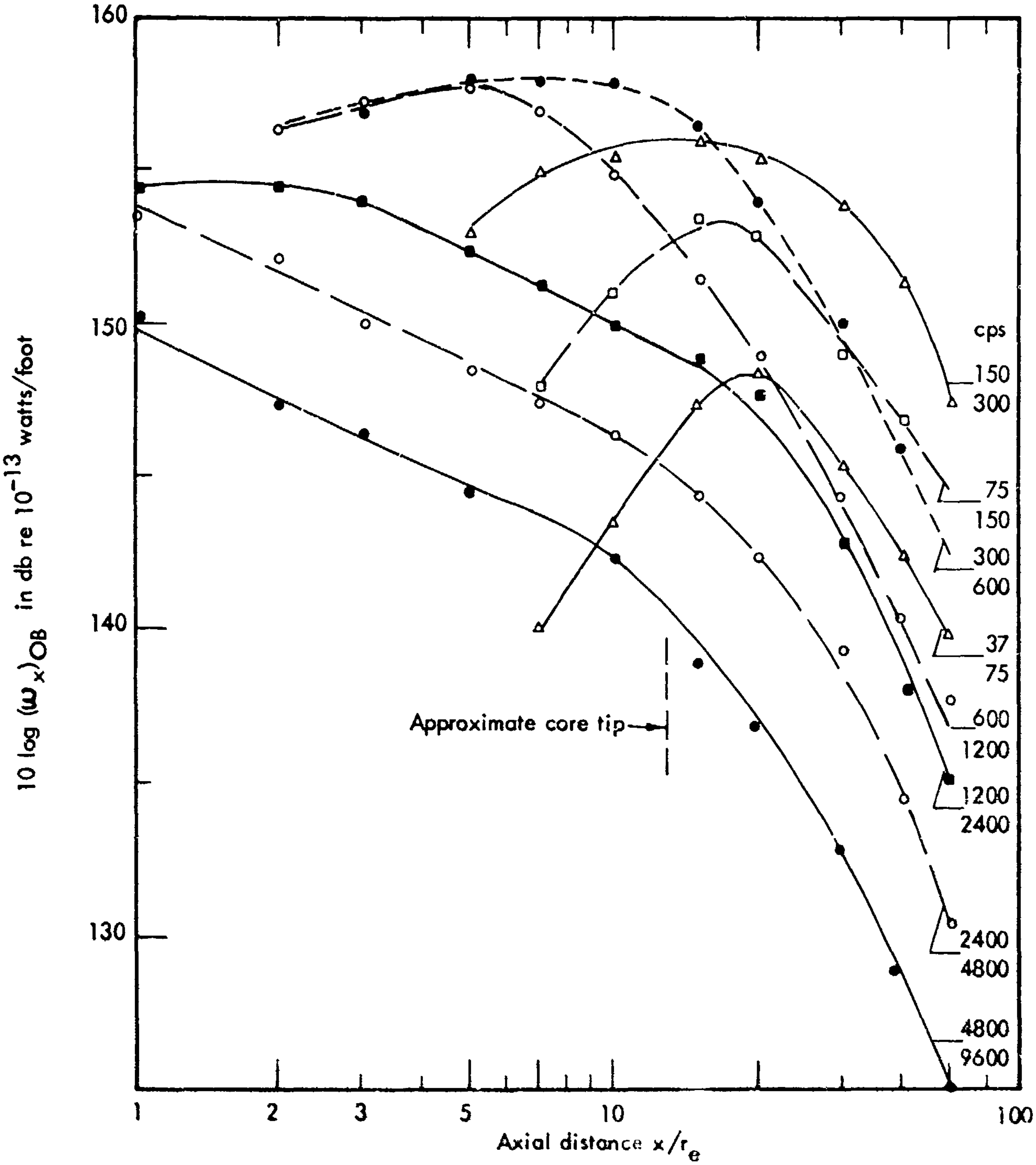

Figure 41. Acoustic power per unit axial length (feet) in octave bands from the 10° boundary measurements.

Throughout the mixing region adjacent to the core, the typical frequency of the turbulence should be proportional to U/x. Hence, it would be expected that the spectra would be proportional to a modified Strouhal number with the usual diameters replaced by x. Figure 42 gives the relative power spectral density (W_{fx}/W_x)normalized for the bandwidth, as a function of a modified axial Strouhal number for the data of figure 41 in the region of ($x/r_e < 13$).

In the region far downstream of the core, the centerline velocity is proportional to $(x/r_e)^{-1}$ and the jet width parameter b is proportional to x. Therefore, the characteristic frequency which is proportional to U/b should vary as $(x/r_e)^{-2}$ for the cold jet, rather than relationship $(x/r_e)^{-1}$ found in the core region. For hot jets, the variation of the speed of sound in this region would be approximately proportional to $(x/r_e)^{-1/2}$. Therefore, the modified Strouhal number should contain $(x/r_e)^{3/2}$. However, the data given in figure 43 do not agree with this reasoning. Rather, it is seen that the best correlation gives a spectrum which is independent of axial distance.

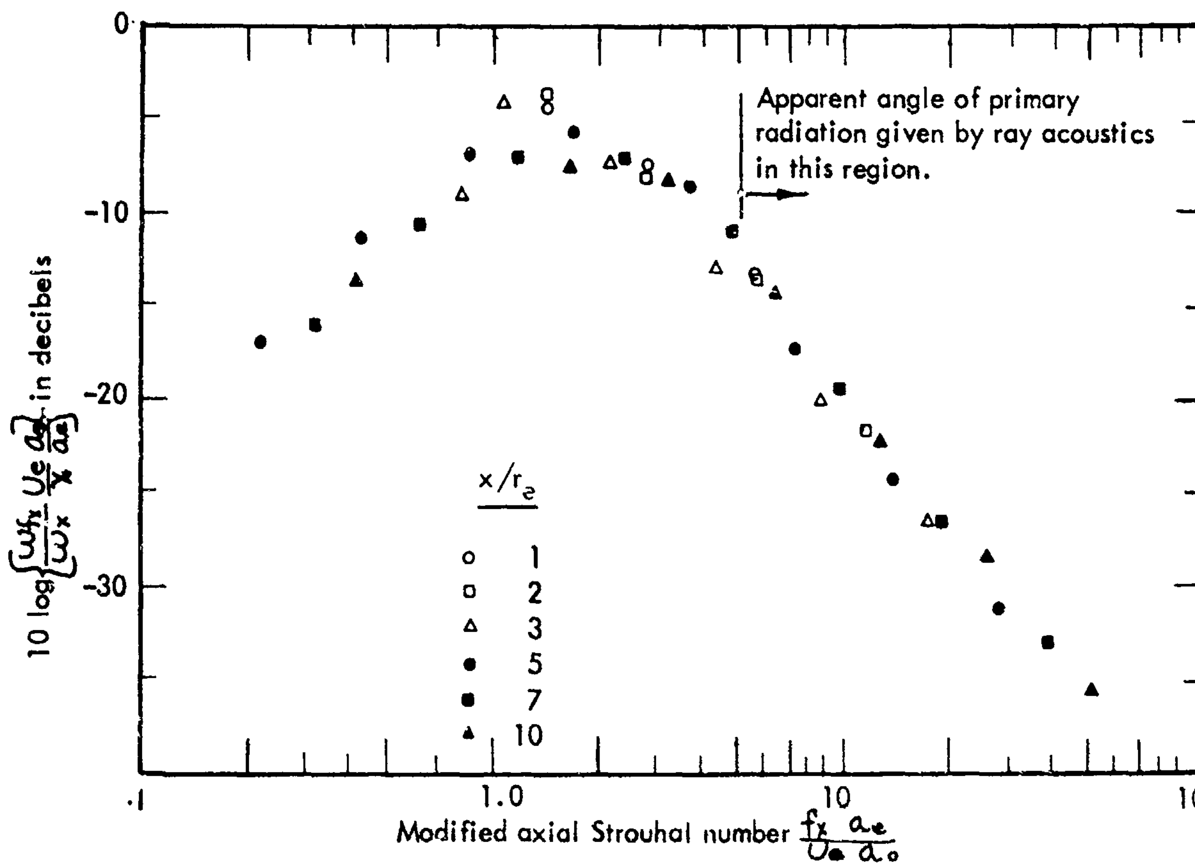

Figure 42. Normalized power spectral density along 10° boundary for J57 in the core region.

The relationships between power and axial position given in the previous three figures apply directly to the measurements along the 10° boundary. However, if these relationships are to be useful in the prediction of power generation from more arbitrary flows, the axial location should be the actual turbulent source position which is upstream of the measurement position. For this purpose the high frequency curves of figure 41 have been shifted upstream in accordance with the average axial distance between the source and the 10° boundary measurement position, as illustrated in figure 27. The lower frequency curves have been shifted by a greater amount in accordance with their higher primary radiation angle such that the maximum value of W_x occurs at the presumed core tip. The results in figure 44 should be a better approximation of the true source locations.

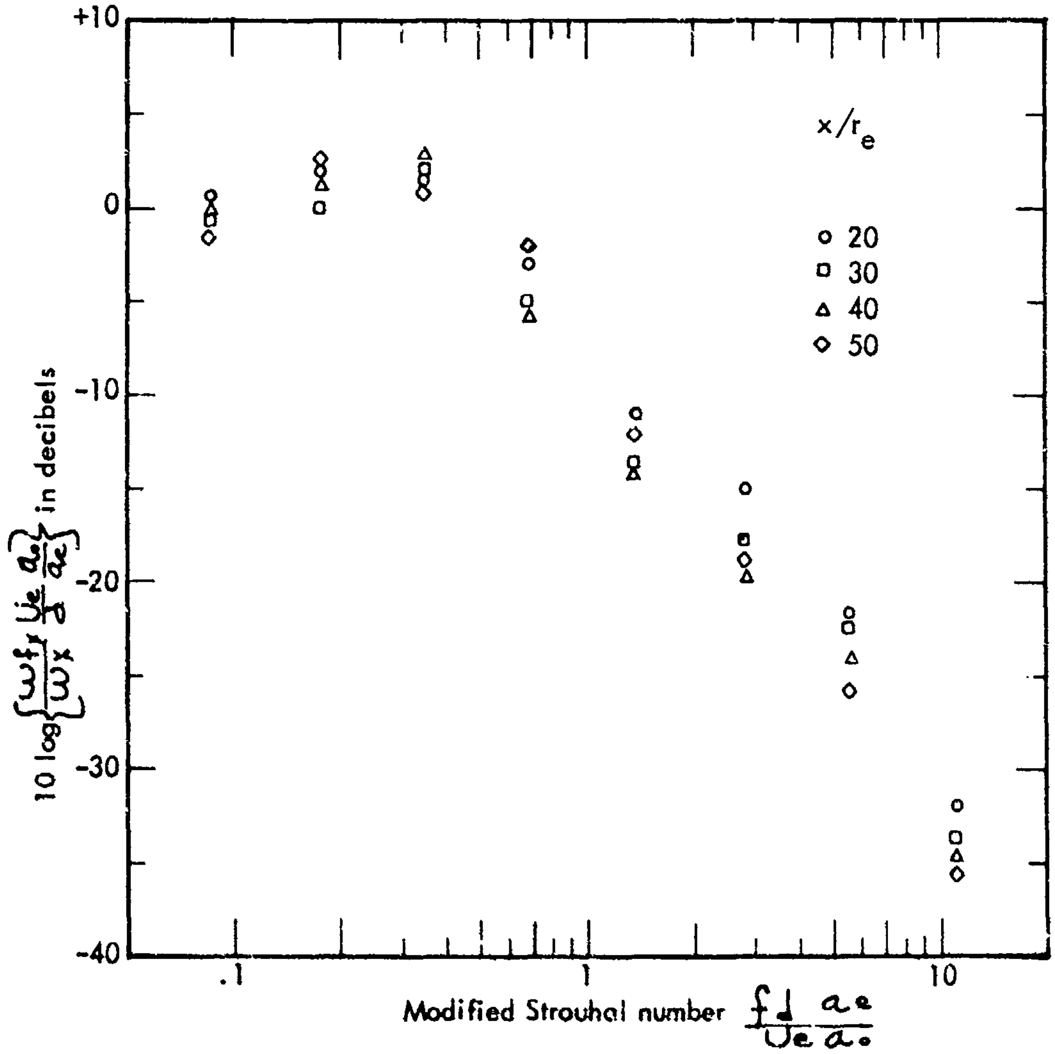

Figure 43. Normalized power spectra along 10° boundary for J57 in downstream region, $x/r_e > 13$.

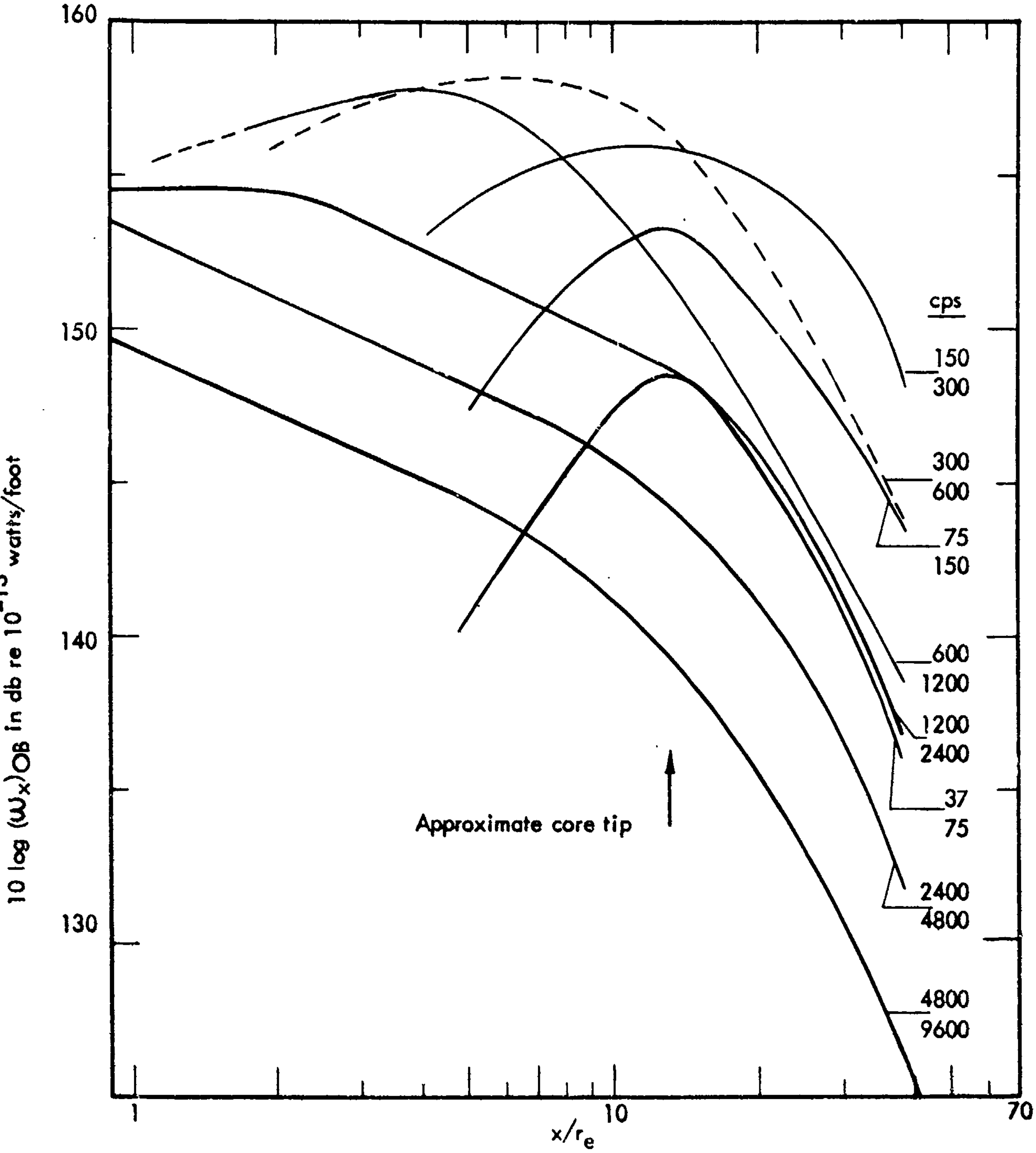

Figure 44. Acoustic power per unit axial length in octave bands shifted to probable source locations

The overall power per unit axial length computed from figures 41 and 44 is presented in figure 45. It is interesting to note that W_x is essentially constant along the core as predicted by Ribner (Ref. 18) and Dyer (Ref. 19) from dimensional considerations. In the downstream region W_x is falling with x/r_e at an increasing rate approaching $(x/r_e)^{-3}$ at $x/r_e = 40$. When the calculated values of jet breadth and centerline are utilized in this transition region, together with the $\rho_o U^8 b^2$ relationship, the curve predicts a much faster decrease of W_x with (x/r_e) than found from the data. Ribner's analysis (Ref. 18) leads to a prediction of $(x/r_e)^{-7}$ in the final downstream region of the jet.

Figure 43 gives a good indication of the reason why the noise generated in the transition region does not approach the $(x/r_e)^{-7}$ or the equivalent $\rho_o U^2 b^2$ relationships. These relationships assume that the power spectrum at any station throughout the jet is a function of U/b. In the mixing region U is constant and b is directly proportional with x and hence the center frequency should vary inversely with (x/r_e). Since this relationship is found true in figure 42, W_x is constant as predicted.

In the downstream region the same consideration for the frequency spectra proportional to U/b implies that the frequency spectra should vary inversely with $(x/r_e)^2$ since U is eventually proportional to $1/x$ and b is proportional to x. However, as figure 43 shows, the spectrum is apparently independent of axial position for $13 < x/r_e < 50$. This implies

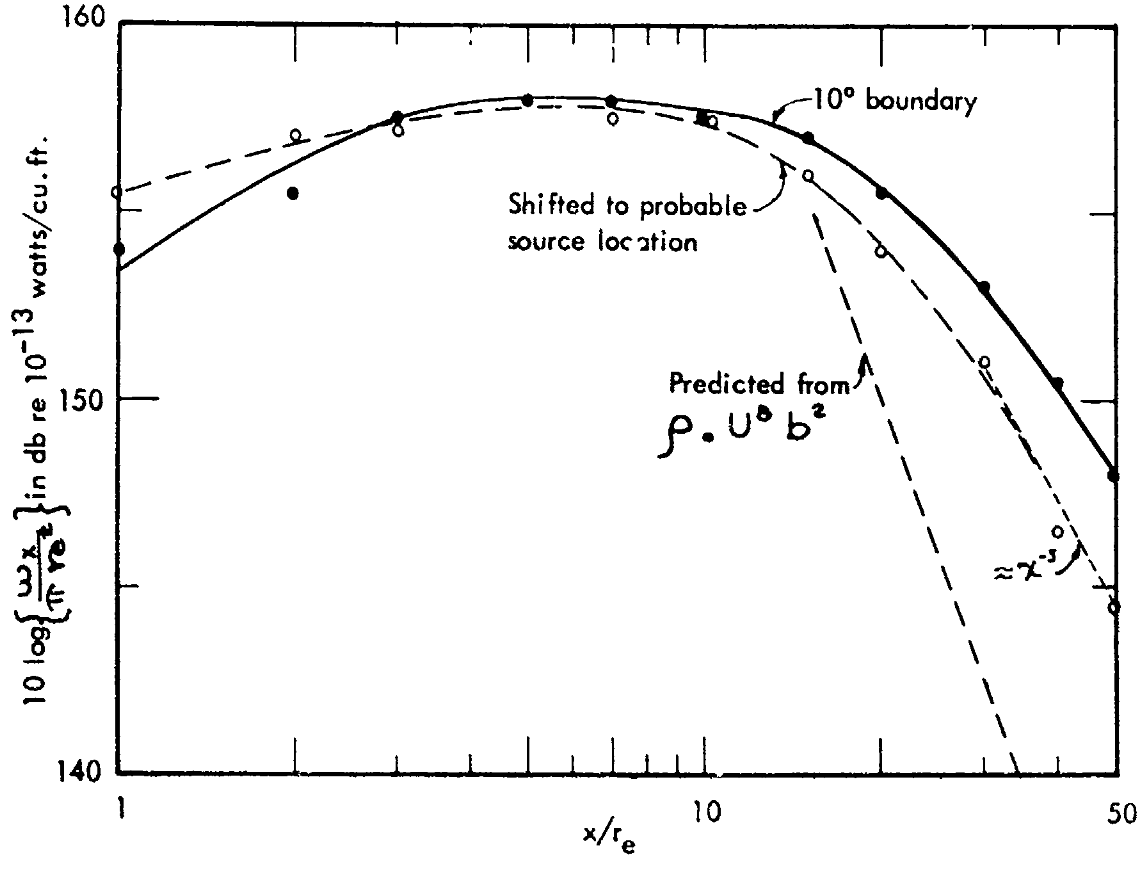

Figure 45. Overall acoustic power per unit axial distance and per unit nozzle area, shifted to probable source location.

that the more intense turbulence generated in the mixing region adjacent to the core does not decay as fast as the mean jet centerline velocity, which is implied somewhat in figure 16. Therefore, the primary generation of noise in this transition region probably results from turbulence developed upstream and convected downstream, with only small alteration through the transition region, rather than locally generated turbulence which follows the local flow parameters.

Figures 46 and 47 give the normalized power spectra for the core and downstream regions, respectively, associated with the "probable" source locations. These curves are essentially similar to figures 42 and 43, except for the slight axial shift; however, they are believed to be more accurate for prediction of noise generated in non-axisymmetric flows.

The relative proportions of total power radiated from the regions x/r_e greater and less than 13 are given in figure 48. As would be expected, the high frequencies are primarily radiated from the core region and the low frequencies from further downstream. However, it is noted that significant quantities of low frequency power are generated in the core region, and high frequencies in the downstream region. Hence, elimination of either mixing results in a decrease of approximately 6 db in the power radiated in one of the two frequency ranges.

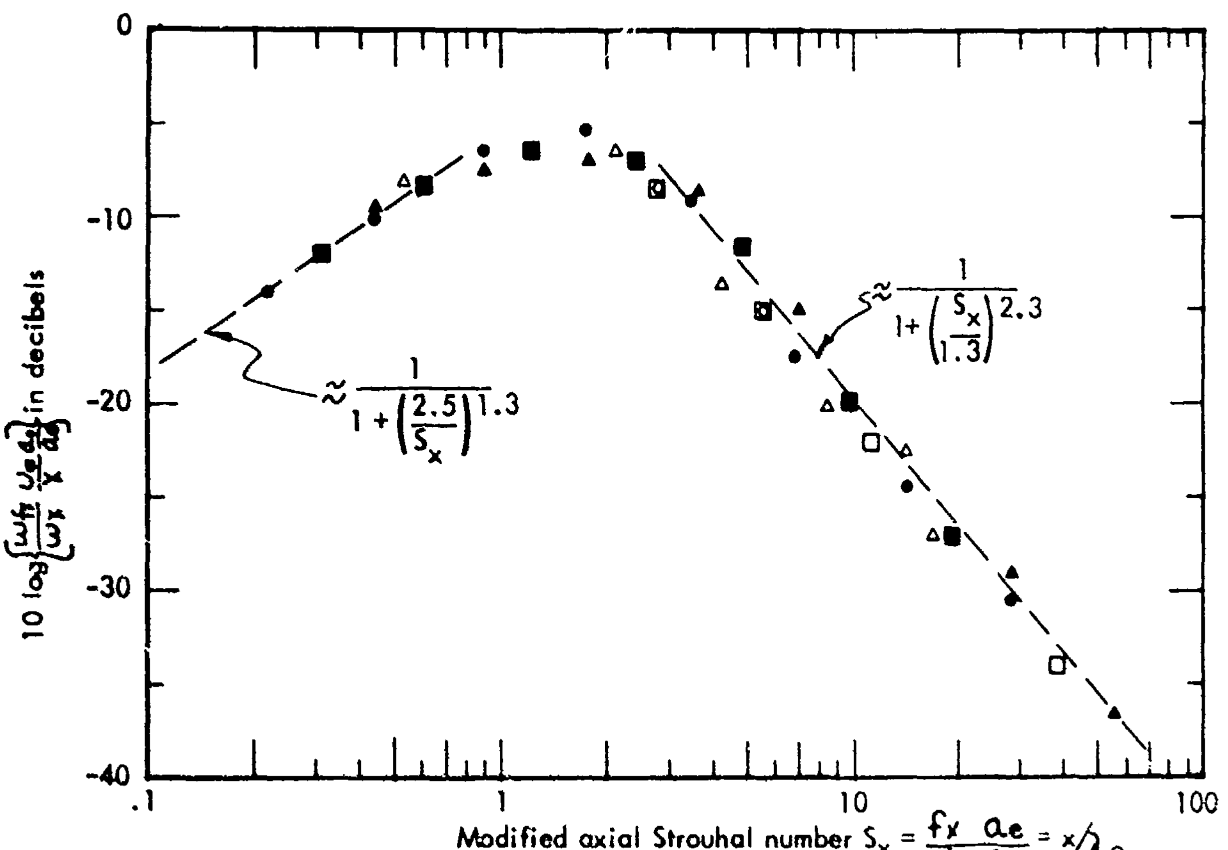

Figure 46. Normalized power spectra in core region from figure 45.

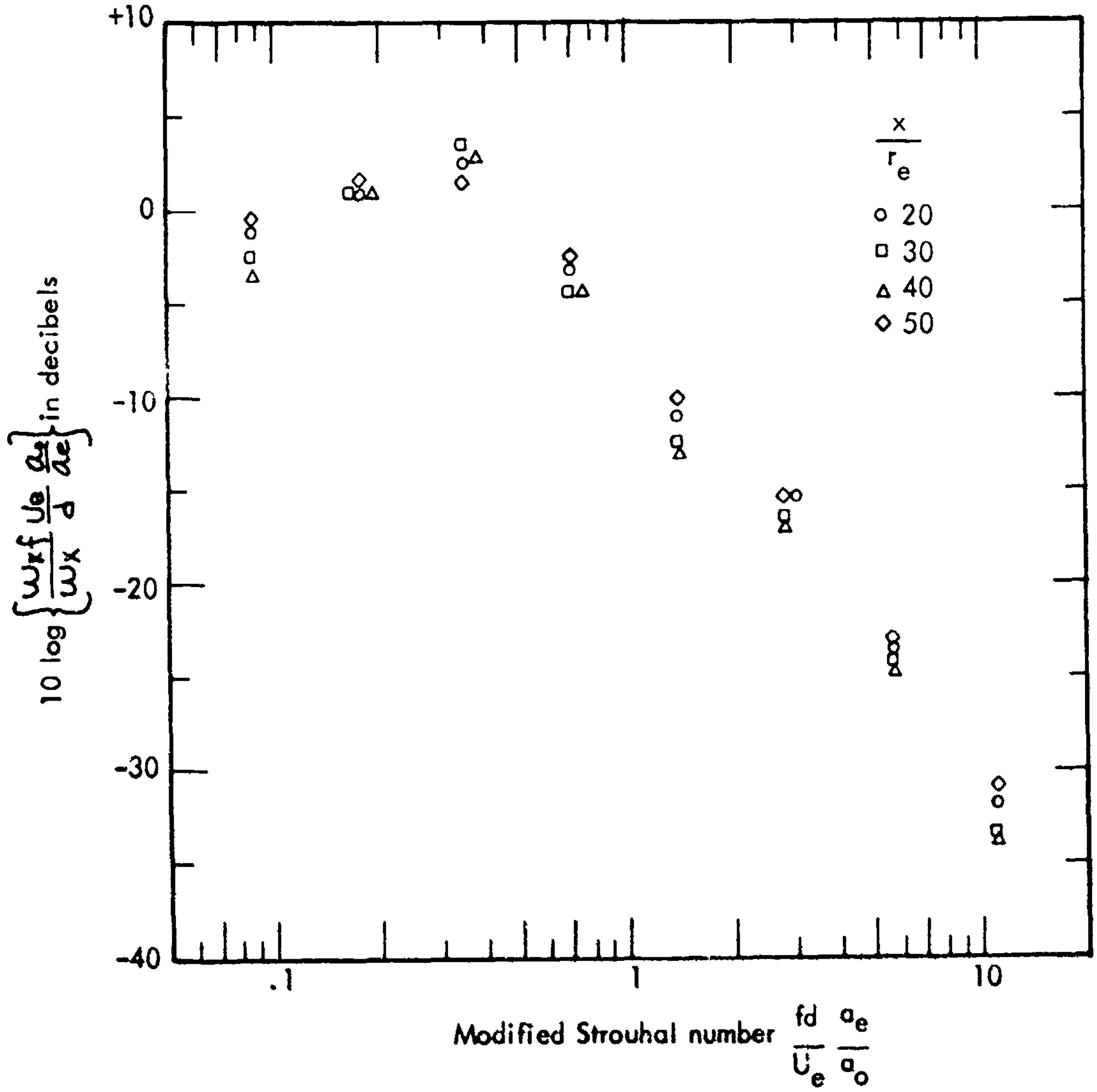

Figure 47. Normalized power spectra in downstream region, from figure 45.

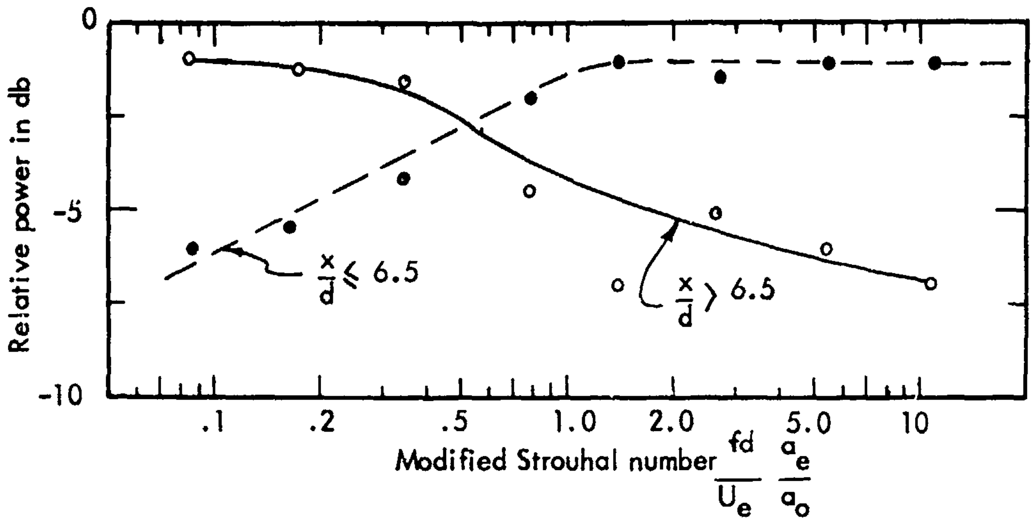

Figure 48. Relative contribution to total power for core region ($\frac{x}{d} \leq 6.5$) and downstream region ($\frac{x}{d} > 6.5$) as a function of dimensionless frequency.

Prediction of Near Field Noise from the Radiation Model

The preceding analysis of the radiation of noise from the jet has shown that the power computed from the 10° boundary is approximately equal to the power computed from far field measurements. Furthermore, this identity was utilized to determine the angular distribution of power as function of x/λ_e along the jet.

A more severe test of the prediction technique is its ability to predict near field noise. However, before discussing the result of this comparison, it is necessary to consider the influence of the ground plane on noise measured in the near field of conventional horizontal jets.

The effects of reflections of sound from a ground plane of variable impedance were discussed by Ingard (Refs. 27, 28) and portions of these results were specialized for the far field for both random and sinusoidal noise by Franken (Ref. 29). These latter results were discussed in detail by Howes (Ref. 30), and extended by Morgan et al (Ref. 10) to the near field by including the effect of the difference in path length between direct and reflected rays on the pressure amplitude. In order to generalize the final results in form suitable for application to arbitrary locations of observation and source points, Franken's approach can be extended directly to the near field as follows.

Consider a source height (h) and receiver height (H) with a separation distance (s) as shown in figure 49. The path length difference (Δ) between direct and reflected sound is

$$\Delta = \sqrt{d^2 + 4\,Hh} - d \approx 2Hh \qquad \text{(in the far field)} \qquad \text{(III-3)}$$

The relative path length (δ) is given by

$$\delta = \frac{d}{d + \Delta} = \left(1 + \frac{4\,Hh}{d^2}\right)^{-1/2} \approx 1 \qquad \text{(in the far field)} \qquad \text{(III-4)}$$

where the time delay τ between reflected and direct wave is simply Δ/a_o, where a_o is the velocity of sound.

The sound pressure at the observation point resulting from a single phase coherent source is the sum of the pressure of the direct wave (p_d) and the pressure of the reflected wave (p_r), and the resulting mean square pressure (p^2) at the observation point is:

$$\overline{p^2} = \overline{(p_d + p_r)^2} = \overline{p_d^{\,2}} + \overline{p_r^{\,2}} + 2\,\overline{p_d p_r} \qquad \text{(III-5)}$$

Noting that p_r equals $\delta\, p_d$ when the reflecting plane has infinite impedance, the mean square pressure at the observation point is:

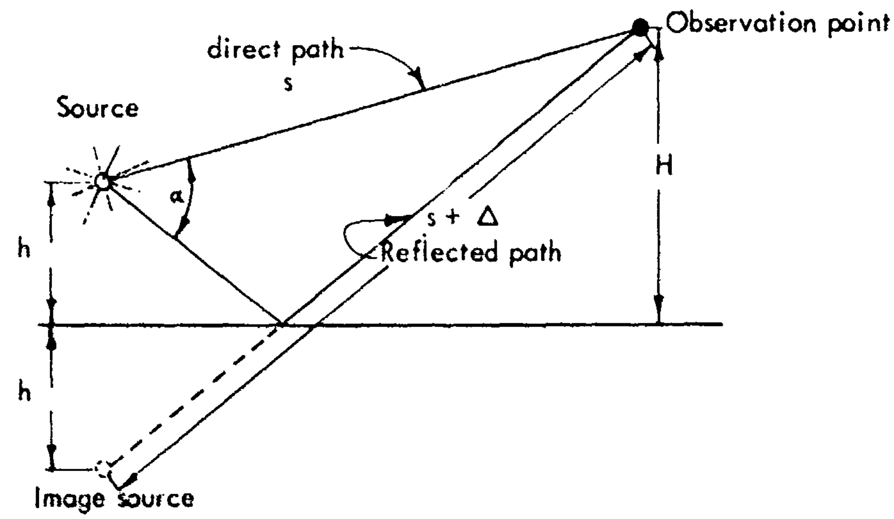

Figure 49. Sketch of geometry between source and observation points.

$$\overline{p^2} = \overline{p_d^2} (1 + \delta^2 + \delta B) \qquad \text{(III-6)}$$

where B equals twice the correlation coefficient between p_d and p_r.

As shown by Franken (Ref. 22), B is given by

$$\frac{\sin 2\pi f_b \tau - \sin 2\pi f_a \tau}{\pi \tau (f_b - f_a)}$$

where f_a and f_b are the upper and lower frequency limits of the filter bandwidth.

For white noise in octave bands, this expression reduces to

$$B = \frac{3 \sin \left(\frac{2\pi f_m \tau}{3} \right)}{\pi f_m \tau} \cos 2\pi f_m \tau \qquad \text{(III-7)}$$

where $\quad f_m = \dfrac{f_a + f_b}{2}$

When τ approaches zero, B approaches two, and if at the same time δ approaches unity, the mean square pressure at the observation point is four times, or 6 db greater than the direct mean square pressure, as would be expected. On the other hand, when f_m becomes large, B approaches zero, so that the observed mean square pressure is twice, or 3 db, greater than the mean square pressure for the direct path. The relationships for the near field case between δ, δ^*, τ and s are given in figure 50, and the relationship between B and $f_m\tau$ is given in figure 51.

An experimental verification of these relationships is summarized in figure 52. The data were obtained at 25 feet distance from a 3 inch diameter hot jet whose centerline was 9 inches above a concrete surface. The parameter Hh was varied by varying the microphone height between 9 and 48 inches, and f_m was varied in accordance with the octave bands measured.

It should be noted that these relationships only apply when the ground surface is hard and non-absorbing. When this restriction is not satisfied, the reflected wave is partially absorbed by the ground, and at great distances the direct wave is also partially absorbed. (Refs. 27, 28) This ground absorption is clearly illustrated in figure 53, which gives the average sound pressure level measured in octave bands at 250 ft. from several J57 engines operating at military power at different locations. The dip in response predicted by figure 51 occurs in the 1200 - 2400 cps frequency band, and is present in the measurements over concrete. However, the large variation in average sound pressure level evident at frequencies above 150 cps for the measurements over absorbing ground surfaces are not predictable by simple reflection theory.

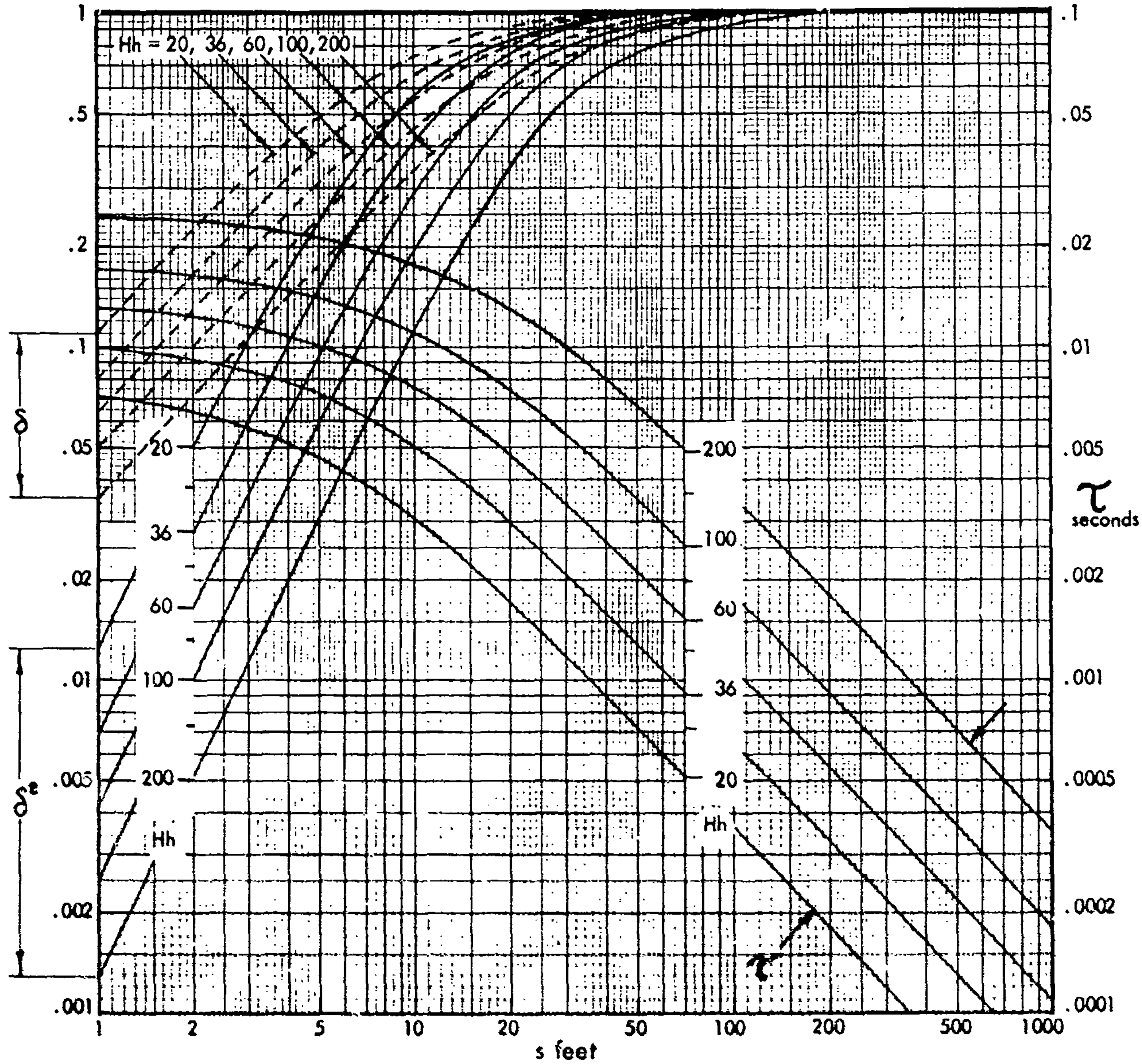

Figure 50. The relations between relative path length δ, δ^2, and time delay τ and the distance s between observation and source points as a function of the product of source and receiver heights (Hh) for computation of the sum of direct and reflected noise.

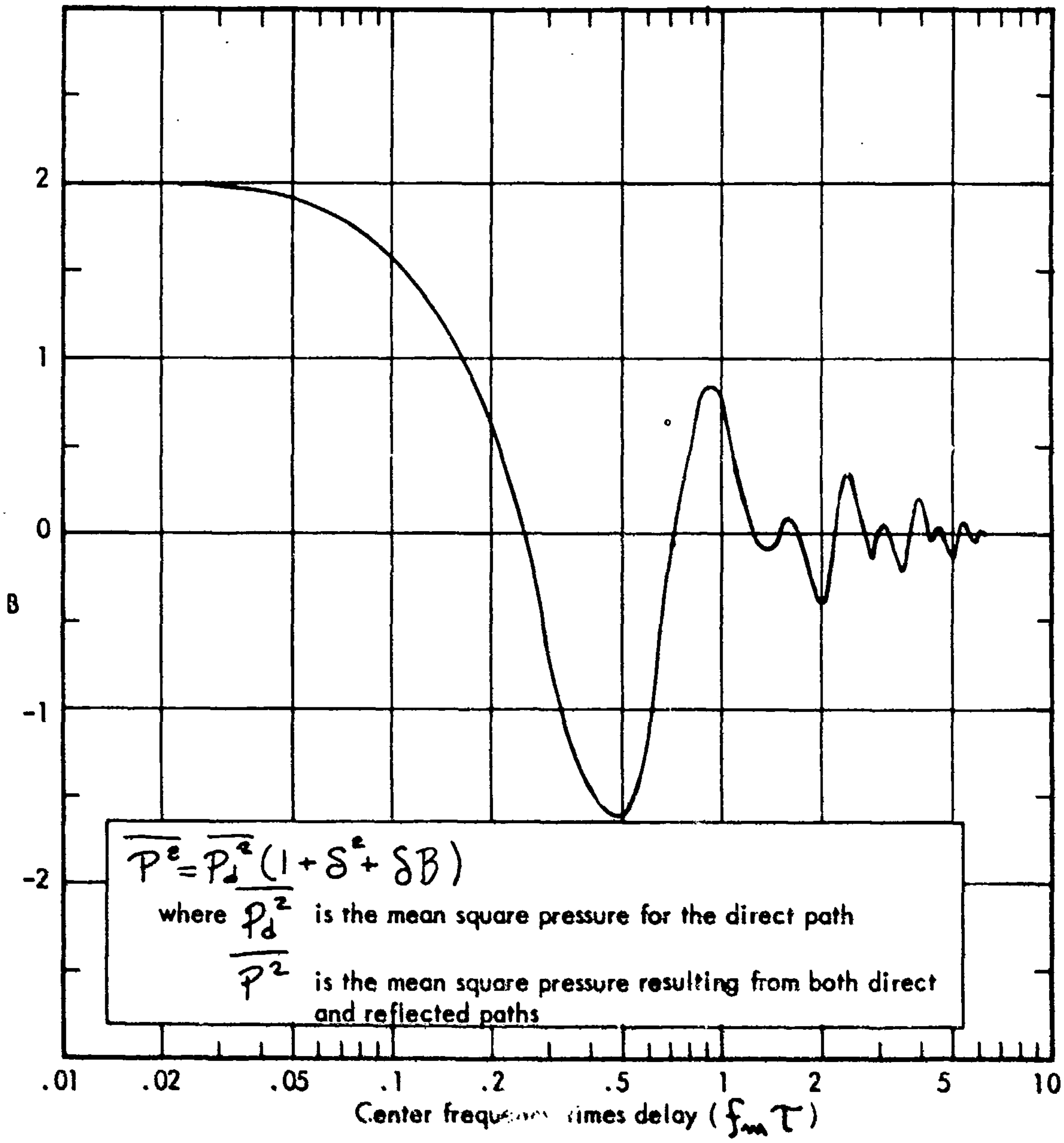

Figure 51. The parameter B (twice the correlation coefficient between direct and reflected wave) as a function of $f_m\tau$ for octave band white noise and infinite impedance reflecting surface.

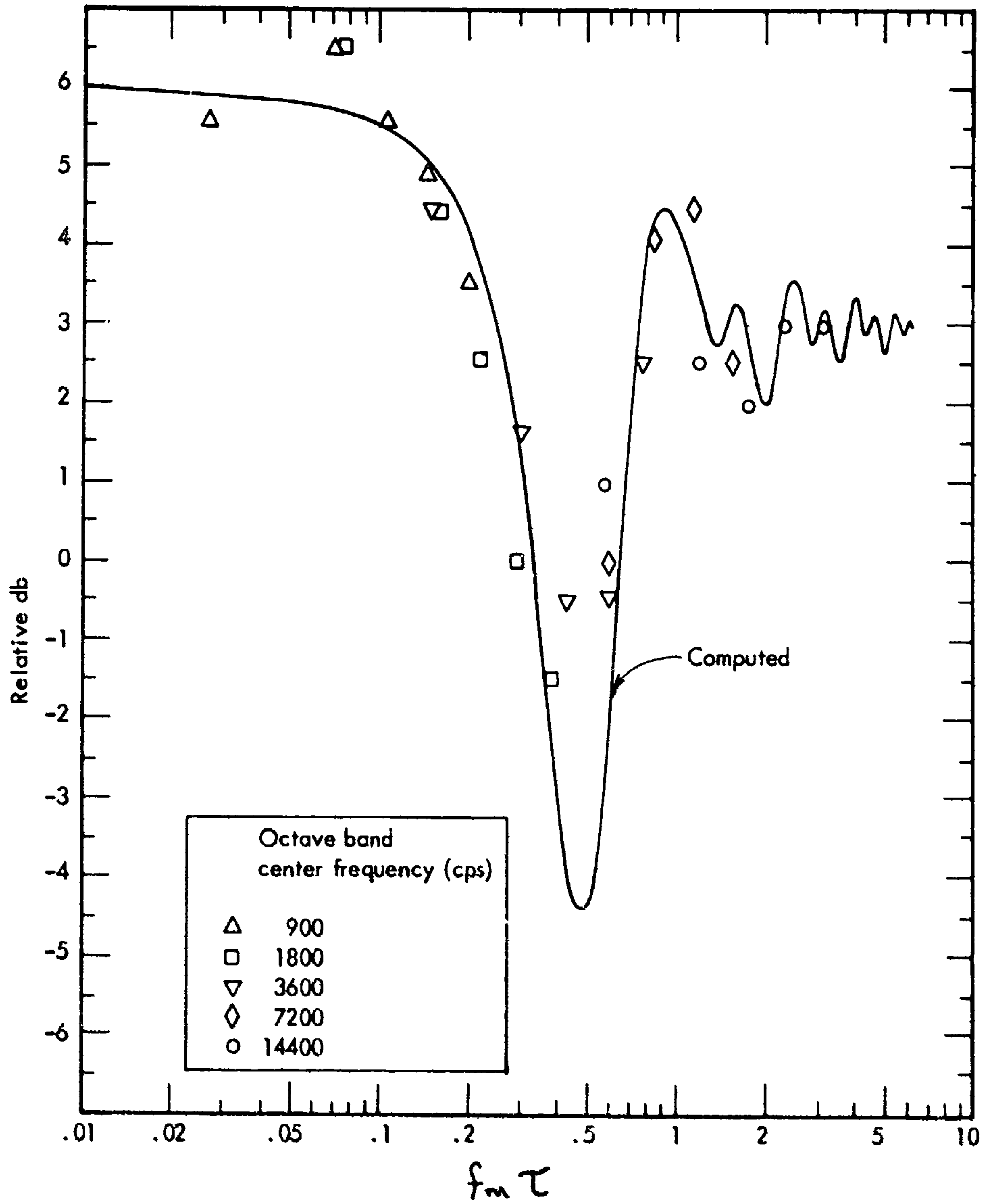

Figure 52. Comparison of data obtained with 1/8 scale jet at 25 ft. radius, 9 in. above ground and for various microphone heights between 9 and 48 in., with computed reflection effect.

Extreme caution must be exercised in applying these results to near field jet noise, even when the reflecting surfaces are hard, because of the assumption of a phase coherent source. In the near field the extended jet source becomes large relative to the distance between observation point and receiver. Hence, it is necessary to divide the jet into several segments and compute the noise at the observation point resulting from each segment. Since the correlation of the noise generated by adjacent segments can be assumed to be zero, the contributions from all segments can be summed on an energy basis, where the effect of ground reflections is accounted for separately in the computation of the noise from each segment. However, when the observation point approaches close to the jet, the angle between the direct and reflected path (α) becomes large, and there is no longer any guarantee of source coherence, since the noise generated in the mixing region around the jet axis at any station is only in phase over a limited angular region. Only very limited data exist in Ref. 1 relative to this point, and it must remain an uncertain factor at this time.

Predictions of near field noise were first made for six positions extending from 40 feet forward to 60 feet aft of the nozzle along a line parallel to, and 20 feet from, the jet axis.

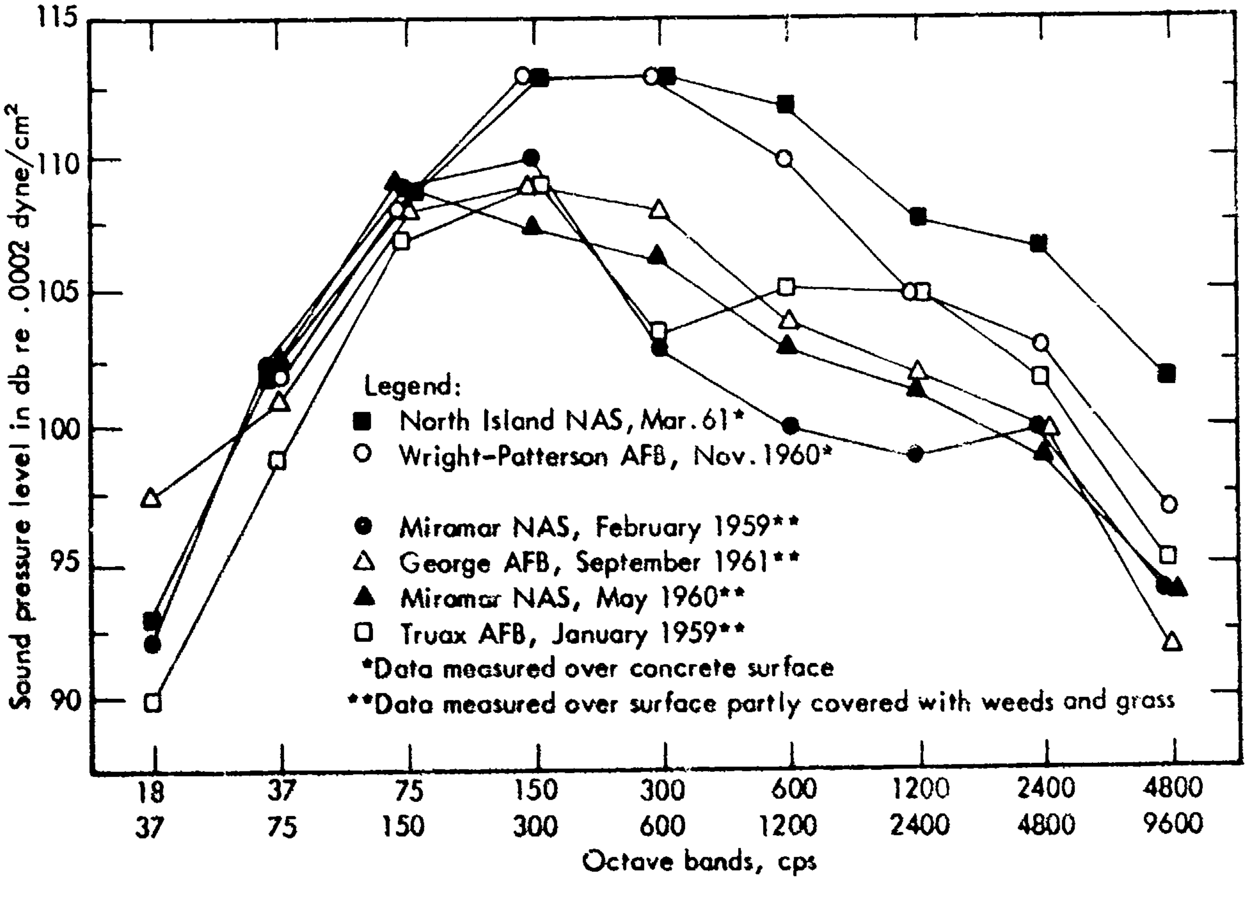

Figure 53. Summary of average far field sound pressure levels (250 ft., 0° - 180°) for the unsuppressed J57 engine operating at military power. (Engine centerline and microphone 6 feet above the ground plane)

This choice enabled a comparison with data from independent noise surveys (Refs. 1, 3, 20 to 26) which were made on J57 engines in conjunction with the evaluation of jet engine ground runup noise suppressors.

For the purpose of prediction, the jet was divided into five segments with average distances from the nozzle of 2.1, 4.2, 8.4, 16.8 and 33.6 feet, respectively, and the power per segment was calculated for each octave band.

Each point in the near field was characterized by its distance from the center of the segments and angle relative to the axis of the jet. Thus, for the k^{th} octave the sound pressure level is

$$spl_i^{(k)} = L\sum_{i=1}^{5} \left[PWL_i^{(k)} + f_i(\theta) - 10 \log (4\pi d_i^2) + 10 \log (1 + \delta^2 + \delta B) \right] \qquad \text{(III-8)}$$

where $PWL_i^{(k)}$ is the power of the i^{th} slice for the k^{th} octave, $f_i(\theta)$ is the

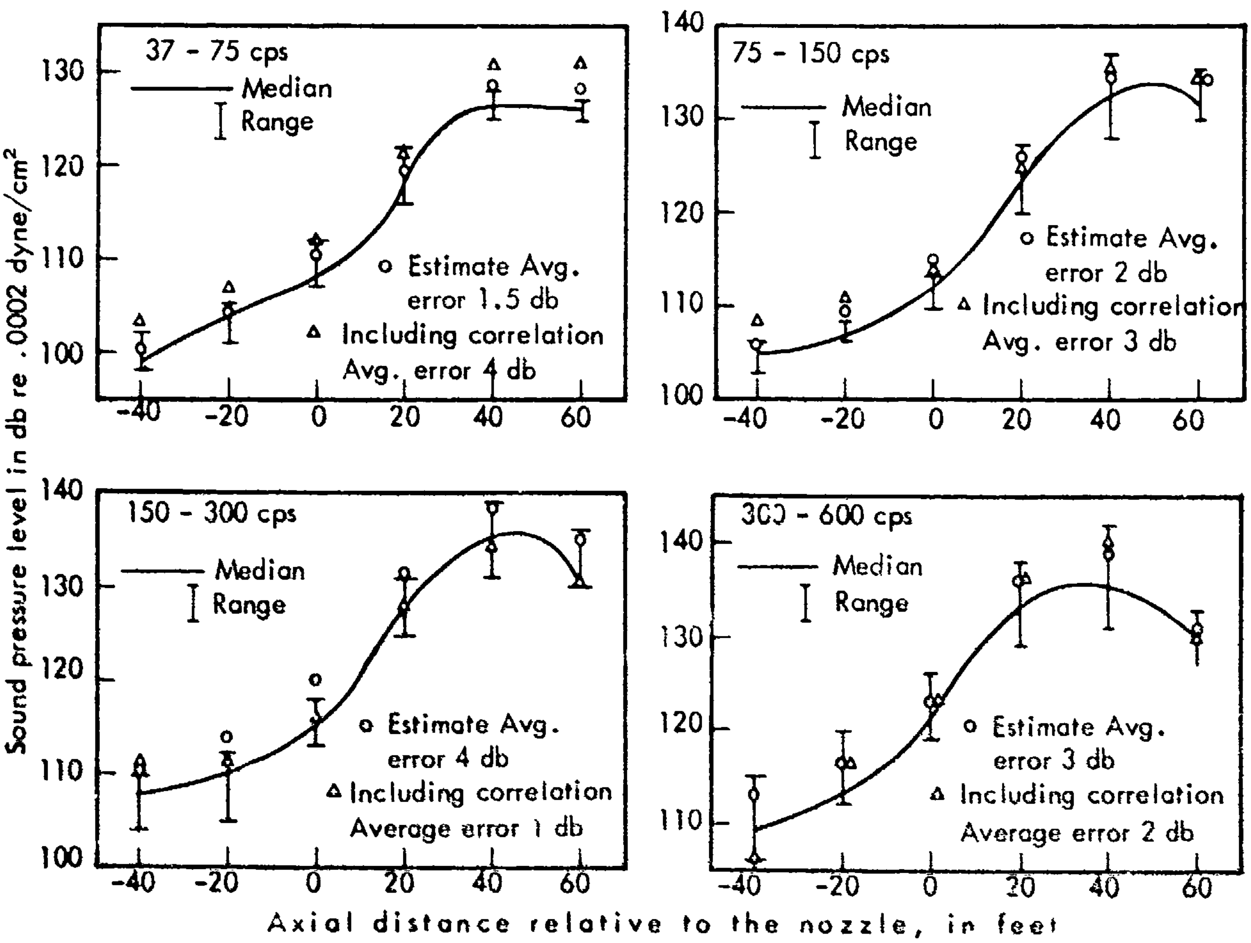

Figure 54. Predicted values of sound pressure level in four octave bands along a line 20 feet from and parallel to the axis of the jet, considering both simple hemispheric radiation and correlated ground reflections, compared to the range and median values of nine measurements on a J57 engine at military power.

directivity for the appropriate x/λ_o of the slice, and d_i is the distance from the center of the i^{th} slice.

The results are shown in figures 54 and 55, for both hemispheric radiation, where the reflected ray is assumed uncorrelated with the direct ray (B = 0), and for correlated reflected and direct waves. Only one value is given in figure 55 because the value of $f_m\tau$ is sufficiently high at these frequencies to insure B = 0 and, therefore, simple hemispherical radiation exists. On each graph the average error between prediction and median of the nine measurements is given. In general, the predictions are within the range of the measured data, and the fit appears most encouraging, particularly between 600 and 4800 cps. It is interesting to note that in the frequency region above 600 cps where the model predicted far field power 2 db greater than computed from the far field measurements, the 20 foot line predictions average less than 1 db higher than the median. Inclusion of the effect of correlation between direct and reflected waves (B = 0) in the low frequency range appears particularly appropriate in the 150 - 300 cps band where the correlation gives cancellation.

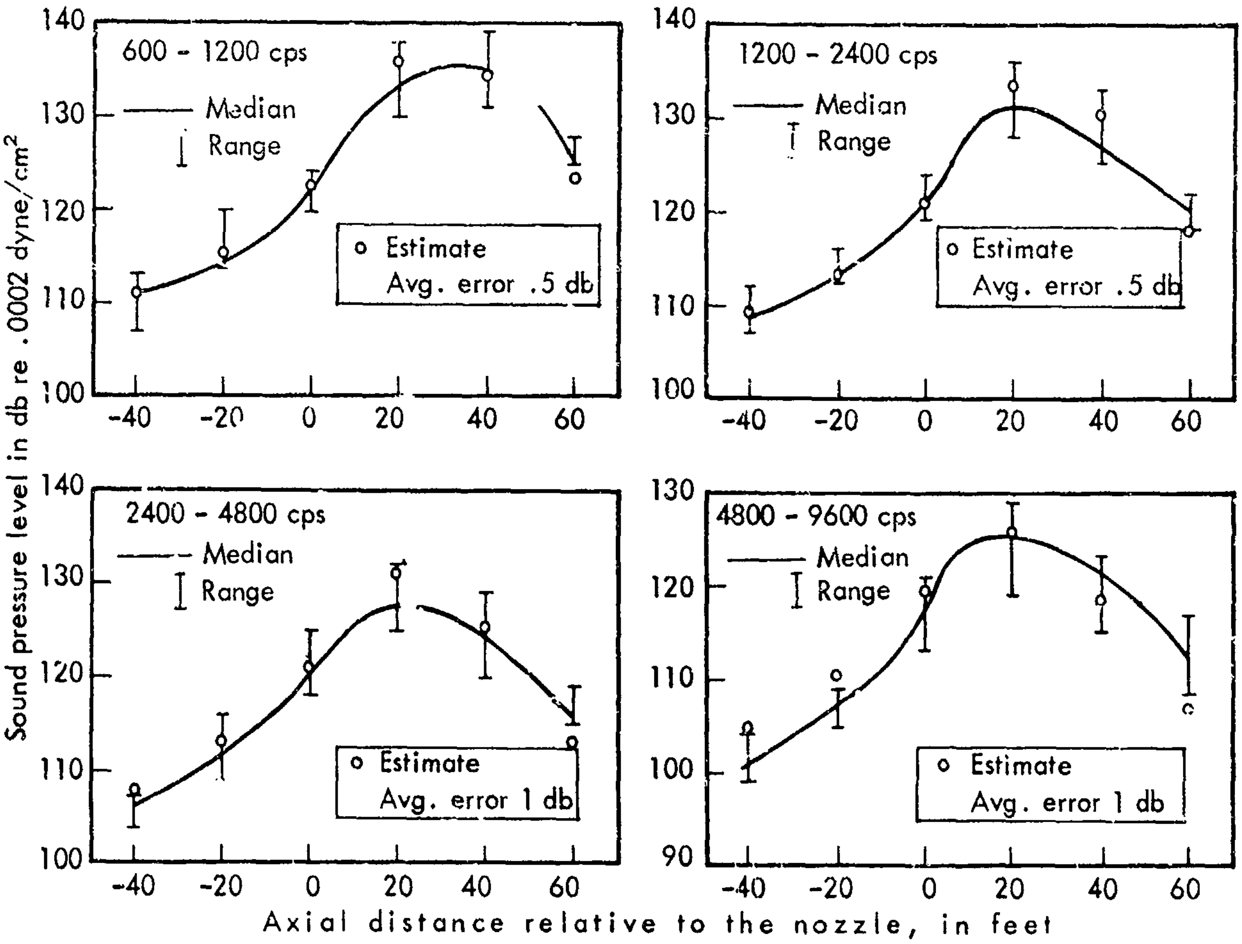

Figure 55. Predicted values of sound pressure level in four octave bands along a line 20 feet from and parallel to the axis of the jet, compared to the range and median values of nine measurements on a J57 engine at military power.

However, this correction increases the average error in the 37 - 75 cps band from 1.5 to 4 db.

Contours of equal sound pressure level were computed for three octave bands, 75 - 150, 300 - 600, and 1200 - 2400 cps, as shown in figure 56. For these computations, ground reflections were assumed to be incoherent (B= 0), giving a 3 db increase over the direct wave. It is clear that this example of idealized contours behaves in the same manner as the measured contours in figures 21 and 22, with the low frequencies radiating farther aft than the high frequencies and with the steep gradient of sound pressure level forward from the nozzle.

The method also enables computation of the apparent jet source location of the sound reaching any point in the near field. This requires solving for $\overline{x}$ in

$$spl_t + 10 \log \overline{x} = \log \sum_{i=1}^{5} spl_i + 10 \log x_i \qquad \text{(III-9)}$$

where spl_i is the sound pressure contributed by each segment of the jet, spl_t is the total sound pressure level at the point, and x_i is the distance downstream for the center of each slice.

These computations were performed for the two octaves between 300 and 1200 cps for the observation points located at 12 and 32 feet downstream and 22.5 feet from the jet axis. These are the points for which correlation data are available (Ref. 1), as illustrated in figure 29. For a center frequency of 1000, the angles derived from data are 102° and 124° for the two positions, respectively, as compared to 102° and 137° calculated from the model using the octave band centered at 850 cps. The angles from data for a center frequency of 400 cps are 103° and 130°, as compared to 95° and 132° calculated for the octave band centered at 425 cps. Thus, it can be seen from the model that the axial location of the apparent source depends upon the angle between the observer and the jet axis. This explains why the correlations performed in the field often have indicated different apparent source locations which were often ascribed to inaccuracy.

Effect of Jet Exit Temperature and Mach Number on Directivity

The relationship between the directional properties of jet noise and the jet flow parameters have been a subject of considerable speculation for many years. The gross effect of temperature on the far field directivity is shown in figure 57 for Mach 1 axisymmetric jets. It is clear from the figure that the increase of temperature shifts the angle of maximum radiation forward.

This shift in the maximum angle of noise from jets at constant Mach number results from refraction in the jet, as first suggested by Hubbard (Ref. 11). A step toward improved understanding of this refraction is the theoretical analysis in Appendix C for propagation from a source on the axis of a zero velocity jet which has a cylindrically symmetrical temperature gradient. These results are not directly applicable to the mixing region adjacent to the core of a real jet which has important velocity gradients and has sources located approximately at the maximum portion of these gradients, as shown in figures 1 to 3. However, the

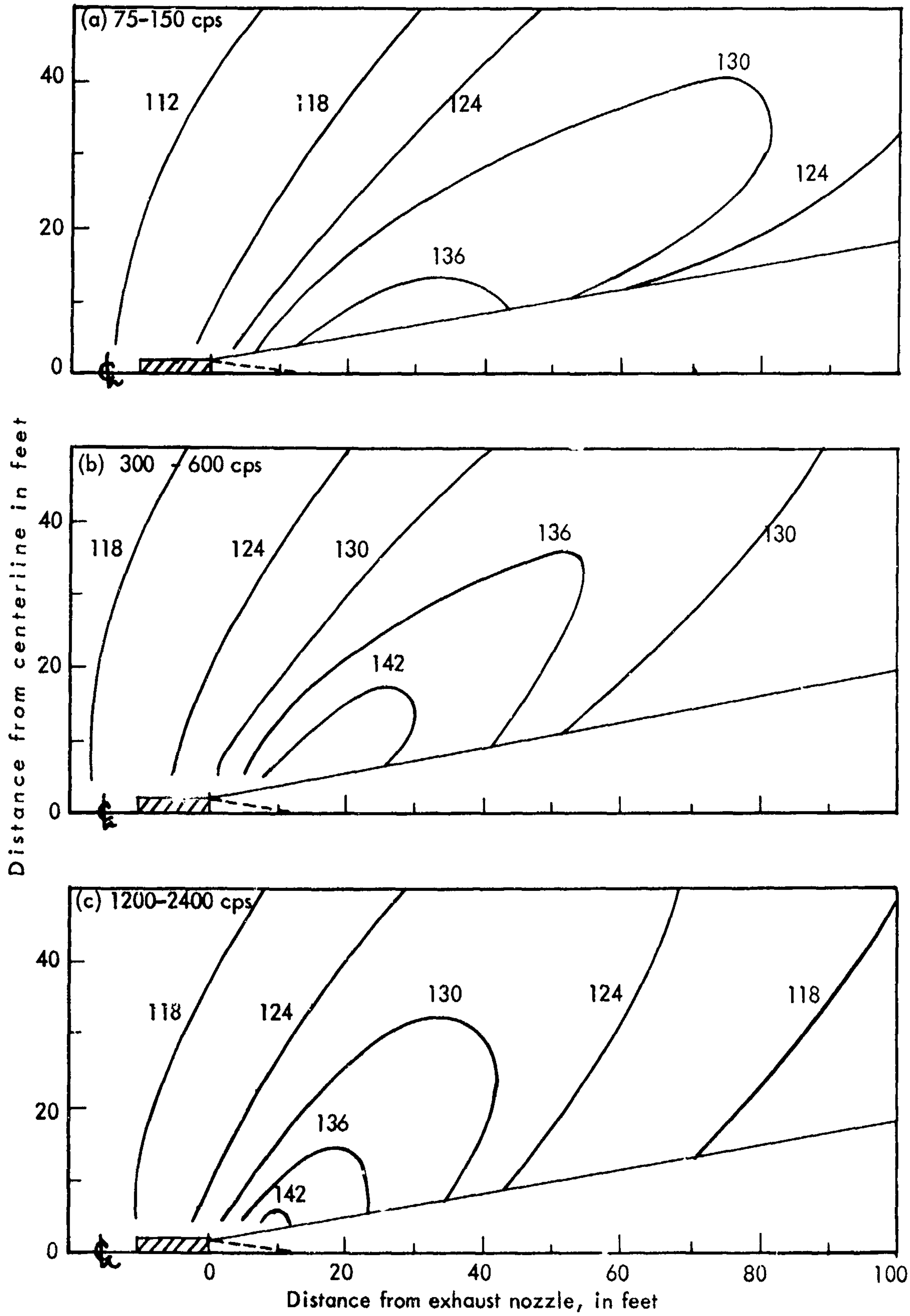

Figure 56. Contours of equal sound pressure level using the near field prediction model without consideration of ground reflection.

assumptions in the theory are approximated in the downstream region of a jet, say beyond 20 diameters. Further, these results are useful in demonstrating the potential magnitude of temperature refraction in affecting the far field directivity.

Because of the time-consuming difficulties involved in removing the restrictions inherent in the Appendix C theory, a series of ray diagrams were constructed for sources located at approximately the maximum velocity gradient and for radiation in the plane containing the jet axis. As noted in conjunction with the discussion of figure 27, the temperature and velocity gradients were assumed coincident and were taken directly from the Laurence data of Ref. 31.

Figures 58 and 59 give two additional examples of ray diagrams for Mach 1 jets at exit static temperatures of 60°F and 2700°F respectively. The results of these two figures, figure 27, and several other similar constructions, are summarized in figure 60. It is interesting to note that ray refraction shifts the angle of maximum radiation forward, away from the jet boundary, both for an increase in flow Mach number at constant temperature, and for an increase in temperature at constant flow velocity. Recognizing, in accordance with

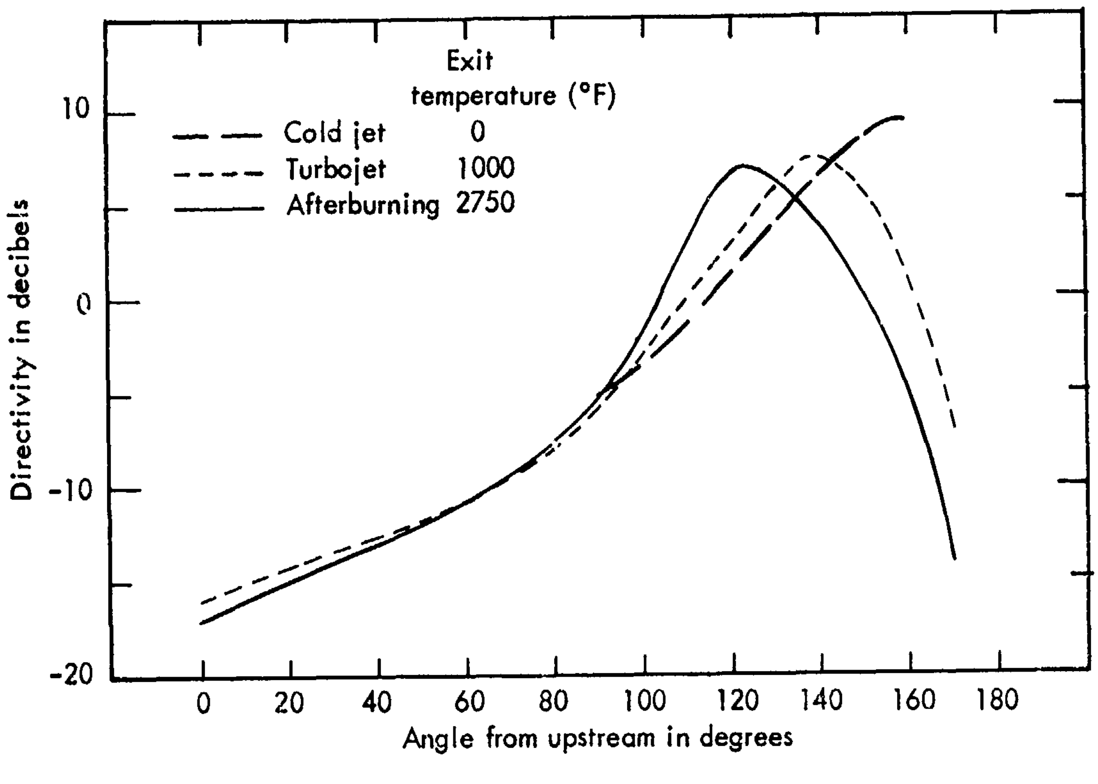

Figure 57. Comparison of the directivity of axisymmetric jets with exit Mach numbers of unity for three values of exit static temperature.

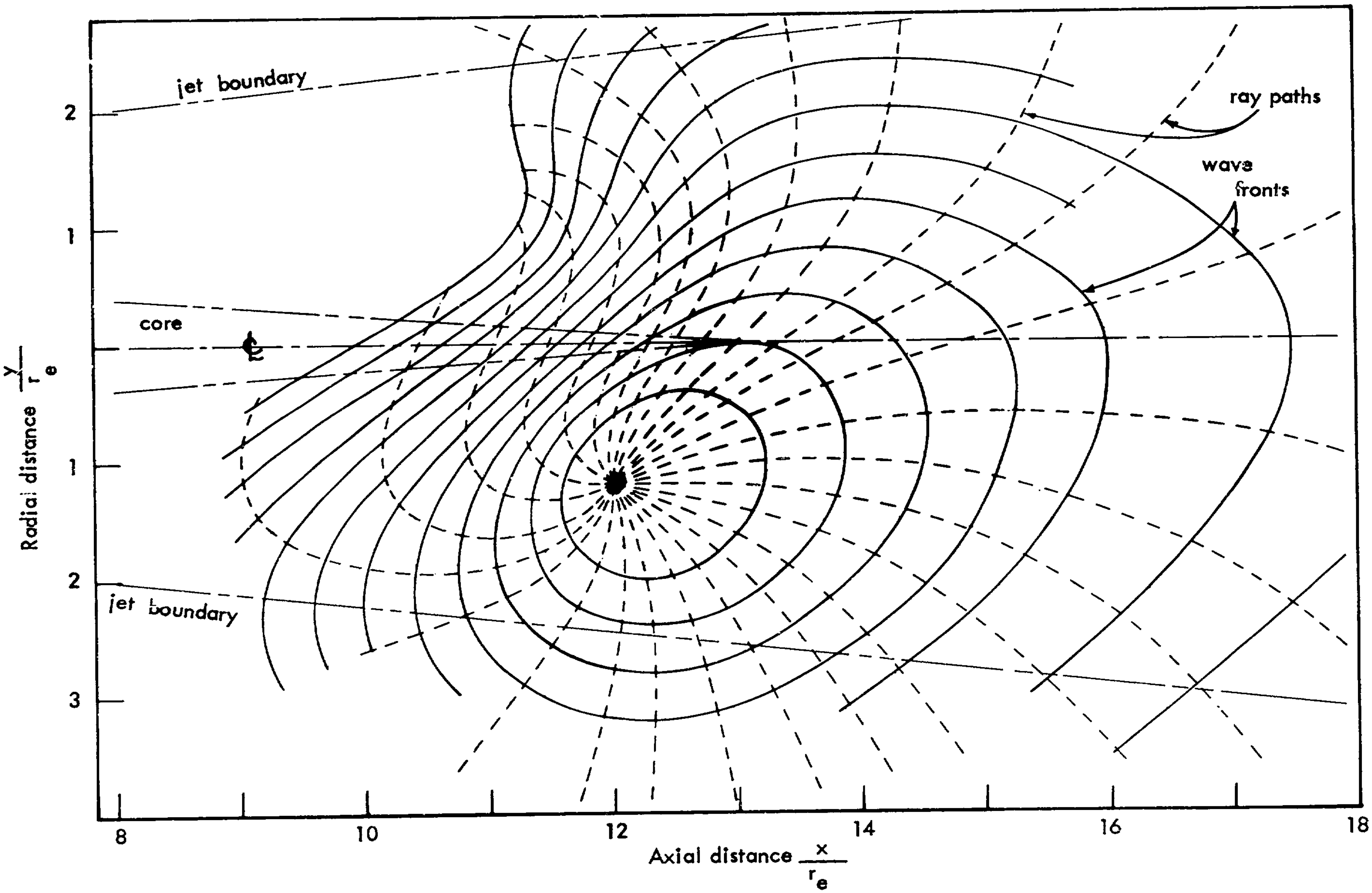

Figure 58. Ray diagram for radiation from simple source located at the center of the jet velocity and temperature gradient, for exit velocity of 1120 ft/sec. and exit temperature of 60°F.

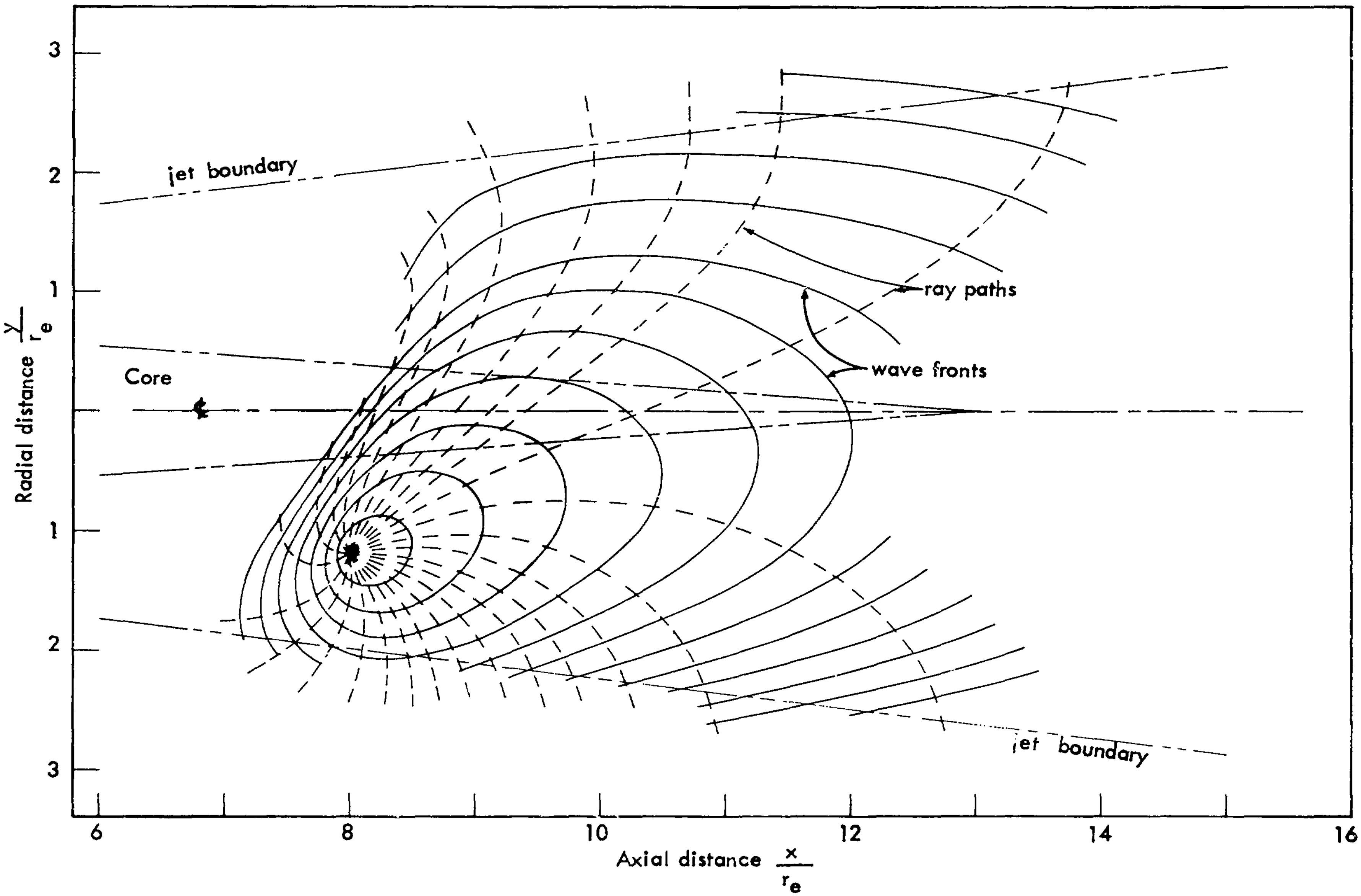

Figure 59. Ray diagram for radiation from simple source located at the center of the jet velocity and temperature gradient, for exit velocity of 2750 ft/sec. and exit temperature of 2700° F.

figure 30, that the ray concept only applies at high values of x/λ_o (for the 1000°F jet, figure 30 shows $x/\lambda_o > 5$ is apparently sufficient), the results of figure 60 demonstrate that refraction of sound in the jet is one of the major factors causing the maximum angle of high frequency sound to be farther forward than the maximum angle of low frequency sound in all jets. This conclusion follows directly, since a greater proportion of the total high frequency sound is radiated from regions of high x/λ_o in comparison to low frequency radiation which is radiated primarily from regions of low x/λ_o.

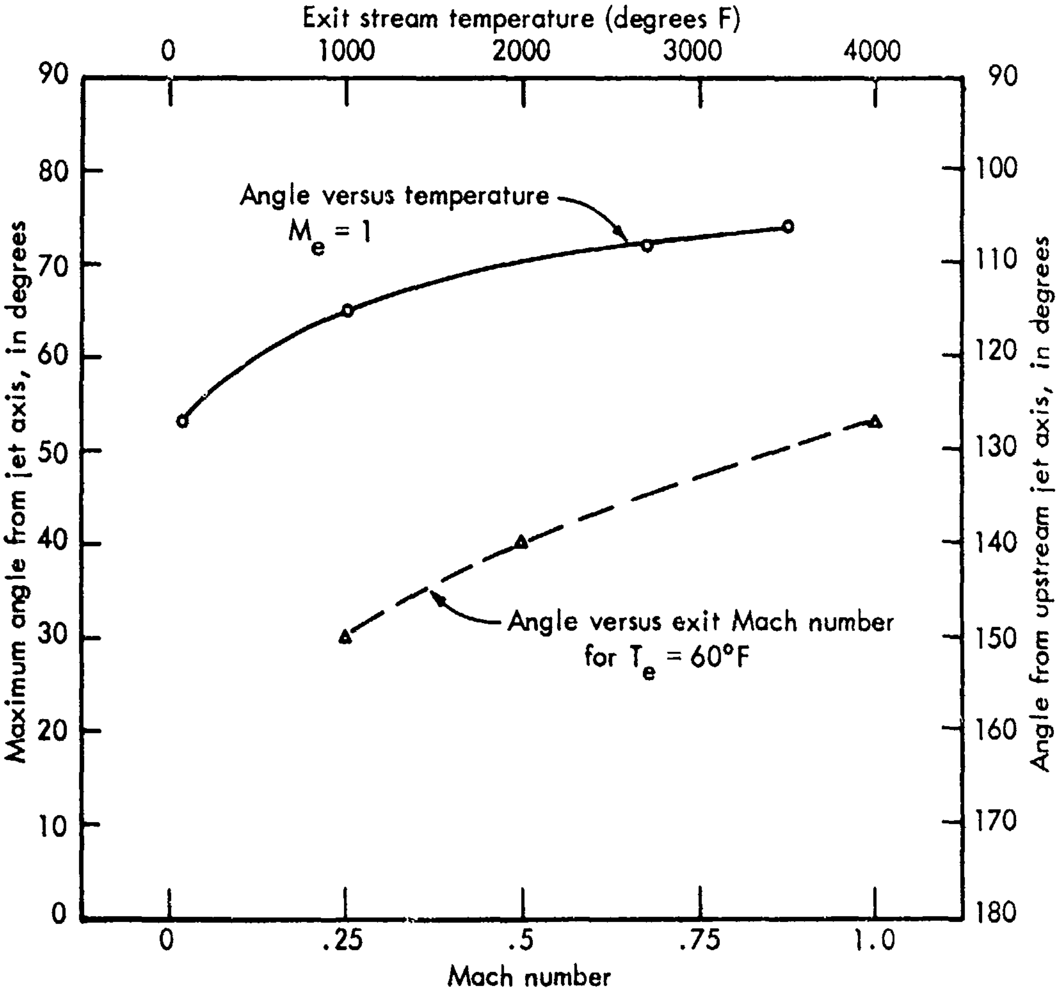

Figure 60. Summary of apparent angle of maximum radiation as a function of Mach number and temperature for simple sound sources located in a jet flow at the approximate position of the maximum gradient, derived from ray diagrams.

These results offer an opportunity to compare the various terms in the new modified wave equation for jet noise propagation derived in Appendix B, as given on the left hand side of equation (B-92). For propagation of sound in a jet with a two dimensional gradient with no sources present, this equation becomes

$$\frac{\overline{D}}{\overline{D}t}\left[\frac{1}{\overline{a}^2}\frac{\overline{D}^2 p}{\overline{D}t^2} - \nabla^2 p\right] + 2\frac{\partial U}{\partial y}\frac{\partial^2 p}{\partial x \partial y} = 0 \tag{III-10}$$

where p is the acoustic pressure

and $\frac{\overline{D}}{\overline{D}t}$ is the total differential operator $\left(\frac{\partial}{\partial t} + U\nabla\right)$

If the right hand gradient term in equation (III-10) is much smaller than either of the other two bracketed terms, then it may be neglected and equation (III-10) reduces to the standard second order differential equation for propagation of sound in moving medium:

$$\frac{1}{\overline{a}^2}\frac{\overline{D}^2 p}{\overline{D}t^2} - \nabla^2 p = 0 \tag{III-11}$$

As shown in Appendix B, the gradient term in equation (III-10) is of the same order as the first term inside the brackets for a typical Fourier component of sound when

$$\frac{1}{\pi f}\quad\frac{\partial U}{\partial y}\frac{1}{(1+M)^3} = 1 \tag{III-12}$$

For the velocity gradient given in figure 12, the maximum value of

$$\frac{\partial U}{\partial y} = \frac{.6U_e}{b}$$ and occurs at $y = b$.

Assuming a typical value of M for the jet as .5 M_e, equation (III-12) becomes

$$1 = \frac{.6\ U_e}{\pi f b(1+.5M_e)^3} = \frac{.6\ a_e\ M_e}{\pi f b\,(1+.5M_e)^3} = \frac{1.2\ M_e}{k_e b(1+.5M_e)^3} \tag{III-13}$$

where k_e is the wave number $\left(\frac{2\pi f}{a_e}\right)$ based on the speed of sound a_e at the jet exit temperature.

When $M_e = 1$, the solution of equation (III-13) gives $k_e b = .36$, or in terms of a wave number (k_o) defined for the ambient speed of sound;

$$k_o b = .36 \frac{a_e}{a_o} \qquad \text{(III-14)}$$

For the axisymmetric Mach 1 Jet, $b = r_e$ at the tip of the core, b/x is essentially constant between the nozzle and the core, and the length of the core (x_t) is, from figure 14, approximately 13 r_e. Combining these relationships, equation (III-14) may be restated in terms of x/λ_o, giving

$$\frac{x}{\lambda_o} = \frac{13}{2\pi}(k_o b) = .75 \frac{a_e}{a_o} \qquad \text{(III-15)}$$

When a_e = 1850 ft/sec., the value of x/λ_o is 1.25 for approximate equality between the gradient term and either one of the other terms in equation (III-10). This is consistent with figure 30, for at small values of x/λ_o (of the order of 1.25 and lower), where the gradient term has importance, the angle of maximum radiation from the jet lies close to the jet boundary. However, when the gradient term becomes much smaller than either of the other terms in equation (III-10), (x/λ_o) > 5 implies the gradient term is less than 25% of either of the other two terms) the angle of primary radiation becomes a constant which approximates the angle given by simple ray considerations. This result is consistent with equation (III-11), since the ray solution is an exact solution for equation (III-11) when the bending of the ray is small in the distance of one wavelength.

This simple evaluation of equation (III-10) can also demonstrate the relationship of the gradient term of equation (III-10) with the generalized power spectrum given in figure 46. For a Mach 1 jet, $U_e = a_e$, and the modified Strouhal number absissa in figure 46 becomes equal to x/λ_o. The spectrum in figure 46 has a low frequency asymptote where the acoustic power/cps increases with increasing x/λ_o, which is valid below x/λ_o of approximately 1.0. Above the low frequencies is a transition region, approximately $1.0 < x/\lambda_o < 2.5$, and a high frequency asymptote, approximately $x/\lambda_o > 2.5$. It is pleasantly surprising that these three regions agree so well with the simple order of magnitude analysis of the importance of the gradient term in equation (III-10). The clear implication is that the full equation (III-10) controls radiation of sound in the jet mixing region adjacent to the core for nondimensional frequencies below and including the spectral maximum, and that equation (III-11) is applicable only at nondimensional frequencies above the spectral maximum.

Therefore, the theoretical solution of noise radiation and generation in jet flows must rest on the solution of equation (B-92), of which equation (III-10) was a simplified version. Until these solutions are available, it is not possible to extend the near field prediction model developed in this section for the 1000°F Mach 1 jet to other temperatures and Mach numbers, except through semi-empirical derivations similar to that utilized for the near field model described for the 1000°F jet. These derivations should be based on a careful set of new model measurements made in free space without a ground plane, where exit Mach number and temperature are varied independently. In the absence of data, the first approximation to an extension of the model in figure 38 to include temperature effects would be to shift the maximum angles and curves by the ratio of ray angle for the new temperature from figure 60 to the ray angle for 1000°F.

In order to make preliminary prediction of the near field noise from jets with exit velocities lower than 1850 ft/sec. and 1000°F, it is best to extrapolate from empirical data. For this purpose the most comprehensive set of near field measurements for heated jets was made by Wolfe (Ref. 2) over a velocity range of 1000 - 1800 ft/sec. Figure 61, taken directly from Wolfe's figure 31 (Ref. 2), gives the value of n in equation (III-16) below:

$$spl' = spl_{ref} + 10 \ n \ \log \frac{U}{1850} \tag{III-16}$$

where spl_{ref} refers to the values obtained for the 1000°F jet at a point, either by the prediction model or directly from the data of Ref. 1, and spl' is the spl estimated for the jet of differing velocity.

Unfortunately, this method does not separate the effect of flow Mach number from flow temperature and for accurate prediction of the spacial distribution of noise from a jet flow, these two parameters must be considered separately. However, until the series of experiments mentioned above are accomplished, these data are probably the most reliable and useful for this purpose.

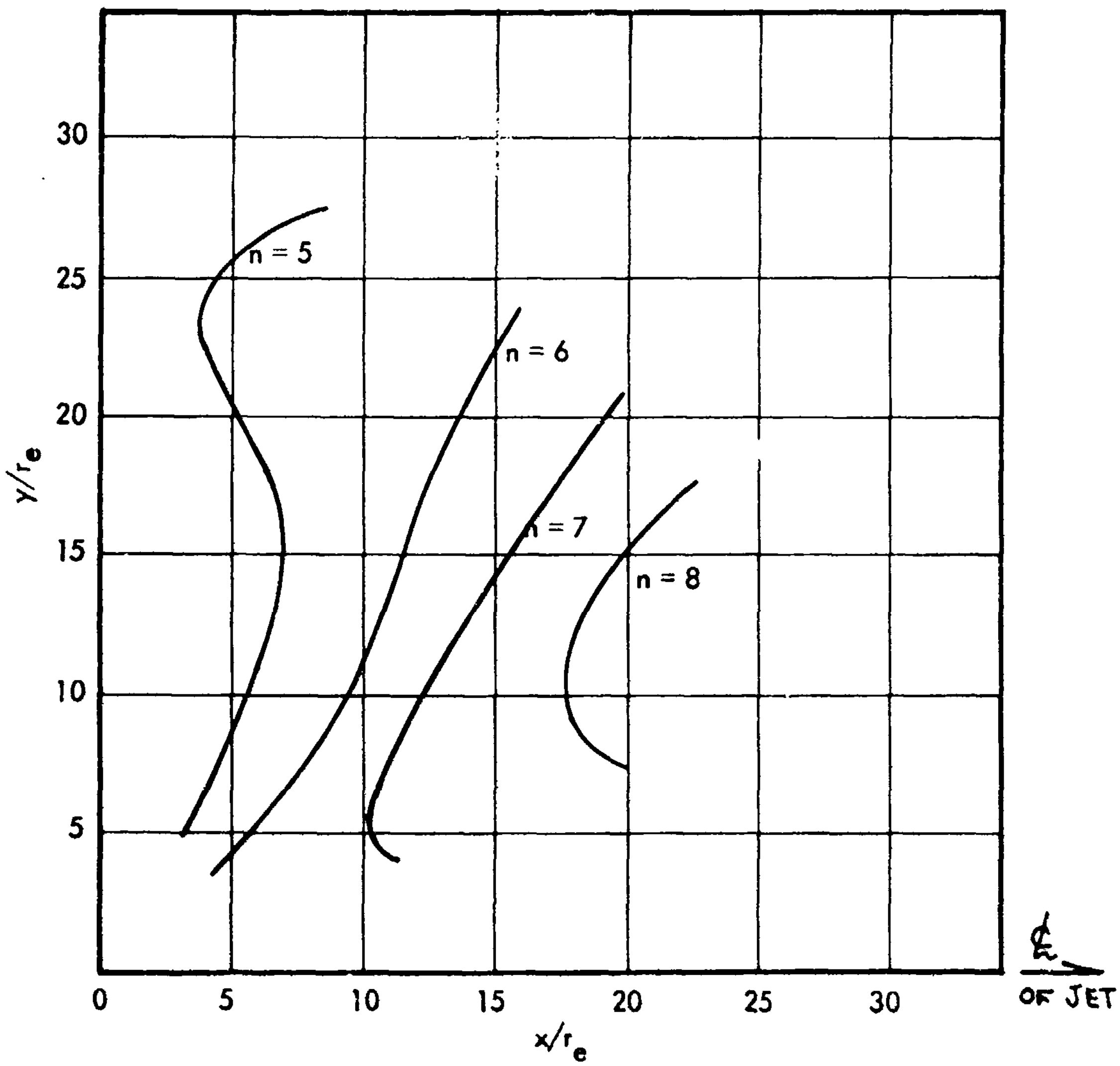

Figure 61. Variation in index 'n' for jet efflux velocity range 1000 – 1800 ft/sec. Data from Wolfe (Figure 31 of reference 2).

LIST OF SYMBOLS USED IN SECTION III

Roman

A	Radiating area
a	Speed of sound
B	Twice correlation coefficient
b	Gradient width parameter
d	Exit diameter
$F(\theta)$	Far field directivity function
$f(\theta)$	Near field angular power distribution function
f	Frequency
H	Receiver height
h	Source height
k	$= 2\pi f/a$
ℓ	Prandtl mixing length
n	Power of U
P	Pressure
PWL	Power level re 10^{-13} watts
s	Source separation distance
spl	Sound pressure level re .0002 dyne/cm^2
r	Radius
S_x	Strouhal number, modified
U	Velocity
$(W_x)_{OB}$	Power per unit axial length summed over all octave bands
x	Axial distance from exit plane
y	Lateral distance from centerline
M	Mach number

Greek

δ	Relative path length
θ	Angle measured from upstream
λ	Acoustic wavelength
$L\Sigma$	Logarithmic sum
σ	Spacial correlation coefficient
τ	Delay time and reflected signal re direct signal
ϕ	Angle of sound pressure maximum re normal to radiating area, A

Subscripts

a	Lower octave band cutoff
b	Upper octave band cutoff
d	Direct

(continued)

List of Symbols Used in Section III (continued)

Subscripts

e	Exit
k	Octave band number
m	Center of frequency band
o	Characteristic of ambient air
r	Reflected
t	Total

Section III

References

1. Howes, W. L., Callaghan, E.E., et al, "Near Noise Field of a Jet Engine Exhaust." NACA Report 1338, 1957.

2. Wolfe, M. O. W., "Near Field Jet Noise." ASTIA AD 154857, AGARD Rept. 112, April - May, 1957.

3. Unpublished data obtained by Bio-Acoustics Branch of Aeromedical Laboratory, WADD in 1955 - 1957.

4. Mayes, W. H., Lanford, W. E., Hubbard, H. H., "Near Field and Far Field Noise Surveys of Solid Fuel Rocket Engines for a Range of Nozzle Exit Pressures." NASA TN D-21, August 1959.

5. Westley, R., Lilley, G.M., "An Investigation of the Noise Field from a Small Jet and Methods for its Reduction." The College of Aeronautics Report No. 53, January 1952.

6. Howes, Walton L., "Similarity of Near Noise Fields of Subsonic Jets." NASA TR-R-94, 1961.

7. Franken, P. A., Kerwin, E. M., et al, "Methods of Flight Vehicle Noise Prediction." ASTIA AD-205776, WADC TR 58-343, November 1958.

8. Eldred, K., Roberts, W., White, R., "Structural Vibrations in Space Vehicles." WADD TR 61-62, December 1961.

9. Greatrex, F. B., "Jet Noise." Fifth Inter. Aero. Conf., Los Angeles, Calif., June 1955.

10. Morgan, W. V., Sutherland, L. C., Young, K. J., and the Boeing Airplane Company Acoustics Group, "The Use of Acoustic Scale Models for Investigating Near Field Noise of Jet and Rocket Engines." WADD TR 61-178, April 1961.

11. Lassiter, L. W., Hubbard, H. H., "Experimental Studies of Noise from Subsonic Jets in Still Air." NACA TN 2757, 1952.

12. Franz, G. J., "The Near Sound Field of Turbulence." David Taylor Model Basin Report No. 982, October 1959.

13. Franklin, R. E., Foxwell, J. H., "Correlation in the Random Pressure Field Close to a Jet." ASTIA AD-216136, ARC 20, 264, N. 31, F.M. 2694, June 1958.

(continued)

Section III References (continued)

14. Eldred, K. M., "Review of the Noise Generation of Rockets and Jets." JASA 32 (1502), 1960.

15. Blokhintsev, D., "The Acoustics of an Inhomogeneous Moving Medium." NACA TM 1399, ASTIA AD-7675, August 1952.

16. Eldred, K. M., et al, "Prediction of Rocket and Turbojet Noise." Presented at 52nd Acoustical Society of America meetings, 1956.

17. Eldred, K. M., "Noise Measurement of Four Rohr Aircraft Model Jet Nozzles." 1958.

18. Ribner, H. S., "On the Strength Distribution of Noise Sources Along a Jet." ASTIA AD-154264, April 1958.

19. Dyer, Ira, Franken, P. A., Westervelt, P. J., "Jet Noise Reduction by Induced Flow." JASA Vol. 30, No. 8, August 1958.

20. Eldred, K. M., Ortega, J., "Acoustical Evaluation of the General Sound Control, Inc., Jet Ground Runup Noise Suppressor." ASD TR 61-544, October 1961.

21. Eldred, K. M., Ortega, J., "Acoustical Evaluation of the Koppers Company, Inc., 30-S, Class II Jet Ground Runup Noise Suppressor." ASD TR, April 1961.

22. Ortega, J., "Acoustical Evaluation of a Kinning Systems, Inc., Prototype Ground Runup Noise Suppressor." Western Electro-Acoustic Laboratory, Inc., 13 May 1960.

23. Ortega, J., "Acoustical Evaluation of the Curtiss-Wright Corporation Models SSEP-2 and SSIP-2 Jet Ground Runup Noise Suppressor." Western Electro-Acoustic Laboratory, Inc., 1961.

24. Eldred, K. M., "Noise Measurements on the Kittell-Lacy Noise Suppressor with F-102 Aircraft at George Air Force Base on 28 and 29 September 1961." Western Electro-Acoustic Laboratory, Inc., 2 October 1961.

25. Eldred, K., Ortega, J., "Acoustical Evaluation of the Air Logistics Corporation Jet Ground Runup Noise Suppressor Model 11000." Western Electro-Acoustic Laboratory, Inc., ASD TR, March 1961.

26. Eldred, K. M., "Acoustical Evaluation of Type II Aircraft Ground Runup Noise Suppressor at Truax Air Force Base, Wisconsin." Western Electro-Acoustic Laboratory, Inc., Unpublished.

(continued)

Section III References (continued)

27. Ingard, U., "Review of the Influence of Meteorological Conditions on Sound Propagation." Acoustical Society of America Symposium on Aircraft Noise, November 14, 1952.

28. Ingard, U., "On the Reflection of a Spherical Sound Wave from an Infinite Plane." JASA Vol. 23, No. 3, May 1951.

29. Franken, P. A., "A Theoretical Analysis of the Field of a Random Noise Source Above an Infinite Plane." NACA TN 3557 November 1955.

30. Howes, W. L., "Ground Reflection of Jet Noise." NASA TR R-35, 1959.

31. Laurence, J. C., "Intensity, Scale and Spectra of Turbulence in Mixing Region of Free Subsonic Jet." NACA Report 1292, 1956.

SECTION IV

CONTROL OF JET NOISE THROUGH DESIGN

One of the primary motivations for jet noise research is the history of sonic fatigue and equipment malfunctions of current flight vehicles. These noise-induced failures are not only costly in an economic sense, but threaten a vehicle's overall reliability and effectiveness as a weapons system. Although experience has shown that satisfactory reliability can be achieved after lengthy testing, redesign, and upgrading of structure and components, this process is costly in time, money, and often performance. If this history is not to be repeated in the design of future vehicles, the noise exposure of flight vehicles must be minimized in the design process.

The various methods or devices which have been or can be proposed for altering the jet noise field involve variation of one or more of four major factors:

- Engine location
- Total acoustic power generated
- Frequency spectra
- Radiation characteristics (directional properties, reflecting or absorbing surfaces, and spacial distribution of noise sources)

The first of these factors can be controlled by the vehicle designer, and the remaining are controlled primarily by the engine designer, often in conjunction with the vehicle designer.

This section discusses these basic factors and examines the modifications of these factors which can be achieved through design. Much of this discussion will be given directly in terms of a 10,000-lb. thrust engine to facilitate comparison with current experience. Furthermore, the discussion is directed primarily toward jets from convergent nozzles, and does not include supersonic rockets.

Engine Location

It is abundently clear from the vast literature on jet noise and the discussions of the previous section that the noise radiated by a jet to locations forward of the nozzle plane is an order of magnitude lower than that radiated to locations aft of the nozzle plane. Therefore, it behooves the designer to accept this bonus, wherever possible in the initiation of new design concepts.

To illustrate this principle, the noise exposure of a twin engine jet flight vehicle was estimated for wing mounted and tail mounted jet engines. The contours of overall spl, given in figure 21 for a 10,000-lb. thrust engine, were superimposed over the vehicle plan and the approximate percentage of total vehicle surface exposed to 6 db increments of noise was computed. The results, given in figure 62, show that the overall noise exposure of the vehicle is reduced over 12 db by moving the engines aft and that areas of extreme noise exposure are eliminated almost entirely. Although these results are only approximate since ground reflections were not considered, they demonstrate conclusively that a large reduction in vehicle noise exposure and resulting vibration can be achieved by placing the engines at the tail of the vehicle. Hence, configurations incorporating tail mounted engines will have, in general, minimal sonic fatigue, and equipment malfunction from noise induced vibration.

Fundamental Jet Noise Parameters

The three remaining basic factors which can be utilized by the designer to control vehicle exposure to jet noise are the total acoustic power, frequency spectra, and directivity of the jet noise source. These factors are determined by the jet flow parameters, and are, except for variation in nozzle geometry, almost entirely established by the engine designer at the initiation of each new engine design. Clearly, if minimum noise is to be achieved, low noise must be a requirement in advanced engine design to insure that it is considered together with all other engine objectives.

The total acoustic power for jet flows from convergent circular nozzles has been shown by many investigators, including (Ref. 1) to be proportional to the eighth power of the nozzle velocity and to the nozzle area.

An empirical equation for predicting the total acoustic power level (PWL) is:*

$$PWL = 146 + 20 \log d_1 + 80 \log \frac{U_e}{1000} \text{, in db re } 10^{-13} \text{ watts} \quad \text{(IV-1)}$$

where U_e is the actual nozzle exit velocity in ft/sec.

and d_1 is the nozzle diameter (d_e) in feet when the nozzle pressure ratio (P.R.) is less than 1.89, and is otherwise given by

$$d_1 = d_e \left[1 + 1.71 \, (.53 \text{ P.R.} - 1) \right]^{1/2}; \; 1.89 \leq PR < 3$$

Note that d_1, as defined for nozzles operating at pressure ratios greater than critical, is simply the diameter of a nozzle operating at 1.89 P.R. with the same total temperature and thrust as the actual nozzle.

The overriding effect of exit velocity on the acoustic power generated by the jet is

*Note that the first approximation of the total power radiated in flight where the external velocity $U_o \neq 0$, is obtained by replacing U_e by $(U_e - U_o)$ and adding ten times the logarithm of the ratio of the core length for $U_o \neq 0$ to the core length for $U_o = 0$ from figure 18 to account for the increased length of the jet noise source.

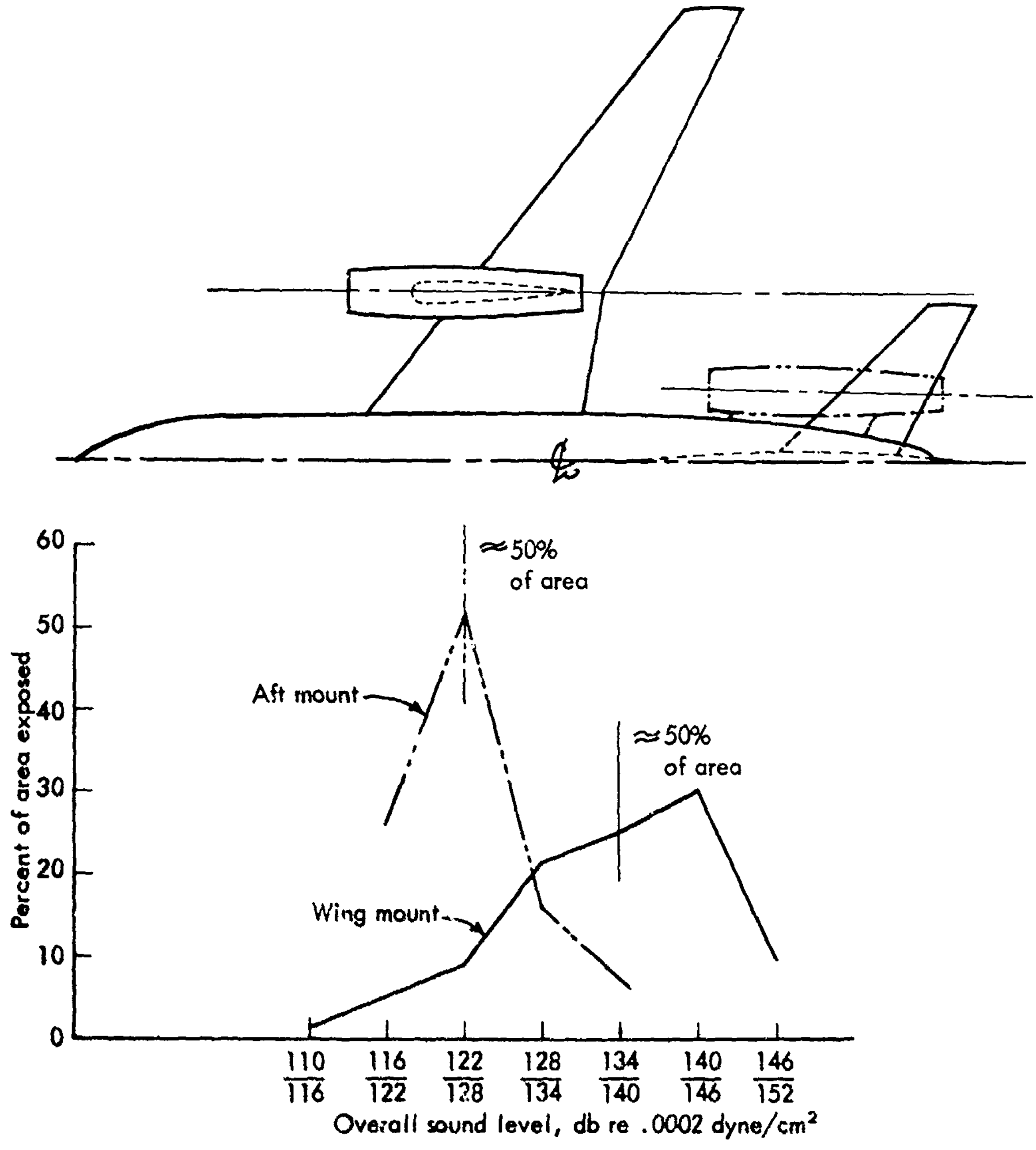

Figure 62. Illustrative comparison of vehicle noise exposure for two engine locations.

summarized for a 10,000 lb. thrust engine in figure 63 for various values of P. R. All exit velocities along the 1.89 P. R. line are sonic and, thus, along this line, lower velocities imply lower exit total temperature (T_{te}) and higher weight flows ($\dot{w}_e$) through the engine. For a non-bypass engine with a fixed engine P.R. and exit area, the lower temperature generally results in lower thermal efficiency. Further, the increase in weight flow, either from lower temperatures or reduced nozzle P.R., results in increased engine size and high speed drag and weight. Therefore, for the conventional non-bypass jet it is necessary to maintain maximum practical temperatures, notwithstanding the large noise reductions attainable with lower exit velocities. As will be seen later, the practical methods by which the designer can obtain the acoustic benefits of reduced velocity include the bypass or turbofan engine and to a lesser extent, the various types of mixing nozzles with or without ejectors.

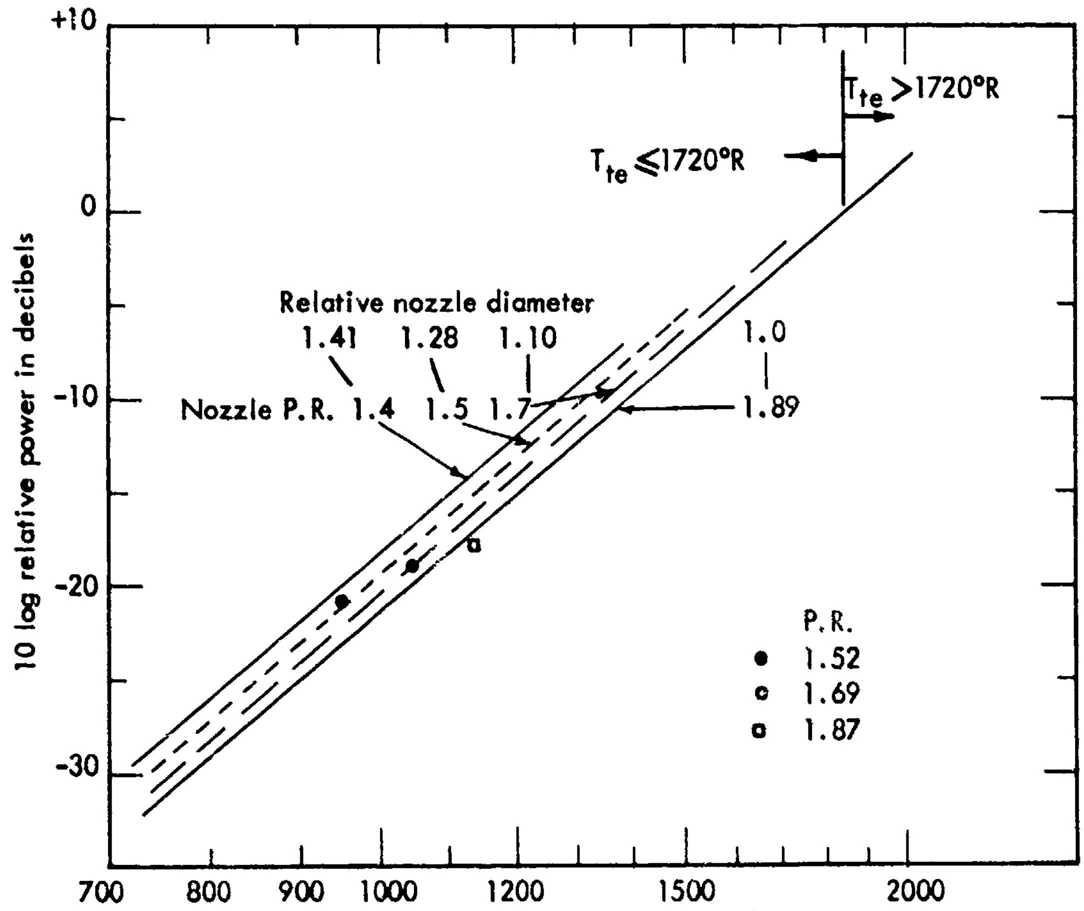

Figure 63. Relative total acoustic power level for a 10,000-lb. thrust engine as a function of exit velocity. Data from Lee, et al.

The normalized frequency spectrum of the total acoustic power radiated from axi-symmetric jets is given in figure 64. For jets from convergent nozzles at a P.R. of 1.89, the exit velocity (U_e) equals the critical sonic velocity (a_*) at the exit plane or throat of the nozzle. Hence, for standard ambient conditions the frequency spectrum is dependent only on the diameter of the jet, with smaller jets characterized by higher frequencies. Thus, the entire frequency spectrum of a jet engine could be shifted to much higher frequencies if the single nozzles were replaced by a number of small nozzles with equal total area. In fact, as first noted by Tyler (Refs. 3, 4) and proved in his ground runup muffler (Ref. 5), if the nozzles were sufficiently small, the characteristic center frequencies of the noise would be in the ultrasonic frequency range, which is both inaudible and rapidly attenuated by atmospheric absorption.

The power spectra for a 10,000 lb. thrust engine at a P.R. of 2.2, overall acoustic power level of 174 db, and a variety of nozzle diameters, are given in figure 65. Since the number of nozzles required for constant thrust is inversely proportional to the square of the nozzle diameter, it is clear that rather large numbers of nozzles are required to obtain an appreciable shift in center frequency. For example, 32 four inch nozzles are required to shift the frequency by a factor of approximately 5.5 and 126 two inch nozzles are required to give a frequency shift by a factor of approximately 11. The potential reductions in the

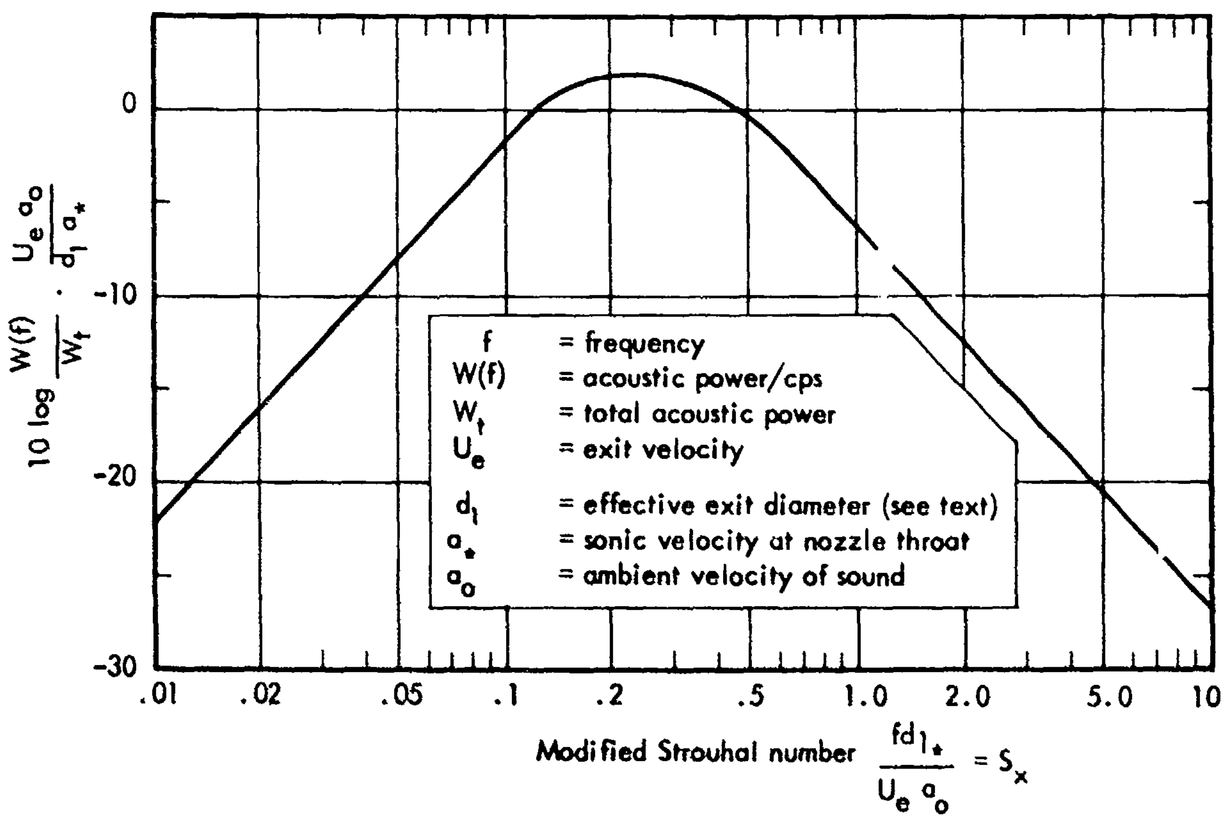

Figure 64. Normalized power spectrum for axisymmetric jets issuing from convergent nozzles.

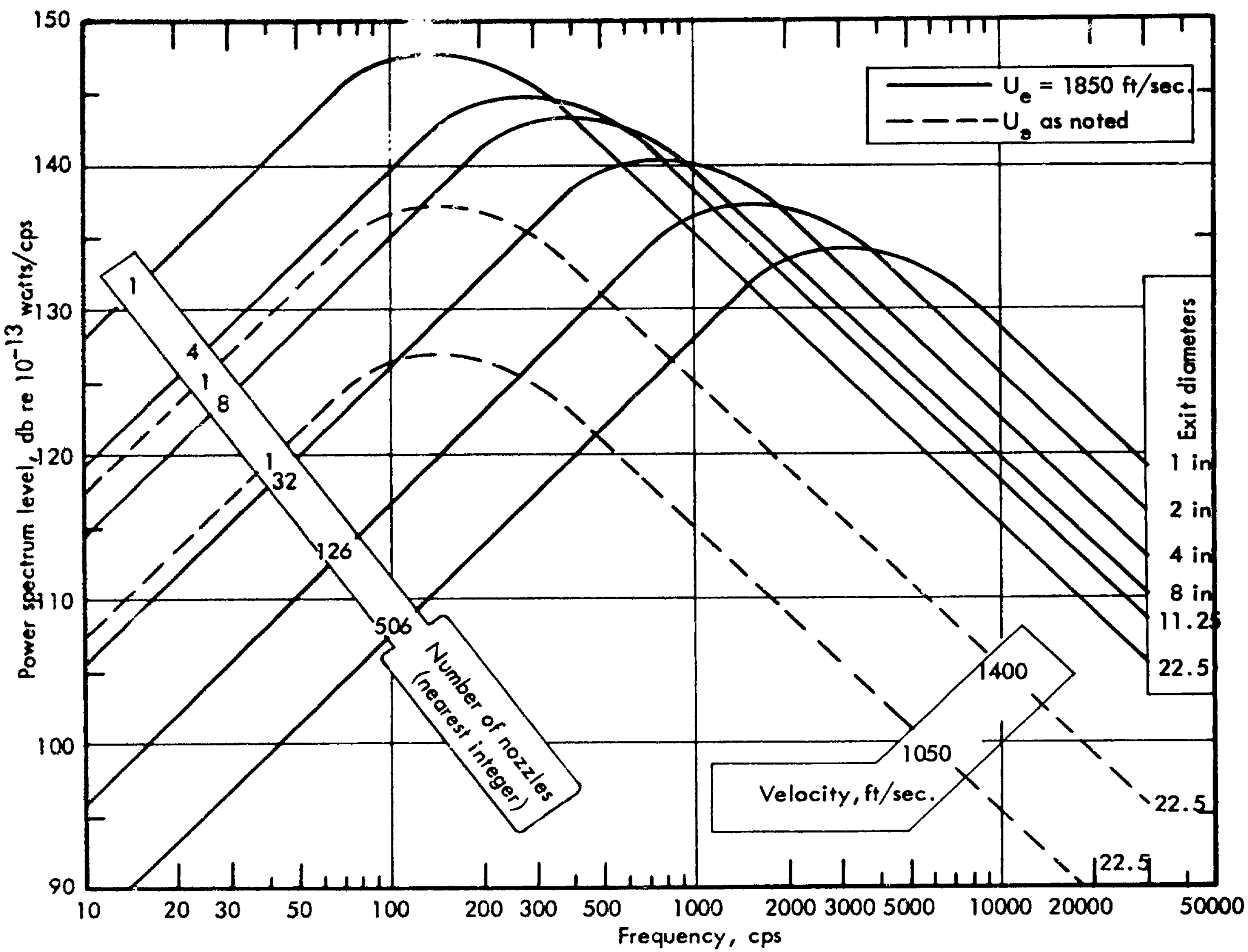

Figure 65. Power spectra of non-interfering axisymmetric jets having a thrust of 10,000 lbs, nozzle P.R. 2.2, exit total temperature 1720°R, together with two jets of lower temperature and exit velocity.

lower frequency noise are impressive, approximately 21 and 30 db for the four inch and two inch nozzles, respectively. However, these low frequency reductions are predicated on the assumption that the individual jets do not interfere with each other and re-combine in a large jet of lower velocity. This assumption requires large center-to-center distance, and hence, a rather large envelope area for the entire configuration. If the jets are spaced closer than approximately three diameters, interference results which increases the low frequency radiation above that given in figure 65, and decreases the high frequency noise radiation relative to figure 65.

In contrast to the large potential improvements obtainable at low frequencies from multiple non-interfering jets, there is an increase in noise radiated at high frequencies over that radiated by the single jet of equal thrust. This increase is of the order of 7 db and 10 db for the four inch and two inch jets respectively. However, in this frequency region interference between the jet flows is beneficial, reducing the magnitude of the increase.

Figure 65 also shows the estimated spectra for two single 10,000 lb. thrust jets operating at the same P.R., but at lower temperature, and thus, at lower velocity. Note that the center frequency of these lower velocity jets is unaltered from the original, since $U_e = a_*$ in all three cases. Therefore, the reduction in total acoustic power estimated in figure 63 applies to all frequencies.

The near field directional properties of the axisymmetric jet at 1000°F have been discussed in detail in the previous section, and the effect of temperature and velocity on these directional properties was discussed briefly in Section III, as well as in Appendix C. As was noted, it is still impossible to give a quantitative generalization of the effects of velocity and temperature, singly or combined, on the noise at an arbitrary point in the near field of a jet issuing from a convergent circular nozzle. Therefore, it is clearly not possible to be quantitative regarding the directional properties of the noise from a jet of completely arbitrary geometry.

However, certain basic relationships were observed which can be applied to arbitrary jet flows. The directivity of noise generated within any region of a jet will be related to b/λ_o where b is a width parameter characterizing the width of the local jet flow gradient. For constant value of $b/\lambda_o < 1$ the directivity function will sharpen and rotate toward the direction of jet flow as the local Mach number in the flow increases. For constant $b/\lambda_o > 5$ and constant local flow Mach number, the directivity function will broaden and rotate away from the direction of jet flow as the temperature is increased. Furthermore, as jet velocity is decreased, the noise radiated to the far field decreases much faster than the turbulent fluctuating pressures themselves. Hence, the sound pressures along the jet boundary do not decrease with velocity at a rate commeasurate with the decrease in total acoustic power. A more exact statement of these conclusions must await the solution of the jet noise equation developed in Appendix B.

It is recognized that the statements in the previous two paragraphs represent the weakest link in the prediction of near field noise reduction, and clearly represent an area where concentrated experimental and theoretical work is required. However, except for regions within approximately one diameter of the jet, the reductions predicted for various nozzle and/or flow configurations based on total radiated acoustic power, are expected to dominate for the range of practical engine-nozzle configurations and jet flows. Therefore, the concepts, methods and conclusions developed relative to various noise suppression devices in the remainder of this section are considered to give usable results for preliminary design.

The various devices which have been proposed and/or developed for the reduction of jet noise act to reduce the gross jet velocity, shift the jet frequency spectrum or both. The following subsections discuss these devices in terms of their noise generating characteristics in an effort to determine methods for predicting these characteristics.

Coaxial Turbofan Flows

Although velocity reduction, per se, involves loss of efficiency and increased engine weight flows, it is possible to attain the objective of lower exit velocity with gains in overall performance with bypass or turbofan engines. This principle was first pioneered by Greatrex of Rolls Royce with the Conway engine, and has been extended in this country by the General Electric CJ 805-23 "aft turbofan" and the Pratt and Whitney JT3D and JT4D "forward turbofans." The bypass ratio, which is the ratio of fan weight flow ($\dot{w}_s$) to primary weight flow ($\dot{w}_p$), varies for these engines between 1 for the Conway to approximately 1.5 for the latter three, all at takeoff thrust.

The modification of a pure jet to a turbofan configuration increases the total thrust by utilizing part of the energy ordinarily exhausted through the nozzle to drive an additional turbine stage which, in turn, drives a compressor for the bypass air. Although the thrust of the primary jet is reduced, the additional bypass flow more than compensates for this reduction, resulting in a significantly greater net thrust. Furthermore, the engine components can be matched for cruise power to achieve a lower fuel consumption per pound of thrust (SFC). This lowered SFC reduces the weight of fuel required to achieve a fixed range and more than compensates for the increased engine weight associated with the bypass stages and their ducting. These performance factors are examined as a function of bypass ratio for a hypothetical engine in Section V.

The jet noise generated by a turbofan engine can be estimated directly from equation (IV-1), together with figures 63 and 64 when the two nozzles are coplanar and at the same velocity. However, in most cases the exhaust velocity of the bypass flow will be lower than the primary velocity, necessitating a more refined method of noise estimation.

Figure 66 gives an example of an annular constant density jet flow for a secondary to primary velocity ratio (U_s/U_p) of .5 and a radius ratio r_s/r_p of 1.5. This solution was constructed from the solutions for a jet exhausting into a uniform stream (the primary jet) and exhausting into ambient (the outer secondary flow) from the Section II and Appendix A solutions. The velocity profiles for this example are further illustrated in figure 67.

It is clear from the figures that the primary jet is wholly surrounded by a uniform flow of .5 U_p from the nozzle to x/r_p equal to 3.5. From x/r_p of 3.5 to 6.3, the surrounding flow velocity varies between .5 and .4 times U_p, and so on. Thus, the flow of the primary jet is constructed for each increment considering the average value of the velocity in the surrounding jet. Therefore, the primary core is not as long as shown in the Section II example (in figure 17) for a constant value of velocity ratio, but is considerably longer than if it were exhausting into the ambient. It is clear from this example that the resulting velocity profiles will be a function of both r_s/r_p and U_s/U_p. Further, it is also clear that the profile eventually approaches, at some axial station, the normal similar profile for a single jet of constant velocity. The flow downstream of this axial station will be identical with that of an equivalent single circular jet of the same exit momentum. When the asymptotic profile is reached, the momentum equation from Appendix A gives for the combined flow:

$$2\pi \int_0^\infty \rho' U_m'^2 e^{-\eta'^2} b'^2 \eta' \, d\eta = \pi \rho' U_m'^2 b'^2$$

where the primes refer to the equivalent flow.

As this combined flow momentum must equal the exit momentum of the annular jets:

$$\pi \rho' U_m'^2 b'^2 = \pi \rho_p U_p^2 r_p^2 + \pi \rho_s U_s^2 \left(r_s^2 - r_p^2 \right)$$

assuming that the nozzle pressure ratio does not exceed 1.89.

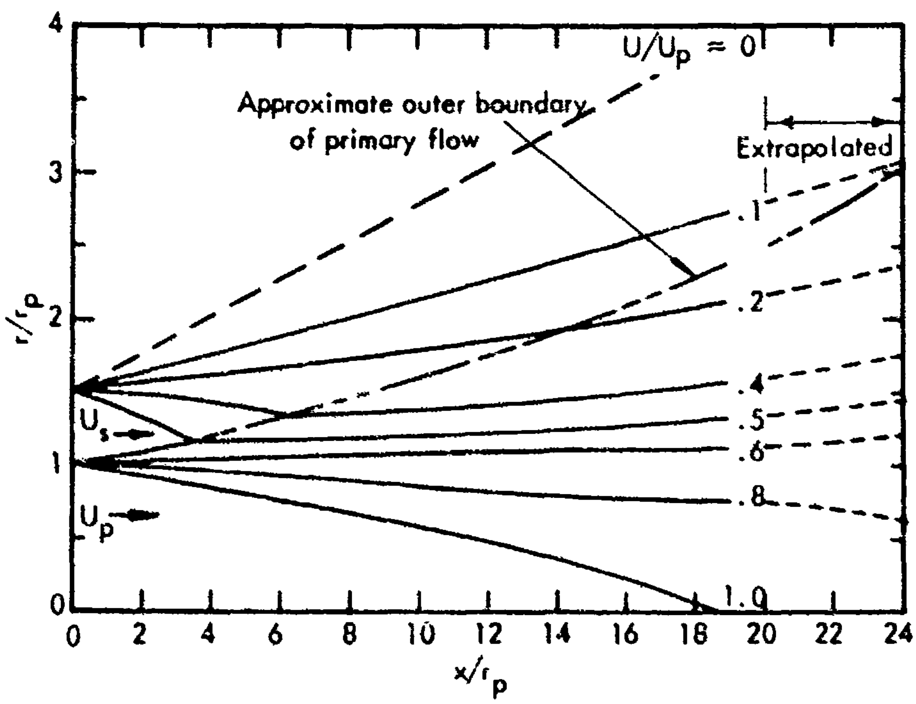

Figure 66. Estimated flow for constant density annular coplaner jet with U_s/U_p = .5 and r_s/r_p = 1.5

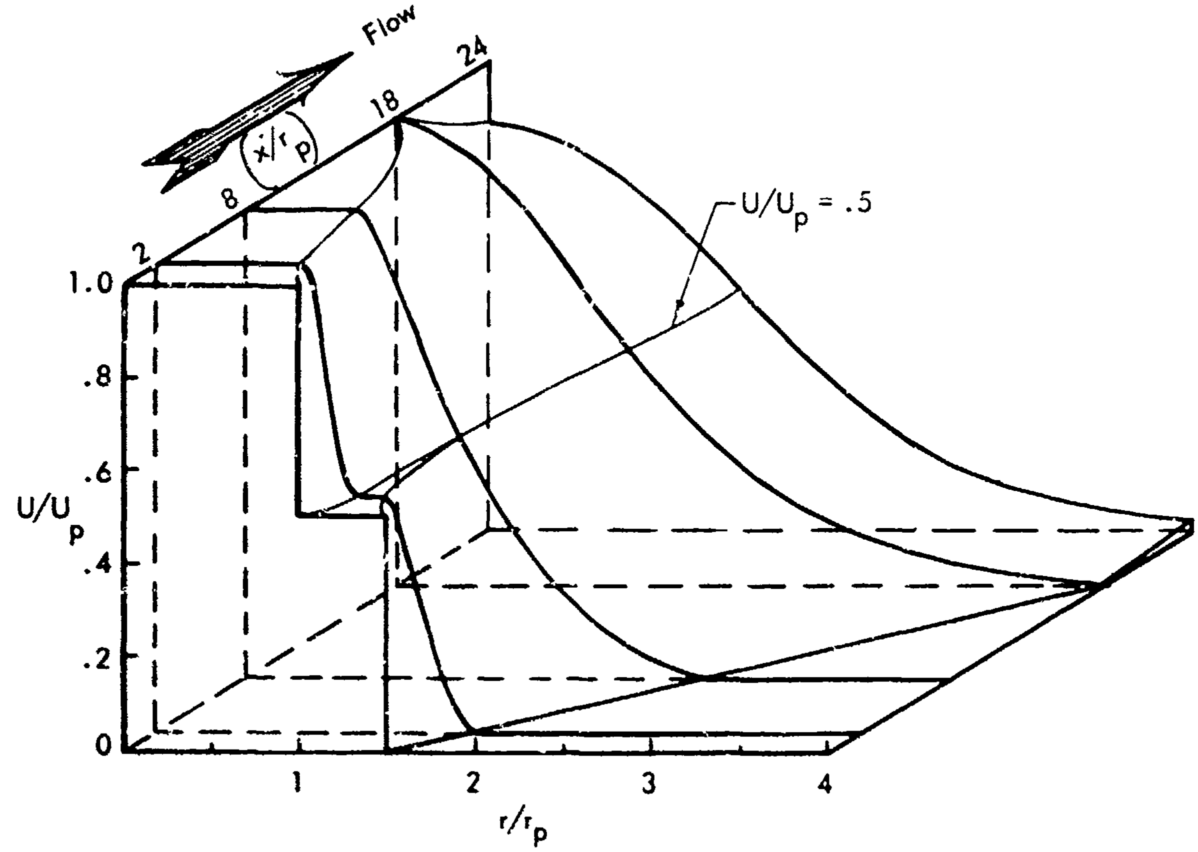

Figure 67. Approximate velocity profiles at various downstream stations for constant density annular coplaner jet with $U_s/U_p = .5$ and $r_s/r_p = 1.5$

Rearranging gives:

$$\frac{U_m'}{U_p} = \frac{r_p}{b'}\left(\frac{\rho_p}{\rho'}\right)^{1/2}\left\{1 + \frac{\rho_s}{\rho_p}\left(\frac{U_s}{U_p}\right)^2\left[\left(\frac{r_s}{r_p}\right)^2 - 1\right]\right\}^{1/2}$$

or, for constant density jets:

$$\frac{U_m'}{U_p} = \frac{r_p}{b'}\left\{1 + \left(\frac{U_s}{U_p}\right)^2\left[\left(\frac{r_s}{r_p}\right)^2 - 1\right]\right\}^{1/2} \qquad \text{(IV-2)}$$

Since equation (IV-2) contains two unknowns, b' and U_m', it cannot be solved exactly without an additional relationship which demands an exact solution of the form developed for single flows in Appendix A. However, a useful approximate solution can be directly obtained when r_s/r_p is large and $(U_s/U_p)^2(r_s/r_p)^2$ is also large compared to unity. In this case, equation (IV-2) reduces to

$$\frac{U_m'}{U_p} = \frac{r_p}{b'}\,\frac{U_s}{U_p}\,\frac{r_s}{r_p} \text{ or } \frac{U_m'}{U_s} = \frac{r_s}{b'} \qquad \text{(IV-3)}$$

But this is exactly the relationship for a single jet with exit velocity of U_s and radius of r_s, as would be expected. Hence, at the tip of the core of the equivalent jet, $b = r_s = r'$ and $U_m' = U_s = U'$. Thus, under these conditions the shrouding flow becomes dominant in determining the final jet.

On the other hand, when r_s/r_p approaches one, the primary flow must be dominant, as is easily seen from equation (IV-2). Here, at the core tip U_m' approaches U_p and b' approaches r_p, as expected. In order to determine the equivalent single jet flow for intermediate values of r_s/r_p and U_s/U_p several graphical solutions were constructed, similar to figure 66. The resulting equivalent jet parameters are summarized in figures 68 and 69. As shown by figure 68, $r'/r_p \cong r_s/r_p$ for $.5 \leqslant U_s/U_p \leqslant 1$, the maximum deviation occurring in the range of $r_s/r_p = 1.5$, where $r'/r_p = 1.35$. However, U'/U_p does not approach U_s/U_p until much larger values of r_s/r_p, except when U_s/U_p approaches one.

It is clear from the flow profile that the total acoustic power generated downstream of the station where the flow profile becomes approximately identical to that of the equivalent jet, is simply the power expected to be generated by the equivalent jet. However, to estimate the total power of the entire jet, it is necessary to consider the noise generated by the flow between the nozzle and the station where equivalence is definitely attained. Referring to figures 66 and 67, the initial flow is characterized by two individual velocity profiles, each of total velocity drop of $.5\ U_p$. Assuming that the noise generated in the jet varies with the eighth power of velocity, the noise generated in this region is very low compared with the remainder of the jet. Now if the flow at $x/r_p = 24$ has reached full equality with an equivalent flow of $U'/U_p = .87$, and $r'/r_p = 1.35$, it is possible to compute the axial position of the equivalent jet nozzle which gives the $x/r_p = 24$ flow conditions. For $x'_t/r' = 13$, and for a Mach 1 jet as in Section II, the axial position of the equivalent nozzle would be at $x/r_p = 24 - 13 \times 1.35 = 6.5$. Coincidentally, this axial position is just beyond the region of

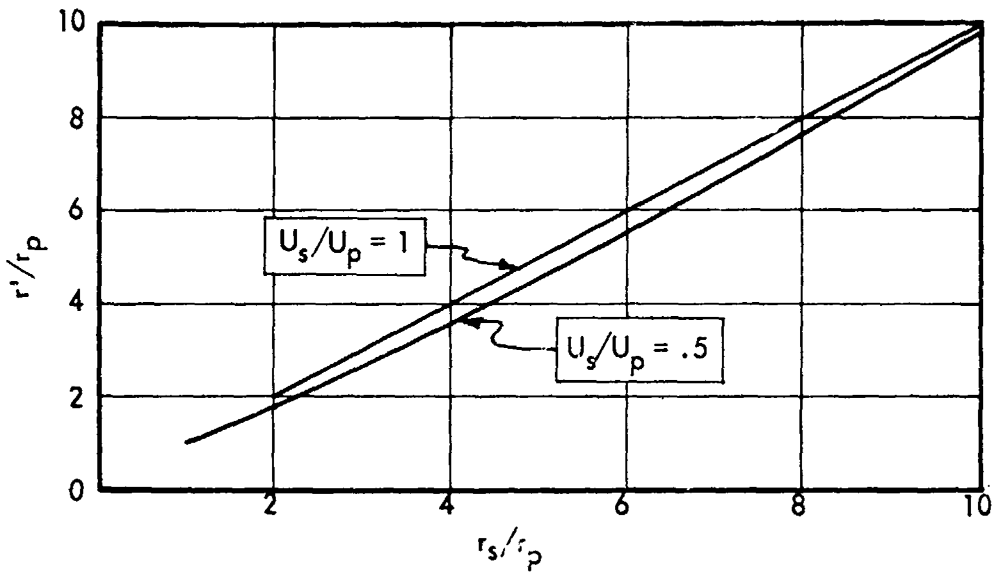

Figure 68. Variation of equivalent jet radius r' for annular constant density jets as a function of radius ratio (r_s/r_p)

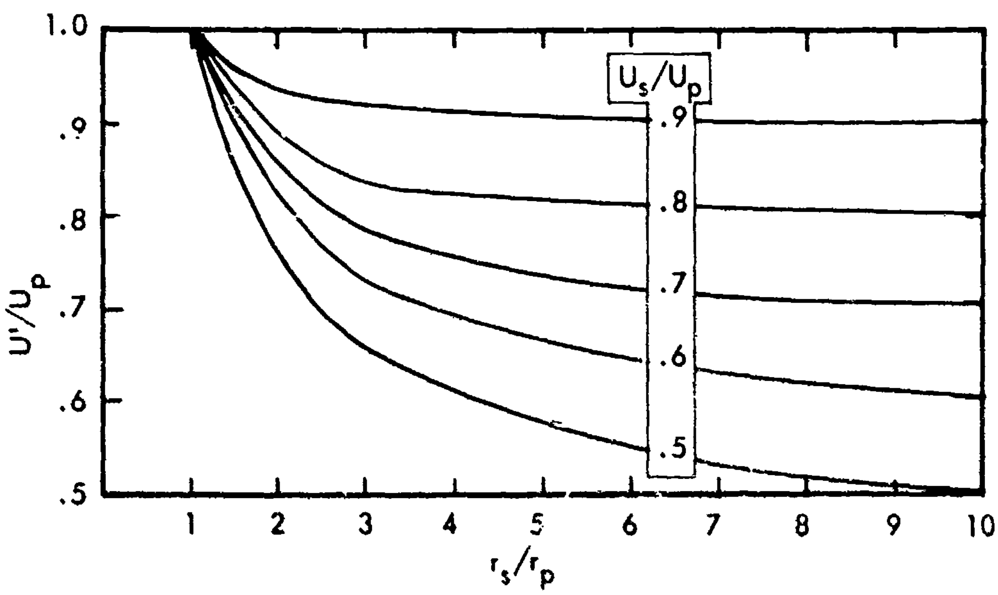

Figure 69. Variation of the ratio of equivalent velocity (U') to primary velocity for annular constant density jets as a function of radius ratio (r_s/r_p) for various values of secondary to primary jet velocity.

the jet where the velocity gradient appears as two individual gradients and thus is at the beginning of the portion of the flow which might be expected to contribute the major portion of the noise. Hence, as a first approximation it would appear that the noise estimated for a total flow of the equivalent jet would closely approximate the actual noise.

This hypothesis may be directly tested against model experiments by Lee et al (Ref. 2). These tests consisted of varying the secondary velocity of an annular coplanar jet with $r_s/r_p \approx 1.5$ and $r_s \approx 2.65$ inches. The total acoustic power levels relative to the power level of the primary flow, measured where $U_s = 0$, are given in figure 70 as a function of U_s/U_p. It is clear from the figure that the minimum power is approximately 2 db less than that of the primary alone and occurs at a ratio of $U_s/U_p = .5$. Considering that the acoustic power is proportional to a high power of U, it is not surprising that the maximum reduction occurs at $U_s/U_p = .5$. In the early portion of the flow where the gradients of the two flows are separate, minimum noise should result when the difference in velocity between the primary and secondary flow equals the difference between the secondary flow and the external flow or ambient. Otherwise, the gradient associated with the greater velocity difference would dominate the noise generation and would result in a higher value than attained with equal differences. The relative values in figure 70 were also calculated for the equivalent jet utilizing figures 68 and 69, together with equation (IV-1). The results of this calculation appear in reasonable agreement with the data.

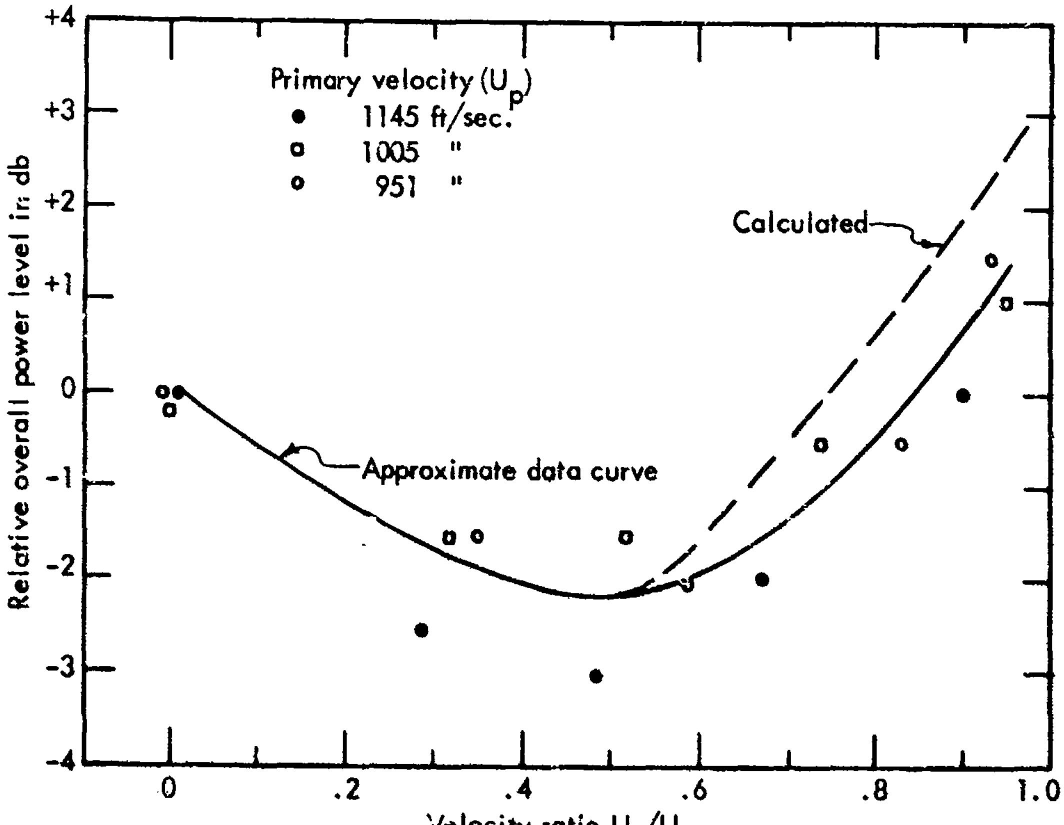

Figure 70. Variation of the ratio of total acoustic power to power measured with zero secondary flow velocity as a function of secondary flow velocity (U_s) for $r_s/r_p = 1.5, T_{pt} = 670°$ R; data from Lee et al.

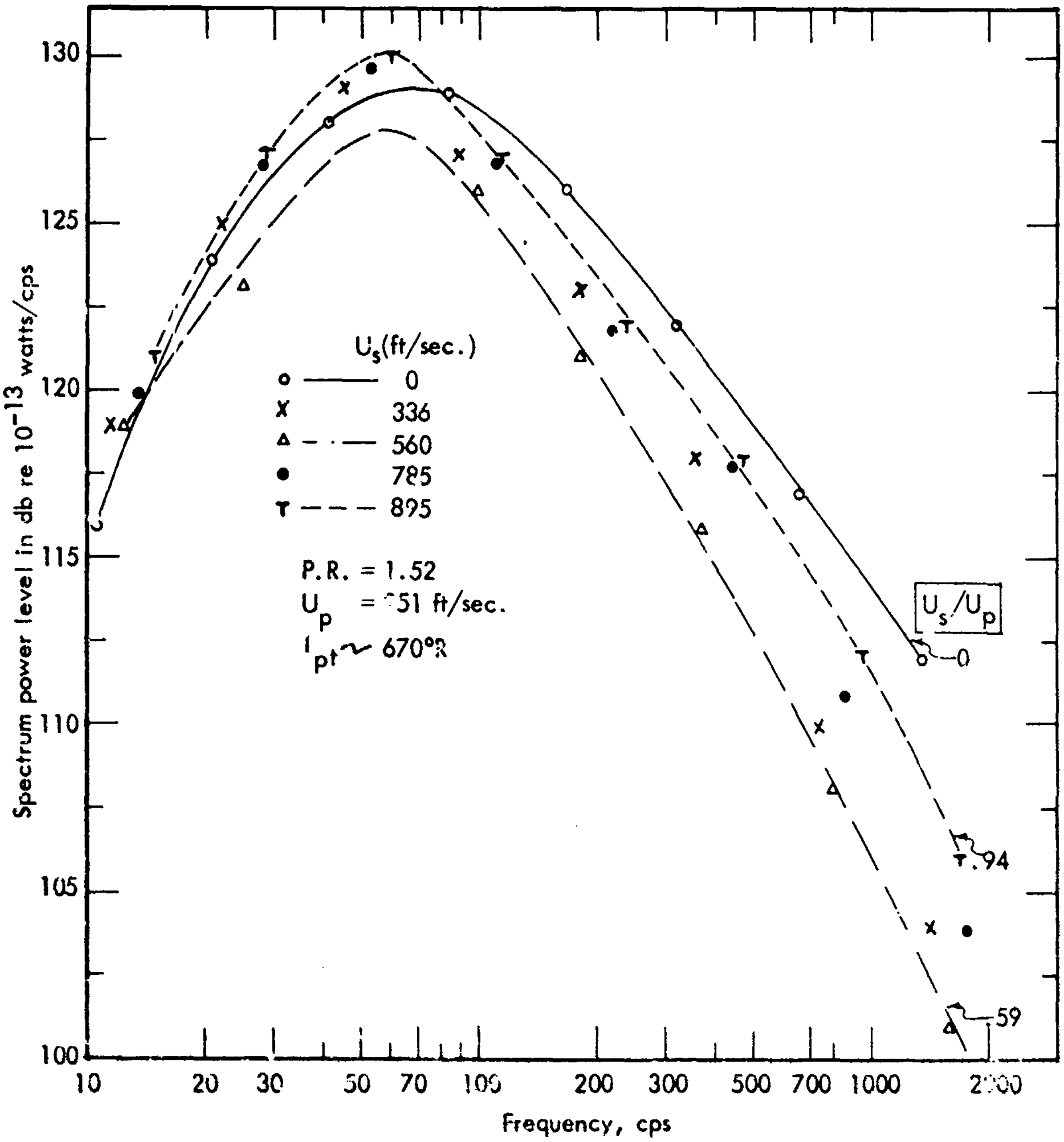

Figure 71. Effect of annular flow velocity U_s for $r_s/r_p = 1.5$. Data from Lee et al, for 5.3 inch nozzle corrected to 10,000 lbs. thrust.

Figure 71 gives the power spectra for one of the three test series from Ref. 2. These spectra have been scaled from the original data to 10,000 lbs. thrust to afford direct comparison with other power spectra in this section. For this purpose, the overall power level scales directly with area or thrust, the diameter scales directly with (thrust),$^{1/2}$ and frequency scales inversely with diameter.

Examination of figure 71 shows that the minimum power for constant thrust is attained by the velocity ratio of .59 which, of those given, most nearly approaches a ratio of .5. Figure 72 compares the power spectrum calculated for the jet equivalent to the U_s = 560 ft/s, U_p = 951 ft/s given in figure 71. Except for the lowest frequency band, the error in calculated power spectrum does not exceed 1 db, and the general agreement appears good. Therefore, it is concluded that the equivalent jet, defined for coplanar annular flows in figures 66 and 67, affords a good prediction of the resulting jet noise.

Figure 73 illustrates these results for a fixed thrust jet of velocity ratio U_p/U_s = .5 in terms of bypass ratio. The ratio of bypass jet exit radius (r_s) to zero bypass jet exit radius r_{p1} increases rapidly for bypass ratios up to 1.5 and then increases slowly to its asymptotic value of 2 at very high bypass ratio. Similarly, the total acoustic power (W') of the equivalent jet decreases rapidly for initial increases of the bypass ratio up to ratios of 3 to 4 and then decreases more slowly to its asymptotic value of -18 db.

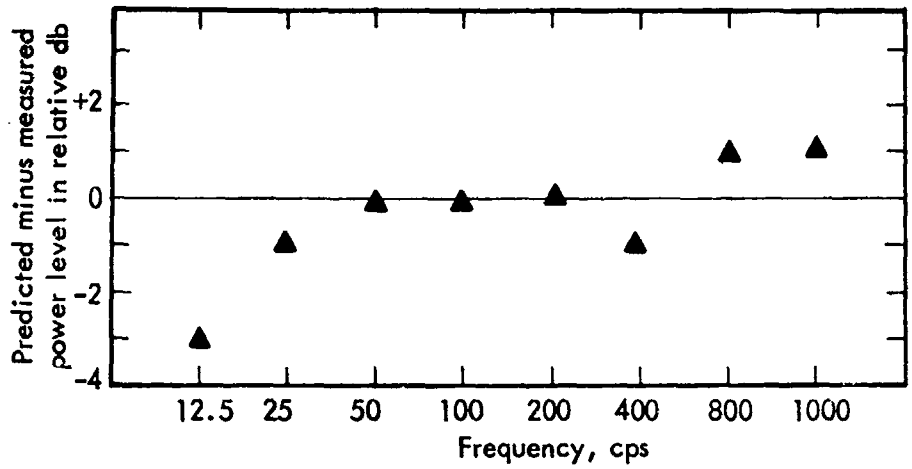

Figure 72. Comparison of predicted minus measured power levels for annular jet (U_s = 560 ft/second, U_p = 951 ft/second) from previous figure.

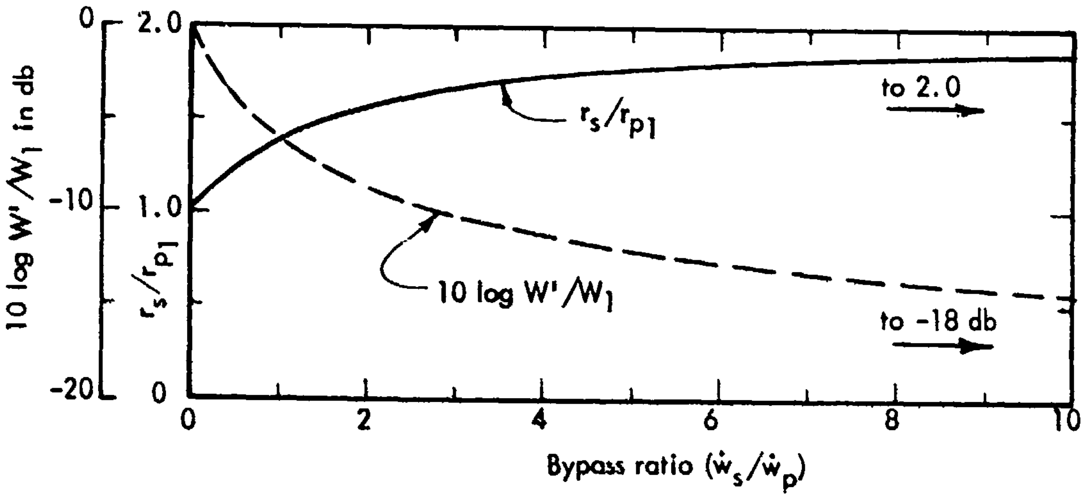

Figure 73. Variation of the ratio of secondary radius (r_s) to original primary radius (r_{p1}), and relative overall sound power level as a function of bypass ratio for a constant density jet of fixed thrust with a velocity ratio (U_s/U_p) of .5.

Mixing Nozzles

The class of mixing nozzles applies to nozzles which subdivide the jet exit flow into many elemental jets which have a total jet exit area approximately equal to the original circular nozzle area, and distribute the elemental jets over a base area larger than the original jet. Several examples (Refs. 6, 7, 8, 9, 10, 11, 12) of mixing nozzles are illustrated in figure 74. As will be shown, the noise reduction of this class of mixing nozzles involves both a frequency shift and a lowering of the velocity of the resulting "mixed jet."

Since a properly designed mixing nozzle can be substituted for a standard circular nozzle, the mixing nozzle offers a possibility of reducing the noise of existing engines. Thus, the development of mixing nozzles has been accomplished by aircraft designers as well as engine designers. Furthermore, the development and qualification of mixing nozzles involve much less hardware and time than the development of an optimum low velocity jet engine. Therefore, great emphasis has been placed in developing this class of nozzle, and intensive experimental research toward this development has been conducted in England and the United States by both industry and government laboratories during the past eight years.

The early interest in mixing nozzles stemmed from Westley's and Lilley's (Ref. 13) observation that insertion of toothlike fingers into a 1-inch cold jet resulted in a considerable reduction of noise. The first full scale application of this concept was made by Greatrex of Rolls Royce (Refs. 6, 14, 15), followed by Callaghan, Howes and North (Refs. 16, 17) of NACA Lewis Laboratory. The results of the full scale experiments confirmed that the overall noise was reduced on the order of 3 to 8 db at the angle of maximum radiation but, unfortunately, the noise was increased toward the side and forward of the jet. Consequently, the reduction in overall acoustic power was only of the order of 1 or 2 db (Ref. 17), with the primary reduction occurring at low frequencies, and a slight increase occurring at high frequencies (Ref. 15).

The desire to minimize the thrust losses inherent with the teeth designs, and simultaneously to retain and maximize the noise reduction resulting from the teeth concept led Greatrex (Ref. 7) to propose and test the corrugated nozzle. His impressive results led to the extensive investigations of corrugated, segmented and tubular nozzles by Boeing, Douglas, Pratt & Whitney, General Electric, NACA and others in this country, as well as Rolls Royce in England. These efforts culminated in flight hardware, some of which is illustrated in figure 74. Further, as a result of these research efforts, a considerable body of far field data is available, particularly from the NACA Lewis Laboratory, for a wide variety of nozzle configurations. However, before examining these results, it is instructive to develop a method for understanding and predicting the fundamental noise generating parameters for these complex nozzles.

The most important and difficult problem in estimating the noise generated by a mixing nozzle of arbitrary geometry is the definition of the jet flow. Once this definition is obtained, the noise can be predicted to varying degrees of accuracy, depending on the complexity of the flow, and upon the noise prediction model which is chosen. Therefore, the following paragraphs begin with an examination of simplified flow models.

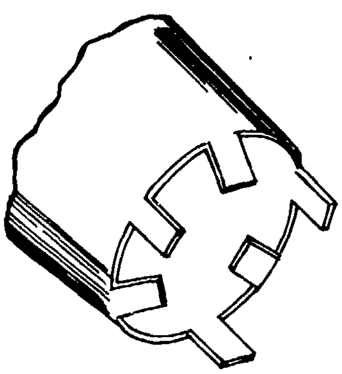

Example of experimental tooth nozzle tested by Greatrex of Rolls-Royce

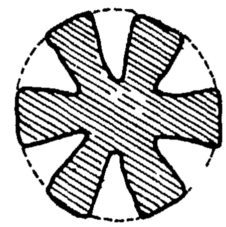

Early example of experimental corrugated nozzle by Greatrex of Rolls-Royce

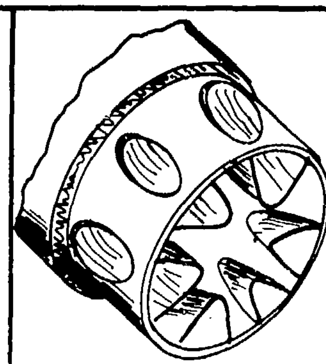

Six-lobe mixing nozzie for Rolls-Royce Avon engine installed on Comet aircraft

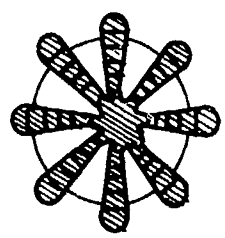

Eight-lobe corrugated nozzle for Rolls-Royce Conway engine installed on Douglas DC-8 aircraft

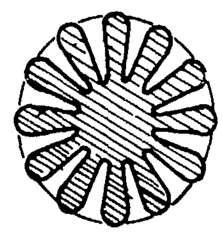

Experimental twelve-lobe corrugated nozzle tested by NACA Lewis Laboratory

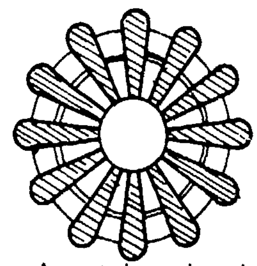

Experimental twelve-lobe corrugated nozzle with centerbody tested by NACA Lewis Laboratory

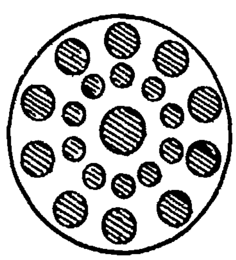

21-tube nozzle developed by Boeing for use with Pratt & Whitney JT-3 engine on 707 aircraft

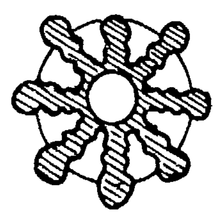

Daisy suppressor (with ejector) developed by Douglas for use with Pratt & Whitney JT-3 engine on DC-8 aircraft

Eight-lobe corrugated nozzle developed by General Electric Co. for their CJ-805-3 engine installed on Convair 880 aircraft

Figure 74. Sketches of several mixing nozzles from references 6, 7, 8, 9, 10, 11, 12.

Figure 75 is a sketch of a section of an axisymmetric nozzle which has several peripheral tube nozzles. The upper half of the sketch illustrates the jet core, the outer boundary of the jet and the .6 U_m velocity contour. The distance (b) between the .6 U_m velocity contour and the core boundary or, downstream of the core, the centerline of an individual axisymmetric jet, was defined in Section II and Appendix A as the normalizing factor in the non-dimensional radial parameter (η) where:

$$\eta = \frac{r - a}{b}$$

with r the radial distance from the jet centerline and a the radius of the core.

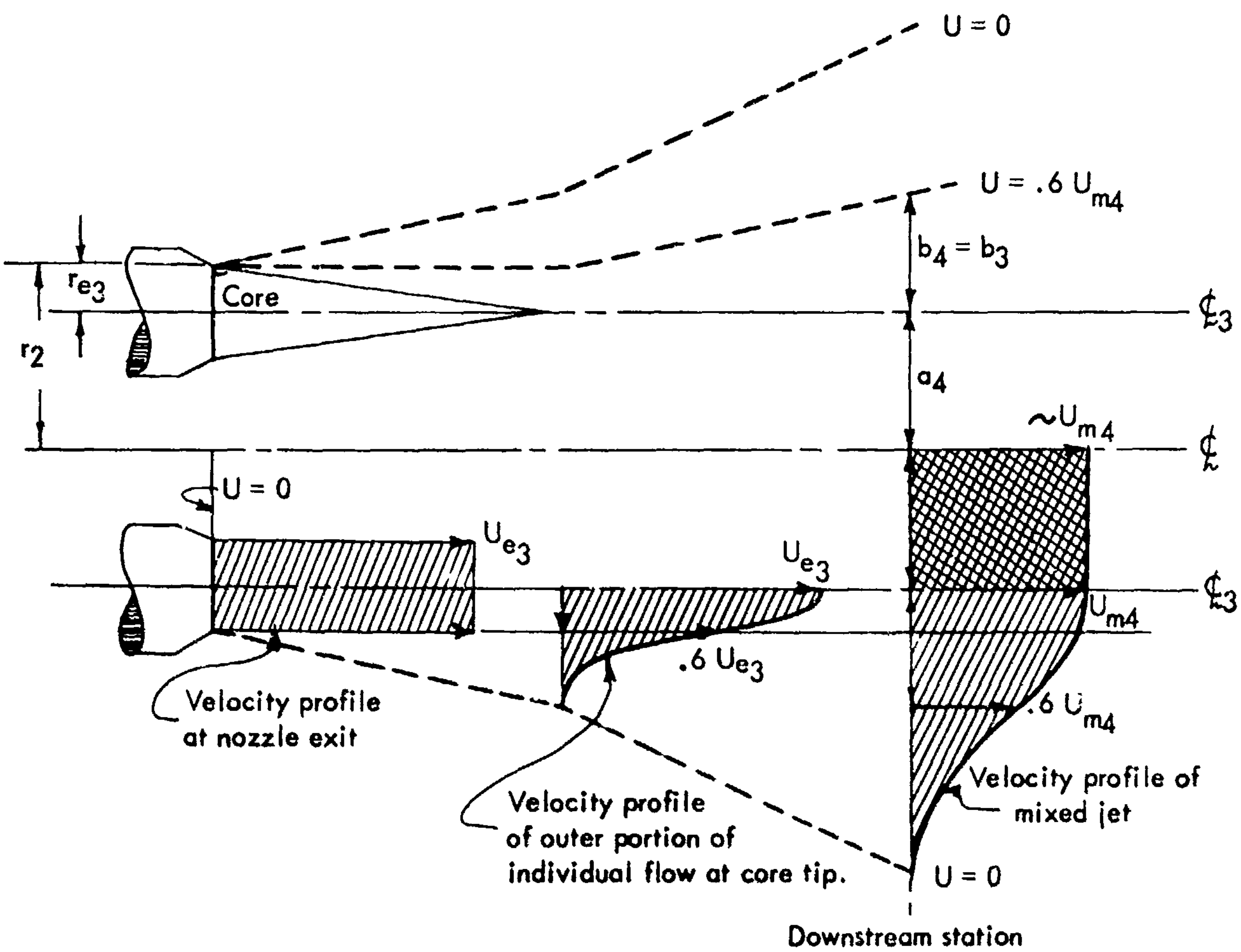

Figure 75. Sketch of two nozzles in the plane containing the axis of a simplified axisymmetric peripheral tube nozzle illustrating development of final mixed jet and the mixing of the individual jets.

The lower half of figure 75 shows a square velocity profile at the tube nozzle exit where $U = U_{e3}$ and the asymptotic tip profile from figure 12. The details of the flow in the center of this nozzle are deliberately omitted, because it is only possible to define them in a rather arbitrary manner for a few very special cases. In this connection, it is noted that a theoretical solution for the internal mixing must consider the radial pressure gradients in the Navier Stokes equation, which, as in Appendix A, are almost always assumed to be zero in turbulent mixing theories. Furthermore, the geometry of even the simplest mixing nozzle is rather forbidding for rigorous theoretical analysis.

Fortunately, the details of this internal mixing near the nozzle appear to have little bearing on the noise generation, except when there is insufficient spacing between the outer nozzle elements to permit the necessary inflow of ambient air to the center of the jet, for example, nozzles E and F of reference 18. When the peripheral spacing is insufficient, the static pressure in the central region of the jet is probably lowered far enough below ambient to cause a deflection of the outer jets toward the center. When this deflection occurs, the internal flow mixing is less complete than would otherwise be anticipated for the geometry and the low frequency noise reduction is reduced.

For the example of figure 75, the total exit momentum ($\mathcal{M}_{e3}$) is

$$\mathcal{M}_{e3} = n \rho_{e3} U_{e3}^2 \pi r_{e3}^2$$

where n is the number of peripheral nozzles.

Assuming the peripheral jets are close enough to combine into a larger, slower moving jet, denoted by subscript 4, at some downstream station, $\mathcal{M}_3 = \mathcal{M}_4$, by momentum continuity. Assuming also that the combined axisymmetric jet can be represented by the asymptotic profile of Section II, then

$$n \rho_{e3} U_{e3} \pi r_{e3}^2 \cong \pi (a_4 + b_4)^2 \rho_4 U_4^2 \qquad \text{(IV-4)}$$

where a_4 is the width of the combined jet core (which may be zero)
b_4 is the normalizing parameter as before, except that it applies to the combined jet.

To the first approximation, the outer circumference of the peripheral tube jets will mix at the normal rate with the atmosphere. In this case, the maximum velocity (U_{m3}) on the centerline of individual tube jets will decrease at axial distances beyond the tube flow core tips until at some axial station it equals the velocity for the internal or central flow. At this axial station the outer width parameter (b_3) for the individual tube flows should approximately equal the width parameter (b_4) for the assumed combined flow. Then downstream of the cores formed by the normal mixing of each peripheral jet, continuity of momentum (from Appendix A) gives:

$$\rho \pi b_3^2 U_{m3}^2 = \rho \pi r_{e3}^2 U_{e3}^2. \tag{IV-5a}$$

For a constant density jet, and at the downstream station where b_3 is assumed equal to b_4 and $U_{m3} = U_{m4}$, a simple substitution in equation (IV-5a) yields:

$$b_4 U_{m4} = r_{e3} U_{e3} \tag{IV-5b}$$

Further, by noting that the centerline distance of the peripheral jets from the final combined flow is $r_2 - r_{e3}$, then

$$a_4 \approx r_2 - r_{e3} \tag{IV-5c}$$

Solving equations (IV-4) and (IV-5) gives for this peripheral tube nozzle:

$$U_{m4} = \frac{(n^{1/2} - 1)\, U_{e3}}{(r_2/r_{e3}) - 1}, \quad b_4 = \frac{r_2 - r_{e3}}{n^{1/2} - 1}$$

$$\text{and } a_4 + b_4 = (r_2 - r_{e3}) \left(\frac{n^{1/2}}{n^{1/2} - 1}\right) \tag{IV-6}$$

The noise radiated from this simplified model should consist of the noise radiated by the outer portion of the individual tube flows before they coalesce at some downstream station, plus the noise radiated by the combined flow further downstream. The combined flow can be considered identical, beyond the station where the flows have combined, to the downstream flow of a jet which issues from a nozzle of radius $r_{e4} = a_4 + b_4$ at a velocity U_{e4} equal to U_{m4}, as shown in figure 76.

Some of the many assumptions which were made in the preceding simplified analysis can be tested with the data taken by Laurence and Benninghoff (Ref. 19) on the flow from the three sector nozzle illustrated in figure 77. For the purpose of these computations, the actual three pie-shaped segment nozzles are replaced by three 1.16 inch radius circular nozzles which have the same area as the actual nozzles. The center of each circular nozzle is assumed to act at the centroid of each segment, as shown in the top of figure 77. From equation (IV-6) U_{m4} is calculated to equal .47 U_{e3}, b_4 equals 2.46 inches, and $(a_4 + b_4)$ equals 4.26. Following the assumptions of the derivation of equation (IV-6), the station where the flows are expected to be combined is located at the position where the maximum or centerline velocity of each of the three peripheral jets would be expected to equal U_{m4}. From figure 16 in Section II the axial velocity of a circular Mach .3 jet of radius r_e falls to .47 of its original velocity at $x/r_e = 29$. Since $r_{e3} = 1.16$ inches, the jet should be fully combined at an axial distance of 33.6 inches from the nozzle, while upstream of this station the outer portion of the three jets would be expected to mix in the normal manner for single jets.

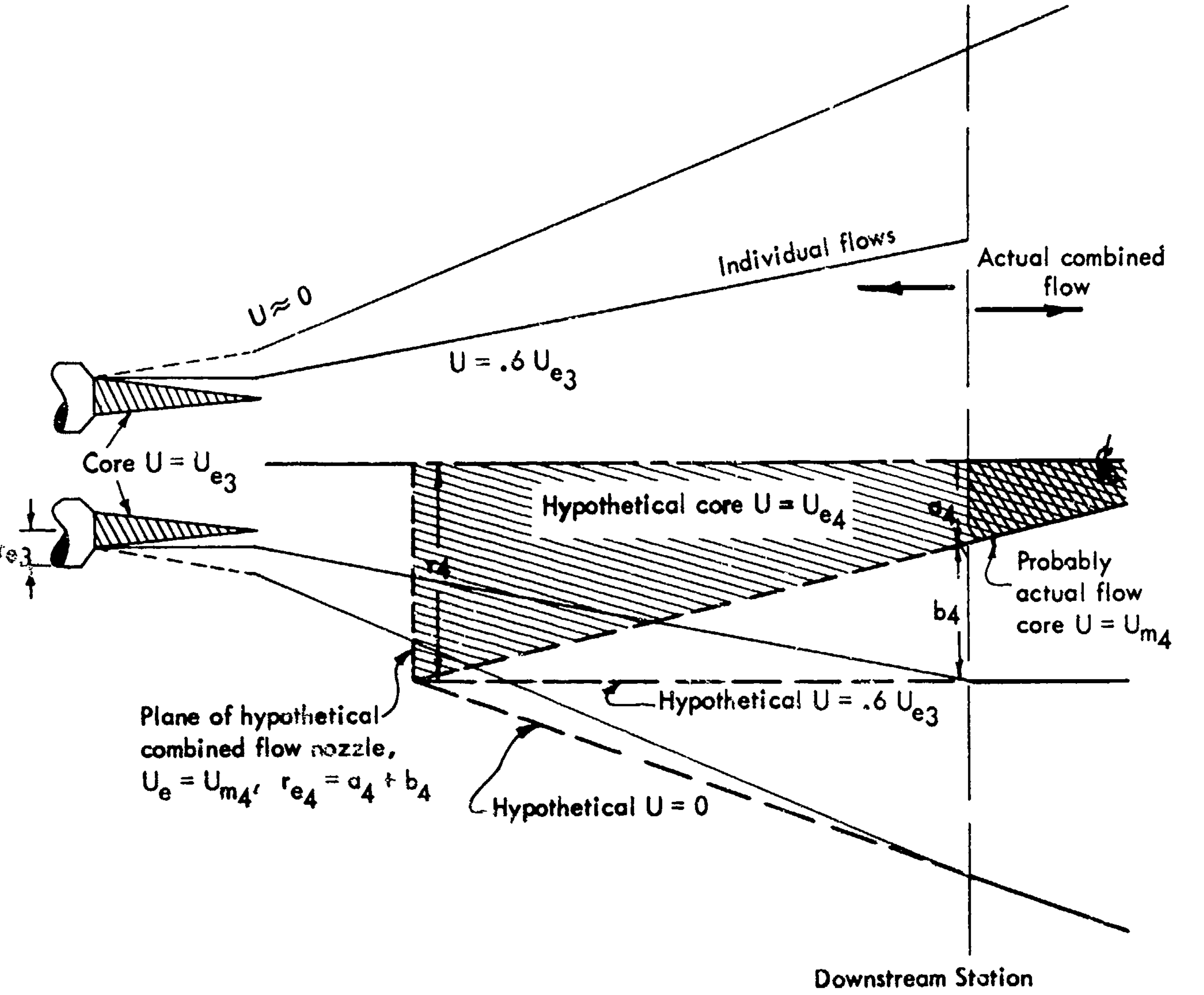

Figure 76. Sketch of two nozzles in the plane containing the axis of a simplified axisymmetric peripheral tube nozzle similar to figure 75, illustrating the super-positioning of a hypothetical nozzle which would result in the actual combined flow beyond some downstream station.

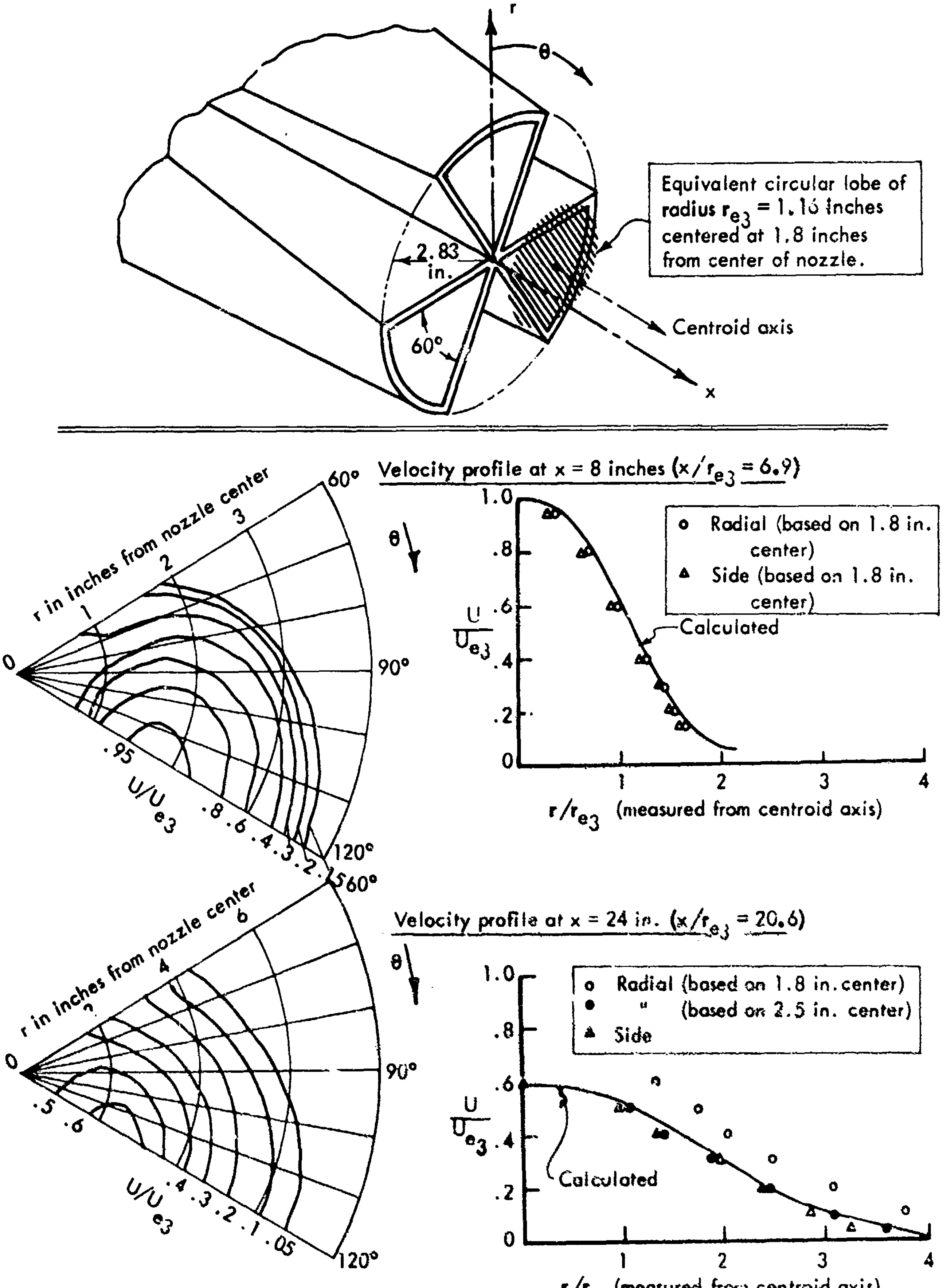

Figure 77. Example of flow data and comparison with calculated profiles for three-lobed nozzle at Mach .3. Data from Laurence and Benninghoff.

The two lower graphs on figure 77 show typical velocity contours measured by Laurence at two downstream locations and compare the profiles based on these contours with the profiles calculated for the individual flows from the relationships given in figures 12 and 16. At the x = 8 inches station where $x/r_{e3} = 6.9$, there is excellent agreement between the calculated and measured profiles, indicating that the outer portion of the individual flows does mix as expected for a single jet throughout the core region. At x = 24 inches, where $x/r_{e3} = 20.6$, the agreement looks good between the velocity profile measured to the side, but the effective center of the individual flow appears shifted radially outward by approximately .5 inch from the assumed center given by the centroid of 1.8 inches from the center of the entire nozzle. Unfortunately, no profiles are given downstream of 24 inches to determine axial station at which the three flows become indistinguishable in the combined flow.

A further confirmation that the turbulence in the outer peripheral mixing zone is similar to that expected for the individual flow is given in figure 78. Here, the normalized mixing length (δ), (see Section II) derived from the measured turbulence intensity and velocity gradient, is given as a function of x/re3, and compared with Laurence's data (Ref. 20) for a single jet shown in figure 9. The agreement gives further evidence

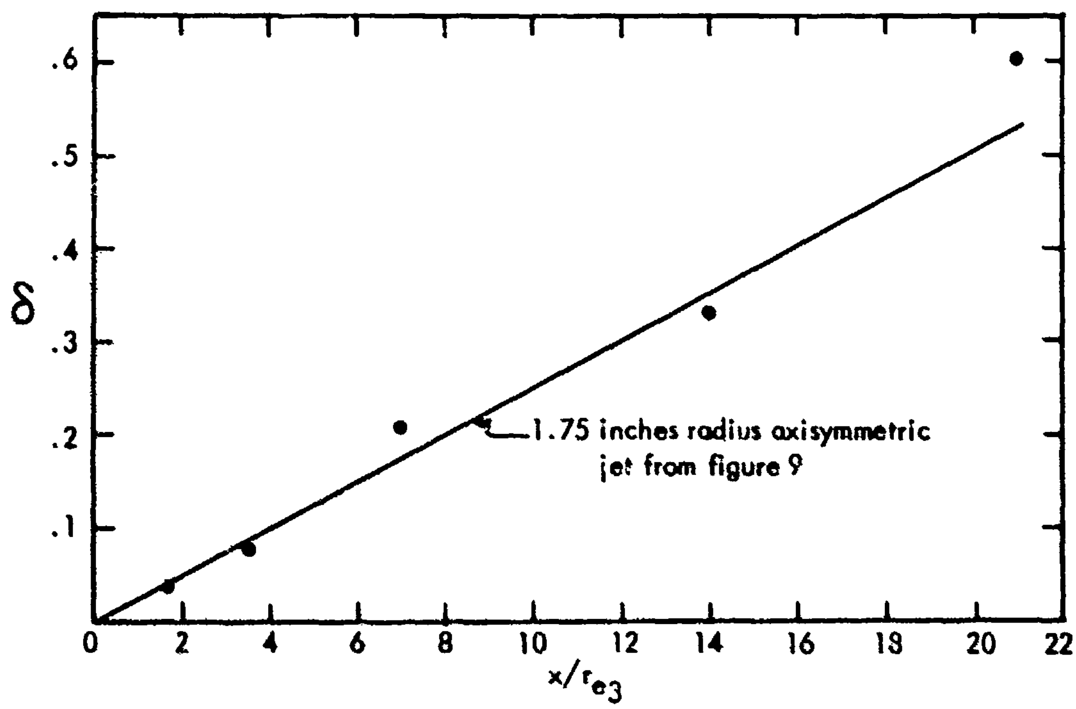

Figure 78. Comparison of δ based on r_{e_3} = 1.16 inches for 3 segment jet at Mach .3 with δ of axisymmetric jet at Mach .3 from figure 9. Data from Laurence and Benninghoff.

that the mixing of the outer portions of the flows from peripheral nozzles is substantially in accordance with the mixing expected for each individual nozzle, at least prior to the station where all the jets coalesce. Therefore, the noise generated in this mixing region should have the frequency characteristic expected for the individual nozzles, as given in figures 64 and 65. Further, the total acoustic power generated can be calculated from equation (IV-1) when the equation is corrected for the total number of nozzles (n) and the ratio of the exposed outer periphery (P_{e3}) of these nozzles to the total periphery of n single nozzles. Thus, for computing the total acoustic power in the initial mixing region, equation (IV-1) becomes

$$\begin{aligned} PWL_3 &= 146 + 10 \log \frac{n\, d_{e3}^2\, P_{e3}}{(n \pi d_{e3})} + 80 \log \frac{U_{e3}}{1000} \\ &= 146 + 10 \log \frac{d_{e3}\, P_{e3}}{\pi} + 80 \log \frac{U_{e3}}{1000} \quad \text{in db re } 10^{-13} \text{ watts} \end{aligned} \qquad \text{(IV-7)}$$

It should be noted that the noise generated by the internal mixing can be neglected because the internal turbulence levels are much lower than those on the periphery, as shown by Laurence (Ref. 19). These lowered values of turbulence would be expected since the total velocity difference between the core of the peripheral jets and that of the internal flow is significantly less than the difference across the outer mixing zone, as soon as the internal flow is initially accelerated.

The noise from combined downstream flow should be approximately equal to the noise generated in a similar downstream region by a jet of exit radius equaling $a_4 + b_4$ and of exit velocity equaling U_{m4}, as illustrated in figure 76. For accuracy, this computation should recognize that the mixing region of the combined jet between the equivalent nozzle of radius $a_4 + b_4$ and the downstream station is non-existent. Hence, the contribution of noise from this region to the total predicted for the combined jet should be subtracted. This correction involves the high frequency portion of the acoustic power spectrum generated by the combined jet. Since for practical mixing nozzles the high frequency power spectrum of total flow is dominated by the noise from the individual tube flows, this correction appears to be an unnecessary complication and can be neglected, although the methodology for the correction exists in this report.

These methods have been applied to the estimation of acoustic power spectra for the three segment nozzle, and the results are given in figure 79. For this particular nozzle, the acoustic power from the mixed flow, which is maximum at a low frequency, is considerably less than the power generated by the individual lobes because the velocity of the combined jet is less than one-half of that of the lobes. Therefore, the primary reduction in acoustic power is evident in the lower frequency region. This computed reduction of power spectra for two nozzle exit velocities is compared in figure 80 to a range of power reductions reported by Lee et al. (Ref. 2) for a similar nozzle over the same range of velocities. It is interesting to note that the computed frequency shift in the acoustic power reduction, which results from the velocity factor in the modified Strouhal number of figure 64, generally agrees with the data.

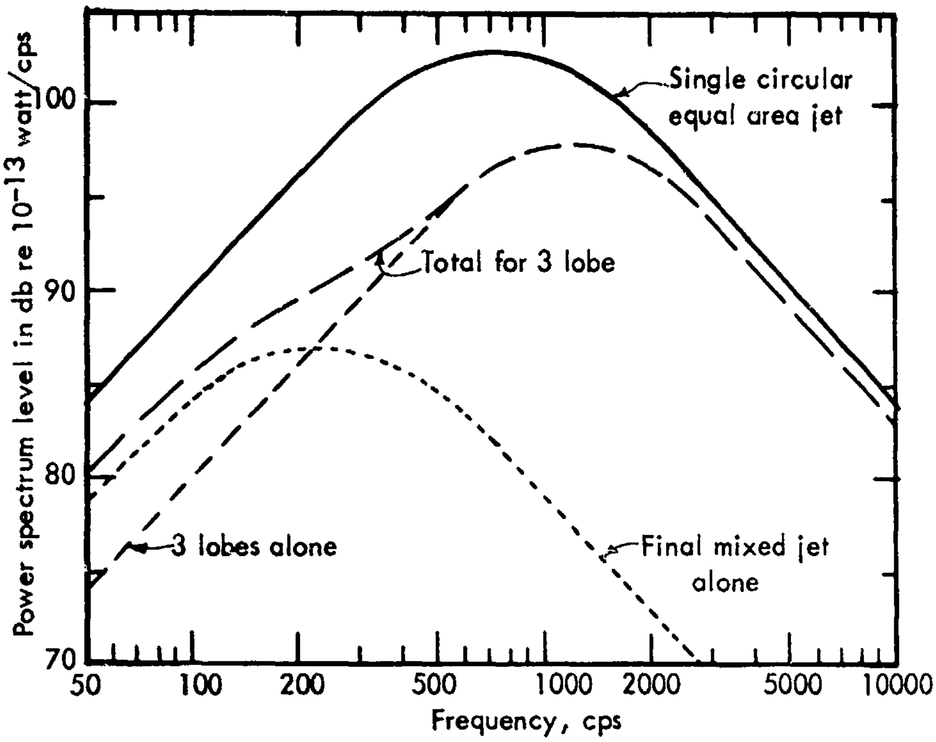

Figure 79. Calculated acoustic power spectrum level for 3 lobe 2.83-inch radius nozzle with exit velocity of 1020 ft/sec. showing contributions of lobe flows and final mixed flow in comparison with equal area circular jet of 2-inch radius.

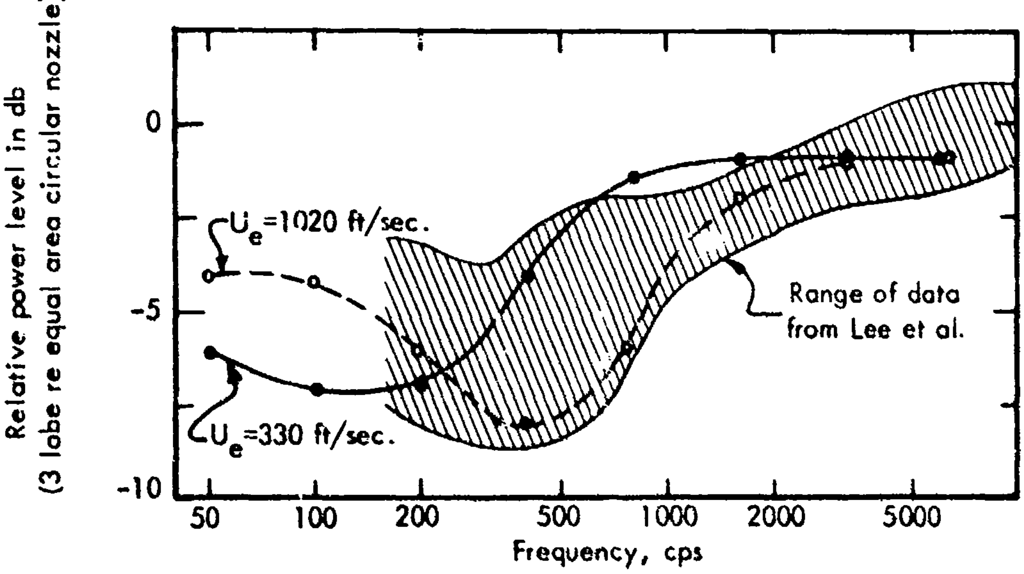

Figure 80. Comparison of acoustic power reduction calculated for three lobe 2.83 inch radius nozzle relative to 2 inch radius circular nozzle with data from Lee et al. for five pressure ratios

The preceding discussion and equations regarding an idealized peripheral tube nozzle and Laurence's three segment nozzle, were limited to constant density jet flows. In order to extend the discussion to jets of practical interest, it is desirable to consider the gross effect of temperature and density. Although, as discussed in Section II, no usable theoretical solution was found for hot high Mach number jets, the data indicated that the core length of the hot jet correlated well with the core length of a cold jet when both were compared at the same flow Mach number. Further, it was inferred that the mixing rates were also similar, and therefore that the constant density velocity profiles, mixing lengths, etc., had useful application in the hot jet case.

Recalling from the preceding discussion that the momentum radius of the combined jet was approximately equal to $a_4 + b_4$, then the area (A_{e4}) required for a jet of constant velocity $U_{e4} = U_{m4}$ which has the same momentum as the original jet is approximately $\pi(a_4 + b_4)^2$. The following brief derivation will give U_{m4} as a function of exit temperature ratio T_{e1}/T_o and area ratio A_{e1}/A_{e4}, where the subscript o refers to the ambient surrounding air and 1 denotes conditions at the nozzle exit of a standard engine, without mixing nozzles.

Assuming that the mixing of the jet takes place at constant static pressure, ($p_{e1} = p_{e4} = p_o$), and that the perfect gas law applies:

$$\rho_{e4} T_{e4} = \rho_{e1} T_{e1} = \rho_o T_o \tag{IV-8}$$

From continuity of mass flow, the total mass flow rate ($\dot{m}_4$) across the plane perpendicular to the jet axis at the station where the flows are combined must equal the nozzle exit mass flow rate ($\dot{m}_{e1}$) plus the mass rate ($\dot{m}_o$) of the inflow from the atmosphere. Thus, for the hypothetical exit of the combined jet:

$$\rho_{e4} A_{e4} U_{e4} = \dot{m}_{e4} = \dot{m}_o + \dot{m}_{e1} \tag{IV-9}$$

From the conservation of heat, disregarding conversion of turbulent energy to heat, and assuming the ratio of specific heats is constant throughout the flow,

$$\dot{m}_{e4} T_{e4} = \dot{m}_{e1} T_{e1} + \dot{m}_o T_o \tag{IV-10}$$

Eliminating $\dot{m}_o$ from equations (IV-9) and (IV-10) and substituting ρAU for m gives:

$$\rho_{e4} A_{e4} U_{e4} (T_{e4} - T_o) = \rho_{e1} A_{e1} U_{e1} (T_{e1} - T_o) \tag{IV-11}$$

Substituting for ρ_{e4} from equation (IV-8) gives:

$$T_{e4} = \frac{U_{e4} T_o}{U_{e4} - \alpha U_e (1 - \beta)} \tag{IV-12}$$

where $\alpha = A_e/A_4$

and $\beta = T_o/T_{e1}$

Assuming that the inflow from the atmosphere is primarily radial, which appears approximately true except for nozzles equipped with ejectors, the axial velocity component (U_o) of the inflowing mass can be neglected, and applying continuity of momentum in the jet,

$$\rho_{e4} A_{e4} U_{e4}^2 = \rho_{e1} A_{e1} U_{e1}^2$$

Substituting for ρ_{e4} from equation (IV-8) and T_{e4} from equation (IV-12) and solving for U_{e4}/U_{e1},

$$\frac{U_{e4}}{U_{e1}} = \frac{1}{2}\left\{ \alpha(1-\beta) \pm \sqrt{\alpha^2(1-\beta)^2 + 4\alpha\beta} \right\} \tag{IV-13}$$

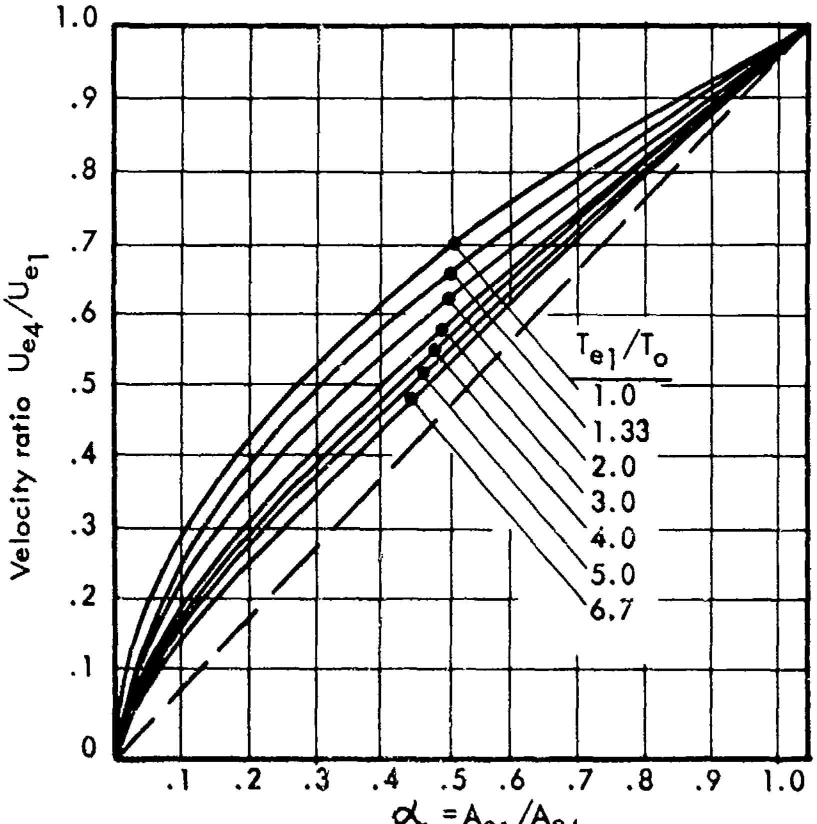

Figure 81. Ratio of the velocity (U_{e4}) of the combined jet to the nozzle exit velocity as a function of area ratio α and with the ratio of the absolute jet exit static temperature to ambient temperature as a parameter.

With this result, which is summarized in figure 81, it is possible to estimate U_{e4}/U_{e1}, once α is determined.

As previously noted, $A_{e4} = \pi(a_4 + b_4)^2$ although neither a_4 nor b_4 can be defined for the hot jet with the precision developed for the constant density jet. Fortunately, the majority of practical nozzles have the equivalent of many small elements, which distribute the nozzle exit area relatively uniformly over the area enclosed by the envelope of the mixing nozzle defined by radius r_2. From the last of equation (IV-6), which is repeated below,

$$r_{e4} = a_4 + b_4 = r_2(1 - r_{e3}/r_2)\left(\frac{n^{1/2}}{n^{1/2} - 1}\right)$$

when $r_{e3}/r_2 \ll 1$ and $n^{1/2} \gg 1$, r_{e4} approaches r_2, the envelope radius, as would be expected. Furthermore, although b_4 and a_4 have not been exactly defined for the combined hot jet flow, it is reasonable to expect that here, too, r_{e4} would similarly converge to r_2. Thus, to a first approximation, A_{e4} can be considered equal to A_2 when the effective radii (r_{e3}) of the individual peripheral nozzles are small and the actual exit area is relatively uniformly distributed over the envelope area (A_2). This assumption enables a direct calculation of the acoustic power estimated for the combined downstream jet flow.

In order to estimate the noise produced by the initial mixing of the elemental jet flows, it should generally be sufficient to consider only those flows on the outer periphery, since all inner flows mix at a lower turbulence level. As noted in the discussion of figure 65, the total acoustic power developed by n separated elemental jets, each of area A_{e3}, is simply n times the acoustic power generated by one of the elemental jets. Thus, if the total area of the elemental nozzles, nA_{e3}, equals the area A_{e1} of the original single circular engine nozzle, the total acoustic power remains unchanged, but the frequency spectrum is shifted, as illustrated by figure 65. When the n elemental jets are in close proximity, as in a mixing nozzle configuration, their total acoustic power generation in the initial mixing region can be considerably less, because only the peripheral mixing zone is of major importance to the noise generation.

Therefore, the total power of the initial mixing process is equal to the total power of the original nozzle of diameter d_{e1} times the ratio of the effective outer perimeter of the mixing nozzle configuration to the total perimeter of the n elemental nozzles. One reasonable approximation of this perimeter ratio R for n nozzles each of radius r_{e3} is given by:

$$R = \frac{r_2/r_{e3} + .18\, n_p - 1}{n} \qquad \text{(IV-14)}$$

where n_p is the number of elemental nozzles on the outer periphery. $(n > n_p \gg 1)$

With the above approximation, the total acoustic power radiated in the initial mixing region for n uniformly distributed elemental nozzles is:

$$PWL_3 = 146 + 20 \log d_{e3} + 10 \log nR + 80 \log \frac{U_{e3}}{1000}, \text{ in db re } 10^{-13} \text{ watt} \quad \text{(IV-15)}$$

and the total power radiated by the combined jet flow is:

$$PWL_4 = 146 + 20 \log d_{e4} + 80 \log \frac{U_{e4}}{1000}, \text{in db re } 10^{-13} \text{ watt} \quad \text{(IV-16)}$$

The spectra associated with these two acoustic powers are derived from figure 64.

The general results of these considerations are clearly illustrated in figures 82 and 83. Figure 82 gives an example of varying the envelope radius and hence the ratio r_2/r_{e1} for an idealized tube mixing nozzle for a 10,000 lb. thrust engine with 1850 ft/sec. exit velocity. Here the diameters of the elemental tubes are held constant at 4 inches. When $r_2/r_{e1} = 1$, the elemental nozzles are distorted and not separated, and the nozzle is simply the original circular axisymmetric nozzle. As the ratio r_2/r_{e1} increases, increasing the separation between the elemental nozzles and increasing the area A_2, the noise spectrum shows two maxima. The spectral peak at the lower frequency results from the combined jet flow. It will be noted that as the ratio r_2/r_{e1} increases indefinitely the low frequency maximum disappears, as expected for elemental jets whose flows do not combine into a single larger low speed jet. In addition, as r_2/r_{e1} increases, the level of the higher frequency maximum, associated with the peripheral elemental flows, increases until it reaches the spectrum generated by the summation of all of the elemental flows, each acting individually. Note that the level of noise from these mixing nozzles at frequencies above the upper frequency maximum is actually greater than the levels generated by flow from the original single nozzle. Thus, the noise reduction of the mixing nozzles is maximum throughout the middle frequency region, a fact which has plagued nozzle designers who desired to reduce the level of high frequency noise reaching the community.

Figure 83 illustrates the effect of varying the radius (r_{e3}) of the elemental nozzles retaining the ratio r_2/r_{e1} constant at 1.5. It is clear that a reduction of element radius, increasing the number of nozzles to retain the necessary constant exit area in accordance with figure 65, reduces the level and increases the frequency of the high frequency peak. Thus, for a fixed ratio of r_2/r_{e1}, the nozzle proposed by Tyler (Ref. 4) which had a very large number of very small elements will give the maximum noise reduction at the higher frequencies.

These methods were applied to the calculation of the acoustic power radiation from the two NACA twelve-lobe nozzles sketched in figure 74. The results of the estimated

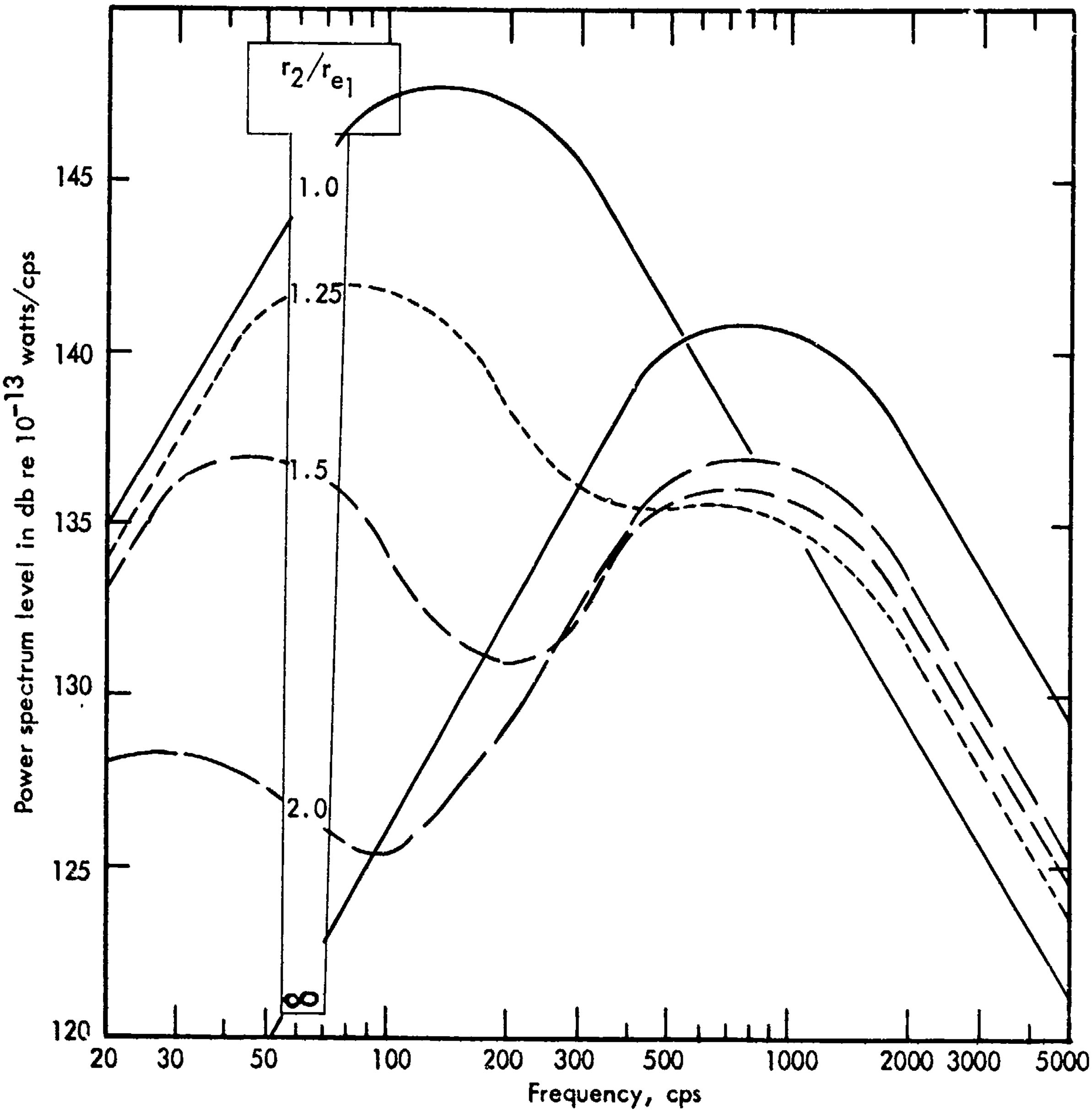

Figure 82. Calculated power spectra for idealized mixing nozzle with elements equivalent to 4-in. diameter tubes as a function of the ratio of the combined flow radius to single jet radius for J57 engine.

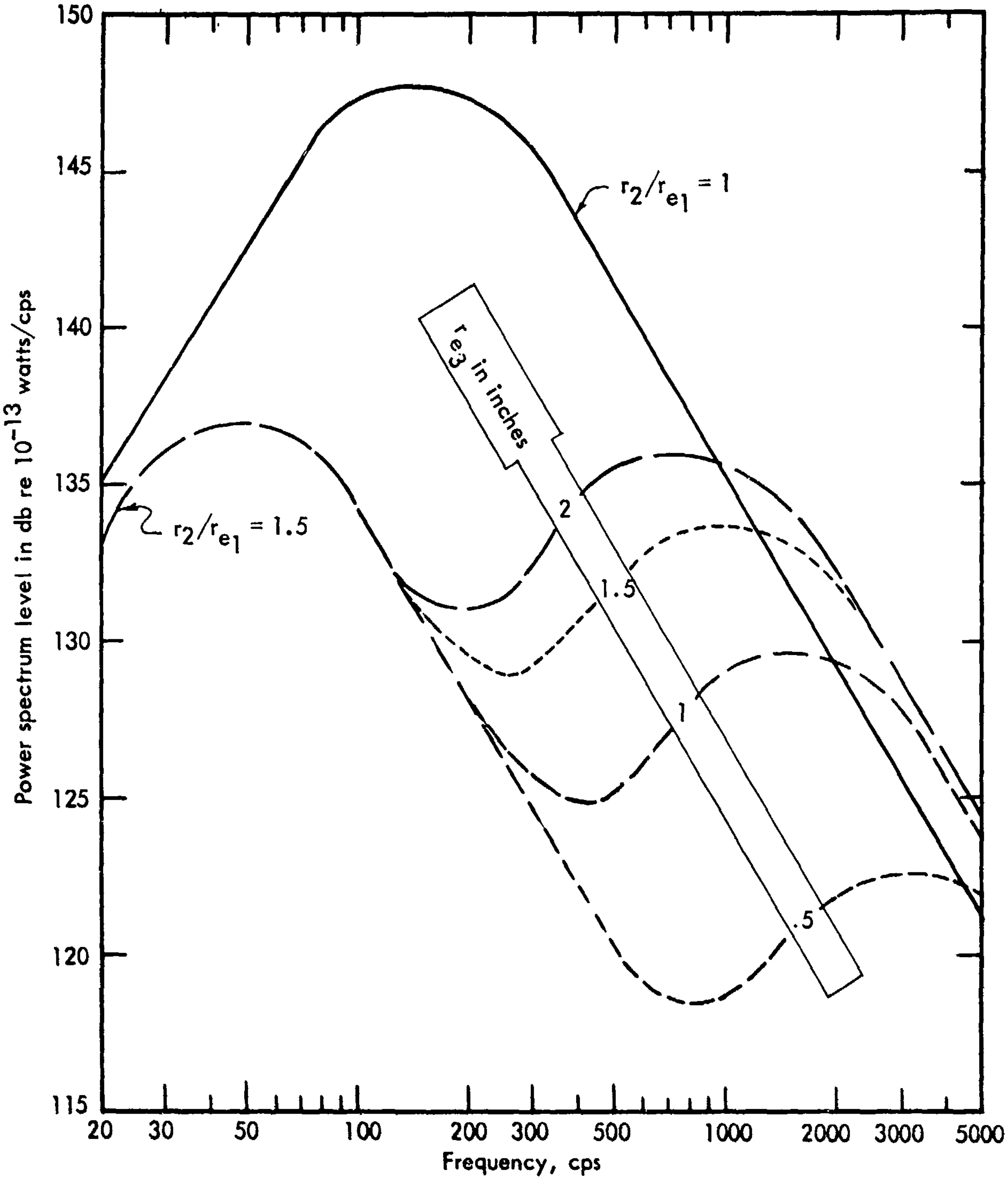

Figure 83. Calculated power spectra for idealized mixing nozzle with ratio of combined flow radius to single jet radius = 1.5 as a function of the radius of a typical element for J57 engine.

power spectra for these two nozzles are compared with the data* (Ref. 8) in figure 84. The agreement appears good in the low frequency region, tending to justify the assumption that $r_{e4} = r_2$ and the calculation of U_{e4} from this assumption and figure 81. The high frequency maximum appears correct as estimated for the nozzle without centerbody but 2 to 3 db low for the nozzle with centerbody. These latter high frequency data also suggest that the r_{e3} chosen for the lobes as scaled from the figure in reference 8 may have been slightly too large, resulting in a lower estimate of the center frequency for the elemental flows. Further, the data suggest that the periphery ratio R, defined by equation (IV-14 is too optimistic when the spacing between the lobes becomes large, violating the original assumption of a relatively uniform distribution of the elemental flows throughout the entire envelope area. Nevertheless, this idealized prediction procedure appears to be a very useful tool in determining the general noise-generating characteristics of an axisymmetric mixing nozzle.

The results of the preceding three figures indicate that the reduction in power spectra from practical mixing nozzles will have fairly well-defined limits, since the envelope radius r_2 and minimum element radius r_{e3} are both limited from practical considerations. The limitations are evident in the range of power spectra for ten examples of tube and corrugated axisymmetric mixing nozzles (Refs. 2, 9, 18, 21, 22), shown in figure 85. The nozzles include 2, 3, 6, 8 and 12-lobe configurations and 11, 19, 21 and 31-tube configurations. The maximum power reduction which is of the order of 15 db at 300 cps was obtained with the 12-lobe nozzle with centerbody, discussed with figure 84. Simultaneously, the maximum increase in high frequency noise in figure 85 resulted from this same nozzle.

Figure 86 gives a similar presentation for 8 nozzles with rectangle envelopes of varying aspect ratios obtained from NACA experiments (Refs. 9, 18). For the majority of these nozzles the ratio A_2/A_{e1} was held approximately constant, accounting for the narrow range in the low frequency power spectra. However, two of these nozzles, E and F, had much poorer low frequency performance than the other six, as shown in the figure. For both of these poorer nozzles the rectangular elements had much higher aspect ratios in comparison with the other six, making it difficult for ambient air to mix with the interior flow. Hence, it is probable that the internal flow could not gain sufficient mass flow to slow down to the velocity expected from the area ratio A_2/A_{e1} and, therefore the actual equivalent area (A_{e4}) of the combined flow is less than A_2. This result emphasizes the importance of providing sufficient access to the central region of the flow for the necessary inflow of air from the surrounding ambient air.

*The measured data for the nozzles given in figure 84 and other similar figures have been derived by applying the measured reductions of acoustic power as reported in the literature, to the generalized J57 spectrum which has been utilized throughout this report. This procedure is necessary to minimize the variations of ground attenuation, for example figure 53, which have affected almost all measurements of jet noise in varying degrees.

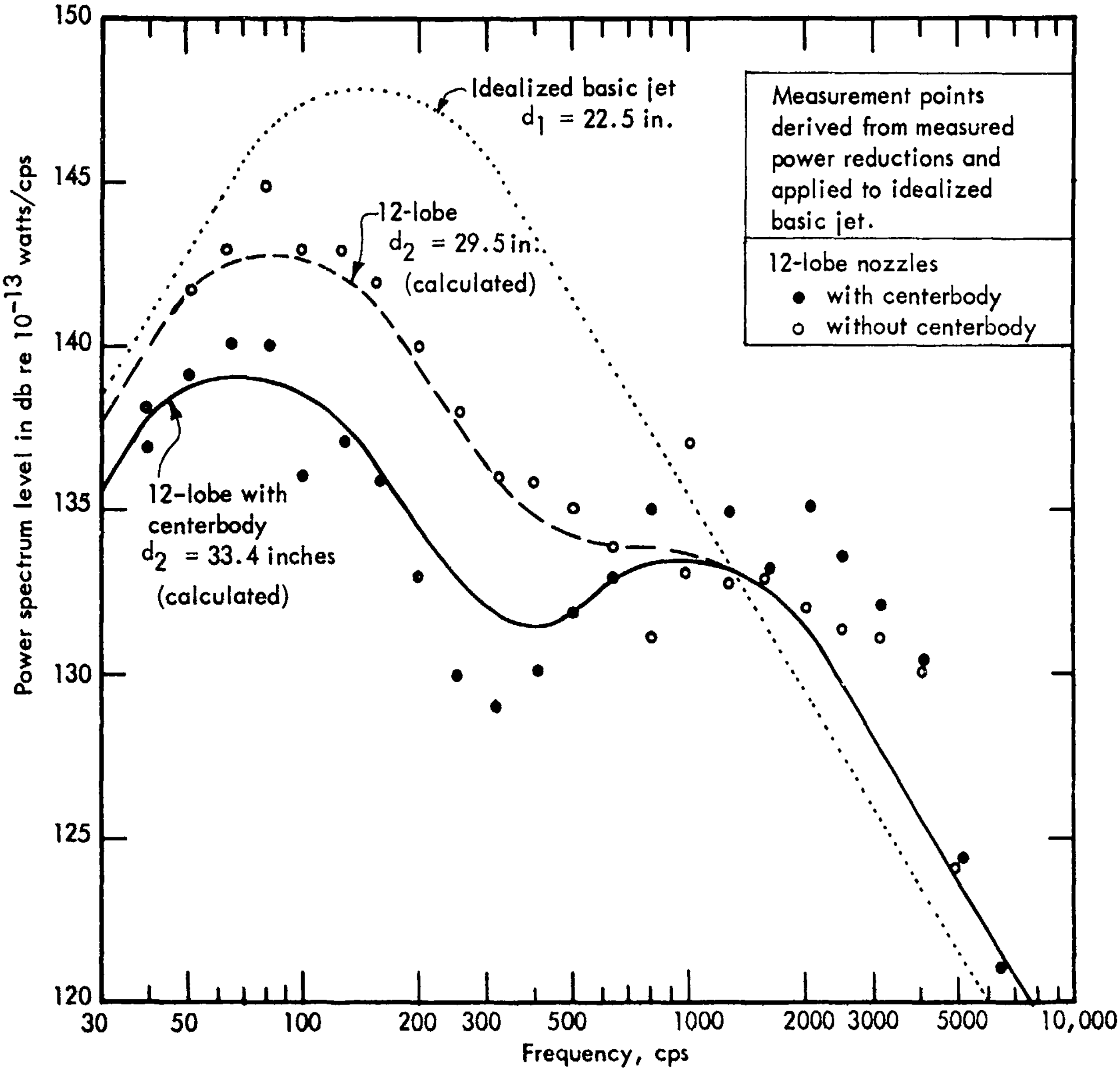

Figure 84. Comparison of calculated power spectra with power spectra derived from measured power reduction for two 12-lobe nozzles in NACA TN 4261 with J57 engine.

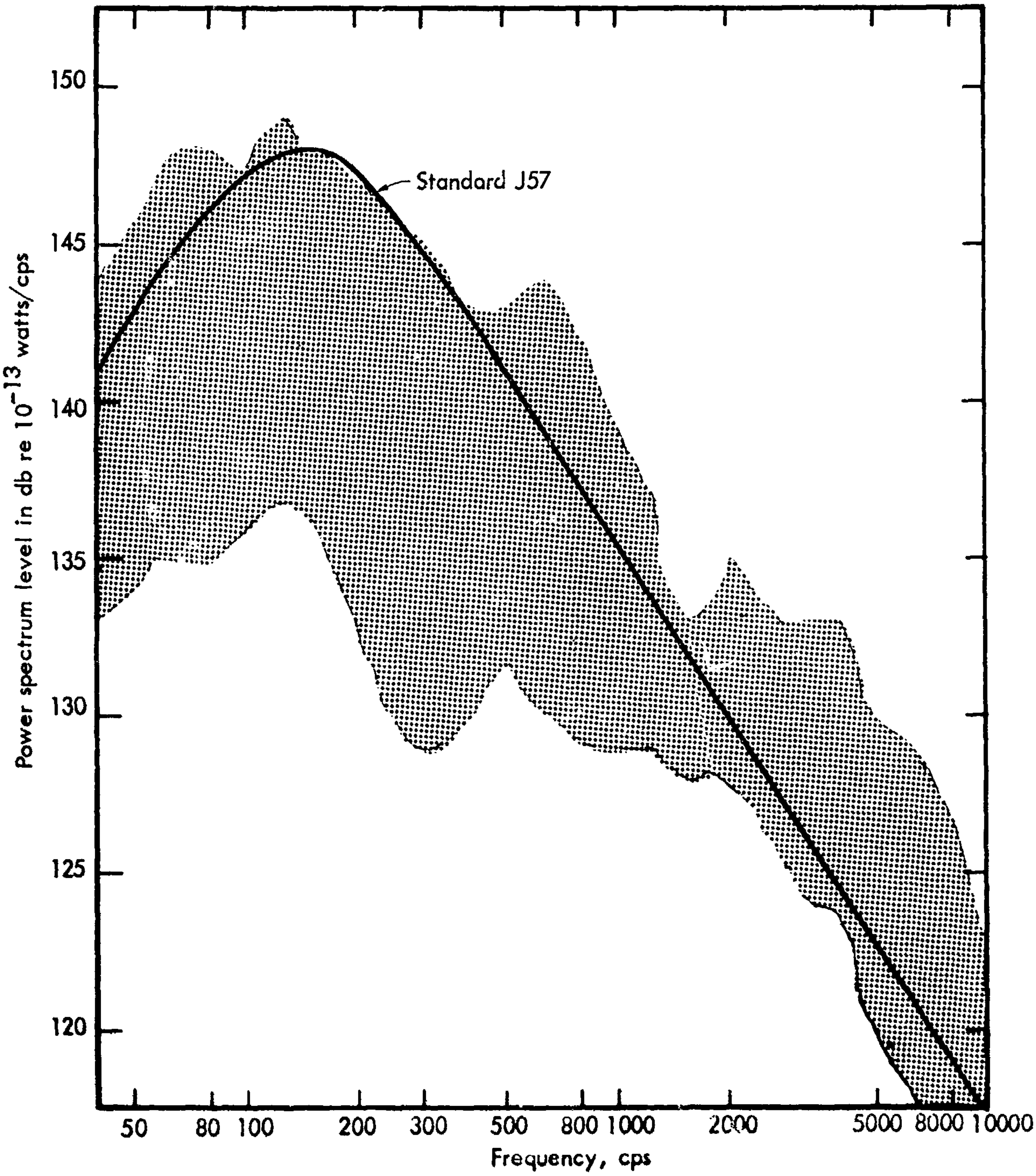

Figure 85. Range of sound power spectra for ten axisymmetric mixing nozzles of lobe and tube type. Original data noise reductions have been applied to standard J57 power spectrum. Data from NASA Report 1387 and TN 4261, General Electric, Rohr and WEAL files.

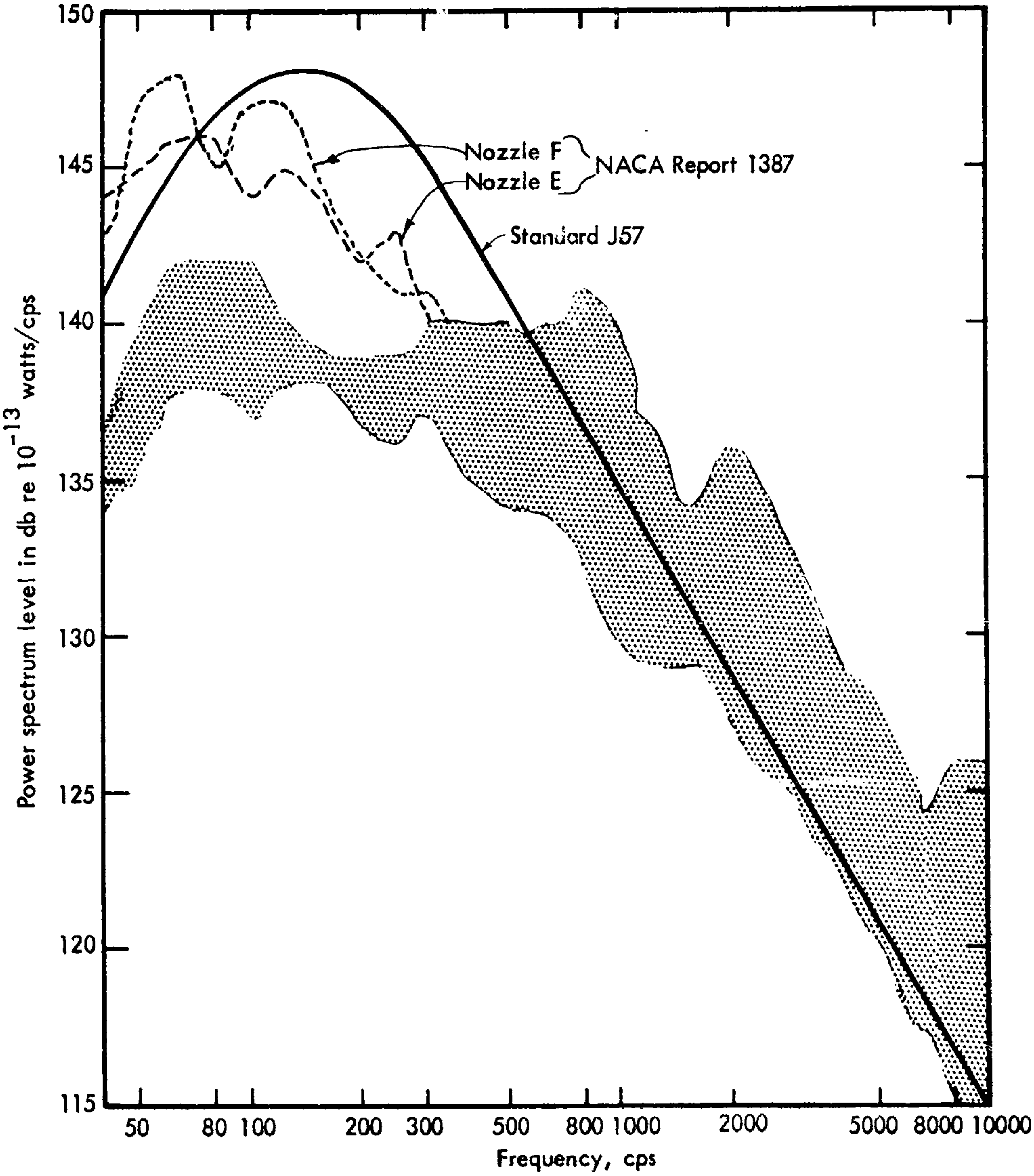

Figure 86. Range of sound power spectra for eight segmented retangular nozzle arrays. Original data noise reductions from NACA Report 1387 and TN 4261 have been applied to standard J57 power spectrum.

The effect of the spacing between the nozzle elements has interested several investigators, including Rollin of NASA (Ref. 23). His investigation was entirely with a rectangular array which does not exactly fulfill the assumptions for the derivation in this section. Nevertheless, it is interesting to compare the reduction in overall acoustic power predicted by these methods with his results. This comparison is given in figure 87. The results of both prediction and experiment agree that a minimum in total acoustic power should be found for this nozzle array at spacing ratios between one and two, and that the effect of the width of the individual rectangular elements is slight. However, the predictions do not account for the effect of nozzle pressure ratio on power reduction which appears in the data in the neighborhood of a spacing ratio of one. Nevertheless, the general agreement is sufficient to indicate that these prediction methods are approximately valid over a considerable range of arbitrary nozzle geometry.

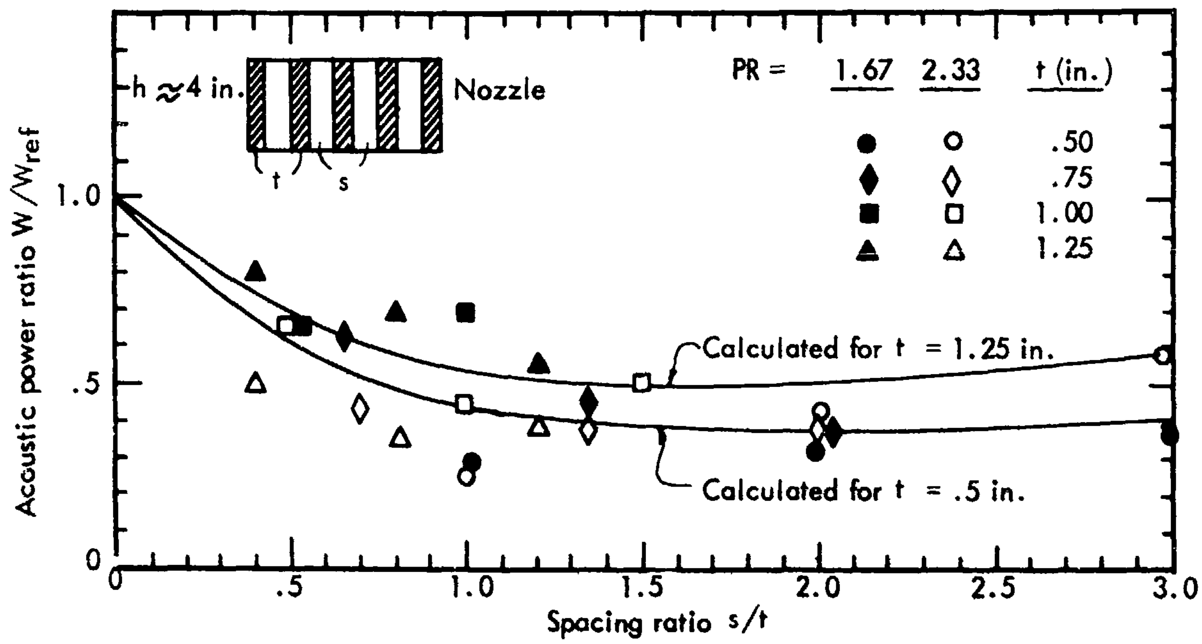

Figure 87. Comparison of calculated variation of relative acoustic power with spacing ratio with measured values for 5-segment rectangular nozzle for several values of segment width. Data from Rollin, NASA TN D-770.

The total acoustic power from an idealized mixing nozzle is the sum of PWL_3 and PWL_4 given in equations (IV-15) and (IV-16) respectively. The results of these equations, as demonstrated in figure 84, appear fairly valid when the nozzle flow is relatively uniformly distributed over the entire envelope area. Therefore, it is useful to apply these equations to determine a measure of the minimum overall acoustic power obtainable by an idealized mixing nozzle. The results are summarized in figure 88, as a function of the ratio of envelope radius to the radius of the original single nozzle for several sizes of typical elements. It is clear from the figure that a relatively large reduction in sound power can be obtained by increasing the envelope radius from 1.25 to 1.5 times the radius of the original jet. In this region of radius ratio, the overall sound power is controlled by the low frequency spectrum of the combined flow, as illustrated in figure 82. However, further increases of the radius ratio beyond approximately 1.5 do not result in further decreases in total acoustic power because the total power becomes controlled by the high frequency noise generated by the initial mixing of the individual elements, and this power increases as element spacing increases.

In addition, figure 88 shows that the total acoustic power is minimized by minimizing the size of the elemental nozzles, which was seen in figure 83. Thus, for a range of elemental nozzle diameters between 4 and 2 inches for an engine of the J 57 class, or more generally for a range of r_{e3}/r_1 between .18 and .09 the maximum acoustic power reduction for an idealized mixing nozzle varies between 5 and 8 db, and is obtained at ratios of r_2/r_{e1} between 1.25 and 1.5. Additional reduction in power requires utilization of smaller elemental nozzle sizes.

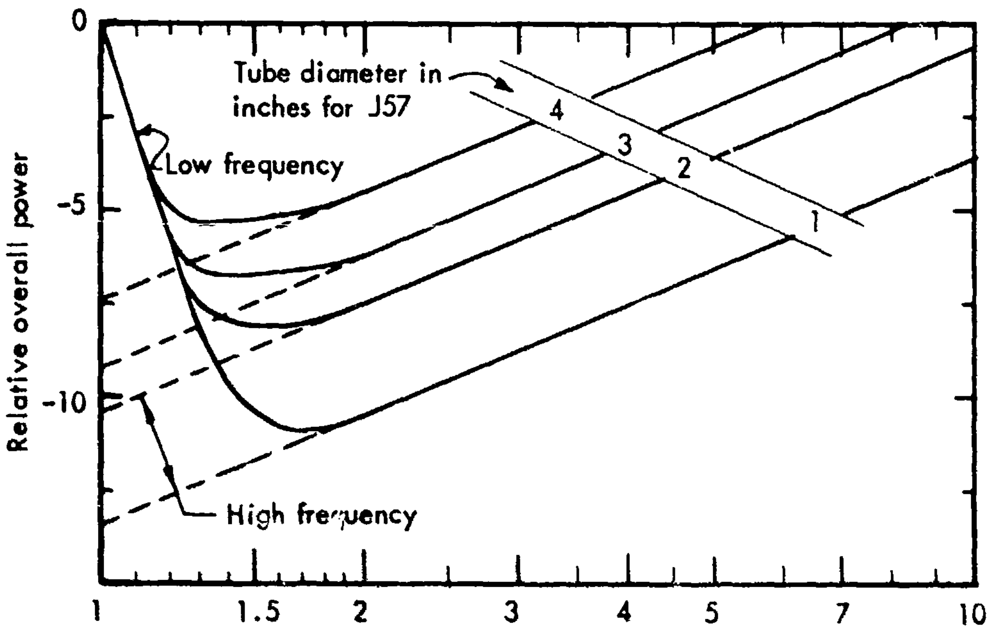

Figure 88. Computed variation in total acoustic power for idealized mixing nozzle relative to standard nozzle for $T_{e1}/T_0=3$, as a function of the ratio of the mixed jet radius to standard nozzle exit radius with element size as a parameter.

Ejector Nozzles

Another method of reducing the velocity of the jet stream, and hence its noise generation, is by the use of an ejector which shrouds the jet. If the ejector is sufficiently long and has sufficient entrance area, it will pump enough secondary air to reduce the average velocity of the jet at the ejector exit and achieve a relatively square profile. If these conditions are fulfilled, the approximate exit velocity from the ejector can be obtained directly from equation (IV-13) or figure 81, which neglect the effect of the axial momentum of the secondary air flowing into the ejector. Although for most practical purposes this secondary air momentum is negligible since the entrance velocity is low, equation (IV-13) can be modified to include the effect of secondary air velocity (U_s) with the following result, as shown by Dyer et al (Ref. 24):

$$\frac{U_4}{U_{e1}} = \frac{1}{2}\left\{\alpha(1-\beta) + \frac{U_s}{U_e} + \sqrt{\alpha^2(1-\beta)^2 + \left(\frac{U_s}{U_{e1}}\right)^2 - 2\alpha\frac{U_s}{U_{e1}}(1+\beta) + 4\alpha\beta}\right. \quad \text{(IV-17)}$$

Unfortunately, an ejector must be many diameters long to obtain sufficient mixing to achieve a relatively square velocity profile and the resulting minimum U_4/U_{e1} predicted by α , the ratio of nozzle exit area to ejector exit area. Therefore, the application of relatively short practical ejectors whose length is of the order of one to two times the diameter of the primary jet to standard nozzles results in almost no reduction in centerline velocity. Hence, as shown by North and Coles (Ref. 25), the corresponding reduction of total sound power is insignificant.

However, considerably better results are achieved (Refs. 26, 27) when an ejector is attached to a mixing nozzle. In this case, an ejector, approximately two standard nozzle diameters long, shrouds the major portion of the initial mixing region. Since in this region the outer periphery of the multiple nozzle is greater than that of the standard nozzle, there is an increase of momentum exchange relative to the standard nozzle and a corresponding increase in the efficiency of the ejector per unit axial length. Therefore, the velocity profile across the exit of an ejector which is combined with a mixing nozzle approaches the idealized square profile much more closely than does the profile of the same ejector when utilized together with a standard nozzle. Consequently, the low frequency portion of the acoustic power from the ejector-mixing nozzle combination approaches the levels shown in figures 82 and 88 where r_2 is considered to be the ejector radius.

In addition to the reduction of low frequency noise generation, the addition of an ejector can reduce the high frequency power generated by the elemental jets on the periphery of the initial mixing region. This reduction results from the reduced velocity difference between the cores of the elemental peripheral jets and the secondary velocity induced in the ejector intake, in accordance with the footnote to equation (IV-1). For example, if the induced secondary velocity U_s is one-tenth of the primary exit velocity, the sound power generated in the shrouded portion of the initial mixing zone would be reduced by approximately $\{80 \log .9\}$, a 4 db reduction compared to the power generated in this region without the ejector. To maximize the net reduction, it appears that the ejector should shroud the entire length of the initial mixing region, where the high frequency noise is generated. Therefore, for a J57 engine with a mixing nozzle whose typical elements have a two-inch radius, it would be desirable to shroud for an axial distance approximately equal to the first 20 - 25 elemental nozzle radii. This ejector would be between 40 and 50 inches long, or of the order of 1.8 to 2.2 times the standard nozzle diameter of 22.5 inches. Note that the optimum length also depends on the ratio between ejector radius and the standard nozzle radius, to assure that its length covers the entire initial mixing zone as previously defined for mixing nozzles.

These comments regarding the effect of the ejector on the high frequency spectra are confirmed by the data (Refs. 26, 27) given in figure 89 for four ejectors with mixing nozzles. Note that the high frequency acoustic power with ejector is less than or equal to that of the standard engine, whereas the high frequency power of the mixing nozzles alone shown in figures 85 and 86 was generally higher than that of the standard engine. This reduction of high frequency power resulting from the addition of an ejector to a mixing nozzle is of importance to community noise and was probably a major consideration in the design of the Douglas 8-lobe Daisy-ejector combination suppression nozzle.

The ejector has additional potential for the reduction of the high frequency noise, if its inner surface is made to be acoustically absorbent. For example, if the ejector covered the entire initial mixing region, and were capable of absorbing all of the high frequency noise generated in this region, shown in figures 82, 83 and 88, the radiated power spectrum should approach the idealized spectrum for the combined jet flow alone. Thus, the absorbing ejector has the potential capability of significantly improving the performance of the mixing nozzle beyond the limits shown in figure 88. Furthermore, the shrouding effect of the ejector will always be of major benefit to structure in the near vicinity of the exhaust nozzle.

Slot Nozzles

It has been shown in the mixing nozzle analysis, figure 82, that achievement of maximum low frequency reduction by replacing a single nozzle with a large number of small nozzles in an axisymmetric array with their higher characteristic frequencies, involves a relatively large separation of the nozzles. Another basic configuration for attaining the potential frequency shift shown in figure 65, is to distribute the elemental nozzles in a long line, perhaps along a wing trailing edge. A major step in this direction is embodied in the high aspect ratio slot nozzle.

Several model scale experiments with slot nozzles have been conducted by NASA, Langley (Refs. 28, 29) to determine both the noise radiation characteristics and the possibilities of utilizing the slot nozzle in conjunction with a wing flap to augment low speed lift. Although no acoustic power data were reported, the various spectra showed the presence of considerably more low frequency energy than would be anticipated from figure 65. Further, the results indicated that the pressure fluctuations on a jet augmented flap would be sufficient to warrant special design of the flap structure to avoid acoustic fatigue.

A full scale experiment on slot nozzles of 14:1 and 100:1 aspect ratio reported by Coles (30) also confirmed that the low frequency noise generated by the slot nozzle, far exceeded that expected for independent circular nozzles of diameter equal to the slot width. The corrected power spectra for Cole's 100:1 slot nozzle, standardized J57, and idealized 126 two inch diameter independent nozzles, are summarized in figure 90. It is clear that the high frequency power generated by the slot nozzle in the vicinity of the

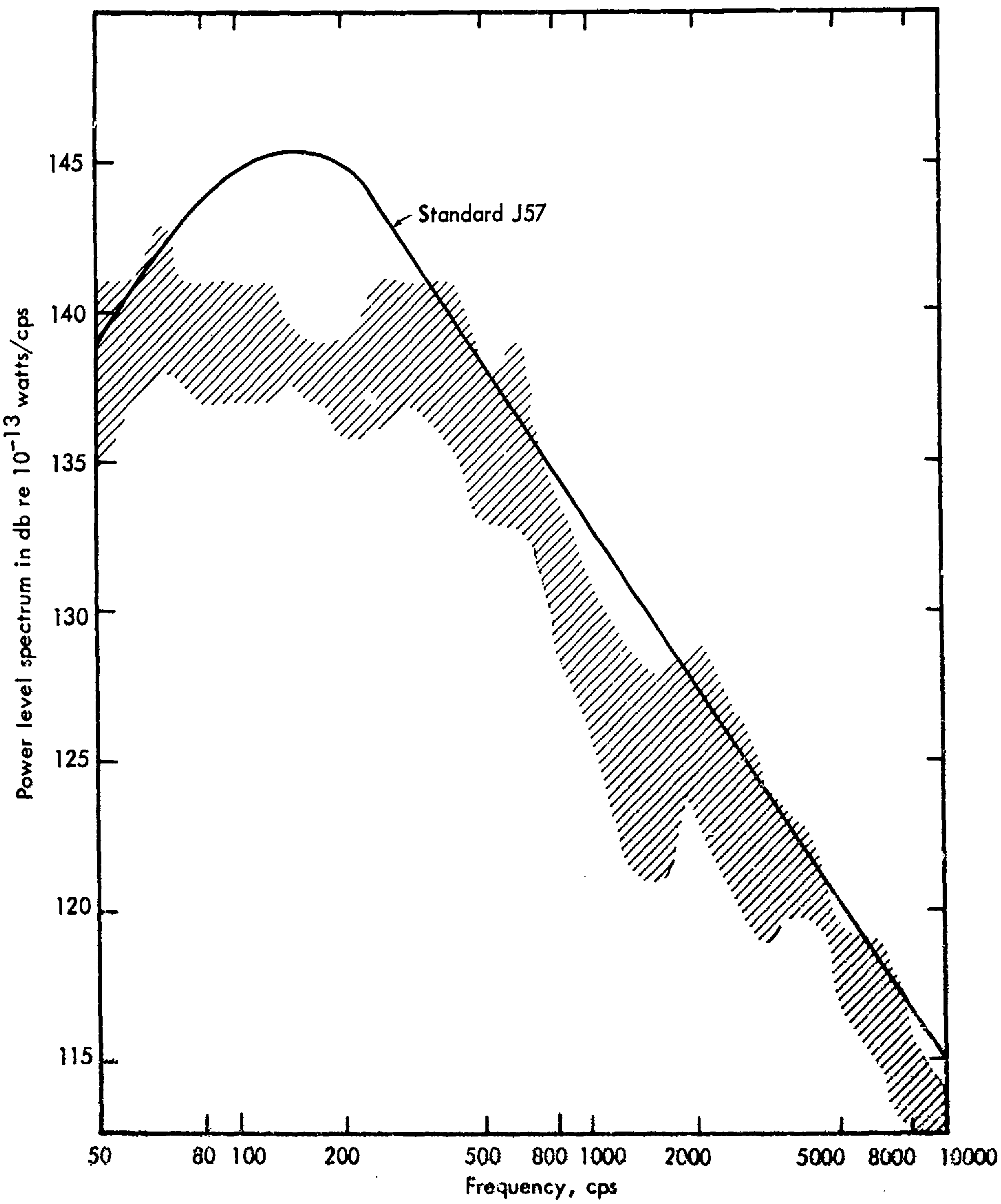

Figure 89. Range of sound power spectra for four mixing nozzle - ejector combinations. Original noise reduction data from NASA TN 4317, 4261 and D-871 have been applied to J57 power spectrum.

peak of the spectrum for two inch nozzles exceeds the power generated by the standard J57. Considering only this high frequency portion of the spectrum, and utilizing the periphery ratio concept which preceded equations (IV-14 and IV-15), it is noted that the periphery of the slot nozzle (33.7 ft.) is approximately one-half that of the 126 two-inch diameter jets (66 ft.). Therefore, it would be expected that the total acoustic power of the high frequency region would be of the order of 3 db less than that of the standard engine. This expectation is approximately confirmed by the data.

However, the flat low frequency portion of the spectra shown by the data is not expected from this initial rough analogy. In fact, it was this apparent inconsistency between data and expectation which partially motivated the analysis of the flow from slot jets in Section II and Appendix A. The results of this analysis showed that the mixing region adjacent to the core of a slot jet, and the length of the core were approximately equivalent to an axisymmetric jet which had a diameter equal to the slot width. However, as shown in figure 20, the velocity downstream of the slot jet core decreased proportional to $x^{-1/2}$, a much slower rate of decay than that of the axisymmetric jet where the centerline decay is proportional to x^{-1}. Therefore, downstream of the core, the acoustic power per unit axial length should decrease as x^{-4} for the slot jet, as compared to x^{-7} predicted for the axisymmetric jet from the same dimensional analysis. It is believed that this lower rate of axial velocity decay is responsible for the jet's generation of the additional low frequency acoustic energy which results in the rather characteristic slot jet power spectrum shown by the data in figure 90.

Figure 90 also contains a first order estimate of the power spectrum of the slot jet. This estimate utilized the power spectra from figure 46, and overall power per unit axial length from figure 45, and the x^{-4} relationship, all adjusted for the slot jet flow solution of Appendix A. The resulting prediction shows a large enhancement of low frequency power relative to the axisymmetric case, which is generated for a very great distance downstream. However, although reasonable agreement of prediction with the data is found above 1000 cps, the estimated low frequency power spectra are considerably lower than the measurements. Although this discrepancy could result from turbulence generated internally in the high flare slot nozzle, it is more probable that the data represent a typical slot noise spectrum. Hence, the increase in low frequency power of the slot jet over the circular jet is greater than the estimate. This result is not surprising in view of the discussion of figures 41 and 48, where it was concluded that the turbulence level in the high Mach number flow does not fall off as rapidly downstream of the core as does the centerline velocity. Hence, as shown in figure 45, the x^{-7} law does not apply until very far downstream. Similar reasoning applied to the slot jet leads to the conclusion that the reduction of power per unit axial length downstream of the slot jet core also is probably slower than the reduction of centerline velocity. Consequently, the x^{-4} law utilized for the estimate gives too much reduction of acoustic power generation with axial distance. Therefore, the estimated low frequency slot jet power spectrum, although exhibiting the proper trend, is too low in level.

These results, although far from providing a good prediction method for the slot jet, do serve to confirm the flat low frequency characteristic of the slot jet power spectrum. Consequently, the reduction in acoustic power spectra attainable with a slot jet is nowhere near that obtained by a large number of nozzles whose diameter is equal to the slot width.

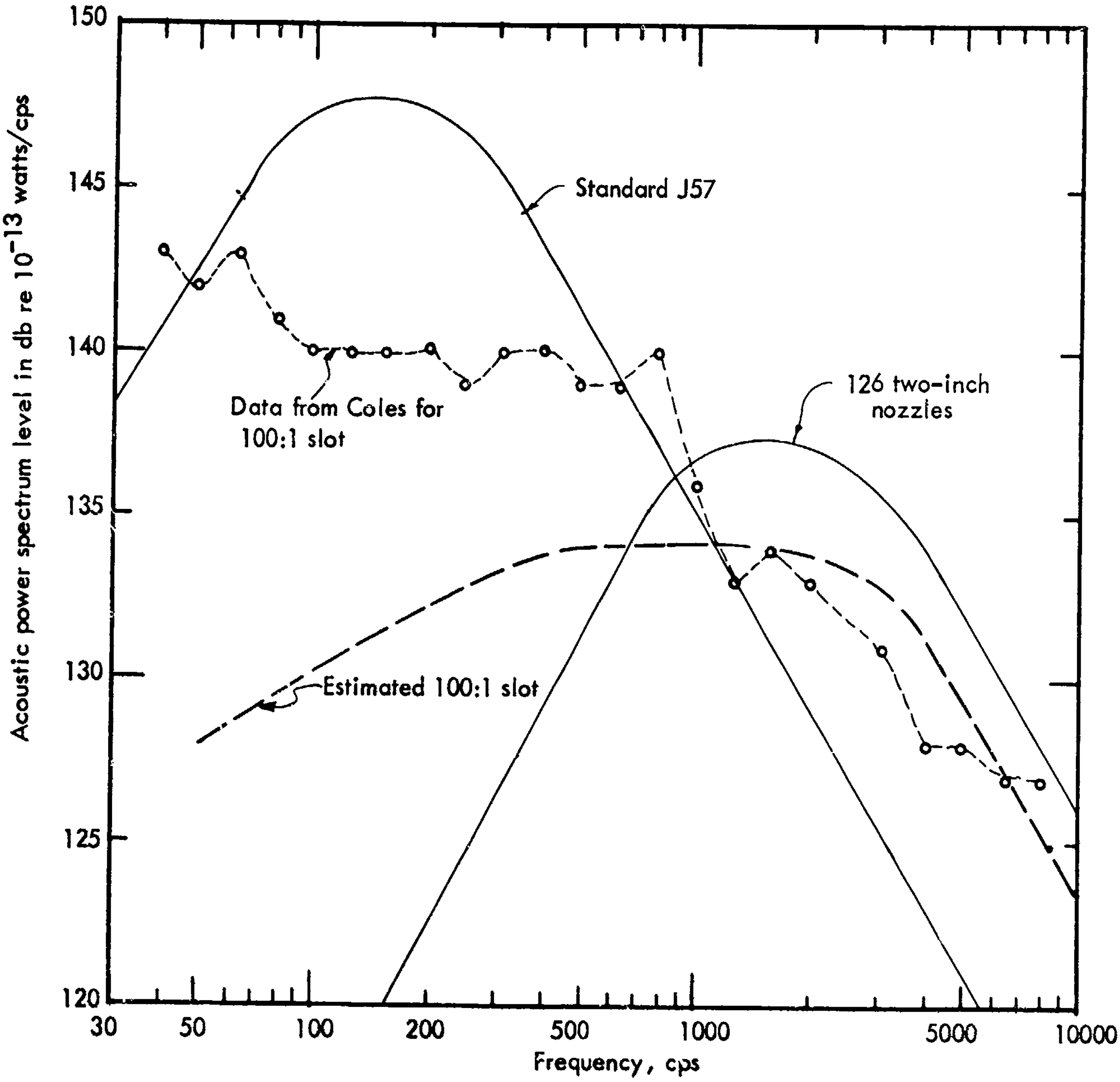

Figure 90. Example of noise from a 100:1 slot nozzle comparing data from Coles, normalized to standard J57 engine, with preliminary estimate.

LIST OF SYMBOLS USED IN SECTION IV

Roman

A	Area
a	Sonic velocity (varies with T)
a	Core radius (varies with x)
b	Gradient width parameter
d	Diameter
f	Frequency
(f)	Per cps
$\mathcal{M}$	Momentum
m	Mass
n	Number of nozzles
P	Periphery
p	Pressure
PR	Pressure ratio
PWL	Power level re 10^{-13} watts
r	Radius
R	Perimeter ratio
s	Rectangular nozzle spacing
T	Temperature
t	Rectangular nozzle width
U	Flow velocity
W	Power
w	Weight
x	Axial distance from nozzle
x_t	Core length

Superscripts

$'$	Equivalent
$\cdot$	Time derivative

Greek

α	A_{e1}/A_{e4}
β	T_o/T_{e1}
δ	Mixing length
η	Radial parameter = $\frac{r - a}{b}$
λ	Wavelength
ρ	Density

Subscripts

$*$	At nozzle throat
o	Ambient
1	Reference or standard jet (P.R. $\leq$ 1.89)
2	Envelope radius of mixing nozzles
3	Characteristic of divided flow
4	Characteristic of combined flow
e	Exit
m	Maximum at a given axial station
P	Perimeter
p	Primary
s	Secondary
t	Total

Section IV

References

1. Eldred, K. M., "Review of the Noise Generation of Rockets and Jets," JASA 32 (1502) 1960.

2. Lee, R., et al, "Research Investigation of the Generation and Suppression of Jet Noise," General Electric Co. Report of 16 January 1961 for the Navy Bureau of Weapons.

3. Tyler, J. M. and Perry, E. C., "Jet Noise," Pratt & Whitney Aircraft Report PWA Inst. 451, 1954.

4. Tyler, J. M., "A Jet Exhaust Silencer," Pratt & Whitney Report 469, 30 March 1955.

5. Tyler, J. M., "Suppression of Jet Engine Noise During Ground Running," Pratt & Whitney Report Inst. 483, 16 April 1956.

6. Greatrex, F. B., "Aeronautical Acoustics - in Particular Jet Noise," Journal of the Royal Aeronautical Society, London, April 1954.

7. Greatrex, F. B., "Jet Noise," Fifth International Aeronautical Conference, June 1955.

8. Ciepluch, et al, "Acoustic, Thrust, and Drag Characteristics of Several Full Scale Noise Suppressors for Turbojet Engines," NACA TN 4261, April 1958.

9. Greatrex, F. B., "Noise Suppressors for Avon and Conway Engines," given at ASME Aviation Conference, Los Angeles, 9-12 March 1959.

10. Adams, H. W., "Mechanical Engineer's Solution for Noise Suppression," given at ASME Aviation Conference, Los Angeles, 9-12 March 1959.

11. Koenig, R. J., "Noise Control Measures for Jet Transport Operation," given at ASME Aviation Conference, Los Angeles, 9-12 March 1959.

12. Photograph in Los Angeles Times dated 30 September 1959, Boeing 21 Tube.

13. Westley, R. and Lilley, G. M., "An Investigation of the Noise Field from a Small Jet and Methods for its Reduction," Rep. No. 53, College of Aeronautics, Cranfield, England (1952).

14. Greatrex, F. B., "Engine Noise," Joint Symposium on Aeronautical Acoustics, (London), 21 May 1953.

(continued)

15. Mercer, D. M. A., et al, "The Effect of 'Teeth' on the Noise from a Jet Engine," WADC TR 54-224, September 1954.

16. Callaghan, E. E., et al, "Tooth Type Noise Suppression Devices on a Full Scale Axial Flow Turbojet Engine," NACA RM E54-B01, 29 March 1954.

17. North, W. J., "Summary Evaluation of Toothed Nozzle Attachments as a Jet Noise Suppression Device," NACA TN 3516, July 1955.

18. Coles, W. D., Callaghan, E. E., "Full Scale Investigation of Several Jet Engine Noise Reduction Nozzles," NACA Report 1387, 1958.

19. Laurence, J. C. and Benninghoff, J. M., "Turbulence Measurements in Multiple Interfering Air Jets," NACA TN 4029, December 1957.

20. Laurence, J. C., "Intensity, Scale and Spectra of Turbulence in Mixing Region of Free Subsonic Jet," NACA Report 1292, 1956.

21. Eldred, K. M., "Noise Measurement of Rohr Aircraft Model Jet Nozzles," Paul S. Veneklasen & Associates Report No. 238-11-1, 14 March 1958.

22. Unpublished data in Western Electro-Acoustic Laboratory, Inc., files.

23. Rollin, Vern G., "Effect of Multiple Nozzle Geometry on Jet Noise Generation," NASA TN D-770, September 1961.

24. Dyer, I., Franken, P. A., P. Westervelt, "Jet Noise Reduction by Induced Flow," Journal of the Acoustical Society of America, August 1958, pg. 761.

25. North, W. J., and Coles, W. D., "Effect of Exhaust Nozzle Ejectors on Turbojet Noise Generation," NACA TN 3573, October 1955.

26. Coles, W. D., Mihaloew, J. A., Callaghan, E. E., "Turbojet Engine Noise Reduction with Mixing Nozzle-Ejector Combinations," NACA TN 4317, August 1958.

27. Coles, W. D., Mihaloew, J. A., Swan, W. H., "Ground and Inflight Acoustic Performance Characteristics of Jet Aircraft Exhaust Noise Suppressors," NASA TN-D-874, August 1961.

28. Maglieri, D. J. and Hubbard, H. H., "Preliminary Measurements of the Noise Characteristics of Some Jet Augmented Flap Configurations," NASA Memo p. 2-4-58L, January 1959.

(continued)

29. Fink, M. P., "Aerodynamic Characteristics, Temperature, and Noise Measurements of a Large Scale External Flow Jet Augmented Flap Model with Turbojet Engines Operating," NASA TN D-943.

30. Coles, W. D., "Jet Engine Exhaust Noise from Slot Nozzles," NASA TN D-60, September 1959.

SECTION V

PERFORMANCE ASPECTS OF NOISE SUPPRESSION NOZZLES AND TURBOFAN ENGINES*

The methods for reducing jet noise discussed in the preceding section included mixing nozzles, ejectors, and slot nozzles. These devices have generally been designed to attach to, and "quiet," existing engines. The other way to reduce jet noise, discussed in Section IV, involves design of entirely new turbofan engines. This section discusses the performance gains and penalties inherent in suppression nozzles and a modern turbofan engine.

Suppression Nozzles

The losses in static sea level thrust for mixing nozzles which have been quoted range between 1% and 12% (Refs. 1, 2, 3, 4, 5, 6) with the better thrust nozzles averaging between 1% and 2%. However, the 12-lobe nozzles with and without centerbody, which were among the best noise reduction nozzles and were utilized for the example of figure 84, had static thrust losses (Ref. 2) of 6% and 3%, respectively. The main reason for this thrust loss is probably the induced low static pressures on the rearward canted areas of the nozzle. In addition to thrust losses on the ground, the mixing nozzles are subject to drag penalties in flight of the order of 1% to 3% of total aircraft drag, resulting from base drag losses, increased skin friction and interference between peripheral nozzle elements at high Mach number.

Unfortunately, the optimization of a mixing nozzle for acoustic performance generally degrades its aerodynamic performance. Maximum noise reduction requires increased nozzle envelope area and increased numbers of uniformly distributed smaller elemental nozzles. On the other hand, optimum thrust and drag performance, for other than a circular nozzle, leads toward minimum segmentation, such as a high aspect ratio slot nozzle or a 4-lobe nozzle arranged in a cross. Both of these latter designs can be designed with nozzle thrust coefficients which are practically equal to the standard circular nozzle. Further, both can be designed to avoid the drag penalties of the lobed nozzles caused essentially by "crowding" the boundary layer flow into narrow, rapidly diverging passages. The slot nozzle offers excellent possibilities in tail-mounted twin engine aircraft configurations, with the nozzle itself forming the trailing edge of the engine pylon.

The arrangement of a tail mounted engine, Caravelle style, is aerodynamically not a simple task. The interference between the body and the converging parts of pylon and nacelle, forming diffusers, under the aggravogated conditions of the very thick body

*The major portion of this section was contributed by R. Kosin of Norair Division of Northrop Corporation, who was the consultant for this program in the area of engine and aircraft performance and design.

boundary layer with local Mach numbers close to one, cause high drag, many times as high as the normal friction drag. This condition can be remedied by enlarging and flattening of the "channel" between body and nacelle. This remedy results automatically from a transformation of the standard nozzle or usual multilobe, etc., nozzle, to a slot nozzle extending to the fuselage. Additional improvement results from a reduction of the pylon trailing edge which in turn results automatically with the configuration. A drag estimate without careful wind tunnel tests is of no real value in a discussion of the problem, but to the experienced aircraft engineer, the logic of the thought will be convincing and if he endeavors to improve an aircraft, he might use wind tunnel and analytical work to clarify the problem to the desired degree.

The use of the slot nozzle in connection with the jet flap principle has been suggested by some authors, hoping to draw some additional benefit from the jet flap application. Extensive wind tunnel work by NASA has shown that the jet flap shows worthwhile gains only with high thrust-weight ratios at which a reasonable glide angle cannot be realized. So, at least at present, the slot nozzle in connection with the jet flap has to be discarded from practical considerations.

The addition of an ejector to a mixing nozzle can result in an increase of static thrust of the order of 1% to 3% (Refs. 1, 2) over the thrust of the mixing nozzle alone. Thus, if the mixing nozzle has a thrust loss of 1% to 2%, relative to the standard circular nozzle, the ejector offers the possibility of recovering this entire loss and achieving static thrust values equal to or greater than achieved with the standard nozzle. This thrust augmentation results from the negative axial pressure acting over the nose of the ejector, resulting from the acceleration of the secondary air flowing into the ejector. This advantage in thrust is generally lost as soon as the aircraft has attained a relatively low flight velocity. Furthermore, at higher aircraft cruise velocities, the drag penalties of a fixed ejector are usually high, up to the order of a 7% increase in total aircraft drag (Refs. 1, 5). Therefore, ejectors for subsonic and transonic aircraft should be retracted during cruise. Note that for supersonic cruise a properly designed ejector yielding a convergent-divergent nozzle can be used in flight to improve overall performance. From an overall performance viewpoint the combination of a 4-lobe nozzle with retracting ejector offers an attractive possibility. Further, from the acoustic requirements, although the 4-lobe design without ejector is far from optimum, the 4-lobe nozzle with absorbing ejector could give good acoustic performance, particularly in the near field in the vicinity of the nozzle.

It is clear from this brief discussion that noise suppression nozzles involve performance penalties, at best on the order of 1% in all categories (Ref. 7), for minimal suppressors. Further, these penalties do not include consideration of the reliability of complex nozzle geometry, relative to fatigue. Therefore, it is desirable to examine the turbofan as an alternative method of reducing jet noise.

Turbofan Performance

The results of Section IV demonstrated that large reductions of jet noise can be achieved by reducing the effective jet velocity, utilizing the bypass or turbofan engine. The limit of these reductions is given by machinery noise, combustion noise, and turbulence developed in the engine flow upstream of the nozzle.

The noise of the rotating machinery can be prevented from radiating from the front of the engine by a sonic throat in the air intake, which allows inlet noise reduction to any desirable practical level. A variable (sonic) throat will be required due to the variation of engine mass flow with flight speed and power setting. However, this variable throat is of no greater complexity than ordinarily encountered with a supersonic inlet, and with some aerodynamic development work the efficiency can be kept high enough for all practical purposes. For the part of the machinery noise emanating from the rear end of the engine, no such simple and effective solution is available. If it is necessary to reduce this part of the engine noise, sound attenuation by duct lining with sound absorbing material or resonators seems to be the only practical answer at present. For sound attenuation with a lined duct, maximum duct length is advantageous, therefore front fans will be favorable to reduce noise radiated by the fan to the rear. However, the mechanical solution of front fans with bypass ratios greater than 1.5 or 2 is not simple, because with high bypass ratios the fan should run with a lower speed than the gas generator compressor to avoid excessive fan tip Mach numbers or too low tip Mach numbers for the gas generator compressor will result, i.e. at least two if not three coaxial shafts or a gear assembly will be necessary.

Generally, it can be stated that the machinery noise will go up with increasing bypass ratio (secondary to primary mass flow rate) while the jet noise in turn will be reduced. Therefore, the design of a turbofan engine with a required noise level is basically determined by the selection of the appropriate bypass ratio if all other means of sound attenuation are equally applied. Increasing the bypass ratio of a turbofan engine requires an increase in energy drop in the turbine and therefore decreases the turbine exhaust velocity. At the same time, a lower turbine gas flow is necessary for an equal total net thrust, both influences tending to reduce the turbine exhaust jet noise. On the other hand, an increased amount of bypass air is exhausted at lesser speeds. The foregoing statements hold generally true only in the subsonic regime with today's available turbine temperatures of about 1500° to 1600°F.

With respect to noise in the technically interesting regime the velocity effect outranks by far the effect of the increased mass, such that with increased bypass ratio the jet noise decreases rapidly. The total engine noise would drop, too, if, as mentioned above, the noise of the rotational machinery could be held low or attenuated sufficiently. A reduction of the relative exhaust speed below a value of, say, 600 to 700 ft/sec. at static or takeoff conditions, is considered useless in view of the machinery noise (Ref. 8). This would correspond to a bypass ratio of about 6, thus, with respect to noise reduction, giving one measure of a practical limit to the bypass ratio.

In order to investigate the effect of bypass ratio on the performance parameters of an engine designed with today's technology, a hypothetical engine of 15,000 lbs. static thrust, and 3000 lbs. cruise thrust for Mach .8 at 35,000 ft. altitude, has been developed. The performance of this hypothetical engine has been approximately computed, assuming the present state of the art for materials and uncooled turbines, and almost optimum engine pressure ratios for each case. The curves should be considered as representative values only, because the matching of a multi-spool bypass engine is a very complex process, depending on a great number of variables and chosen conditions.

Figure 91 shows the effect of bypass ratio on both turbine and fan exhaust velocities for the two flight conditions at the stated thrusts. Note that although both velocities drop rapidly with increased bypass ratio, the turbine velocity remains considerably above that of the fan. Therefore, for bypass ratios less than approximately 2, for which r_s/r_p is less than approximately 1.5 the effective velocity for noise generation is close to the primary velocities as shown for constant density coaxial jets in figure 69. Consequently, considerable acoustic improvement would result for the low bypass ratio engines if the primary nozzle were designed as an aerodynamically clean mixing nozzle, for example a 4-lobe nozzle.

Figure 92 gives the net thrust per unit nozzle area, and figure 93 gives the thrust per unit mass flow and the nozzle areas as a function of bypass ratio. The influence of bypass ratio on the power plant weight can be derived from figures 94 through 96. Figure 94 shows the specific static sea level thrust, i.e. static sea level thrust divided by weight, and the total net thrust of bypass engines at static sea level and at Mach 0.8 at 35,000 ft., as compared to the same values of the basic gas generator. In figure 95 the increment in engine size and weight due to bypass ratio for the conditions of equal thrust at Mach 0.8 at 35,000 ft. can be seen. Note that in the comparisons, equal cruise thrust has been selected as the best parameter to be held constant for this study. Figure 95 also shows the accompanying increment in static sea level thrust and the decrease in primary (gas generator) air flow.

The total air flow of the bypass engines, in comparison to the air flow of the jet engine with the same cruise thrust, is shown in figure 96, together with the weight of the installed bypass engines including cowling and jet nozzles in comparison to the jet engine power plant of equal cruise thrust.

To summarize the bypass engine analysis, figure 97 shows the weight expenditure for installed engine, including cowling and cruise fuel, per pound of cruise thrust for three significant flight regimes (medium range, transcontinental and transatlantic). The optimum bypass ratios are about 2, 3 and 4, in that order. As can be seen from figure 95, the takeoff thrust shows a healthy increase with bypass ratio if the cruise thrust (and the throttle ratio) is kept constant. Therefore, the takeoff performances of the airplanes with higher bypass ratios will be more satisfactory from the point of view of safety and increased altitude over nearby neighborhoods.

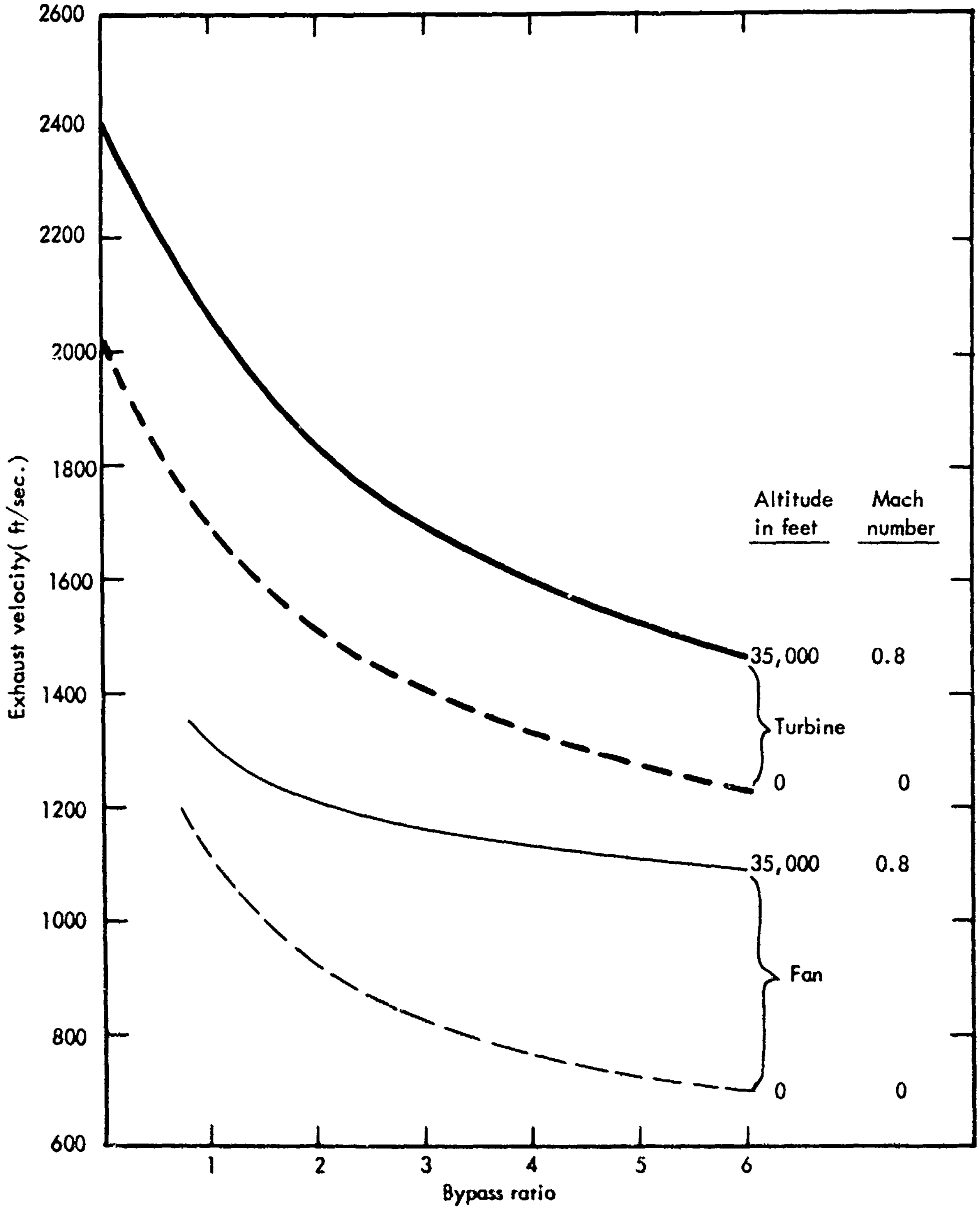

Figure 91. Exhaust velocity for primary flow from turbine and secondary flow from fan as a function of bypass ratio for hypothetical turbofan engine.

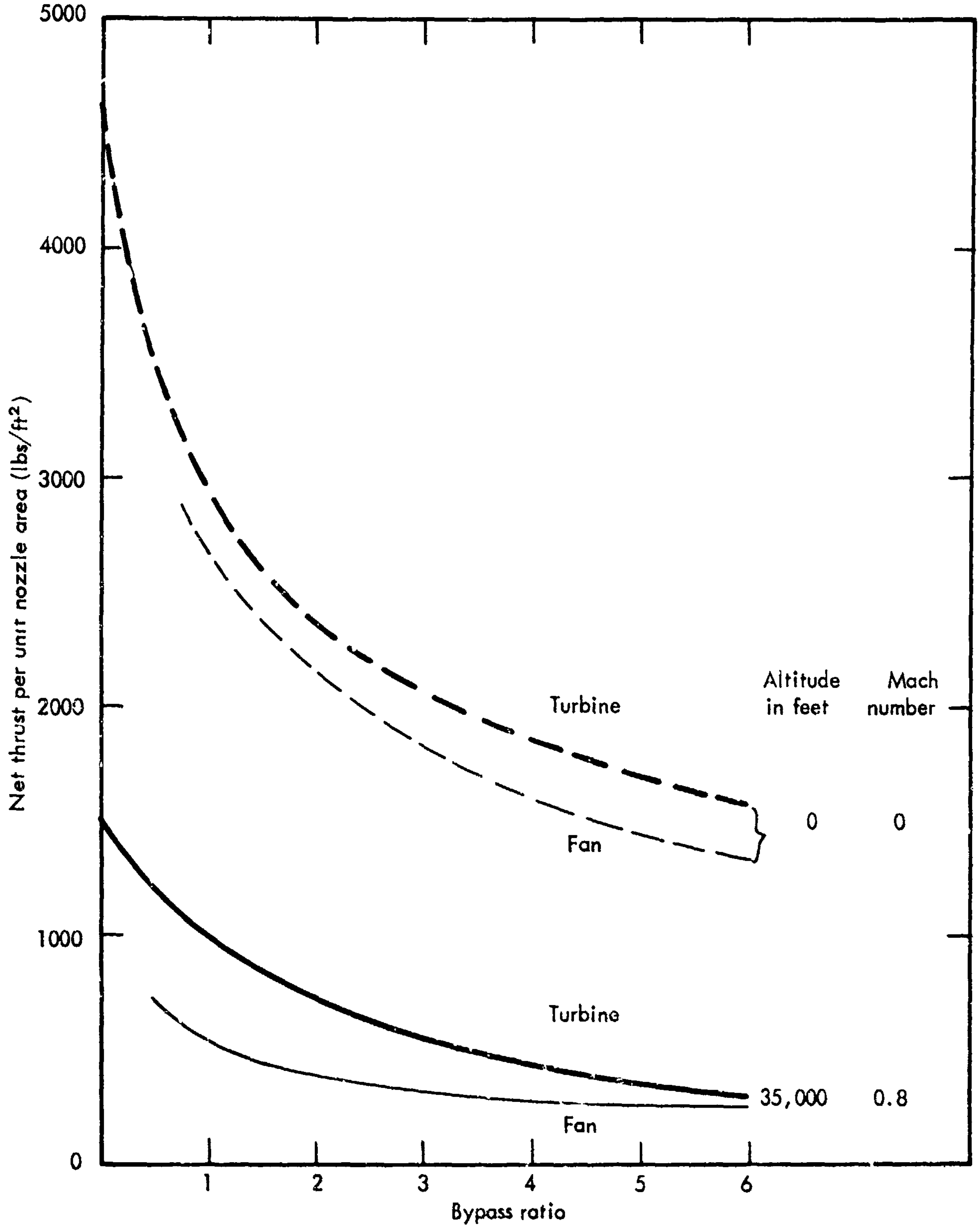

Figure 92. Net thrust per unit nozzle area for primary flow from the turbine and secondary flow from the fan as a function of bypass ratio for a hypothetical turbofan engine.

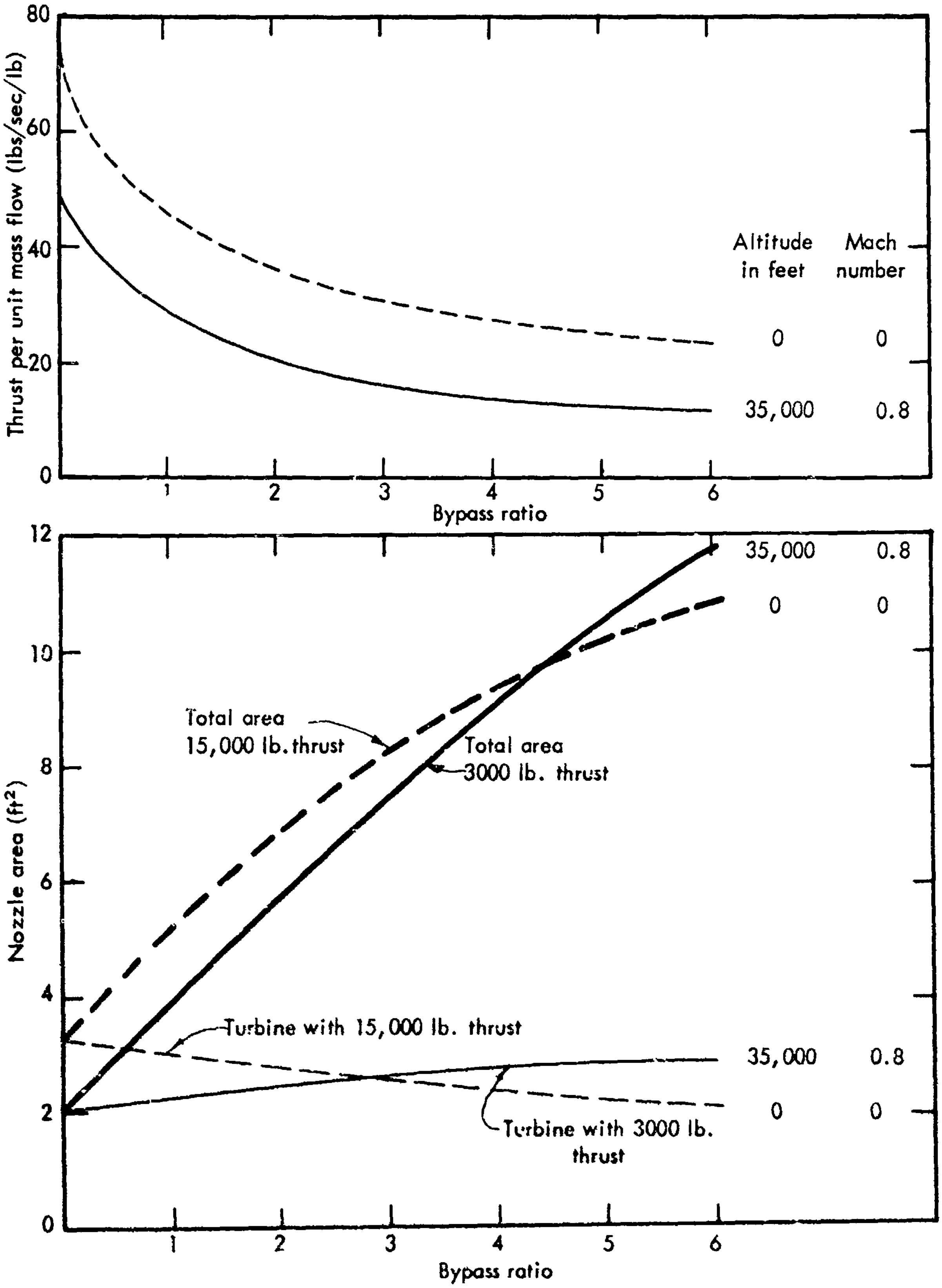

Figure 93. Thrust per unit mass flow and nozzle area for primary flow from the turbine and secondary flow from the fan as a function of bypass ratio for a hypothetical turbofan engine.

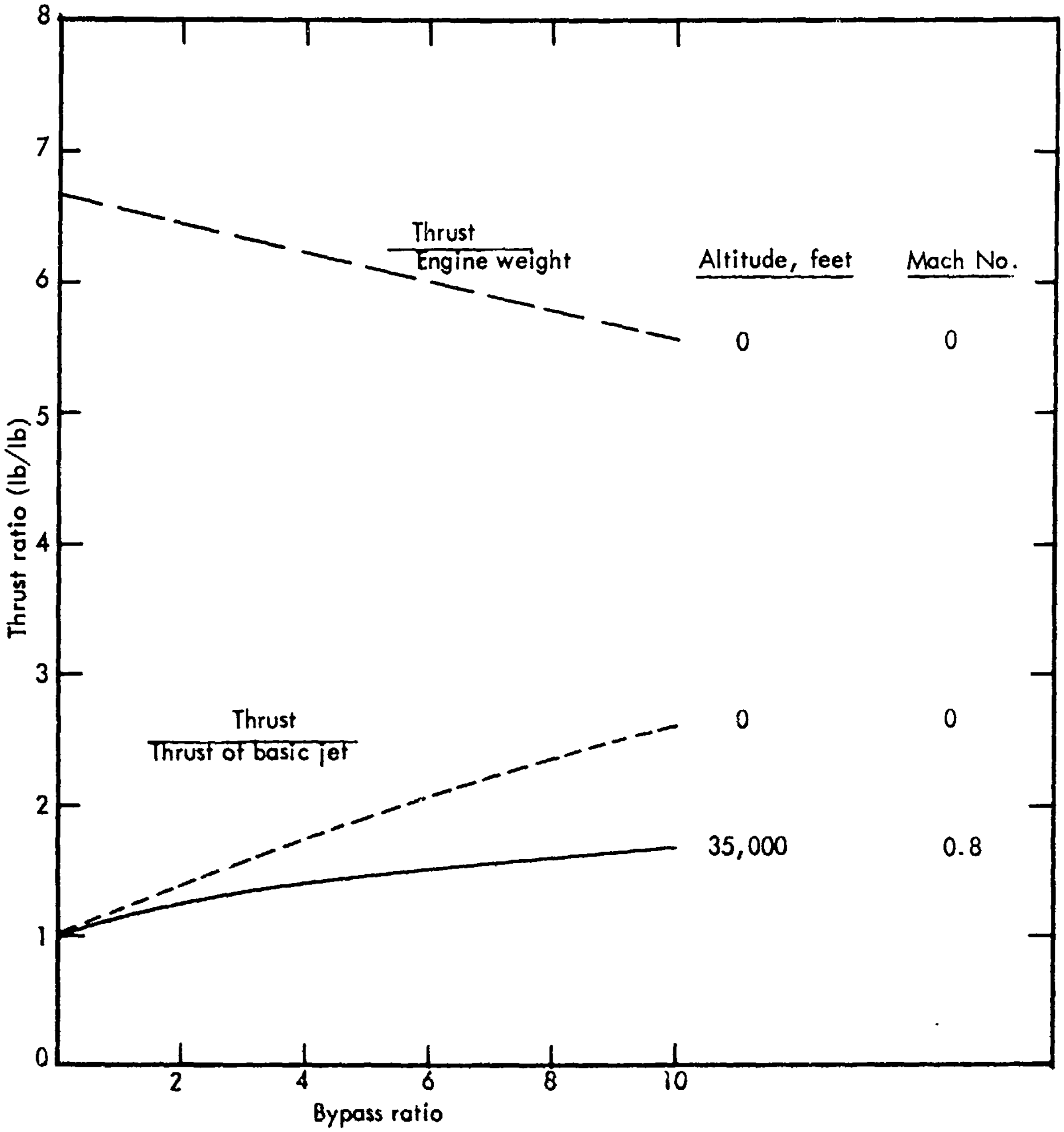

Figure 94. Specific static sea level thrust and ratio of thrust to thrust of basic jet gas generator for constant primary fuel for hypothetical turbofan engine as a function of bypass ratio.

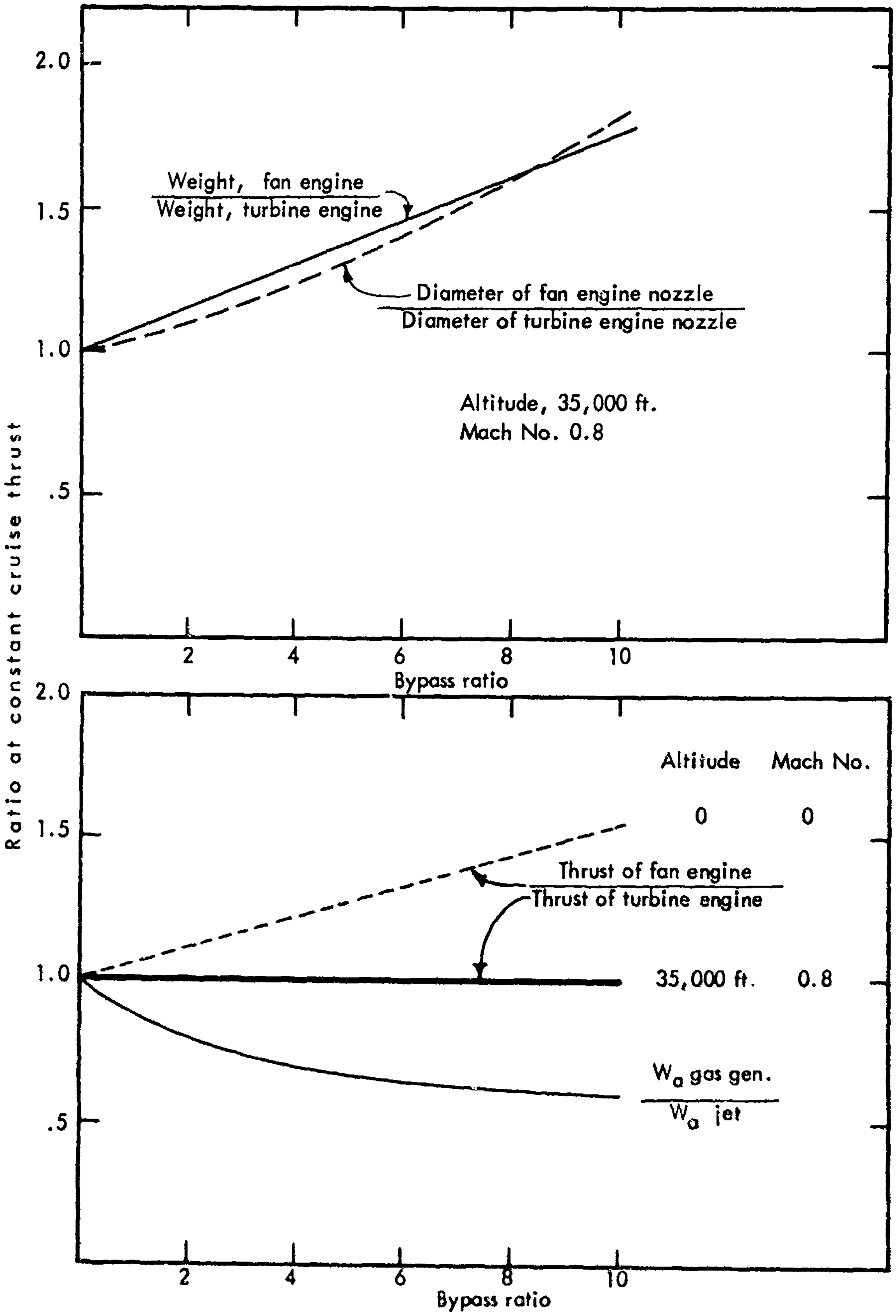

Engines with equal thrust at 35,000 ft altitude, Mach No. 0.8

Figure 95. Relative size and weight, static thrust and primary mass flow for hypothetical turbofan engine which has constant cruise thrust as a function of bypass ratio.

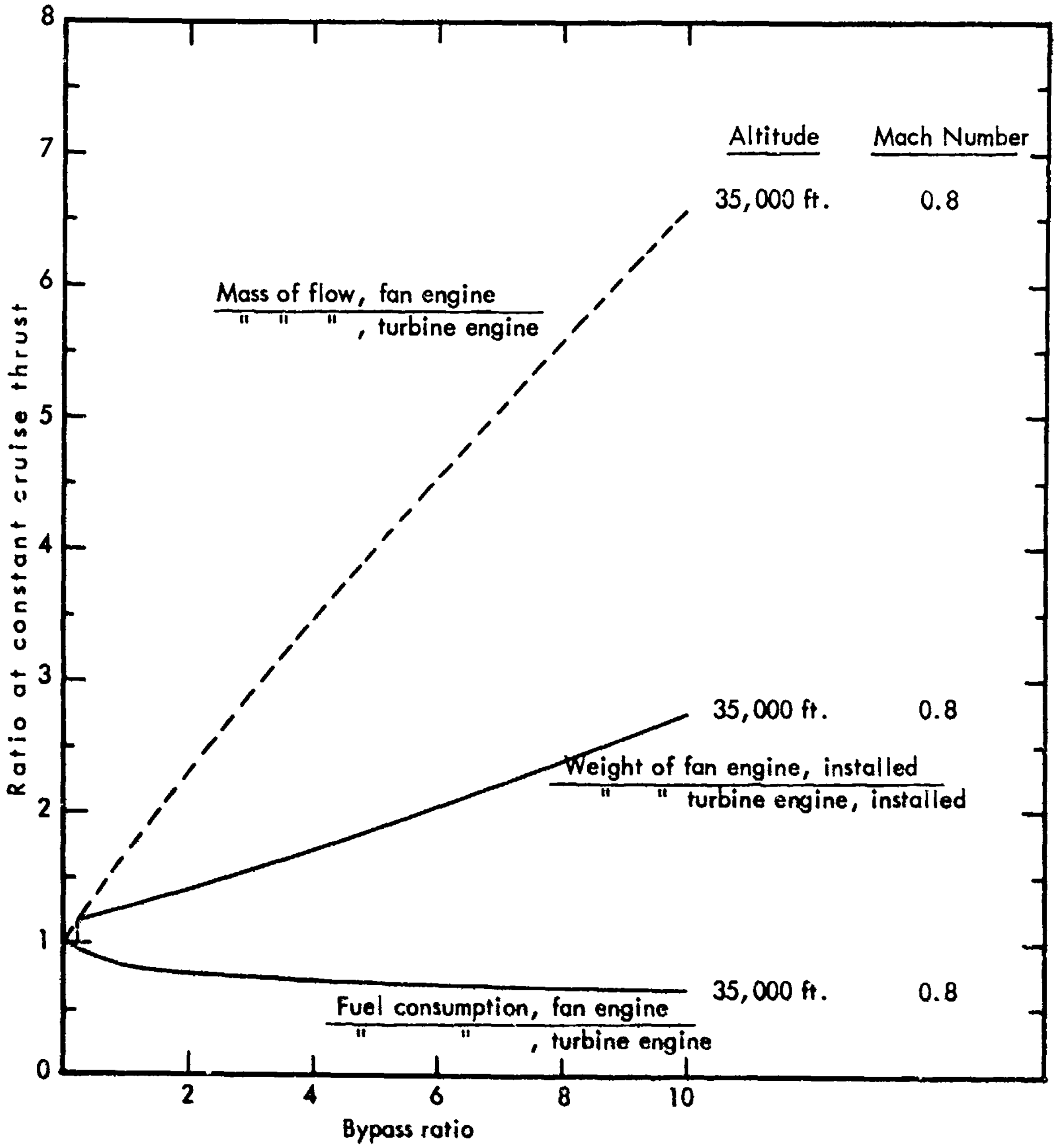

Figure 96. Ratio of total air flow, weight of complete engine including cowling and nozzles, and fuel consumption for hypothetical fan engine to basic turbine engine as a functi n of bypass ratio with cruise thrust held constant.

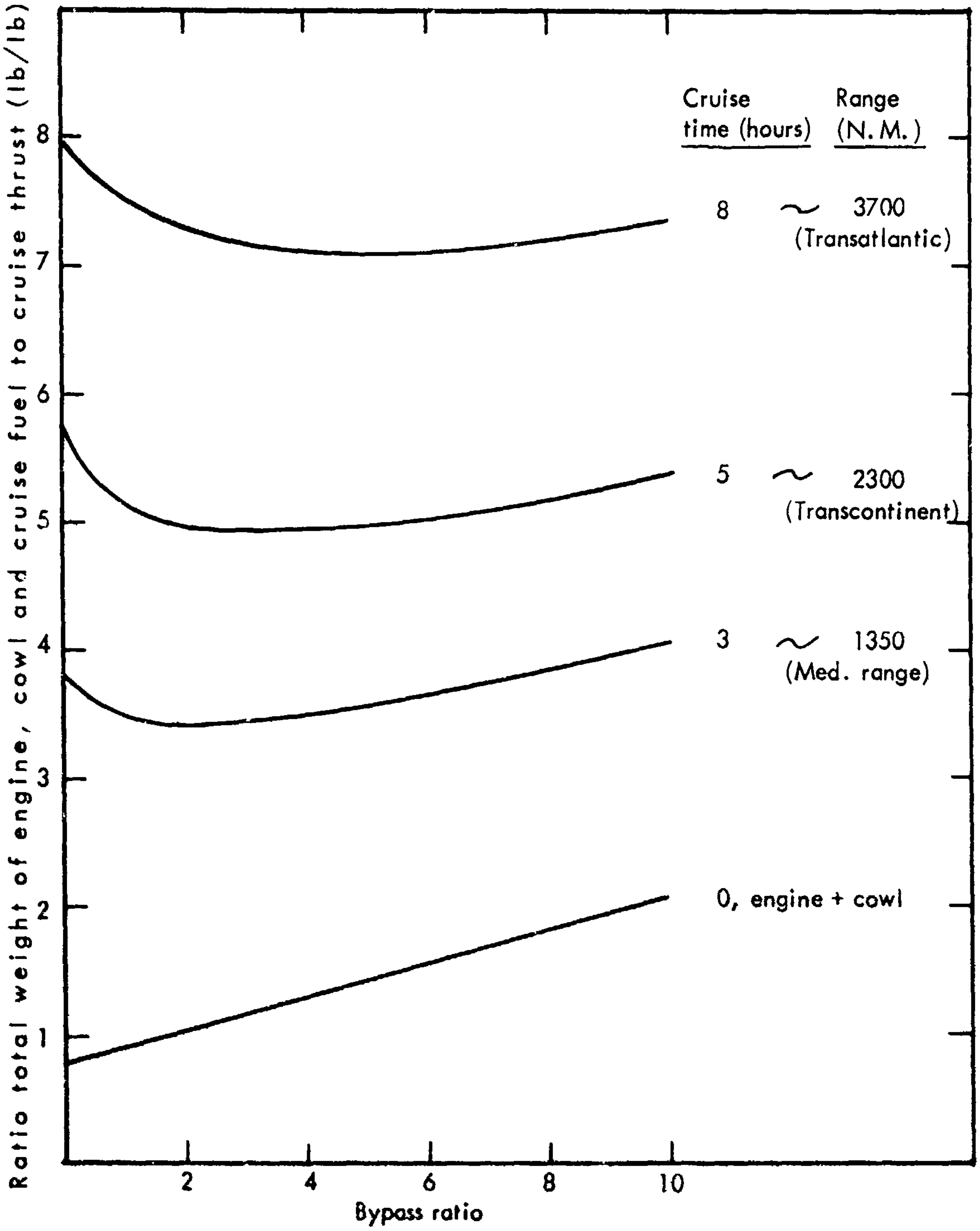

Figure 97. Ratio of total weight of engine, cowl and cruise fuel to cruise thrust as a function of bypass ratio for various length missions for hypothetical turbofan engine.

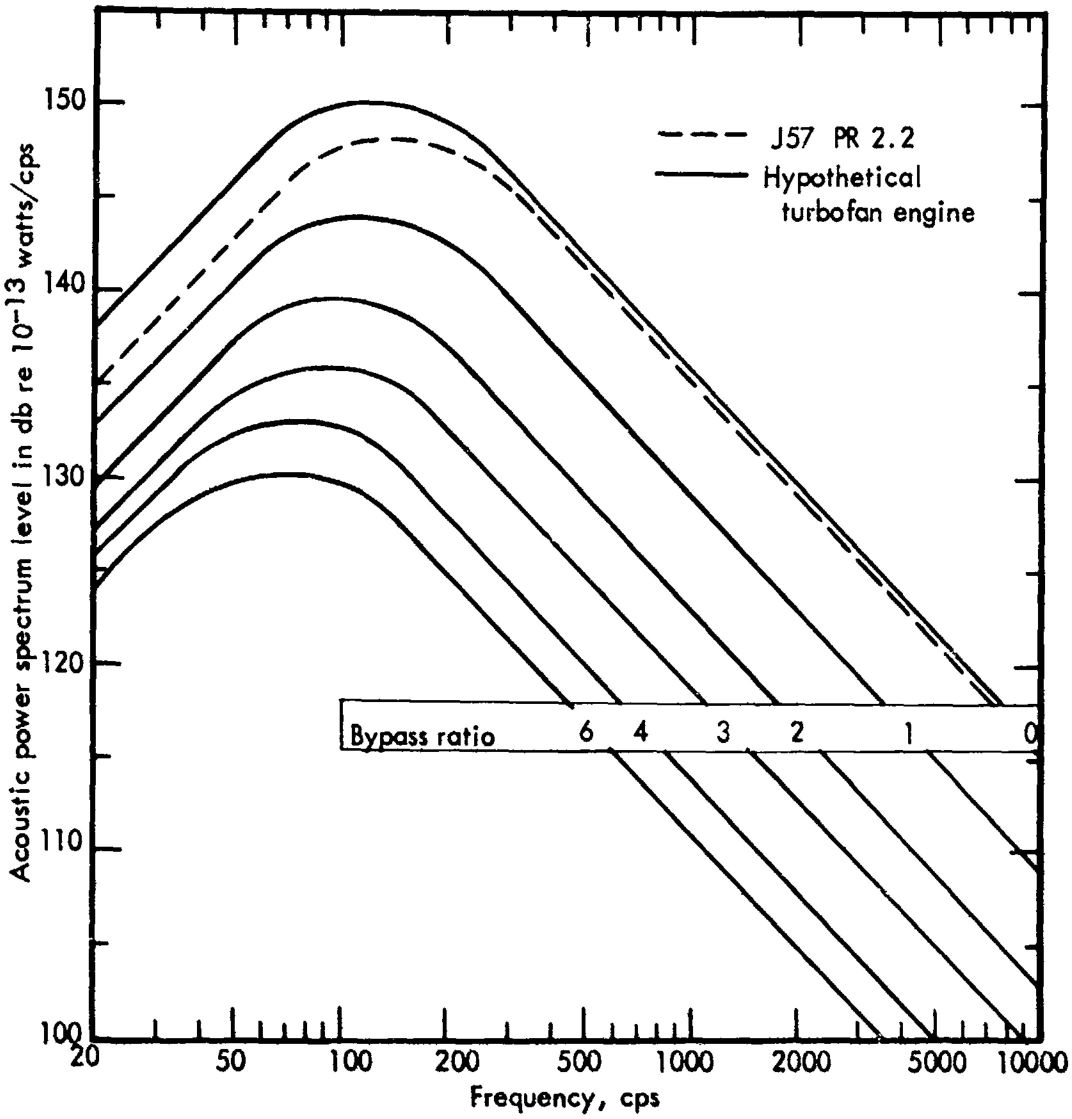

Figure 98. Estimated power spectra of hypothetical turbofan engine scaled to 10,000 lbs. thrust at various bypass ratios compared to standard J57.

In the study for figure 97, the increase in drag with increasing bypass ratio, as well as the decrease in fuel consumption for takeoff, climb, let down, and loiter, have been neglected. It is fair to assume that these influences will balance or tip the scale in favor of the higher bypass ratios. As can be seen from figure 97, a bypass ratio of 3 is no real penalty for the medium range engine, a bypass ratio of 4 is truly acceptable for the transcontinental engine and 5 for the transatlantic engine, if so desired with respect to sound attenuation.

Note that these engine data are not statistical values, but data which could be achieved with engines to be developed with the state of the art of 1962 - 1964, and which do not have the penalty of utilizing existing hardware.

The acoustic performance for a hypothetical bypass engine derived from figures 91 to 94 has been computed by the methods of Section IV, accounting for the variation of density with temperature. The resulting power spectra for an engine scaled at 10,000 lbs. rated thrust are given in figure 98 for various bypass ratios, and the variation of overall power level with bypass ratio is given in figure 99 for several rated static thrusts. Note that these predictions do not include the effect of compressor and fan noise, or combustion noise and internal turbulence. However, for near field application to the sonic fatigue problem the discrete compressor and fan frequencies are above the frequency ration of concern, and any noise resulting from internal turbulence or combustion can probably be adequately controlled to these power levels, if the problem arises.

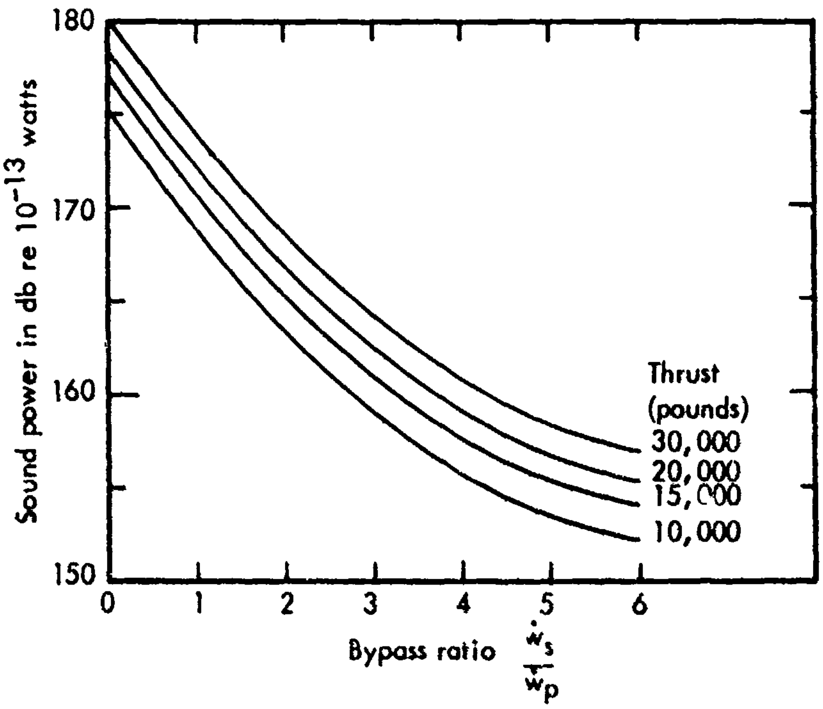

Figure 99. Estimated variation of overall sound power level with bypass ratio for hypothetical turbofan engines scaled to various rated thrusts.

LIST OF SYMBOLS USED IN SECTION V

r	Nozzle radius
w	Weight

Subscripts

a	Airflow
p	Primary flow
s	Secondary flow

SECTION V

References

1. Coles, W. D., Mihaloew, J. A., Swann, W. H., "Ground and Inflight Acoustic Performance Characteristics of Jet Aircraft Exhaust Noise Suppressors," NASA TN D-874, August 1961.

2. Coles, W. D., Mihaloew, J. A., Callaghan, E.E., "Turbojet Engine Noise Reduction with Mixing Nozzle-Ejector Combinations," NACA TN 4317, August 1958.

3. Coles, W. D., Callaghan, E. E., "Full Scale Investigation of Several Jet Engine Noise Reduction Nozzles," NACA Report 1387, 1958.

4. Ciepluch, et al, "Acoustic, Thrust and Drag Characteristics of Several Full Scale Noise Suppressors for Turbojet Engines," NACA TN 4261, April 1958.

5. North, W. J., "Transonic Drag of Several Jet Noise Suppressors," NACA TN 4269, April 1958.

6. Schmeer, J. W., et al, "Transonic Performance Characteristics of Several Jet Noise Suppressors," NASA TN D-388, July 1960.

7. Greatrex, F. B., "Noise Suppressors for Avon and Conway Engines," given at ASME Aviation Conference, Los Angeles, 9-12 March 1959.

8. Wilde, G. L., J.R.A.S. September 1961, page 611.

APPENDIX A

JET FLOW

The noise generating characteristics of a jet are directly related to the jet flow and mixing parameters. Numerous investigators (Refs. 1, 2, 3) have investigated the mixing of a jet issuing from a tiny hole or slot of very small width. These solutions are, in general, applicable to a finite jet in the region well downstream of the core, an axial distance of approximately 1.5 to 2 core lengths. Since the noise from the jet is primarily generated in the mixing region along the core, these downstream solutions are not directly applicable.

A fundamental solution for the core region of an axisymmetric constant velocity jet exhausting into ambient air was given by Kuethe (Ref. 4) and a solution was given by Squire and Trouncer (Ref. 5) for an axisymmetric constant density jet exhausting into a moving airstream. A more recent report by Warren (Ref. 6) considers a supersonic axisymmetric jet of constant enthalpy exhausting into ambient air. Both of the latter investigators assumed a cosine distribution for the velocity profiles which has mathematical advantages, whereas Kuethe developed a more exact asymptotic expression from the basic equations through an iterative procedure. Kuethe's profile fits the data slightly better than the cosine distribution, but is difficult to extend to other cases of interest.

These previous solutions all contain at least one empirical constant, generally derived from constant density flows of very low Mach number. However, examination of various flow data demonstrates a clear Mach effect which decreases the rate of jet spread for increased Mach numbers. Since the jets of primary interest are either sonic or supersonic at the nozzle, it is desirable to incorporate Mach effects into the flow solution. Furthermore, since the effect of a moving airstream, either from forward flight speed or shrouding secondary flow, is of interest to the jet noise problem, it is also desirable to consider this effect together with the Mach effect. In addition, it is also desirable to compare the difference between the flow from a slot nozzle of finite width and the flow of an axisymmetric nozzle.

Therefore, a systematic series of solutions was undertaken to include the flow in the core region from the following:

a. Slot nozzle, zero external velocity, constant density , variable Mach number
b. Axisymmetric nozzle, zero external velocity, constant density, variable Mach number
c. Axisymmetric nozzle, variable external velocity, constant density, variable Mach number

The solutions for the core region were extended downstream to approximate the entire jet flow in order to understand the differing low frequency noise generating mechanisms between slot and axisymmetric jet. It should be noted that complete similarity does not begin until approximately two core lengths downstream. Hence, this extension of the results from the core is only approximately correct in the transition region.

The results of the following derivations are compared to available data and discussed in Section II of the text.

Slot Jet of Constant Density

The steady turbulent flow for the two-dimensional slot jet must satisfy the equation of continuity:

$$\frac{\partial \rho u}{\partial x} + \frac{\partial \rho v}{\partial y} = 0 \tag{A-1}$$

and the Navier Stokes equation:

$$\rho u \frac{\partial u}{\partial x} + \rho v \frac{\partial u}{\partial y} = \frac{\partial \tau}{\partial y} \tag{A-2}$$

where constant pressure is assumed throughout the mixing region and viscous stresses are neglected in comparison to the turbulent stresses. These equations can be combined and integrated with respect to y, (Refs. 5, 7, 8) to give:

$$\frac{\partial}{\partial x}\int_0^Y \rho u^2 dy - u_y \frac{\partial}{\partial x}\int_0^Y \rho u \, dy = \tau_y \tag{A-3}$$

Here, the first term represents the change of momentum with respect to x in a one-half section of the jet bounded by the center plane and the plane y = Y, as shown in figure 100. The second term gives the inward momentum across the plane Y associated with the change in mass flow within the region with respect to x, times the velocity at plane Y. The third term gives the stress acting on the region at plane Y.

This equation can be solved directly by assuming an appropriate velocity profile and determining a suitable expression for τ. The experimental data show that the velocity profiles in the mixing region adjacent to the core are approximately similar when compared to the parameter

$\eta = \frac{y - a}{b}$ for $y \gg a$, and 0 for $y < a$

where a is the outer edge of the core
and b is a width parameter.

The data also indicate, as shown in figure 12 in the body of this report, that the velocity profile is well approximated by an exponential of the form

$$u = u_e e^{-\eta^2/2}$$

This profile was also advanced by Reichardt (Refs. 1, 9) for the downstream region of an axisymmetric jet where complete similarity exists. Because the exponential profile agrees with the data and is convenient to evaluate at the outer boundary, it has been utilized for all of the flow equations in this series.

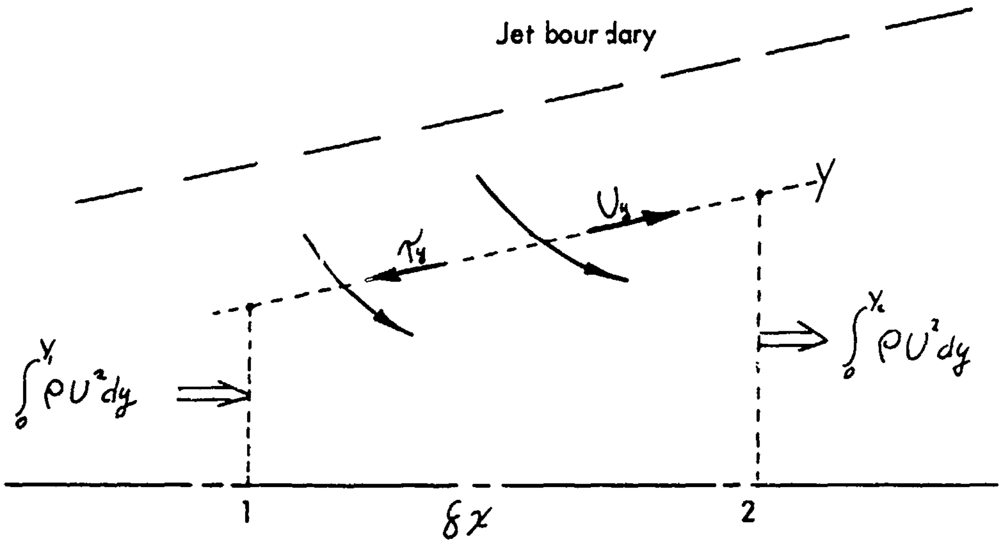

Change in rate of momentum / unit width 1 - 2 $= \int_0^{Y_2} \rho U^2 dy - \int_0^{Y_1} \rho U^2 dy = \delta x \frac{d}{dx} \int_0^{Y} \rho U^2 dy$

Change in rate in momentum / unit width due to inflow of mass across 1—2 $= U_y \left(\int_0^{Y_2} \rho U dy - \int_0^{Y_1} \rho U dy \right) = \delta x \, U_y \frac{d}{dx} \int_0^{Y} \rho U dy$

Change in rate of momentum due to shear stress $= \delta x \, \tau_y$

Figure 100. Balance of momentum rates in jet element.

The shear stress τ equals $-\rho\overline{uv}$ where u and v are the fluctuating turbulent velocities. Prandtl's original mixing length hypothesis (Ref. 1) gives:

$$u \sim v \sim l\frac{dU}{dy}$$

$$\tau \sim \rho l^2 \left|\frac{dU}{dy}\right| \frac{dU}{dy} = \rho k c^2 b^2 \left|\frac{dU}{dy}\right| \frac{dU}{dy}$$

where l, the mixture length, equals cb
and k is an empirical constant of the nature of a correlation coefficient.

Equation (A-3) can be directly evaluated at the outer boundary, Y_o, where

$$U_{y_o} = \tau_{y_o} = 0 \text{ giving } \frac{\partial}{\partial x}\int \rho U^2 dy = 0$$

$$\text{Hence: } \int_0^{y_o} \rho U^2 dy = \text{constant.} \qquad \text{(A-4)}$$

At the nozzle $Y_o = h/2$ where h is the nozzle height, and $U = U_e$ for a rectangular profile. Therefore, the constant is

$$\rho_e U_e^2 \frac{h}{2},$$

which is one-half of the momentum of the jet per unit width.

Substituting the velocity profile in equation (A-4), and noting that the outer boundary can be chosen as ∞ because of the asymptotic nature of the profile, gives

$$\int_0^{\infty} \rho_e U_e^2 e^{-\eta^2} dy = \rho_e U_e^2 \frac{h}{2} \qquad \text{(A-5)}$$

$$\text{which becomes } \int_0^{a} dy + b\int_{\eta=0,\, y=a}^{\infty} e^{-\eta^2} d\eta = \frac{h}{2}$$

$$\text{Integrating: } a + \frac{\sqrt{\pi}}{2} b = \frac{h}{2} \qquad \text{(A-6)}$$

Thus, the edge of the core and all lines of constant U/U_e are straight throughout the region external to the core.

In order to obtain the relationship between a, b and x, equation (A-3) is evaluated at $Y = a + b$, or $\eta = 1$, where the velocity U_y is approximately $.61 U_e$. Substituting the velocity profiles and the expression for τ in equation (A-3) gives:

$$\frac{\partial}{\partial x}\int_0^{a+b} \rho_e U_e^2 e^{-\eta^2} dy - U_e e^{-\frac{1}{2}}\frac{\partial}{\partial x}\int_0^{a+b} \rho_e U_e e^{-\eta^2/2} dy = -k c^2 b^2 \rho U_e^2 \eta^2 \frac{e^{-\eta^2}}{b^2}$$

which becomes

$$\frac{\partial}{\partial x}\left\{\int_0^{a} dy + b\int_{\eta=0, y=a}^{1} e^{-\eta^2} d\eta - .61\int_0^{a} dy - .61\, b\int_{\eta=0, y=a}^{1} e^{-\eta^2/2} d\eta\right\} = -.37 k c^2$$

Integrating: $\frac{\partial}{\partial x}\left[.39 a + .23 b\right] = -.37 k c^2$ (A-7)

Since kc^2 is assumed to be independent of x, equation (A-7) can be directly integrated with respect to x, and the constant can be determined at the nozzle where $b = x = 0$ and $a = h/2$. Therefore, equation (A-7) becomes:

$$a + .59b = -.95\, k\, c^2 x + .5\, h \quad \text{(A-8)}$$

Simultaneous solution of equations (A-8) and (A-6) yields

$$b = 3.2\, k\, c^2 x \quad \text{(A-9)}$$

and the tip of the core, where $a = 0$

$$b = .56\, h$$

$$\frac{x_t}{h} = \frac{.175}{k\, c^2} \quad \text{(A-10)}$$

The constant $(k\, c^2)$ is the single empirical constant required to give the entire flow field adjacent to the core. It can be directly obtained from a measurement of core length, or evaluated indirectly by an empirical determination of ℓ/b and k separately. These approaches are both discussed in connection with the axisymmetric jet solution, and the value of $(k\, c^2)$ is obtained from axisymmetric jet data. The resulting flow field is illustrated in the body of the report and compared with Laurence's measurements (Ref. 8).

This solution for the region adjacent to the core for the constant density slot jet can be extended downstream through the transition region with the assumption that the exponential profile,

remains valid, and where now $\eta = y/b$, since $a = 0$, and U_m is the maximum velocity on the centerline. The solution requires determination of U_m and b as a function of x.

In this downstream region, equation (A-5) becomes

$$\int_0^{\infty} b \rho_e U_m^2 e^{-\eta^2} d\eta = \rho_e U_e^2 \frac{h}{2}$$

Hence: $\sqrt{\pi}\, b\, U_m^2 = U_e^2\, h$ (A-11)

Equation (A-3), evaluated at Y = b, or η = 1, becomes

$$\frac{\partial}{\partial x}\int_0^1 b\, U_m^2 e^{-\eta^2} d\eta - .61\, U_m \frac{\partial}{\partial x}\int_0^1 b\, U_m e^{-\eta^2/2} d\eta = -.37\, k c^2 U_m^2$$

Since bU_m^2 is a constant with respect to x, the first term is zero and the remaining terms give

$$\frac{1}{U_m}\frac{\partial}{\partial x}\left(U_m b\right) = .715\, k c^2$$

Substituting for b from equation (A-11) and differentiating;

$$h\, U_e^2 \frac{dU_m}{U_m^3} = -1.27\, k c^2 dx$$

which integrates to $\left(\frac{U_e}{U_m}\right)^2 = 2.54\, k\, c^2 \frac{x}{h}$ + constant.

The constant can be evaluated at the tip of the core where $U_e = U_m$ by equation (A-10), giving

$$\frac{U_m}{U_e} = \left[1 + 2.54\, k c^2\left(\frac{X - X_t}{h}\right)\right]^{-1/2} \quad \text{(A-12)}$$

and

$$b = .56\left[1 + 2.54\, k c^2\left(\frac{X - X_t}{h}\right)\right] \quad \text{(A-13)}$$

It should be noted that U_m/U_e varies as $x^{-1/2}$ for the slot jet rather than x^{-1} for the axisymmetric jet. This extends the axial length of the mixing zone which is of importance to low frequency noise generation further downstream for the slot jet in comparison with the axisymmetric jet.

Axisymmetric Jet of Constant Velocity

The steady flow for a turbulent axisymmetric jet must satisfy the equation of continuity in cylindrical coordinates:

$$r\frac{\partial \rho U}{\partial x} + \frac{\partial r \rho V}{\partial r} = 0 \quad \text{(A-14)}$$

and the Novier Stokes equation

$$r\rho U\frac{\partial U}{\partial X} + r\rho V\frac{\partial U}{\partial r} = \frac{\partial \tau r}{\partial r} \qquad \text{(A-15)}$$

where constant pressure is assumed throughout the mixing region and the viscous stresses are neglected in comparison to the turbulent stresses. Again, as in the case of the slot jet, these equations can be combined and integrated with respect to r to give:

$$\frac{\partial}{\partial X}\int_0^R \rho U^2 r\,dr - U_R\frac{\partial}{\partial X}\int_0^R \rho U r\,dr = \tau_r R \qquad \text{(A-16)}$$

This result gives the summation of the axial changes of momentum within the region bounded by a conical surface R in the same manner previously described for equation (A-3) for the slot jet.

Following the development of the slot jet, the similarity parameter utilized in expressing the velocity profile is:

$$\eta = \frac{r-a}{b} \quad \text{for } r \gg a \text{, and } = 0 \text{ for } r < a$$

and the velocity profile is given by an exponential

$$U = U_0 + (U_c - U_0)\,e^{-\eta^2/2} = U_0 + U^* e^{-\eta^2/2}$$

where U_0 = the freestream velocity external to the jet.

The shear stress, τ, is also of the same form developed previously, where

$$\tau \sim \rho l^2 \left|\frac{dU}{dr}\right| \frac{dU}{dr}$$
$$= \rho k c b^2 \left|\frac{dU}{dr}\right| \frac{dU}{dr}$$

Equation (A-16) may be directly evaluated at the outer boundary (R_0) of the mixing region where the shear stress $\tau = 0$ and $U_R = U_0$, giving

$$\frac{\partial}{\partial X}\int_0^{R_0} \rho U (U - U_0)\, r\,dr = 0$$

Hence,

$$\int_0^{R_0} \rho U (U - U_0)\, r\,dr = \text{a constant} \qquad \text{(A-17)}$$

At the nozzle $R_o = r_e$ and $U = U_e$ for a rectangular velocity profile. Therefore, the constant is

$$\rho U_e (U_e - U_o)\, r_e^2/2$$

which is the excess jet momentum M, divided by 2π. Substituting the exponential velocity profile, equation (A-17) becomes

$$\int_0^{R_o} \rho\left(U_o + U^* e^{-\eta^2/2}\right) U^* e^{-\eta^2/2}\, r\, dr = \rho\, U_e U^* \frac{r_e^2}{2} = \frac{M}{2\pi}$$

This expands to give

$$\int_0^{a} \rho\, U_e U^* r\, dr + \int_{\eta=0,\, r=a}^{\infty} \rho\, U_o U^* e^{-\eta^2/2} (b\eta + a)\, b\, d\eta$$

$$+ \int_0^{\infty} \rho\, U^{*2} e^{-\eta^2} (b\eta + a)\, b\, d\eta = \rho\, U_e U^* \frac{r_e^2}{2}$$

Integration and rearrangement yields

$$a^2 + 2ab\left[\frac{U_o}{U_e}\sqrt{\frac{\pi}{2}} + \frac{U^*\sqrt{\pi}}{U_e\ 2}\right] + 2b^2\left[\frac{U_o}{U_e} + \frac{U^*}{2U_e}\right] = r_e^2$$

or

$$a^2 + \sqrt{\pi}\,(1.41p + 1)\,ab + \frac{(2p+1)}{m}\, b^2 = r_e^2 \qquad \text{(A-18)}$$

where $p = \dfrac{U_o}{U_e}$

and $m = \dfrac{U_e}{U^*}$

The relationship between a, b and x can be obtained by evaluating equation (A-16) at R = a + b, where $\eta = 1$. Substitution of the exponential profile and the expression for τ in equation (A-16) gives

$$\frac{\partial}{\partial x}\int_0^{a+b}\rho\left[U_o+U^*e^{-\eta^2/2}\right]^2 r\,dr - U_{a+b}\frac{\partial}{\partial x}\int_0^{a+b}\rho\left[U_o+U^*e^{-\eta^2/2}\right] r\,dr$$

$$= -\rho k c^2 U^{*2}\eta^2 e^{-\eta^2}(a+b)$$

which expands to

$$\frac{\partial}{\partial x}\left\{\int_0^a U_e^2 r\,dr + \int_a^{a+b} U_o^2 r\,dr + \int_{\eta=0,\,r=a}^{1} U^* e^{-\eta^2/2}\left[2U_o+U^*e^{-\eta^2/2}\right](b\eta+a)\,b\,d\eta\right\}$$

$$-(U_o+.61U^*)\frac{\partial}{\partial x}\left\{\int_0^a U_e r\,dr + \int_a^{a+b} U_o r\,dr + \int_{\eta=0,\,r=a}^{1} U^* e^{-\eta^2/2}(by+a)\,b\,d\eta\right\}$$

$$= -.37 k c^2 U^{*2}(a+b)$$

Integration and substitution of p and m as in the previous equation results in

$$\frac{\partial}{\partial x}\left\{.195 m a^2 + (.22+.24p)ab + (.077+.085p)b^2\right\}$$

$$= -.37 k c^2 (a+b) \tag{A-19}$$

Simultaneous solution of equations (A-18) and (A-19) is considerably more awkward than in the solution of the final equations for the two-dimensional jet since (b + a) is not necessarily independent of x. It is therefore necessary to evaluate the dependence of (b + a) on x for each value of the velocity ratio (U_o/U_e) for which a solution is obtained.

The remainder of this discussion of the constant density jet is divided into two subsections, the first considering the entire jet flow with zero external velocity, and the second considering the flow in the core region with freestream velocity.

Constant Density Jet with Zero External Velocity

When the freestream velocity U_o is zero, $p = 0$, and m = 1, allowing a considerable simplification of equations (A-18) and (A-19), giving

$$a^2 + \sqrt{\pi}\,ab + b^2 = r_e^2 \tag{A-18a}$$

and

$$\frac{\partial}{\partial x}\left\{.195a^2 + .22ab + .077b^2\right\} = -.37kc^2(a+b) \tag{A-19a}$$

At the nozzle, equation (A-18a) reduces to $a = r_e$, since $b = 0$, and at the tip of the core, where $a = 0$, it reduces to $b = r_e$. Solution of (A-18a) for intermediate values of a and b demonstrates that the value of $(a + b)$ remains within 3% of r_e over the entire range of the core, as shown in figure 101. Hence, equation (A-19a) can be integrated directly to give

$$a^2 + 1.13\,ab + .39b^2 = -1.9kc^2(b+a)x + E$$

At the nozzle $b = x = 0$ and therefore the constant $E = a^2 = r_e^2$. At the tip of the core $a = 0$ and $b = r_e$ and $x = x_t$ so that

$$.61\,r_e = 1.9\,c^2 k\,x_t$$

$$\text{or} \qquad \frac{x_t}{r_e} = \frac{.32}{kc^2} \tag{A-20}$$

In order to give a comparison with the flow from the slot jet downstream of the core, the solution for the constant density axisymmetric jet with zero external velocity is extended. In this downstream region $a = 0$ and hence $\eta = \frac{r}{b}$. Furthermore, the center-line velocity U_m is a function of axial distance and the assumed velocity profile becomes

$$U = U_m e^{-\eta^2/2}$$

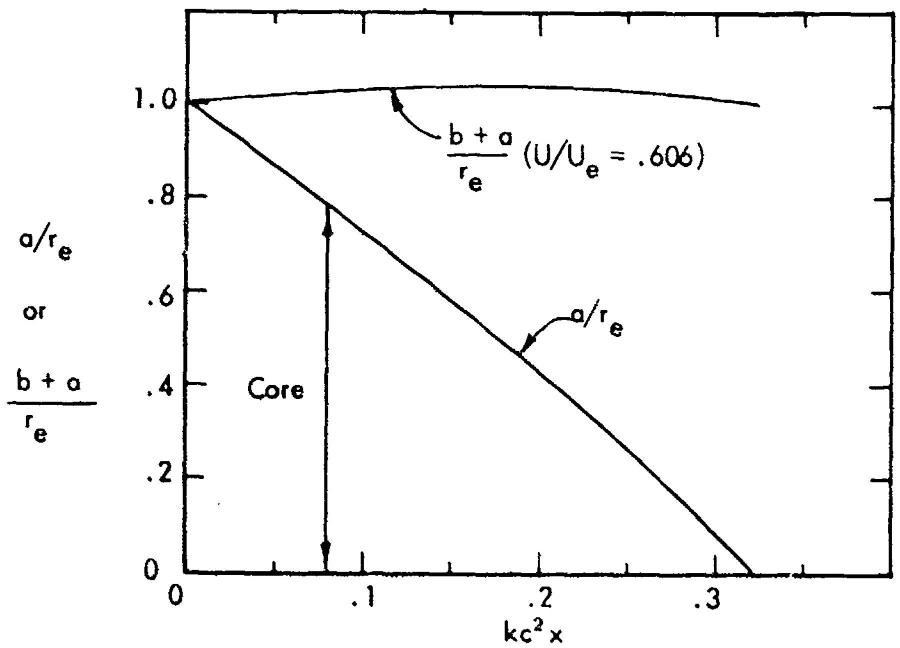

Figure 101. Variation of a and a + b with kc^2x for constant density axisymmetric jet with a zero external velocity.

With this substitution, equation (A-18) gives

$$U_e^2 \, r_e^2 = U_m^2 b \qquad \text{for } X \gg X_t \tag{A-21}$$

where b is clearly the momentum radius at any axial station downstream of the tip.

Similar substitution in equation (A-19) gives

$$\frac{\partial}{\partial X}\left(.315 U_m^2 b^2\right) - .238 U_m \frac{d}{dX}\left(U_m b^2\right) = -.37 kc^2 b\, U_m^2 \tag{A-22}$$

The first term is zero since $U_m^2 b^2$ is proportional to the total momentum which is independent of x. Substitution of equation (A-21) in (A-22) gives

$$\frac{db}{dX} = 1.56\, kc^2$$

which integrates to

$$b = 1.56\, kc^2 X + N$$

The constant N is evaluated at the tip of the core where $x = x_t$ and $U_m = U_c$, with the result that

$$b = \left[1 + 1.56\, kc^2 \left(\frac{X - X_t}{r_e}\right)\right] r_e \tag{A-23}$$

and

$$\frac{U_m}{U_e} = \frac{1}{1 + 1.56\, kc^2 \left(\frac{X - X_t}{r_e}\right)} \tag{A-24}$$

Constant Density Jet with Variable External Velocity

Equations (A-18) and (A-19) can be solved for any value of $U_o/U_e < 1$. When the ratio $U_o/U_e = 1$, no mixing occurs and only parallel flow exists. These intermediate solutions are of particular interest in the region adjacent to the core, since they give the elongation of the jet core for an aircraft in flight, enabling an estimate of the change in noise source location and character. Further, the solutions can also be directly applied to the mixing of concentric jet flows.

The equations were solved for both core length and width at the tip for three intermediate values of U_o/U_e, as given below. In the solution, the variation of (b + a) with x was found to be approximately linear, allowing use of a simple linear correction term in equation (A-19) prior to integration.

Velocity ratio	b at core tip	length of core x_t
0	1.00 r_e	$.32/kc^2$
.25	.92 r_e	$.48/kc^2$
.5	.82 r_e	$.83/kc^2$
.75	.76 r_e	$1.82/kc^2$
1	0.00 r_e	∞

It is clear from the table that the presence of external velocity results in a significant elongation of the jet core, while at the same time reducing its width. Thus, the noise generated by a jet of a moving aircraft is distributed over a considerably greater axial distance in comparison to the static jet, resulting in gross distortions of the near field contours.

LIST OF SYMBOLS USED IN APPENDIX A

Roman

a	Distance from centerline to boundary of core
b	Velocity gradient width parameter
c	ℓ/b
h	Width of rectangle slot jet
k	Proportionality coefficient for shear stress
ℓ	Prandtl mixing length
m	U_e/U^*
p	U_o/U_e
r	Radius
u	rms turbulent velocity
U	Mean flow velocity along the x-axis
V	Mean flow velocity along the y- or r-axis
x	Axial distance from nozzle exit
y	Lateral distance from centerline

Greek

η	Nondimensional radial parameter $\frac{r - a}{b}$
ρ	Density
τ	Shear stress

Subscripts

e	Exit
m	Maximum at a given axial station
o	Condition external to jet flow
t	Core tip

Superscript

$*$	$(U_e - U_o)$

APPENDIX A

References

1. Schlichting, Hermann, "Boundary Layer Theory," Pergamon Press, 1955.

2. Pai, S., "Fluid Dynamics of Jets," vanNostrand Co., 1954.

3. Szablewski, W., "The Diffusion of a Hot Air Jet in Air in Motion," NACA TM 1288, 1960.

4. Kuethe, A. M., "Investigations of the Turbulent Mixing Regions Formed by Jets," Journal of Applied Mechanics, pp A-87 - 95, 1935.

5. Squire, H. B., Trouncer, J., "Round Jets in a General Stream," RAE Report No. Aero. 1904, January 1944.

6. Warren, W. R., "The Mixing of an Axially Symmetric Compressible Jet with Quiescent Air," Aero. Eng. Lab. Report No. 252, Princeton University, September 1953.

7. Goldstein, S., "Modern Developments in Fluid Dynamics," Vol. I, Oxford at the Clarendon Press, 1938.

8. Liepmann, H. W., Laufer, J., "Investigations of Free Turbulent Mixing," NACA Report 1257, 1947.

9. Reichardt, H., "On a New Theory of Free Turbulence," Zamm, Vol. 21, No. 5, October 1941.

10. Laurence, J. C., "Intensity, Scale and Spectra of Turbulence in Mixing Region of Free Subsonic Jet," NACA Report 1292, 1956.

APPENDIX B

DERIVATION OF MODIFIED ACOUSTIC EQUATION FOR TURBULENT JET EXHAUSTS

The purpose of this section is to derive a linear partial differential equation which describes, for an axially uniform jet exhaust, the production of noise by the fluctuating turbulent flow, and the refraction and convection of the resulting acoustic field by the mean flow, the radial mean flow gradient and the radial mean temperature gradient. The derivation proceeds in a straightforward mathematical manner from the equation of mass continuity and the Navier-Stokes equations by considering the pressure, density and velocity at each point in the flow to be a linear superposition of means, fluctuating turbulent perturbations and minute acoustic perturbations. In this analysis the acoustic "particle velocities" and their distortions by refraction in a high shear gradient flow are not neglected as is done in refs. 1 and 3.

It is assumed that sufficiently accurate acoustic field equations can be obtained from the linearization of the fundamental hydrodynamical equations, and that the acoustic forcing function is associated with the small error or imbalance obtained in describing the mean and turbulent flows, less acoustic perturbations, by these flow equations. The scattering of sound is not considered, and this effect is suppressed by neglecting terms in the acoustic field equations which describe the erratic refraction and convection of propagated acoustic waves due to time variations in the flow velocity, velocity gradients and temperature gradients.

In order to obtain a single equation for acoustic pressure or density fluctuations, these linearized field equations must be combined in such a manner as to eliminate (not neglect) the acoustic particle velocities. If the particle velocities are neglected, the low frequency characteristics of the jet exhaust cannot be accurately described. Since only linear operators are involved, this step can be done systematically. However, for the general case, in which axial mean flow gradients are retained, the resulting equation is so formidable as to be of no practical value. When the exhaust is axially uniform, that is, when the axial gradients of mean flow velocity and mean density (associated with mean temperature) are neglected, this equation is considerably simplified and appears to be amenable to solution. Such an approximation is reasonable since the width of the gradient in the thin mixing region around the core increases linearly along the flow axis at an included angle of approximately 5 degrees.

This equation is a third order partial differential equation containing terms which depend directly on the mean velocity gradient magnitudes and which influence both the refraction of sound waves and their production within the turbulent flow. An order of magnitude analysis is presented which shows that such terms are not negligible at the characteristic frequency of the jet and are of greatest importance for the low frequency sound waves. The terms do become negligible, however, for frequencies well above the characteristic jet frequency depending, of course, upon the magnitude of the mean velocity gradient. When these terms are neglected, the acoustic equation reduces precisely to that given by Ribner in Ref. 3.

The papers of Lighthill and Ribner (Refs. 1, 2, 3) are important contributions to the fundamental understanding of jet noise as viewed respectively from the points of view of both quadropole and simple source generation. The above authors begin with the same equation for aerodynamically generated sound, namely

$$\frac{\partial^2 \rho}{\partial t^2} - \nabla^2 P = \frac{\partial^2 T_{ij}}{\partial x_i \partial x_j}$$

$$T_{ij} = \rho v_i v_j + (P - a_o^2 \rho)\delta_{ij} - \left(\eta' + \frac{4}{3}\eta\right)\frac{\partial v_i}{\partial x_j} ,$$

but their use of this equation in defining the jet noise field and estimating the sound levels produced are fundamentally different. Lighthill first notes the quadropole nature of the

forcing function, $\dfrac{\partial^2 T_{ij}}{\partial x_i \partial x_j}$, and takes an integral solution of this equation in the form of Kirchoff's retarded potential solution of electromagnetic theory; and, by several mathematical manipulations, obtains a free field volume integral of $\partial^2 T_{ij}/\partial t^2$. By transferring to a moving "eddy convection" coordinate system, Lighthill obtains the motion correction factor $(1 - M_c \cos \theta)^{-3}$ for a frozen pattern of acoustic quadropoles being axially convected by the flow. Then for high shear gradients, Lighthill approximates $\partial^2 T_{ij}/\partial t^2$ by considering only the predominant mean shear amplification terms,

$$\frac{\partial P}{\partial t}\left[\frac{\partial U}{\partial x_2}, \frac{\partial U}{\partial x_3}\right]$$

This approach leads to several important explanations of the jet noise phenomena; however, this approximation of the integral solution of the above equation constitutes only a first iterative solution for cold jets in which refractive gradient effects were not truly accounted for. Ribner, on the other hand, deals primarily with the above differential equation, rather than an integral equation. With the assumption that the turbulent flow is essentially imcompressible, Ribner is able to represent the sound field as being produced by a convected field of simple sources, a conceptually simpler approach. The equation obtained by Ribner shows more directly than Lighthill's the effects of this convection and the refraction of the sound waves by the mean velocity gradient. By considering special space and time correlation functions for the turbulent flow and by allowing for "pattern fluctuations" of the convected sources, Ribner obtains an explanation of, and is able to eliminate, the infinite amplitude peak associated with Lighthill's motion correction factor $(1 - M_c \cos \theta)^{-3}$. Finally, applying the same restrictive assumption as does Lighthill, Ribner shows the equivalence of the simple source and quadropole concepts in obtaining the famous U^8 law and x° and x^{-7} laws.

In summary, Lighthill's analysis adequately predicts jet noise for low Mach number cold flows where refractive effects are a minimum; in particular, as shown in Ref. 2, the theory gives a good estimation of the noise generated by homogeneous turbulence where there is no mean flow. Ribner's equation (Ref. 3) is considered to be accurate for high frequencies well above the jet characteristic frequency and/or for low shear gradient magnitudes. In this regime, by allowing the speed of sound to vary through the flow according to the variation of the mean temperatures of the flow, the equation adequately describes both the refraction and convection of the sound waves for cold and hot flows. Presently there exists a question as to the effect of Ribner's assumption of incompressibility on the production of noise in a hot flow. The modified acoustic equation derived in this appendix extends the frequency regime down to and below the characteristic frequency of the jet, and adequately describes the convection and refraction of the sound waves propagating through a heavily sheared hot or cold jet flow. The acoustic forcing function is more complicated than those of Lighthill and Ribner, but may simplify upon further analysis and correlation with measured results.

In order to clearly show the differences between the equations of Lighthill and Ribner and the present equation, and in order to fill in the necessary background, a brief mathematical review of the works of Lighthill and Ribner is presented preceding the development of the modified acoustic equation.

Background

The fundamental equations defining the mean fluid flow, turbulence and associated acoustic disturbances in a jet are the equation of mass continuity,

$$\frac{\partial \rho}{\partial t} + \rho \frac{\partial v_j}{\partial x_j} + v_j \frac{\partial \rho}{\partial x_j} = Q \tag{B-1}$$

and the Navier-Stokes equations,

$$\rho\left[\frac{\partial v_i}{\partial t} + v_j \frac{\partial v_i}{\partial x_j}\right] - \eta \nabla^2 v_i - \left(\eta' + \frac{1}{3}\eta\right)\frac{\partial^2 v_j}{\partial x_i \partial x_j} + \frac{\partial P}{\partial x_i} = F_i \tag{B-2}$$

($i = 1, 2, 3$), the summation convention on j being assumed in each case. The turbulent motion of the fluid is initiated by flow instability at the boundary of the laminar flow region and the propagating acoustic perturbations are in turn generated in the turbulence by small imbalances between fluid inertia and internal fluid stress. Thus, there are no external applied forces acting and neither are there actual mass sources and sinks, so that the three force components, F_i, per unit volume, and the mass flow rate, Q, per unit volume may be set equal to zero.

Equations (B-1 and B-2) may be combined to give the momentum equations, by multiplying (B-1) by v_i and adding the resultant equation to (B-2), giving

$$\frac{\partial}{\partial t}(\rho v_i) + \frac{\partial}{\partial x_j}(\rho v_i v_j) - \eta \nabla^2 v_i - \left(\eta' + \frac{1}{3}\eta\right)\frac{\partial^2 v_j}{\partial x_i \partial x_j} + \frac{\partial P}{\partial x_i} = F_i + v_i Q \tag{B-3}$$

($i = 1, 2, 3$), the F_i and Q quantities being retained only for generality.

A partial differential equation for density fluctuations in the fluid may be obtained by first differentiating (B-1) with respect to time,

$$\frac{\partial^2 \rho}{\partial t^2} + \frac{\partial^2}{\partial t \partial x_j}(\rho v_j) = \frac{\partial Q}{\partial t} \tag{B-4}$$

differentiating (B-2) with respect to x_i, and adding the three resultant equations for $i = 1, 2, 3$,

$$\frac{\partial^2}{\partial t \partial x_i}(\rho v_i) + \frac{\partial^2}{\partial x_i \partial x_j}(\rho v_i v_j) - \eta \frac{\partial^3 v_i}{\partial x_i \partial x_j \partial x_j} - \left(\eta' + \frac{1}{3}\eta\right)\frac{\partial^3 v_j}{\partial x_i \partial x_i \partial x_j} + \frac{\partial^2 P}{\partial x_i \partial x_i} = \frac{\partial}{\partial x_i}\left[F_i + v_i Q\right] \tag{B-5}$$

the summation convention now being applied to both i and j ; then subtracting (B-5) from (B-4), giving

$$\frac{\partial^2 \rho}{\partial t^2} = \frac{\partial^2}{\partial x_i \partial x_j}(\rho v_i v_j) + \frac{\partial^2 P}{\partial x_i \partial x_i} - \left(\eta' + \frac{4}{3}\eta\right)\frac{\partial^3 v_i}{\partial x_i \partial x_j \partial x_j} + \frac{\partial Q}{\partial t} - \frac{\partial}{\partial x_i}\left[F_i + v_i Q\right] \tag{B-6}$$

To complete the formulation, the quantity $a_o^2 \nabla^2 \rho$ is subtracted from both sides of (B-6), giving

$$\frac{\partial^2 \rho}{\partial t^2} - a_o^2 \nabla^2 \rho = \frac{\partial^2 T_{ij}}{\partial x_i \partial x_j} + \frac{\partial Q}{\partial t} - \frac{\partial}{\partial x_i}\left[F_i + v_i Q\right] \tag{B-7}$$

where

$$T_{ij} = \rho v_i v_j + (P - a_o^2 \rho)\delta_{ij} - \left(\eta' + \frac{4}{3}\eta\right)\frac{\partial v_i}{\partial x_j} \tag{B-8}$$

$$= \rho v_i v_j + (P - a_o^2 \rho)\delta_{ij} - \eta\left[\frac{\partial v_i}{\partial x_j} + \frac{\partial v_j}{\partial x_i} - \frac{2}{3}\frac{\partial v_k}{\partial x_k}\delta_{ij}\right] - \eta'\frac{\partial v_k}{\partial x_k}\delta_{ij} \tag{B-9}$$

Here, T_{ij}, having the units of stress, is called the stress tensor, and this quantity completely defines the state of internal compressive and shearing stress within the fluid.

Setting F_i and Q equal to zero to obtain now the proper mathematical model for aerodynamically generated sound, (B-7) becomes

$$\frac{\partial^2 \rho}{\partial t^2} - a_o^2 \nabla^2 \rho = \frac{\partial^2 T_{ij}}{\partial x_i \partial x_j} \qquad \text{(B-10)}$$

This is the fundamental equation derived and used by Lighthill in Ref. 1 to study aerodynamic noise generation. It is to be noted that (B-10) is the standard acoustic wave equation, with a forcing function, and thus describes the generation and propagation of sound waves in a uniform medium at rest. Since no assumptions were made in obtaining (B-10), the acoustic field defined by (B-10) is identical to the actual sound field generated by the real turbulent flow.

As discussed in Ref. 1, there are two main advantages of approaching the jet noise problem through (B-10). First, the acoustic disturbances of the fluid are very weak relative to the fluid disturbances generating the noise so that no back-reaction on the main flow is expected by the sound field, and hence it is reasonable to consider the acoustic disturbances as produced by forced oscillations in the fluid as shown in (B-10). Secondly, the complex generation, convection, refraction and scattering of the sound waves by the chaotic turbulent flow can be simplified conceptually to the well known propagation of sound waves through a hypothetical quiescent medium in which equivalent externally applied fluid stresses T_{ij} act. These equivalent stresses are distributed throughout the volume of the turbulent flow field and are essentially zero in magnitude outside this field.

With the particular form of the forcing function of (B-10), Lighthill (Ref. 1) was able to show directly the essential quadropole nature of the generation of sound by the flow field. Of the nine terms in the forcing function, $\partial^2 T_{ij}/\partial x_i \partial x_j$, consider for example the term $\partial^2 T_{12}/\partial x_1 \partial x_2$. This term may be written in the expanded form

$$\begin{aligned} \frac{\partial^2 T_{12}(x_1, x_2, x_3)}{\partial x_1 \partial x_2} = \lim_{\substack{\Delta x_1 \to 0 \\ \Delta x_2 \to 0}} \Big[& (\Delta x_1)^{-1} (\Delta x_2)^{-1} T_{12}(x_1 + \Delta x_1, x_2 + \Delta x_2, x_3) \\ & - (\Delta x_1)^{-1} (\Delta x_2)^{-1} T_{12}(x_1 + \Delta x_1, x_2, x_3) \\ & - (\Delta x_1)^{-1} (\Delta x_2)^{-1} T_{12}(x_1, x_2 + \Delta x_2, x_3) \\ & + (\Delta x_1)^{-1} (\Delta x_2)^{-1} T_{12}(x_1, x_2, x_3) \Big] \end{aligned} \qquad \text{(B-11}$$

Noting that $\partial^2 T_{12} / \partial X_1 \, \partial X_2$ is comparable to $\partial Q / \partial t$ in (B-7), it is clear that each of the four terms in (B-11) is analogous to the time rate of change of the mass flow rate per unit volume of a simple acoustic source. The four simple sources are separated by distances (ΔX_1) and (ΔX_2) lying in the (x_1, x_2) - plane, and hence form a lateral point quadropole in this plane. Similarly for each of the terms in $\partial^2 T_{ij} / \partial X_i \partial X_j$, lateral quadropoles being obtained if $i \neq j$ and longitudinal quadropoles being obtained if $i = j$.

Another principal advantage of (B-10) is that its solution may be set down immediately by use of Kirckhoff's retarded-potential solution of the wave equation, (Ref. 4). This solution has the form

$$\rho(X_i, t) = \rho_0 + \frac{1}{4\pi a_0^2} \int_V \frac{1}{r} \frac{\partial^2 T_{ij}(y_k, t')}{\partial y_i \partial y_j} dV(y_k) + \frac{1}{4\pi} I_s(\rho) \qquad \text{(B-12)}$$

where

$$t' = t - \frac{r}{a_0} \qquad \text{(B-13)}$$

$$r = \sqrt{(x_1 - y_1)^2 + (x_2 - y_2)^2 + (x_3 - y_3)^2} \qquad \text{(B-14)}$$

and where represents the volume of the turbulent flow field, outside of which T_{ij} equals zero. When there are no reflecting surfaces in the sound field generated by the flow, the term $I_s(\rho)$ equals zero, otherwise its value is non zero and is defined by the equation (Ref. 4),

$$I_s(\rho) = \int_S \frac{l_j}{r} \frac{\partial \rho(y_k, t')}{\partial y_j} dS(y_k) + \frac{\partial}{\partial X_j} \int_S \frac{l_j}{r} \rho(y_k, t') \, dS(y_k) \qquad \text{(B-15)}$$

where

$$l_j = \frac{\partial y_j}{\partial n} = \text{direction cosine} \qquad \text{(B-16)}$$

n = coordinate normal to the reflecting surface

and where the two integrals are to be taken over th entire surface of the reflector.

Now expand the following integral

$$\frac{\partial}{\partial x_i}\int_V \frac{1}{r}\frac{\partial T_{ij}(y_k,t')}{\partial y_j}\,dV(y_k) = \int_V \frac{\partial}{\partial x_i}\left(\frac{1}{r}\right)\frac{\partial T_{ij}(y_k,t')}{\partial y_j}\,dV(y_k)$$

$$+\int \frac{1}{r}\frac{\partial T_{ij}(y_k,t')}{\partial y_i\,\partial t'}\frac{\partial t'}{\partial x_i}\,dV(y_k)$$

$$= -\int_V \frac{\partial}{\partial y_i}\left(\frac{1}{r}\right)\frac{\partial T_{ij}(y_k,t')}{\partial y_j}\,dV(y_k)$$

$$-\int_V \frac{1}{r}\frac{\partial T_{ij}(y_k,t')}{\partial y_i\,\partial t'}\frac{\partial t'}{\partial y_i}\,dV(y_k)$$

$$= -\int_V \frac{\partial}{\partial y_i}\left[\frac{1}{r}\frac{\partial T_{ij}(y_k,t')}{\partial y_j}\right]dV(y_k)$$

$$+\int_V \frac{1}{r}\frac{\partial^2 T_{ij}(y_k,t')}{\partial y_i\,\partial y_j}\,dV(y_k)$$

$$= -\int_S \frac{l_i}{r}\frac{\partial T_{ij}(y_k,t')}{\partial y_j}\,dS(y_k)$$

$$+\int_V \frac{1}{r}\frac{\partial^2 T_{ij}(y_k,t')}{\partial y_i\,\partial y_j}\,dV(y_k) \qquad \text{(B-17)}$$

where the divergence theorem is used to obtain the surface integral, and where by definition

$$\frac{\partial^2 T_{ij}(y_k,t')}{\partial y_i\,\partial y_j} \equiv \left.\frac{\partial T_{ij}(y_k,t)}{\partial y_i\,\partial y_j}\right|_{t\rightarrow t-\frac{r}{a_0}}$$

In a similar fashion, the following integral is expanded to give

$$\frac{\partial^2}{\partial x_i \partial x_j}\int_V \frac{1}{r} T_{ij}(y_k, t')\, dV(y_k) = \int_S \frac{l_i}{r} \frac{\partial T_{ij}(y_k, t')}{\partial y_i}\, dS(y_k)$$

$$+ \frac{\partial}{\partial x_i}\int_S \frac{l_j}{r} T_{ij}(y_k, t')\, dS(y_k)$$

$$- \int_V \frac{1}{r} \frac{\partial^2 T_{ij}(y_k, t')}{\partial y_i \partial y_j}\, dV(y_k) \qquad \text{(B-18)}$$

Substitution of (B-18) into (B-12) gives the integral solution in the slightly different but useful form (to be used in applying the motion correction discussed later).

$$\rho(x_i, t) = \rho_0 + \frac{1}{4\pi a_0^2} \frac{\partial^2}{\partial x_i \partial x_j}\int_V \frac{1}{r} T_{ij}(y_k, t')\, dV(y_k)$$

$$+ \frac{1}{4\pi a_0^2} \frac{\partial}{\partial x_i}\int_S \frac{l_j}{r} T_{ij}(y_k, t')\, dS(y_k)$$

$$+ \frac{1}{4\pi a_0^2}\int_S \frac{l_i}{r} \frac{\partial T_{ij}(y_k, t')}{\partial y_j}\, dS(y_k) + \frac{1}{4\pi} I_S(\rho) \qquad \text{(B-19)}$$

Upon neglecting reflecting surfaces (B-19) simplifies to

$$\rho(x_i, t) = \rho_0 + \frac{1}{4\pi a_0^2} \frac{\partial^2}{\partial x_i \partial x_j}\int_V \frac{1}{r} T_{ij}(y_k, t')\, dV(y_k) \qquad \text{(B-20)}$$

which is the form given by Lighthill (Ref. 1).

Performing the differentiation with respect to x_i and x_j on the integrals in (B-19), which differentiations obviously must include the change of t' with x_k, gives the entire integral solution of (B-10) with reflecting surfaces and in terms of the time rates of change of the fluctuating stresses, T_{ij}:

$$\rho(x_i,t) = \rho_0 + \frac{1}{4\pi a_0^4}\int_V \frac{1}{r}\,\frac{(x_i-y_i)(x_j-y_j)}{r^2}\,\frac{\partial^2 T_{ij}(y_k,t')}{\partial t^2}\,dV(y_k)$$

$$-\frac{1}{4\pi a_0^3}\int_V \frac{1}{r^2}\left[\delta_{ij} - \frac{3}{r^2}(x_i-y_i)(x_j-y_j)\right]\frac{\partial T_{ij}(y_k,t')}{\partial t}\,dV(y_k)$$

$$-\frac{1}{4\pi a_0^2}\int_V \frac{1}{r^3}\left[\delta_{ij} - \frac{3}{r^2}(x_i-y_i)(x_j-y_j)\right]T_{ij}(y_k,t')\,dV(y_k)$$

$$+\frac{1}{4\pi a_0^2}\int_S \frac{l_i}{r}\,\frac{\partial}{\partial y_i}\left[T_{ij}(y_k,t') + a_0^2\,\rho(y_k,t')\,\delta_{ii}\right]dS(y_k)$$

$$+\frac{1}{4\pi a_0^2}\,\frac{\partial}{\partial x_i}\int_S \frac{l_j}{r}\left[T_{ij}(y_k,t') + a_0^2\,\rho(y_k,t')\,\delta_{ij}\right]dS(y_k) \qquad \text{(B-21)}$$

This solution (B-21), which is more general than that given by Lighthill (Ref. 1), displays separately the contributions of the turbulent flow to the far field, near field, and near-near acoustic field. The basic result of the Lighthill paper (Ref. 1) consists of the first integral term of (B-21), namely

$$\rho(x_i,t) = \rho_0 + \frac{1}{4\pi a_0^4}\int_V \frac{(x_i-y_i)(x_j-y_j)}{r^3}\,\frac{\partial^2 T_{ij}(y_k,t')}{\partial t^2}\,dV(y_k) \qquad \text{(B-22)}$$

which defines the total radiated sound in the far field of the noise source. For distances which are very large relative to the dimensions of the flow field, this equation can be further simplified to

$$\rho(x_i,t) = \rho_o + \frac{1}{4\pi a_o^4}\frac{x_i x_j}{x^3}\int_V \frac{\partial^2 T_{ij}(y_k,t')}{\partial t^2}\, dV(y_k) \tag{B-23}$$

where

$$x^2 = x_1^2 + x_2^2 + x_3^2 \tag{B-24}$$

Following Lighthill's approach of Ref. 1, a significant simplification of the acoustic forcing function is made based on the following two physical arguments. First, the effect on the propagated sound waves of the small viscous stresses is essentially one of damping, both in the region of turbulent flow and in the uniform medium external to the flow field, so that the equation (B-8) reduces to

$$T_{ij} \approx \rho v_i v_j + (P - a_o^2 \rho)\delta_{ij}$$

Secondly, if the flow is unheated, except for kinematic heating due to pressure fluctuations, the term $(P - a_o^2\rho)$ is nearly equal to zero in the turbulent flow and is exactly zero outside of the turbulent flow. Thus, for "cold flows",

$$T_{ij} \approx \rho v_i v_j \tag{B-25}$$

these being commonly known as the fluctuating Reynold's stresses.

The turbulence in a high velocity jet flow is generated primarily in the thin high-shear region between the conical jet core and the boundary of the jet flow. Statistical analyses show that the measured random velocity fluctuations in a fixed point in this region are partially time-correlated for small time intervals, and that the velocity fluctuations measured at two points, oriented in the direction of the jet flow, are space-correlated for small separation distances. The time correlation at the single point can be transformed to a space correlation by application of a mean flow velocity; and, it is found that with the proper choice of this mean flow velocity, the resulting space correlation curve can be made to fit approximately the space correlation curve obtained from the two-point measurements. It is concluded then that small, but finite, spacial regions exist within the flow over which the turbulent velocity fluctuations are correlated, and that associated with these regions, often called eddies, is a mean downstream convection velocity.

It is clear now that since the fluctuating turbulent velocities are correlated over a so-called eddy volume, the effective acoustic forcing function, $\partial^2(\rho v_i v_j)/\partial y_i \partial y_j$, must similarly be correlated over the same volume, neglecting large fluctuations in fluid density. Thus the volume distribution of quadropole radiators within an eddy volume may be combined to form, approximately, a single eddy quadropole radiator which is convected downstream at some convection velocity, i.e. the velocity correlation curve over the eddy volume is replaced by a square form such that the fluctuating turbulent velocities are perfectly correlated within the eddy volume and perfectly uncorrelated with the velocity fluctuations outside the eddy volume. Each of the point-quadropoles in an eddy then fluctuates in phase with the quadropole at the center of the volume and can be replaced by the center quadropole which is now assumed to have a strength equal to the average quadropole strength times the volume of the eddy. This approach is due to Lighthill (Ref. 1) who further visualizes the jet exhaust as being composed of a set of non-overlapping eddy volumes of the type just defined, and hence as a discrete set of point-quadropoles which are convected downstream at some average eddy convection velocity. The average eddy volume may vary throughout the flow, and as Lighthill points out in Ref. 1, allowance can be made for a variable convection velocity in the flow.

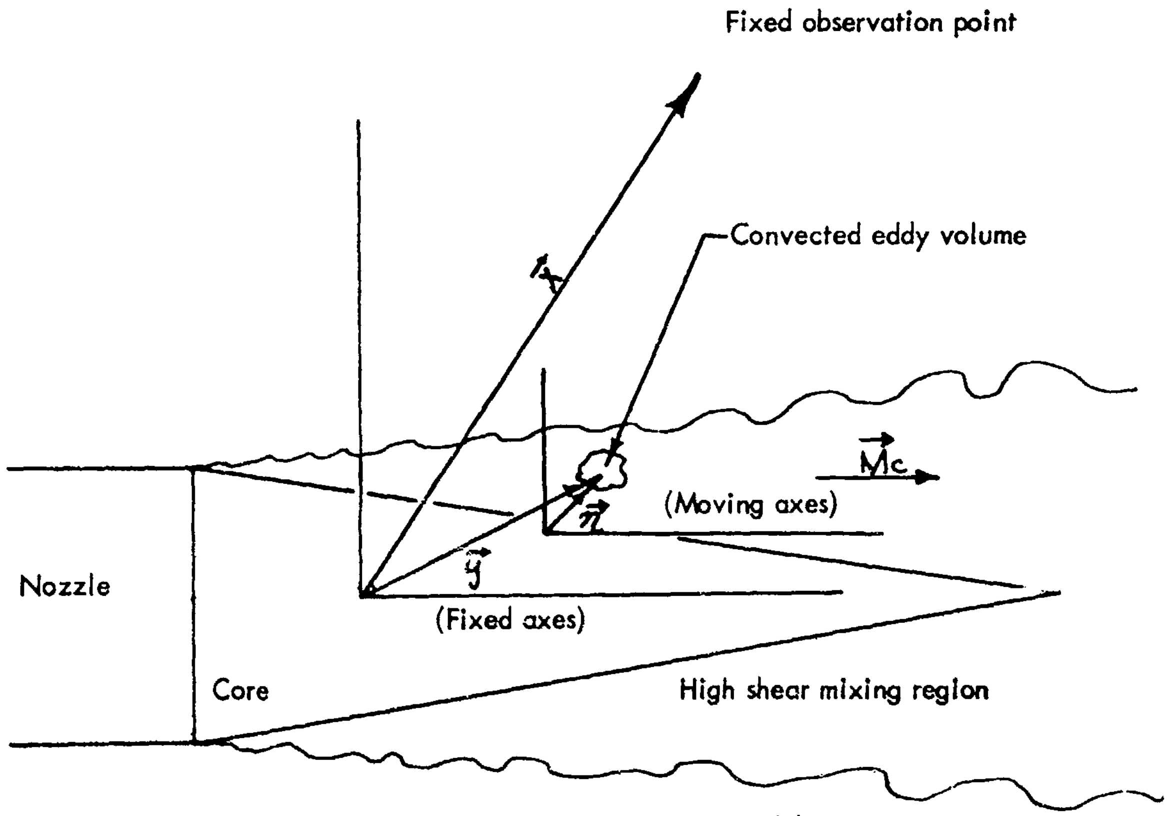

Figure 102. A diagram showing the transformation from fixed (y_k) to moving (η_k) coordinates.

With this idealized acoustical model of the jet exhaust it is possible to separate out the effect on the overall jet sound field, of the convection motion of the quadropole generators. To do this, Lighthill transforms the integrand of the volume integral in (B-20) from the fixed y_K - coordinate system to an η_K - coordinate system which moves with the quadropole radiators at a convection velocity $a_o \vec{M_c}$, where the vector $\vec{M_c}$ is the convection Mach number (see figure 102). Consistent with the retarded potential type solution in a quiescent medium, as given by (B-20), the two coordinate systems are easily related as follows: an acoustic disturbance generated at $\vec{y}$ at time t' by fluctuations in the stresses $T_{ij}(y_k, t')$ will propagate at velocity a_o from $\vec{y}$ to the observation point $\vec{x}$ in the time interval $\frac{r}{a_o}$ where $r = \left|\vec{x} - \vec{y}\right|$. If the time of arrival at $\vec{x}$ is t, then $t = t' + \frac{r}{a_o}$ so that the retarded time t' is, as before

$$t' = t - \frac{r}{a_o} = t - \frac{\left|\vec{x} - \vec{y}\right|}{a_o}$$

At this time t, the position of the element of volume $dV(y_k)$ from which the acoustical signal emanated is

$\vec{y} - (a_o\vec{M}_c)\frac{r}{a_o}$ or $\vec{y} + \vec{M}_c\, r$. If $\vec{\eta}$ denotes the fixed position vector of this same element of volume referred to the η_k - coordinate system, and if it is assumed that at time t the η_k - and y_k - coordinate systems are coincident, then

$$\vec{\eta} = \vec{y} + \vec{M}_c\, r \tag{B-26}$$

The stress tensor associated with the moving volume element is then written, in the retarded time form of (B-12) as

$$T_{ij}\left(\eta_k, t - \frac{r}{a_o}\right) \text{ or } T_{ij}\,(\eta_k, t').$$

The moving volume element $dV(y_k)$ is transformed to the volume element $dV(\eta_k)$ fixed in the η_k - coordinate system by the Jacobian of the transformation in (B-26). This Jacobian, J, equals the determinant of the transformation matrix:

$$\left[d\eta_i\right] = \left[\frac{\partial \eta_i}{\partial y_j}\right] \cdot \left[dy_j\right] = J \cdot \left[dy_j\right]$$

$$\begin{bmatrix} d\eta_1 \\ \\ d\eta_2 \\ \\ d\eta_3 \end{bmatrix} = \begin{bmatrix} \left[1 - \frac{M_{c1}}{r}(x_1 - y_1)\right] & -\frac{M_{c1}}{r}(x_2 - y_2) & -\frac{M_{c1}}{r}(x_3 - y_3) \\ \\ -\frac{M_{c2}}{r}(x_1 - y_1) & \left[1 - \frac{M_{c2}}{r}(x_2 - y_2)\right] & -\frac{M_{c2}}{r}(x_3 - y_3) \\ \\ -\frac{M_{c3}}{r}(x_1 - y_1) & -\frac{M_{c3}}{r}(x_2 - y_2) & \left[1 - \frac{M_{c3}}{r}(x_3 - y_3)\right] \end{bmatrix} \begin{bmatrix} dy_1 \\ \\ dy_2 \\ \\ dy_3 \end{bmatrix}$$

Evaluating the determinant gives

$$J = 1 - \frac{M_{ck}}{r}(x_k - y_k) = 1 - \frac{\vec{M}_c \cdot (\vec{x} - \vec{y})}{\vec{x} - \vec{y}} \tag{B-27}$$

Since

$$dV(\eta_k) = J\, dV(y_k)$$

then

$$\frac{dV(y_k)}{r} = \frac{dV(\eta_k)}{|\vec{x} - \vec{y}| - \vec{M}_c \cdot (\vec{x} - \vec{y})} \tag{B-28}$$

Thus, for a reflection-free sound field, (B-20) becomes

$$\rho(x_i, t) = \rho_o + \frac{1}{4\pi a_o^2} \frac{\partial^2}{\partial x_i \partial x_j} \int_V T_{ij}(\eta_k, t') \frac{dV(\eta_k)}{|\vec{x} - \vec{y}| - \vec{M}_c \cdot (\vec{x} - \vec{y})} \tag{B-29}$$

In order to obtain a form comparable to (B-22), the integrand of (B-29) is differentiated with respect to x_i and x_j assuming that the η_k are fixed. From the definition of r

$$\frac{\partial r}{\partial x_i} = \frac{(x_k - y_k)}{r} \frac{\partial (x_k - y_k)}{\partial x_i}$$

$$= \frac{(x_k - y_k)}{r}\left[\delta_{ki} - \frac{\partial y_k}{\partial x_i}\right]$$

$$= \frac{(x_i - y_i)}{r} - \frac{(\vec{x} - \vec{y}) \cdot \partial \vec{y} / \partial x_i}{r} \tag{B-30}$$

and from the coordinate transformation

$$\vec{\eta} = \vec{y} + \vec{M}_c r$$

$$\frac{\partial \vec{y}}{\partial x_i} = -\vec{M}_c \frac{\partial r}{\partial x_i} \tag{B-31}$$

Combining (B-30) and (B-31) gives

$$\frac{\partial r}{\partial x_i} = \frac{x_i - y_i}{|\vec{x} - \vec{y}| - \vec{M}_c \cdot (\vec{x} - \vec{y})} \tag{B-32}$$

Also

$$\frac{\partial}{\partial x_i}\left[\vec{M}_c \cdot (\vec{x} - \vec{y})\right] = M_{ck}\left[\delta_{ki} - \frac{\partial y_k}{\partial x_i}\right] =$$

$$M_{ci} - \vec{M}_c \cdot \frac{\partial \vec{y}}{\partial x_i} = M_{ci} + M_c^2 \frac{\partial r}{\partial x_i} \tag{B-33}$$

Combining (B-32) and B-33) gives

$$\frac{\partial}{\partial x_i}\left[\left|\vec{x}-\vec{y}\right| - \vec{M}_c \cdot (\vec{x}-\vec{y})\right] = M_{ci} + \frac{(1 - M_c^2)(x_i - y_i)}{\left|\vec{x}-\vec{y}\right| - \vec{M}_c \cdot (\vec{x}-\vec{y})} \tag{B-34}$$

With(B-32) and B-34), the differentiation of (B-29) can proceed directly, giving

$$\rho(x_i,t) = \rho_o + \frac{1}{4\pi a_o^4}\int_V \frac{(x_i-y_i)(x_j-x_j)}{R^3} \frac{\partial^2 T_{ij}(\eta_\kappa,t')}{\partial t^2} dV(\eta_\kappa)$$

$$- \frac{1}{4\pi a_o^3}\int_V \left[\frac{\delta_{ij}}{R^2} + 2\,\frac{M_{ci}(x_j-y_j)+M_{cj}(x_i-y_i)}{R^3}\right.$$

$$\left. - \frac{3(1-M_c^2)(x_i-y_i)(x_j-y_j)}{R^4}\right] \frac{\partial T_{ij}(\eta_\kappa,t')}{\partial t} dV(\eta_\kappa)$$

$$- \frac{1}{4\pi a_o^2}\int_V \left[\frac{(1-M_c)^2\delta_{ij}-2M_{ci}M_{cj}}{R^3} + 3(1-M_c^2)\frac{M_{ci}(x_j-y_j)+M_{cj}(x_i-y_i)}{R^4}\right.$$

$$\left. - \frac{3(1-M_o^2)(x_i-y_i)(x_j-y_j)}{R^5}\right] T_{ij}(\eta_\kappa,t')\, dV(\eta_\kappa) \tag{B-35}$$

where

$$R = \left|\vec{x}-\vec{y}\right| - \vec{M}_c \cdot (\vec{x}-\vec{y}) \tag{B-36}$$

Letting the observation point $\vec{x}$ recede to the far field of each of the moving quadropoles in the jet gives

$$\rho(x_i,t) = \rho_o + \frac{1}{4\pi a_o^4}\int_V \frac{(x_i-y_i)(x_j-y_j)}{R^3} \frac{\partial^2 T_{ij}(\eta_\kappa,t')}{\partial t^2} dV(\eta_\kappa) \tag{B-37}$$

since the second and third integrals represent near field and near-near field contributions which fall off to negligible magnitudes in the far field. (B-37) is the result given by Lighthill (Ref. 1).

If $|\vec{x}| \gg |\vec{y}|$ (B-37) can be further reduced to

$$\rho(x_i,t) = \rho_o + \frac{1}{4\pi a_o^2} \frac{x_i x_j}{x^3(1-M_c \cos\theta)^3} \int_V \frac{\partial^2 T_{ij}(\eta_\kappa, t')}{\partial t^2} dV(\eta_\kappa) \quad \text{(B-38)}$$

where θ is the angle between the jet axis and the observation position vector $\vec{x}$. Comparison of (B-38) with (B-23) shows that the effect of the quadropole convection on the far field acoustic amplitude is represented by the factor $(1 - M_c \cos\theta)^{-3}$. Lighthill points out in Ref. 1 that at low Mach numbers the difference between the integral in (B-23) and that of (B-38) is simply one of space variation due to the motion of the η_κ - axes in the latter case. He argues that this space variation effectively constitutes a field of octopole generators. Since the radiation efficiency of these octopoles is significantly less than quadropoles, the former may be neglected and the two integrals of (B-23) and (B-38) are, to sufficient accuracy, identical in magnitude. Thus $(1-M_c \cos\theta)^{-3}$ is the only correction factor that needs to be considered.

As a final comment on Lighthill's approach to jet noise, the importance of the velocity gradients in amplifying the sound generated in the flow is now considered. The first time derivative of T_{ij} may be written in the convenient form, noting the form of T_{ij} given in (B-25),

$$\frac{\partial T_{ij}}{\partial t} = \frac{\partial}{\partial t}(\rho v_i v_j) = v_j \frac{\partial(\rho v_i)}{\partial t} + v_i \frac{\partial(\rho v_j)}{\partial t} - v_i v_j \frac{\partial \rho}{\partial t} \quad \text{(B-39)}$$

For unforced aerodynamic flow in which viscous stresses may be neglected, the equation of momentum (B-3) may be written in the simpler form

$$\frac{\partial(\rho v_i)}{\partial t} + \frac{\partial(\rho v_i v_\kappa)}{\partial x_\kappa} + \frac{\partial P}{\partial x_i} = 0$$

or

$$\frac{\partial(\rho v_i)}{\partial t} + \frac{\partial(\rho v_i v_\kappa + P\delta_{i\kappa})}{\partial x_\kappa} = 0 \quad \text{(B-40)}$$

Also, (B-1) can be written in the more convenient form

$$\frac{\partial \rho}{\partial t} + \frac{\partial(\rho v_\kappa)}{\partial x_\kappa} = 0 \quad \text{(B-41)}$$

Substitution of (B-40) and (B-41) into (B-39) gives

$$\frac{\partial T_{ij}}{\partial t} = - v_j \frac{\partial(\rho v_i v_k + P\delta_{ik})}{\partial x_k} - v_i \frac{\partial(\rho v_j v_k + P\delta_{jk})}{\partial x_k} + v_i v_j \frac{\partial(\rho v_k)}{\partial x_k}$$

which, upon combining and rearranging the derivatives, gives

$$\frac{\partial T_{ij}}{\partial t} = P\delta_{ik}\frac{\partial v_j}{\partial x_k} + P\delta_{jk}\frac{\partial v_i}{\partial x_k} - \frac{\partial}{\partial x_k}\left(\rho v_i v_j v_k + P\delta_{ik} v_j + P\delta_{jk} v_i\right) \tag{B-42}$$

Since the last three terms of (B-42) are pure space derivatives, these represent octopole contributions to radiation field and may therefore be neglected. The significant portion of $\partial T_{ij}/\partial t$ thus reduces to

$$\frac{\partial T_{ij}}{\partial t} = P\left[\frac{\partial v_j}{\partial x_i} + \frac{\partial v_i}{\partial x_j}\right] = P e_{ij} \tag{B-43}$$

where e_{ij} is called the space rate of strain tensor.

(B-43) has been derived using the fixed y_k - coordinates or its equivalent, the fixed x_k - coordinates. It would seem more correct, however, to use the moving η_k - coordinates since these appear in the argument of T_{ij} in (B-38). In this case

$$\frac{dT_{ij}}{dt} = \frac{\partial(\rho v_i v_j)}{\partial t} + a_o M_{ck}\frac{\partial(\rho v_i v_j)}{\partial x_k} \tag{B-44}$$

It is seen immediately, however, that the added term is a pure space derivative and also represents an octopole contribution to the sound field and may thus be neglected. This agrees with Lighthill's conclusion that the volume integrals appearing in (B-23) and (B-38) can, for all practical purposes, be considered equal, since their intergrands are approximately equal.

Since high velocity jet flows into free air are characterized by large mean shear gradients, it is clear that for a mean flow of velocity U in the x_1 direction and mean velocity gradients in the x_2 and x_3 directions, the predominant terms in $\partial T_{ij}/\partial t$ are

$$\frac{\partial T_{ij}}{\partial t} = P\bar{e}_{ij} \tag{B-45}$$

where $\bar{e}_{ij}$ is the mean strain rate tensor, or

$$\frac{\partial T_{12}}{\partial t} = P\bar{e}_{12} = P\frac{\partial U}{\partial x_2} \tag{B-46}$$

$$\frac{\partial T_{13}}{\partial t} = P\bar{e}_{13} = P\frac{\partial U}{\partial x_3} \tag{B-47}$$

These two tensor elements can, for say a cylindrical jet exhaust, be combined into a single radial term

$$\frac{\partial T}{\partial t} = P\frac{\partial U}{\partial r}$$

r being the polar coordinate measured perpendicular to the axis of flow.

Substitution of (B-45) into (B-38) gives

$$\rho(x_i,t) = \rho_o + \frac{1}{4\pi a_o^4}\,\frac{x_i\,x_j}{x^3(1-M_c\cos\theta)^3}\int_V \bar{e}_{ij}\,\frac{\partial P(y_k,t')}{\partial t}\,dV \tag{B-48}$$

It is now clear that the effect of a mean shear is to amplify the pressure fluctuations generated at a point in the flow, in proportion to the magnitude of the mean shear gradient.

It is not desirable to carry the Lighthill discussion further, as it would be necessary to introduce acoustic intensity and total acoustic power and to enter into a detailed consideration of statistical analysis of space and time correlations. For the present purpose, the above discussion presents the essential features of Lighthill's approach to aerodynamically generated sound.

The recent approach given by Ribner in Ref. 3 differs from Lighthill in several respects and presents several new and interesting features. Ribner begins with Lighthill's equation (B-10) above, with T_{ij} defined as in (B-25), that is

$$\frac{\partial^2 \rho}{\partial t^2} - a_o^2 \nabla \rho = \frac{\partial^2 (\rho v_i v_j)}{\partial x_i \partial x_j}$$

or

$$\frac{\partial^2 \rho}{\partial t^2} - \nabla^2 \rho = \frac{\partial^2 (\rho v_i v_j)}{\partial x_i \partial x_j} \tag{B-49}$$

Expanding the right side of (B-49) gives

$$\frac{\partial^2 \rho}{\partial t^2} - \nabla^2 P = 2\left[\rho v_i \frac{\partial^2 v_j}{\partial x_i \partial x_j} + v_i \frac{\partial \rho}{\partial x_i} \frac{\partial v_i}{\partial x_j} + v_i \frac{\partial \rho}{\partial x_j} \frac{\partial v_j}{\partial x_i}\right] + v_i v_j \frac{\partial^2 \rho}{\partial x_i \partial x_j} + + \rho\left[\frac{\partial v_i}{\partial x_i} \frac{\partial v_j}{\partial x_j} + \frac{\partial v_i}{\partial x_j} \frac{\partial v_j}{\partial x_j}\right] \tag{B-50}$$

Now, differentiating the equation of mass continuity (B-1) with respect to x_i, multiplying by v_j and summing over i, gives

$$\rho v_i \frac{\partial^2 v_j}{\partial x_i \partial x_j} + v_i \frac{\partial \rho}{\partial x} \frac{\partial v_j}{\partial x_j} + v_i \frac{\partial \rho}{\partial x_j} \frac{\partial v_j}{\partial x_i} = -v_i \frac{\partial^2 \rho}{\partial x_i \partial t} - v_i v_j \frac{\partial^2 \rho}{\partial x_i \partial x_j} \tag{B-51}$$

Substitution of (B-51) into (B-50) gives

$$\frac{\partial^2 \rho}{\partial t^2} + 2 v_i \frac{\partial^2 \rho}{\partial x_i \partial t} + v_i v_j \frac{\partial^2 \rho}{\partial x_i \partial x_j} - \nabla^2 P = \rho\left[\frac{\partial v_i}{\partial x_i} \frac{\partial v_j}{\partial x_j} + \frac{\partial v_i}{\partial x_j} \frac{\partial v_j}{\partial x_i}\right] \tag{B-52}$$

Now define the operator D/D_t as

$$\frac{D}{Dt} = \frac{\partial}{\partial t} + v_j \frac{\partial}{\partial x_j} \tag{B-53}$$

so that

$$\frac{D^2}{Dt^2} = \frac{\partial^2}{\partial t^2} + 2 v_j \frac{\partial^2}{\partial x_j \partial t} + v_i v_j \frac{\partial^2}{\partial x_i \partial x_j} + \frac{D v_j}{Dt} \frac{\partial \rho}{\partial x_j} \tag{B-54}$$

In terms of this operator (B-52) becomes

$$\frac{D^2 \rho}{Dt^2} - \nabla^2 P = \rho\left[\frac{\partial v_i}{\partial x_i} \frac{\partial v_j}{\partial x_j} + \frac{\partial v_i}{\partial x_j} \frac{\partial v_j}{\partial x_i}\right] + \frac{D v_j}{Dt} \frac{\partial \rho}{\partial x_j} \tag{B-55}$$

Consider a single volume element of fluid at x_k moving through the flow field with velocities v_i. By constructing a coordinate system η_k, which moves with this fluid element, and by associating (B-55) with the density and pressure fluctuations of this fluid, (B-55) takes the form

$$\frac{\partial^2 \rho}{\partial t^2} - \nabla^2 P = \rho\left[\frac{\partial v_i}{\partial \eta_i}\frac{\partial v_j}{\partial \eta_j} + \frac{\partial v_i}{\partial \eta_j}\frac{\partial v_j}{\partial \eta_i}\right] + \frac{\partial v_j}{\partial t}\,\frac{\partial \rho}{\partial \eta_j} \qquad \text{(B-56)}$$

Ribner (Ref. 3) neglects the last term on the right of (B-56), probably on the basis that following the motion of the fluid this term should be small. It is to be noted, however, that $\partial v_j / \partial t$ represents the acceleration of the particle of fluid and hence the acceleration of the moving axis. Ribner's form of (B-56) is

$$\frac{\partial^2 \rho}{\partial t^2} - \nabla^2 P = \rho\left[\frac{\partial v_i}{\partial \eta_i}\,\frac{\partial v_j}{\partial \eta_j} + \frac{\partial v_i}{\partial \eta_j}\,\frac{\partial v_j}{\partial \eta_i}\right] = \rho\,\frac{\partial^2 (v_i v_j)}{\partial \eta_i \partial \eta_j}\bigg|_{v_i = 0} \qquad \text{(B-57)}$$

The density, ρ, pressure P, and velocity v_i, are now written as a linear superposition of the ambient (o), incompressible (°), and compressible (') components of these quantities. (The following is Ribner's notation.)

$$\begin{aligned} P &= P_o + P^{(0)} + P^{(1)} \\ \rho &= \rho_o + \rho^{(0)} + \rho^{(1)} \\ v_i &= \phantom{\rho_o +{}} v_i^{(0)} + v_i^{(1)} \end{aligned} \qquad \text{(B-58)}$$

Substitution of (B-58) into (B-57) gives

$$\frac{\partial^2 \rho^{(1)}}{\partial t^2} - \nabla^2 P^{(1)} = -\frac{\partial^2 \rho^{(0)}}{\partial t^2} + \nabla^2 P^{(0)} + \rho_o\,\frac{\partial^2 (v_i^{(0)} v_j^{(0)})}{\partial \eta_i\,\partial \eta_k}\bigg|_{v_i^{(0)} = 0} \qquad \text{(B-59)}$$

$$+\left[\rho\,\frac{\partial^2 (v_i v_j)}{\partial \eta_i\,\partial \eta_j} - \rho_o\,\frac{\partial^2 (v_i^{(0)} v_j^{(0)})}{\partial \eta_i\,\partial \eta_j}\right]$$

If the fluid were incompressible, then for the single fluid element being considered, $\rho^{(1)} = P^{(1)} = 0$ and $\partial^2 \rho^{(0)}/\partial t^2 = 0$ so that

$$\nabla^2 P^{(0)} = -\rho_o\,\frac{\partial^2 (v_i^{(0)} v_j^{(0)})}{\partial \eta_i\,\partial \eta_j}\bigg|_{v_i = 0} \qquad \text{(B-60)}$$

Equation (B-60) defines the pressure field of a turbulent flow assuming that the fluid is incompressible. The condition of incompressibility is, according to Ribner (Ref. 3), a close approximation even up to low supersonic Mach numbers. Ribner imposes this condition on (B-59) and further assumes that the bracketed terms can be neglected as a small contributor to far field acoustic noise. Hence, following the motion of the fluid element,

$$\frac{\partial^2 \rho^{(1)}}{\partial t^2} - \nabla^2 p^{(1)} = -\frac{\partial^2 \rho^{(0)}}{\partial t^2} \tag{B-61}$$

or referred once again to fixed coordinates

$$\frac{D^2 \rho^{(1)}}{D t^2} - \nabla^2 p^{(1)} = -\frac{D^2 \rho^{(0)}}{D t^2} \tag{B-62}$$

The left side of (B-62) contains terms which contribute to the scattering of sound waves as they propagate through the erratic eddying flow. Such effects, which are not of interest here, are eliminated by replacing D/D_t with $\overline{D}/\overline{D}_t$ where

$$\frac{\overline{D}}{\overline{D}_t} = \frac{\partial}{\partial t} + U \frac{\partial}{\partial x_1} \tag{B-63}$$

Here U is the flow velocity parallel to the jet axis, and it is assumed that the axial gradient $\frac{\partial U}{\partial x_1}$ can be neglected. With these restrictions, (B-62) becomes

$$\frac{\overline{D}^2 \rho^{(1)}}{\overline{D} t^2} - \nabla^2 \rho^{(1)} = -\frac{D^2 \rho^{(0)}}{D t^2} \tag{B-64}$$

or

$$\frac{1}{a^2} \frac{\overline{D}^2 p^{(1)}}{\overline{D} t^2} - \nabla^2 p^{(1)} = -\frac{D^2 \rho^{(0)}}{D t^2} \tag{B-65}$$

which is Ribner's final equation for jet flow noise. As a first order approximation, Ribner further assumes that

$$p^{(0)} = a^2 \rho^{(0)}$$

or that

$$\frac{1}{a^2} \frac{\overline{D}^2 p^{(1)}}{\overline{D} t^2} - \nabla^2 p^{(1)} = -\frac{D^2 \rho^{(0)}}{D t^2} \approx -\frac{1}{a^2} \frac{D^2 p^{(0)}}{D t^2} \tag{B-66}$$

(B-66) shows that the far field acoustic pressure perturbations $P^{(1)}$ are driven by the near field pressure perturbations, $P^{(o)}$, where the latter are determined as if the flow were essentially incompressible and result from inertial effects within the unsteady eddying flow. Further, (B-65) shows that the effective acoustic sources are simple sources resulting from the minute pulsations or dilatations of the fluid at each point in the flow. This replaces Lighthill's volume distribution of acoustic quadropole sources.

The effective convection of the acoustic sources within the jet can be seen from the expanded form of $D^2\rho^{(o)}/Dt^2$

$$\frac{D^2\rho^{(o)}}{Dt^2} = \frac{\partial^2\rho^{(o)}}{\partial t^2} + 2v_i\frac{\partial^2\rho^{(o)}}{\partial x_i\partial t} + v_i v_j\frac{\partial^2\rho^{(o)}}{\partial x_i\partial x_j} \tag{B-67}$$

When the mean flow is zero, v_i and v_j result solely from unsteady flow and represent the dilatation of the fluid as it moves through regions of rarefaction and condensation. For such flows, only the first term may predominate; however, for high velocity jet flows, the last term is of the same order as the first term (Ref. 3).

It is interesting to note that Lighthill's convected quadropoles were analyzed as a "frozen pattern" of acoustic sources moving along the flow axis. The resulting correction factor for this convection was shown to be $(1 - M_c \cos\theta)^{-3}$ (Ref. 1). Ribner, on the other hand, allowed for a pattern fluctuation during convection through the space - time correlation function, and found that this "softens" the directional effect due to convection and eliminates the infinite amplitude associated with $M_c \cos\theta = 1$ in Lighthill's convection factor.

Derivation of Modified Acoustic Equations for Jet Noise

With the above background it is possible to proceed rather directly with the derivation of an equation which more accurately accounts for the effects of high shear flow gradients on the production, refraction and convection (the latter two being inseparable) of sound in high velocity jet flows. The particle velocities associated with sound waves are considered in the fundamental flow equations and eliminated from these basic equations to give a single equation for the acoustic disturbances. This equation is much like that of Ribner's but is of a higher order and contains additional terms which depend directly upon the shear gradient magnitudes. Such terms are shown to be important at frequencies equal to and below the characteristic frequency of the jet. In addition, a minimum of restrictions are made concerning the temperature and mean temperature gradients in the flow.

The forms of the mass continuity and Navier-Stokes equations to be used are:

$$\frac{\partial \rho}{\partial t} + \rho \frac{\partial v_j}{\partial x_j} + v_j \frac{\partial \rho}{\partial x_j} = Q \qquad \text{(B-68)}$$

$$\rho\left[\frac{\partial v_i}{\partial t} + v_j \frac{\partial v_i}{\partial x_j}\right] + \frac{\partial P}{\partial x_i} = F_i \qquad \text{(B-69)}$$

Consider now an acoustic disturbance, generated by Q and/or the F_i, to be propagating through a steady flow field having steady velocity gradients and with steady temperature gradients. The defining acoustic equations are taken to be the linearized forms of (B-68) and (B-69). These linear equations are obtained by neglecting products of acoustic quantities and neglecting all dc terms. Thus denoting mean quantities with a bar (—), (B-68) and (B-69) become:

$$\bar{\rho}\left[\frac{\partial v_i}{\partial t} + \overline{v_j}\frac{\partial v_i}{\partial x_j} + v_j \frac{\partial \overline{v_i}}{\partial x_j}\right] + \rho \overline{v_j}\frac{\partial \overline{v_i}}{\partial x_j} + \frac{\partial P}{\partial x_i} = F_i \qquad \text{(B-70)}$$

$$\frac{\partial \rho}{\partial t} + \bar{\rho}\frac{\partial v_j}{\partial x_j} + \rho \frac{\partial \overline{v_j}}{\partial x_j} + \overline{v_j}\frac{\partial \rho}{\partial x_j} + v_j \frac{\partial \bar{\rho}}{\partial x_j} = Q \qquad \text{(B-71)}$$

Further, assuming a mean flow velocity, $\overline{v_1} = U$, along with the x_1 - axis and setting $\overline{v_2} = \overline{v_3} = 0$ gives

$$\bar{\rho}\left[\frac{\partial v_1}{\partial t} + U \frac{\partial v_1}{\partial x_1} + v_j \frac{\partial U}{\partial x_j}\right] + \rho U \frac{\partial U}{\partial x_1} + \frac{\partial P}{\partial x_1} = F_1 \qquad \text{(B-72)}$$

$$\bar{\rho}\left[\frac{\partial v_2}{\partial t} + U \frac{\partial v_2}{\partial x_1}\right] + \frac{\partial P}{\partial x_2} = F_2 \qquad \text{(B-73)}$$

$$\bar{\rho}\left[\frac{\partial v_3}{\partial t} + U \frac{\partial v_3}{\partial x_1}\right] + \frac{\partial P}{\partial x_3} = F_3 \qquad \text{(B-74)}$$

$$\frac{\partial \rho}{\partial t} + \bar{\rho}\frac{\partial v_j}{\partial x_j} + \rho\frac{\partial U}{\partial x_1} + U\frac{\partial \rho}{\partial x_1} + v_j\frac{\partial \bar{\rho}}{\partial x_j} = Q \qquad \text{(B-75)}$$

The velocities v_i are the acoustic "particle velocities". It is desirable to eliminate these from (B-72) - (B-75) in order to obtain a single equation for density and pressure fluctuations. This can be done in a systematic manner; however, the resulting equation is so formidable as to be of no practical value. However, if the mean flow velocity U and the mean density $\bar{\rho}$ are axially uniform, i.e. do not vary with x_1, this equation can be greatly simplified.

Assuming, then, that

$$\frac{\partial U}{\partial x_1} = \frac{\partial \bar{\rho}}{\partial x_1} = 0 \qquad \text{(B-76)}$$

the above equations reduce to the form

$$\frac{\bar{D}(\bar{\rho}v_1)}{\bar{D}t} + \alpha(\bar{\rho}v_2) + \beta(\bar{\rho}v_3) + \frac{\partial p}{\partial x_1} = F_1 \qquad \text{(B-77)}$$

$$\frac{\bar{D}(\bar{\rho}v_2)}{\bar{D}t} + \frac{\partial p}{\partial x_2} = F_2 \qquad \text{(B-78)}$$

$$\frac{\bar{D}(\bar{\rho}v_3)}{\bar{D}t} + \frac{\partial p}{\partial x_3} = F_3 \qquad \text{(B-79)}$$

$$\frac{\bar{D}\rho}{\bar{D}t} + \frac{\partial(\bar{\rho}v_1)}{\partial x_1} + \frac{\partial(\bar{\rho}v_2)}{\partial x_2} + \frac{\partial(\bar{\rho}v_3)}{\partial x_3} = Q \qquad \text{(B-80)}$$

where

$$\alpha = \frac{\partial U}{\partial x_2} \qquad \beta = \frac{\partial U}{\partial x_3}$$

The quantities $(\bar{\rho}v_i)$ can be eliminated from (B-77) - (B-80) by substitution into the operational equation:

$$\frac{\bar{D}^2}{\bar{D}t^2}\Big[(B\text{-}80)\Big]-\frac{\bar{D}}{\bar{D}t}\frac{\partial}{\partial X_1}\Big[(B\text{-}77)\Big]-\frac{\bar{D}}{\bar{D}t}\frac{\partial}{\partial X_2}\Big[(B\text{-}78)\Big]-\frac{\bar{D}}{\bar{D}t}\frac{\partial}{\partial X_3}\Big[(B\text{-}79)\Big]$$

$$+2\alpha\frac{\partial}{\partial X_1}\Big[(B\text{-}78)\Big]+2\beta\frac{\partial}{\partial X_1}\Big[(B\text{-}79)\Big] \qquad \text{(B-81)}$$

Noting that

$$\frac{\bar{D}}{\bar{D}t}\frac{\partial}{\partial X_1}=\frac{\partial}{\partial X_1}\frac{\bar{D}}{\bar{D}t} \qquad \text{(B-82)}$$

$$\frac{\bar{D}}{\bar{D}t}\frac{\partial}{\partial X_2}=\frac{\partial}{\partial X_2}\frac{\bar{D}}{\bar{D}t}-\alpha\frac{\partial}{\partial X_1} \qquad \text{(B-83)}$$

$$\frac{\bar{D}}{\bar{D}t}\frac{\partial}{\partial X_3}=\frac{\partial}{\partial X_3}\frac{\bar{D}}{\bar{D}t}-\beta\frac{\partial}{\partial X_1} \qquad \text{(B-84)}$$

the resulting equation is

$$\frac{\bar{D}}{\bar{D}t}\left[\frac{\bar{D}^2\rho}{\bar{D}t^2}-\nabla^2 P\right]+2\alpha\frac{\partial^2 P}{\partial X_1\partial X_2}+2\beta\frac{\partial^2 P}{\partial X_1\partial X_3}=$$

$$=\frac{\bar{D}}{\bar{D}t}\left[\frac{\bar{D}Q}{\bar{D}t}-\frac{\partial F_i}{\partial X_i}\right]+2\alpha\frac{\partial F_2}{\partial X_1}+2\beta\frac{\partial F_3}{\partial X_1} \qquad \text{(B-85)}$$

where P and ρ may be related by the local steady state speed of sound in the flow,

$$P=\bar{a}^2\rho \qquad \text{(B-86)}$$

For an axially uniform steady flow field (cold or hot), (B-85) defines the true production of sound for applied forces F_i and mass sources Q, and defines the true convection and refraction of the generated sound through this flow. It is seen that the lateral gradients α and β have a direct effect both upon the distortion of the sound field and production of sound, the latter being evidenced by the enhancement of the axial gradients of the lateral applied force components.

When the direct gradient terms are not significant, the left side of (B-85) reduces to the left side of (B-64); the resulting equation is then

$$\frac{\overline{D}^2\rho}{\overline{D}t^2} - \nabla^2\rho = \frac{\overline{D}Q}{\overline{D}t} - \frac{\partial F_i}{\partial x_i} \qquad \text{(B-87)}$$

In order to relat this equation (B-85) to jet noise, it is necessary to determine F_i and Q in terms of the turbulent density, pressure and velocity fluctuations. Define ρ, P, v_i as the linear superposition of mean, fluctuating turbulent and acoustic components:

$$\begin{aligned} \rho &= \overline{\rho} + \tilde{\rho} + \rho_a \\ P &= \overline{P} + \tilde{P} + P_a \\ v_i &= \overline{v}_i + \tilde{v}_i + v_{ia} \end{aligned} \qquad \text{(B-88)}$$

Now, substitute (B-88) into (B-68) and (B-69) and assume that (a) products of acoustic quantities can be neglected due to their relative smallness; (b) products of acoustic and fluctuating turbulent quantities can be neglected as these contribute only to scattering of the sound; (c) products of acoustical quantities and $\overline{v}_2$ and $\overline{v}_3$, or derivatives of the latter, can be neglected as $\overline{v}_2, \overline{v}_3$ are quite small and do not alter the refraction of sound; (d) the mean flow velocity U and the mean density $\overline{\rho}$ when associated with acoustic quantities do not vary with x_1, nor do their lateral gradients vary with x_1.

The resulting equations are the same as (B-77) - (B-80) but with F_i and Q defined as follows:

$$\left.\begin{aligned} F_i &= -\rho\frac{Dv_i}{Dt} - \frac{\partial P}{\partial x_i} \\ Q &= -\frac{D\rho}{Dt} - \rho\theta \\ \theta &= \frac{\partial v_j}{\partial x_j} \\ \frac{D}{Dt} &= \frac{\partial}{\partial t} + v_j\frac{\partial}{\partial x_j} \end{aligned}\right\} \begin{aligned} \rho &= \overline{\rho} + \tilde{\rho} \\ P &= \overline{P} + \tilde{P} \\ v_i &= \overline{v}_i + \tilde{v}_i \end{aligned} \qquad \text{(B-89)}$$

In performing the substantive derivative operation, $\frac{\overline{D}}{\overline{D}t}$, in (B-81), it is reasonable to use the more general operation $\frac{D}{Dt}$, for F_i and Q, since the use of $\frac{\overline{D}}{\overline{D}t}$ on the left side of

(B-77) - (B-80) merely suppresses the scattering of propagated sound which is not the case for F_i and Q. Hence, the desired equation defining jet noise is

$$\frac{\bar{D}}{\bar{D}t}\left[\frac{1}{\bar{a}^2}\frac{\bar{D}^2 P_a}{\bar{D}t^2} - \nabla^2 P_a\right] + 2\alpha\frac{\partial^2 P_a}{\partial x_1 \partial x_2} + 2\beta\frac{\partial^2 P_a}{\partial x_1 \partial x_3} =$$

$$= \frac{D}{Dt}\left[\frac{DQ}{Dt} - \frac{\partial F_i}{\partial x_i}\right] + 2\alpha\frac{\partial F_2}{\partial x_1} + 2\beta\frac{\partial F_3}{\partial x_1} \qquad \text{(B-90)}$$

with F_i and Q defined by (B-89). For comparison with Ribner's equation (B-65), the quantity $\left[\frac{DQ}{Dt} - \frac{\partial F_i}{\partial x_i}\right]$ is determined. From (B-89)

$$-\left[\frac{DQ}{Dt} - \frac{\partial F_i}{\partial x_i}\right] = \frac{D^2\rho}{Dt^2} + \frac{D(\rho\theta)}{Dt} - \frac{\partial}{\partial x_i}\left[\rho\frac{Dv_i}{Dt} + \frac{\partial P}{\partial x_i}\right] =$$

$$= \frac{D^2\rho}{Dt^2} + \rho\frac{D\theta}{Dt} + \theta\frac{D\rho}{Dt} - \frac{\partial\rho}{\partial x_i}\frac{Dv_i}{Dt} - \rho\left[\frac{D\theta}{Dt} + \frac{\partial v_i}{\partial x_j}\frac{\partial v_j}{\partial x_i}\right] - \nabla^2 P =$$

$$= \left[\frac{\partial^2\rho}{\partial t^2} + 2v_j\frac{\partial^2\rho}{\partial t\,\partial x_j} + v_i v_j\frac{\partial^2\rho}{\partial x_i\,\partial x_j}\right] - \rho\left[\frac{\partial v_i}{\partial x_i}\frac{\partial v_j}{\partial x_j} + \frac{\partial v_i}{\partial x_j}\frac{\partial v_j}{\partial x_i}\right] + \theta\left[\frac{D\rho}{Dt} + \rho\theta\right] - \nabla^2 P \qquad \text{(B-91)}$$

Ribner obtained the first bracketed terms on the RHS of (B-90)(see B-65, B-67) and assumed complete cancellation of the second bracketed term with $\nabla^2 P$. Thus, the only difference lies in the term $\theta\left[\frac{D\rho}{Dt} - \rho\theta\right]$ which arises from eliminating the particle velocities. Because of the small magnitude of the dilatation θ, and because $D\rho/Dt$ is proportional to ω rather than to ω^2, as in $\partial^2\rho/\partial t^2$, this added term is relatively small and may be neglected. Accepting the above cancellation, which seems sufficiently accurate for the present, (B-90) becomes

$$\frac{\bar{D}}{\bar{D}t}\left[\frac{1}{\bar{a}^2}\frac{\bar{D}^2 P_a}{\bar{D}t^2} - \nabla^2 P_a\right] + 2\alpha\frac{\partial^2 P_a}{\partial X_1 \partial X_2} + 2\beta\frac{\partial^2 P_a}{\partial X_1 \partial X_3} =$$

$$\left.\frac{D^3\rho}{Dt^3}\right|_{\frac{Dv_i}{Dt}=0} - 2\alpha\frac{\partial}{\partial X_1}\left[\rho\frac{Dv_1}{Dt} + \frac{\partial P}{\partial X_2}\right] - 2\beta\frac{\partial}{\partial X_1}\left[\rho\frac{Dv_1}{Dt} + \frac{\partial P}{\partial X_3}\right] \qquad \text{(B-92)}$$

The relative order of magnitude of the terms $2\alpha\frac{\partial^2 P_a}{\partial X_1 \partial X_2}$, $2\beta\frac{\partial^2 P_a}{\partial X_1 \partial X_3}$,

can be estimated by comparing them with $\frac{1}{\bar{a}^2}\frac{\bar{D}^3 P_a}{\bar{D}t^3}$. Let a typical Fourier component of

P_a be

$$P_a = A\, e^{i(KX + \omega t)}$$

Then

$$\frac{\left|2\alpha \frac{\partial^2 P_a}{\partial X^2}\right|}{\left|\frac{1}{\bar{a}^2}\frac{D^3 P_a}{D^3 t}\right|} \approx \frac{2\alpha a^2 K^2}{(\omega + UK)^3} = \frac{2\alpha}{\omega(1+M)^3}$$

Let M be an average flow Mach number, say 1/2 M_o, and let $\alpha \approx \frac{.6\, U_o}{R}$ where R is the radius of the exhaust exit and $\omega = 2\pi f$. Then

$$\frac{2\alpha}{\omega(1+M)^3} \approx \frac{.2\, U_o}{fR\left(1+\frac{M_o}{2}\right)^3}$$

For an exit velocity of 1020 ft/sec., a flow Mach number of $M_o = 1.0$ and a nozzle radius of .5 ft., this quantity equals

$$\frac{120}{f}$$

The above ratio of absolute magnitudes equals unity for f = 120 cps and is of the order of 1/2 at f = 240 cps, which for the example given is approximately the characteristic frequency of the jet. The two additional gradient terms, therefore, should not be ignored.

The solution of (B-91) is presently being investigated by the author for various types of acoustic sources, such as simple sources, dipoles, etc., and for various gradient shapes and flow Mach numbers.

LIST OF SYMBOLS USED IN APPENDIX B

a	Speed of sound
D/Dt	Total differentiation operator = $\partial/\partial t + v_j \, \partial/\partial x_j$
$\bar{D}/\bar{D}t$	Total differentiation operator = $\partial/\partial t + U \, \partial/\partial x_1$
e_{ij}	Strain rate tensor = $\partial v_i/\partial x_j + \partial v_j/\partial x_i$
f	Frequency, cps
F_i	Applied force component
I_s	Surface integral; (Equation B-15)
J	Jacobian of transformation from fixed y_k - to moving η_k - coordinates
M	Mach number
n	Coordinate along surface normal
P	Pressure
Q	Mass source or sink flow rate
r	Distance between fluid element at $\vec{y}$ and observation point at $\vec{x} = \lvert \vec{x} - \vec{y} \rvert$
r	Cylindrical polar coordinate
R	$\lvert \vec{x} - \vec{y} \rvert - \vec{M}_o \cdot (\vec{x} - \vec{y})$
S	Surface area
t	Time
t'	Retarded time in uniform quiescent medium = $t - r/a_o$
T_{ij}	Fluid stress tensor
U	Mean jet flow velocity
V	Volume
v_i	Fluid velocity component

x_i	=	Position of fixed observation point with respect to fixed axes
y_i	=	Position of moving element of fluid with respect to fixed axes
α	=	Lateral mean velocity gradient = $\partial U / \partial X_2$
β	=	Lateral mean velocity gradient = $\partial U / \partial X_3$
δ_{ij}	=	Kronecker delta = 0 if $i \neq j$, = 1 if $i = j$
η	=	Shear viscosity coefficient
η'	=	Compressive friction coefficient
η_i	=	Position of moving element of fluid with respect to moving axes
θ	=	Dilatation = $\partial v_j / \partial X_j$; also, angle between jet axis and observation vector x
ρ	=	Fluid density
ω	=	Circular frequency, rad/sec.
∇^2	=	$\partial^2/\partial X_1^2 + \partial^2/\partial X_2^2 + \partial^2/\partial X_3^2$
Δ	=	Finite difference operator

Superscripts

o	Denotes near field component
1	Denotes far field component
–	Denotes mean or time average
→	Denotes vector quantity
~	Denotes fluctuating turbulent component

Subscripts

i, j, k	Denote components of vector quantities along the 1, 2, 3 axes*
s	Denotes surface

*Note: The 1 – axis is always parallel to the mean flow axis of the jet exhaust for both the fixed and moving coordinate systems.

Subscripts (continued)

o	Denotes ambient value
a	Denotes acoustic perturbation value
c	Denotes convection
$\vert\ \vert$	Denotes absolute magnitude

APPENDIX B

References:

1. Lighthill, M. J., "On Sound Generated Aerodynamically; I. General Theory," Proceedings of The Royal Society, Series A, Vol. 211, 1952.

2. Lighthill, M. J., "On Sound Generated Aerodynamically; II. Turbulence as a Source of Sound," Proceedings of the Royal Society, Series A, Vol. 222, 1954.

3. Ribner, H. S., "A Theory of the Sound from Jets and Other Flows in Terms of Simple Sources," UTIA Report No. 67, AFOSR TN 60-950, July 1960.

4. Feshbach, H., Morse, P. M., "Methods of Theoretical Physics," McGraw-Hill, Vol. I., 1953.

APPENDIX C

SOUND PROPAGATION IN A CYLINDRICALLY SYMMETRIC TEMPERATURE DISTRIBUTION

In an attempt to extract the qualitative features at least of jet noise propagation at the presence of a temperature distribution (hot jet), the propagation of sound from a source imbedded in a finite cylindrically symmetric temperature distribution will be considered here. (The atmosphere is assumed to be otherwise homogeneous.) The particular choice of the distribution is dictated by that existing in a hot jet, which, in general, follows a bell-shaped curve.*

If the z-axis is the axis of symmetry, then the temperature will depend only on the coordinate r; in particular, the chosen dependence is

$$T(r) = T_o + \frac{A}{\cosh^2 \alpha r} \qquad \text{(C-1)}$$

where T_o = ambient (atmospheric) temperature - degrees Rankine,

$A = T_s - T_o$ = height of temperature distribution - degrees F,

$T_s = T(0)$ = temperature along z-axis - degrees Rankine, and

α is a width parameter.

Under these circumstances, the sonic velocity will be given by

$$c^2(r) = C_o^2 \left[1 + \frac{\beta}{\cosh^2 \alpha r} \right] \qquad \text{(C-2)}$$

where C_o = speed of sound in the homogeneous atmosphere

$$\beta = \frac{A}{T_o} = \frac{(T_s - T_o)}{T_o}$$

Equation (C-1) has been plotted for $T_s = 900°F$, $T_o = 60°F$ in figure 103, and is compared with a typical hot jet profile of the same T_s value. The value of α, which controls essentially the width of the distribution, is fixed by demanding that $T_s - T_o$ falls to half its value at the same distance that the jet temperature falls to half its original value.

In the subsequent sections, an analysis based on ray acoustics and wave theory, respectively, is presented for the particular variation of the speed of sound given by Eq. (C-2).

---

*It is explicitly assumed here that the temperature distributions existing in a jet are well approximated by the measured velocity profiles.

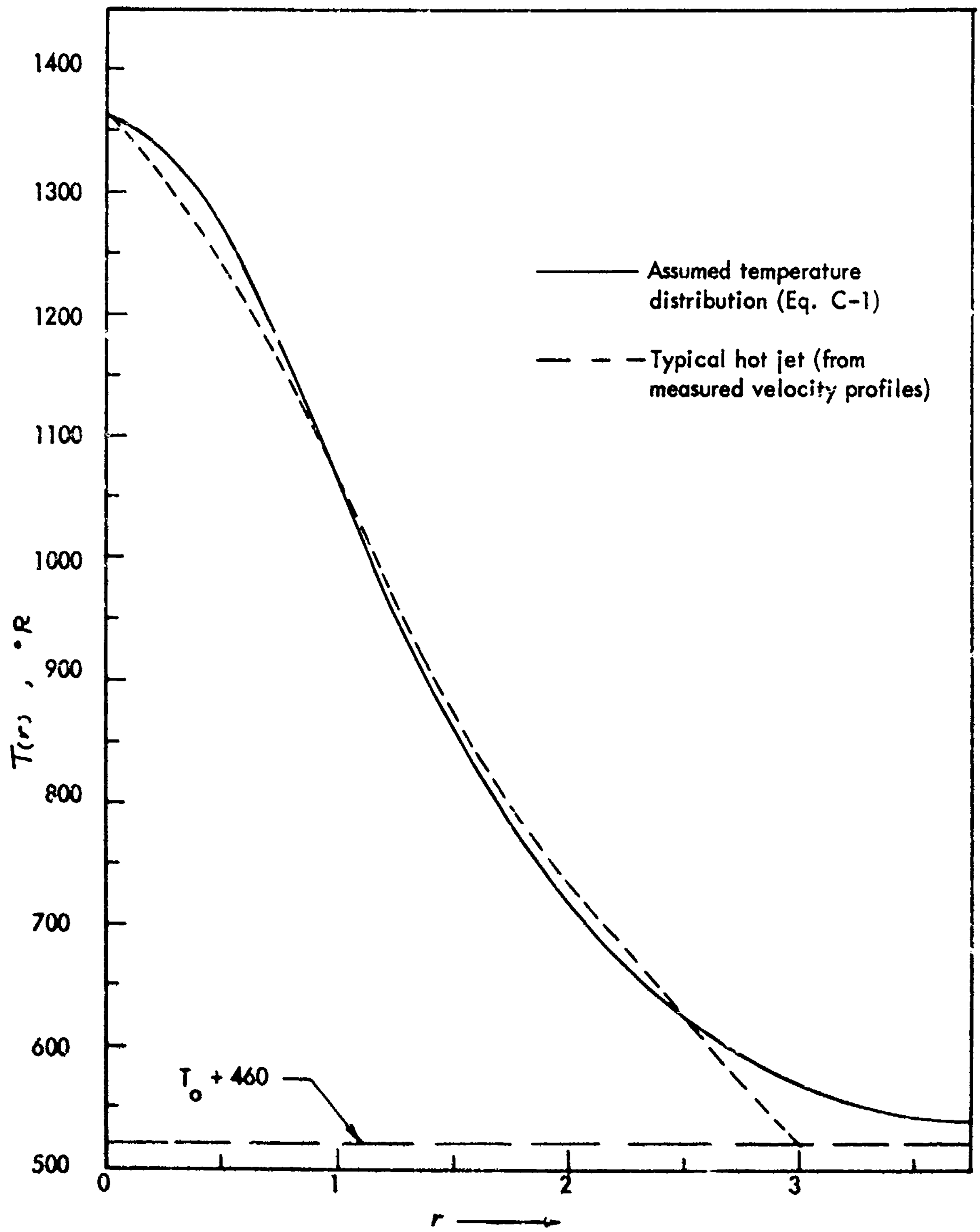

Figure 103. Comparison of typical hot jet profile and assumed temperature distribution. (T_s = 900°F; T_o = 60°F; α = .68).

GEOMETRICAL ACOUSTICS APPROXIMATION

Inasmuch as an analysis based on ray acoustics (high frequency approximation) can be helpful in gaining some insight in the way sound propagates in a non-homogeneous medium, this section will present a calculation of the ray paths and the intensity distribution for the case under consideration. Reflecting boundaries near the source will not be considered here, for in this case the use of the approximation becomes impractical.

The Ray Paths

Consider a z - r plane. A ray starts at the source (assumed located at the origin) making an angle ϕ_s with the z - axis; let the velocity at the source be c_s (figure 104). Denote the angle which the tangent to the ray at a point (r, z) makes with the vertical by ϕ and the velocity at that point by c (r).

The ray path can be determined from Fermat's principle, which requires that the integral $\int \frac{ds}{c}$ be stationary, i.e.

$$\delta \int \frac{ds}{c} = 0$$

where ds is an increment of the path, c the sonic velocity, and δ the symbol for the variation of a functional. In the present case, c = c(r), so that

$$ds = \left[(dr)^2 + (dz)^2 \right]^{\frac{1}{2}} = \left[1 + \dot{z}^2 \right]^{\frac{1}{2}} dr$$

The variation problem then becomes

$$\delta \int \frac{(1+\dot{z}^2)^{\frac{1}{2}}}{c(r)} dr = 0$$

for which there corresponds the Euler equation

$$\frac{d}{dr}\left[\frac{1}{c(r)} \frac{\dot{z}}{(1+\dot{z}^2)^{\frac{1}{2}}} \right] = 0$$

Hence, $$\frac{\dot{z}^2}{1+\dot{z}^2} = \frac{c^2(r)}{A^2}$$

or $$z = \int \frac{c(r)}{\sqrt{A^2 - c^2(r)}} dr$$

where A is a constant. Substitution of $\dot{z} \equiv \frac{dz}{dr} = \cot\phi$ yields $A = \frac{c(r)}{\cos\phi}$

which is, in fact, Snell's law; the usual form of the law results if we let

$$A = c_s / \cos\phi_s$$

Thus, the equation to be integrated is

$$z = \int \frac{c(r)\, dr}{\sqrt{c_s^2 \cos^{-2}\phi_s - c^2(r)}} \tag{C-3}$$

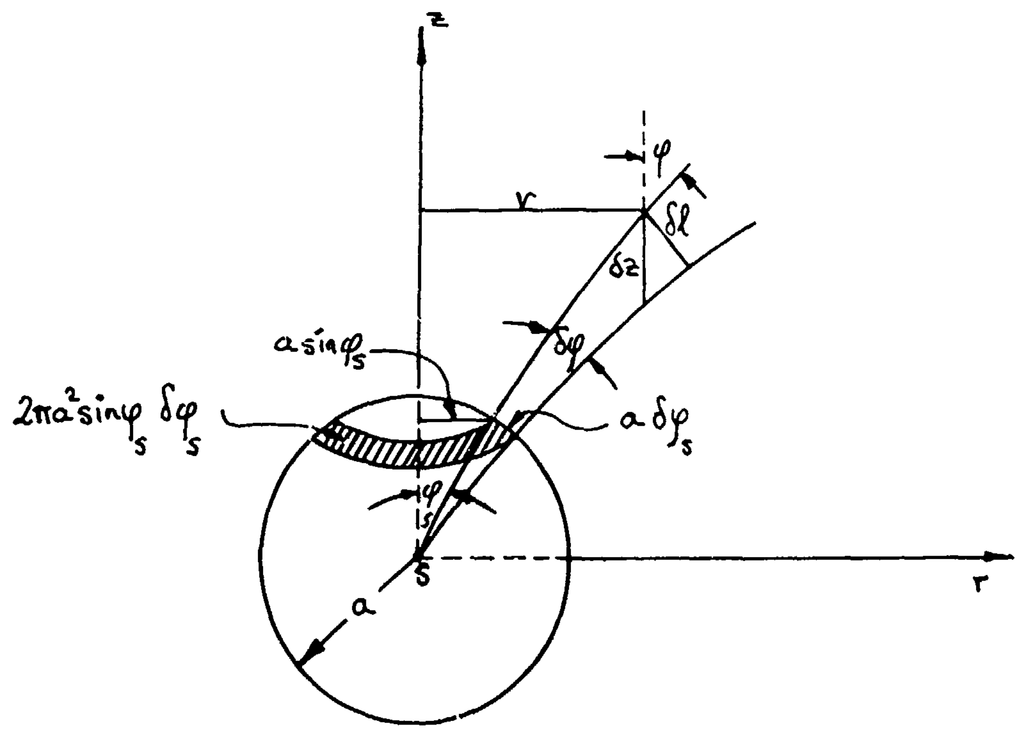

Figure 104. Geometry for the calculation of the intensity distribution by considering the geometrical divergence of the rays.

Alternatively, Eq. (C-3) can be derived by assuming Snell's law and making use of the geometry of the situation. Substituting for $c^2(r)$ and $c^2_s = c^2(o)$ from Eq. (C-2) and simplifying, we obtain

$$Z = \frac{1}{\sqrt{a-1}} \int_0^{r} \frac{\sqrt{\cosh^2 \alpha r + \beta}}{\sqrt{\cosh^2 \alpha r - \gamma}} \, dr \tag{C-4}$$

where $a = \dfrac{1+\beta}{\cos^2 \phi_s}$; $\gamma = \dfrac{\beta}{a-1} = \dfrac{\beta \cos^2 \phi_s}{\beta + \sin^2 \phi_s}$

Let $\cosh^2 \alpha r + \beta = \dfrac{1}{W}$ (C-5)

to obtain

$$Z = -\frac{K}{2} \int_{W_1}^{W_2} \frac{dW}{W\sqrt{(1-\beta W)(1-\delta W)(1-\epsilon W)}}$$

or

$$Z = -\frac{iK}{2\sqrt{\beta\delta\epsilon}} \int_{W_1}^{W_2} \frac{dW}{W\sqrt{(W-\beta^*)(W-\delta^*)(W-\epsilon^*)}} \tag{C-6}$$

where

$$\left.\begin{aligned} &\delta = \beta + \gamma = \frac{\beta(\beta+1)}{\beta + \sin^2\phi_s} \; ; \quad \epsilon = \beta + 1 \\ &K = \frac{1}{\alpha\sqrt{a-1}} = \frac{\cos\phi_s}{\alpha\sqrt{\beta + \sin^2\phi_s}} \; ; \; \beta^* = \frac{1}{\beta} \; ; \; \delta^* = \frac{1}{\delta} \; ; \; \epsilon^* = \frac{1}{\epsilon} \\ &W_1 = \frac{1}{(1+\beta)} \; ; \quad W_2 = \frac{1}{(\cosh^2 \alpha r + \beta)} \end{aligned}\right\} \tag{C-7}$$

The integral in Eq. (C-6) can now be reduced to a sum of two elliptic integrals by a further transformation of the variable (Ref. 2). Let

$$q^2 = \frac{(W-\beta^*)}{(W-\delta^*)} \tag{C-8}$$

to obtain immediately

$$z = -\frac{i\kappa}{\sqrt{\beta\delta\epsilon(\beta^* - \epsilon^*)}} \int_{q_1}^{q_2} \left[\frac{q^2 - 1}{q^2\delta^* - \beta^*} \right] \frac{dq}{\sqrt{(1-q^2)(1-\eta^2 q^2)}}$$

$$= -\frac{\kappa}{\sqrt{\delta}} \int_{q_1}^{q_2} \frac{(q^2-1)\,dq}{(q^2\delta^* - \beta^*)\sqrt{(q^2-1)(1-\eta^2 q^2)}}$$

or finally

$$z = -\left\{ C_1 \int_{q_1}^{q_2} \frac{dq}{\sqrt{(q^2-1)(1-\eta^2 q^2)}} + C_2 \int_{q_1}^{q_2} \frac{dq}{(q^2\nu - 1)\sqrt{(q^2-1)(1-\eta^2 q^2)}} \right\} \qquad \text{(C-9)}$$

where,

$$\left.\begin{aligned}
C_1 &= \kappa\sqrt{\delta} = \frac{\cos\phi_s \sqrt{\beta(\beta+1)}}{\alpha(\beta + \sin^2\phi_s)} \\
C_2 &= \frac{\kappa(\delta - \beta)}{\sqrt{\delta}} = \frac{\beta\cos^3\phi_s}{\alpha\sqrt{\beta(\beta+1)}\,(\beta + \sin^2\phi_s)} \\
\eta^2 &= \frac{\delta^* - \epsilon^*}{\beta^* - \epsilon^*} = \sin^2\phi_s \\
\nu &= \frac{\delta^*}{\beta^*} = \frac{\beta + \sin^2\phi_s}{\beta + 1} \\
q_1 &= \csc\phi_s \\
q_2 &= \frac{\sqrt{1+\beta}\cosh\alpha r}{\left[(\beta + \sin^2\phi_s)\cosh^2\alpha r - \beta\cos^2\phi_s\right]^{1/2}}
\end{aligned}\right\} \qquad \text{(C-10)}$$

The integrals appearing in Eq. (C-9) are elliptic integrals of the first and third kind, respectively. For numerical evaluation purposes, they are now expressed in the Legendre normal forms, by making the further transformation (Ref. 3)

$$q^2 = \sin^2\psi + \frac{\cos^2\psi}{\eta^2} \tag{C-11}$$

which yields

$$\alpha z = \sqrt{\frac{\beta+1}{\beta}}\left[\frac{\cos\phi_s}{\beta+\sin^2\phi_s}\right]\left[\beta F(\psi,k) + \sin^2\phi_s\, \Pi(\psi,\mu,k)\right] \tag{C-12}$$

where

$$F(\psi,k) = \int_0^{\psi}\frac{d\psi}{\sqrt{1-k^2\sin^2\psi}} \equiv \int_0^{\psi}\frac{d\psi}{\Delta\psi}$$

$$\Pi(\psi,\mu,k) = \int_0 \frac{d\psi}{(1-\mu\sin^2\psi)\,\Delta\psi}$$

$$k^2 = \cos^2\phi_s \text{ (modulus)} \tag{C-13}$$

$$\mu = \frac{\beta+\sin^2\phi_s}{\beta} \text{ (parameter)}$$

$$\psi = \sin^{-1}\left[\frac{\sqrt{\beta}\,\sinh\alpha r}{\left\{(\beta+\sin^2\phi_s)\cosh^2\alpha r - \beta\cos^2\phi_s\right\}^{1/2}}\right]$$

The integral $F(\psi,k)$ can readily be evaluated for a given ϕ_s with the use of available tables (Ref. 3); the integral $\Pi(\psi,\mu,k)$ can be expressed in a number of ways, e.g. in terms of Jacobian Theta and Zeta functions ; noting, however, that the parameter is always greater than unity (except in the limiting case of $\sin\phi_s = 0$). Use can be made of an addition theorem relating the integral of a parameter greater than unity to that of a parameter less than unity (Ref. 4):

$$\Pi(\psi,\mu,k) = F(\psi,k) - \Pi(\psi,\mu',k)$$

$$+\left[\frac{\mu}{(\mu-1)(\mu-k^2)}\right]^{1/2}\tanh^{-1}\left[\sqrt{\frac{(\mu-1)(\mu-k^2)}{\mu(1-k^2\sin^2\psi)}}\tan\psi\right]$$

where $\mu' = \frac{k^2}{\mu} < 1$ (Tables of $\Pi(\psi, \mu, k)$ for $\mu < 1$ are available, (Ref. 5).) Substitution of the above expression in Eq. (C-12) yields the final result

$$\alpha z = \sqrt{\frac{\beta+1}{\beta}}\left[\frac{\cos\phi_s}{\beta+\sin^2\phi_s}\right]\left[(\beta+\sin^2\phi_s)\,F(\psi,k) - \sin^2\phi_s\,\Pi(\psi,\tfrac{k^2}{\mu},k)\right.$$
$$\left. + \sin^2\phi_s\left[\frac{\mu}{(\mu-1)(\mu-k^2)}\right]^{1/2}\tanh^{-1}\left[\sqrt{\frac{(\mu-1)(\mu-k^2)}{\mu(1-k^2\sin^2\psi)}}\cdot\tan\psi\right]\right] \quad \text{(C-14)}$$

It is clear from Eq. (C-13) and Eq. (C-14) that all rays emanate from the origin, and in the limiting cases of $\phi_s = 0°$; $\phi_s = 90°$ the rays are straight lines along the z - and r-axis, respectively.

Ray paths for five values of ϕ_s have been plotted in figures 105, 106 for = 1.61 and β = 5.077, corresponding to a temperature at the source of approximately 900°F and 2700°F, respectively, and an ambient temperature of 60°F. As one would expect, the rays are "bent" toward the horizontal, while inside the temperature distribution; at some distance αr, at which ambient temperature has been virtually reached, they become straight lines. The "exit" angles at this distance are indicated in the figure. It is to be noted that the bending becomes more pronounced as ϕ_s decreases. The plot is symmetric about the (αr)- and (αz)-axis, and the three-dimensional picture results by rotating the r-z plane through 2π about the z - axis.

Intensity Distribution

With the knowledge of the ray paths, the intensity distribution can easily be determined by considering the geometrical divergence of the rays (Ref. 6). The procedure used here will be that applied by Pridmore-Brown and Ingard to the case of a temperature-stratified atmosphere (Ref. 7).

Let Q be the total power output of a spherical source and the radius of a small sphere centered on the source. Consider two neighboring rays leaving the source at ϕ_s and $\phi_s + \delta\phi_s$ (figure 104). If these rays are rotated about the z-axis, a certain amount of power, δQ, flows through the space bounded by the two surfaces formed, and it is equal to the power which falls on the sphere zone cut out by these rays:

$$\delta Q = \frac{Q}{4\pi a^2}\cdot 2\pi(a\sin\phi_s)(a\,\delta\phi_s) = \frac{Q\sin\phi_s}{2}\,\delta\phi_s$$

The intensity, I, at any point in the plane will then be the ratio of this power, δQ, to the area through which it flows at that distance ($=2\pi r\,\delta l$), δl being the perpendicular separation between the rays. Thus,

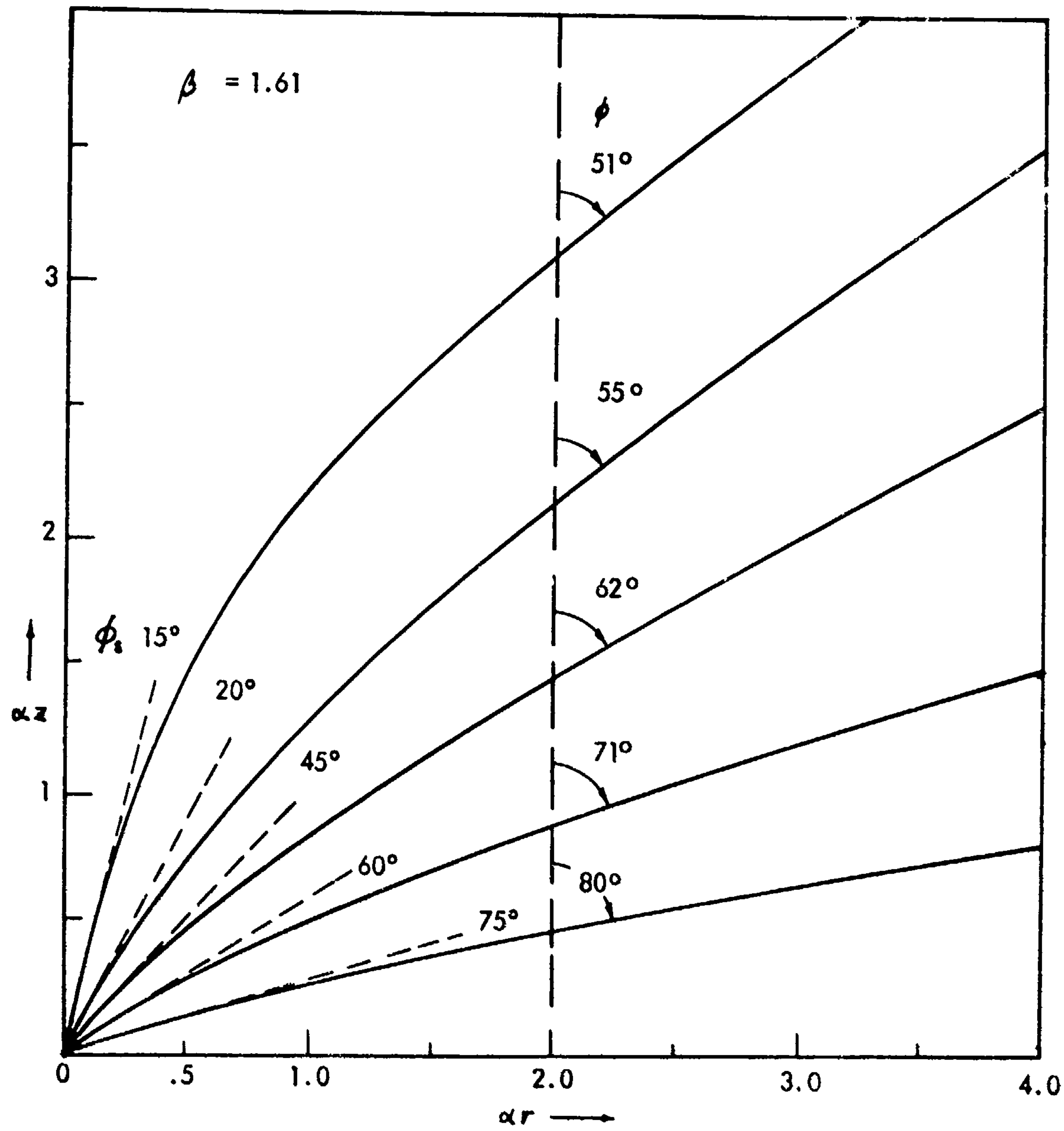

Figure 105. Calculated ray paths for β = 1.61 (T_s = 900°F, T_o = 60°F). Vertical broken line represents the virtual boundaries of the temperature distribution.

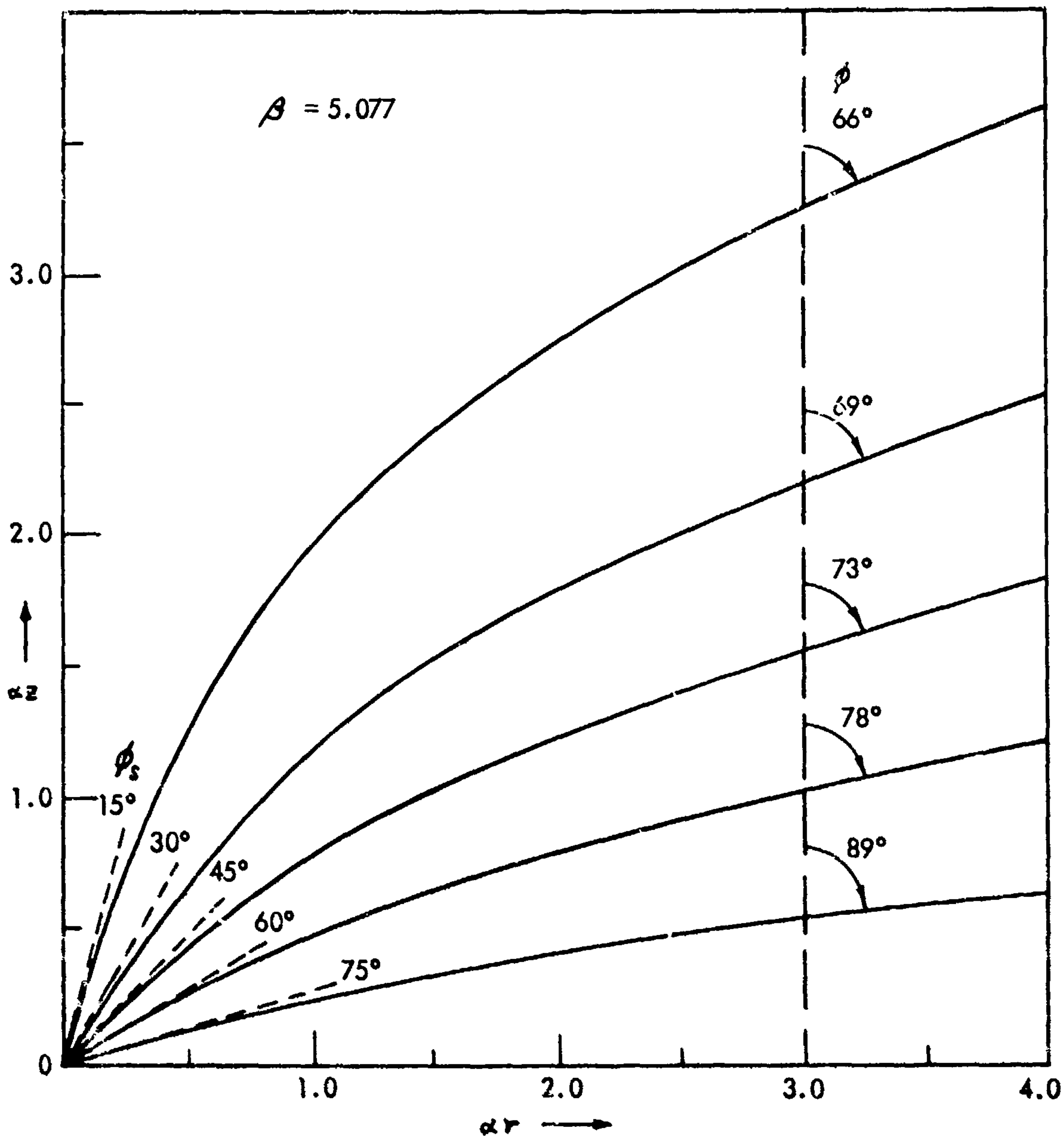

Figure 106. Calculated ray paths for β = 5.077 (T_s = 2700°F, T_o = 60° F). Vertical broken line represents the virtual boundaries of the temperature distribution.

$$I = \frac{Q \sin \phi_s}{4 \pi r} \quad \frac{\delta \phi_s}{\delta \ell} \tag{C-15}$$

where the value of $\delta \ell$ is calculated with the aid of figure 104.

$$\begin{aligned} \delta \ell &= \sin \phi \, \delta Z = \sin \phi \, \delta \int dz \\ &= \sin \phi \, \delta \int \cot \phi \, dr \\ &= - \sin \phi \int \frac{\delta \phi}{\sin^2 \phi} \, dr \end{aligned} \tag{C-16}$$

Since we will be interested in the intensity as a function of distance rather than a function of the angle ϕ, we now substitute in the integrand for $\delta \phi$ and $\sin^2 \phi$: From Snell's law

$$\frac{\cos \phi}{\cos \phi_s} = \frac{c(r)}{c_s}$$

$$\frac{\cos(\phi + \delta\phi)}{\cos(\phi_s + \delta\phi_s)} = \frac{c(r) + \delta c}{c_s}$$

Neglecting δ_c and expanding the cosines, one obtains

$$\frac{\delta \phi}{\delta \phi_s} = \frac{\tan \phi_s}{\tan \phi} \tag{C-17}$$

Also using Eq. (C-2), Snell's law reads

$$\frac{\cos^2 \phi}{\cos^2 \phi_s} = \frac{\left[1 + \frac{B}{\cosh^2 \alpha r} \right]}{\left[B + 1 \right]}$$

whence

$$\left.\begin{aligned}
\sin^2\phi' &= (1-b)\left[\frac{\cosh^2\alpha r - \gamma}{\cosh^2\alpha r}\right] \\
\tan\phi &= \sqrt{\frac{1-b}{b}}\left[\frac{\cosh^2\alpha r - \gamma}{\cosh^2\alpha r + \beta}\right]^{1/2} \\
b &= \frac{\cos^2\phi_s}{\beta+1} \;;\; \gamma = \frac{\beta\cos^2\phi_s}{\beta+\sin^2\phi_s}
\end{aligned}\right\} \tag{C-18}$$

Substitution of Eq. (C-17) and Eq. (C-18) into Eq. (C-16) yields

$$\frac{\delta \ell}{\delta\phi_s} = \sqrt{\frac{b}{(1-b)^3}}\;\sin\phi\,\tan\phi_s\left[\int\frac{\sqrt{\cosh^2\alpha r+\beta}}{\sqrt{\cosh^2\alpha r-\gamma}}\,dr + \gamma\int\frac{\sqrt{\cosh^2\alpha r+\beta}}{(\cosh^2\alpha r-\gamma)^{3/2}}\,dr\right] \tag{C-19}$$

The first integral is precisely that appearing in the calculation of the ray paths, and, hence, from Eq. (C-4)

$$\int_0^r \frac{\sqrt{\cosh^2\alpha r+\beta}}{\sqrt{\cosh^2\alpha r-\gamma}}\,dr = \frac{\sqrt{\beta+\sin^2\phi_s}}{\cos\phi_s}\,(z) \tag{C-20}$$

To evaluate the second integral we proceed as in the previous section. Performing the transformation of Eq. (C-5), and Eq. (C-8) and Eq. (C-11), we obtain

$$\int_0^r \frac{\sqrt{\cosh^2\alpha r+\beta}}{(\cosh^2\alpha r-\gamma)^{3/2}}\,dr = \frac{1}{\alpha\sqrt{\delta}\,\sin^2\phi_s\,(\delta\beta^*-1)}\left[E(\psi,k) - \sin^2\phi_s\,F(\psi,k)\right] \tag{C-21}$$

where δ and β^* are defined in Eq. (C-7), $F(\psi,k)$ in Eq. (C-13) and

$$E(\psi,k) = \int_0^\psi \sqrt{1-k^2\sin^2\psi}\;d\psi \equiv \int_0^\psi \Delta\psi\;d\psi$$

is the elliptic integral of the second kind. Substituting Eq. (C-20), (C-21) into Eq. (C-19) and evaluating the constant coefficients, we obtain

$$\frac{\delta\phi_s}{\delta\ell} = \left[\frac{\alpha\sin\phi_s\cos\phi_s(\beta+\sin^2\phi_s)}{\sqrt{\beta+1}\quad\sin\phi}\right]\cdot$$

$$\left[\sqrt{\beta+1}\,(\alpha z)\sin^2\phi_s + \sqrt{\beta}\cos\phi_s\cdot\left\{E(\psi,k) - \sin^2\phi_s\,F(\psi,k)\right\}\right]^{-1}$$

which, when substituted into Eq. (C-15) yields for the intensity

$$I = \frac{Q}{4\pi r}\left[\frac{\alpha \sin^2\phi_s \cos\phi_s (\beta + \sin^2\phi_s)}{\sqrt{\beta+1} \quad \sin\phi}\right] \cdot$$

$$\left[\sqrt{\beta+1}\,(\alpha z) \sin^2\phi_s + \sqrt{\beta}\, \cos\phi_s \left\{ E(\psi,k) - \sin^2\phi_s F(\psi,k)\right\}\right]^{-1}$$

The intensity from the <u>same</u> source in the homogeneous medium is

$$I_o = \frac{Q}{4\pi\rho^2} \quad ; \quad \rho^2 = r^2 + z^2$$

so that

$$\frac{I}{I_o} = \frac{(\alpha\rho)^2}{(\alpha r)}\left[\frac{\sin^2\phi_s \cos\phi_s \;(\beta + \sin^2\phi_s)}{\sqrt{\beta+1} \quad \sin\phi}\right] \cdot$$

$$\left[\sqrt{\beta+1}\,(\alpha z) \sin^2\phi_s + \sqrt{\beta}\, \cos\phi_s \cdot \left\{ E(\psi,k) - \sin^2\phi_s F(\psi,k)\right\}\right]^{-1} \quad \text{(C-22)}$$

On the other hand, for a directional source I' with a directivity pattern $f(\phi_s)$

$$\left(\frac{I}{I_o}\right)' = \frac{I}{I_o} \cdot \frac{f(\phi_s)}{f(\phi)}$$

where ϕ is the angle which the observer makes with the vertical.

With the use of Eq. (C-14), Eq. (C-22) has been computed along five ray paths for $\beta = 1.61$ and $\beta = 5.077$ (corresponding to temperatures at the source of 900°F and 2700°F, respectively), and has been plotted as a function of the dimensionless parameter $(\alpha\rho)$ in figures 107 and 108. It is seen that along any given ray, the relative intensity increases with $(\alpha\rho)$, approaching asymptotically some constant value. Apparently, this is due to the "focusing" effort of the temperature distribution (decrease in the divergence of the rays). Close to the source there exists a relative decrease in the intensity, becoming more pronounced for rays of smaller ϕ_s values, which, in fact, suffer considerable "bending" while inside the temperature distribution (figures 105 and 106). Evidently, the noted effect is due to the difference in the path lengths traversed when the temperature distribution is and is not present. An increase in β results in a "shift" of the plot closer to the source and in an increase of the maxima and minima in the intensity along the ray paths. This effect is consistent with the fact that for higher values the rays are "bent" more severely and are "focused" more effectively.

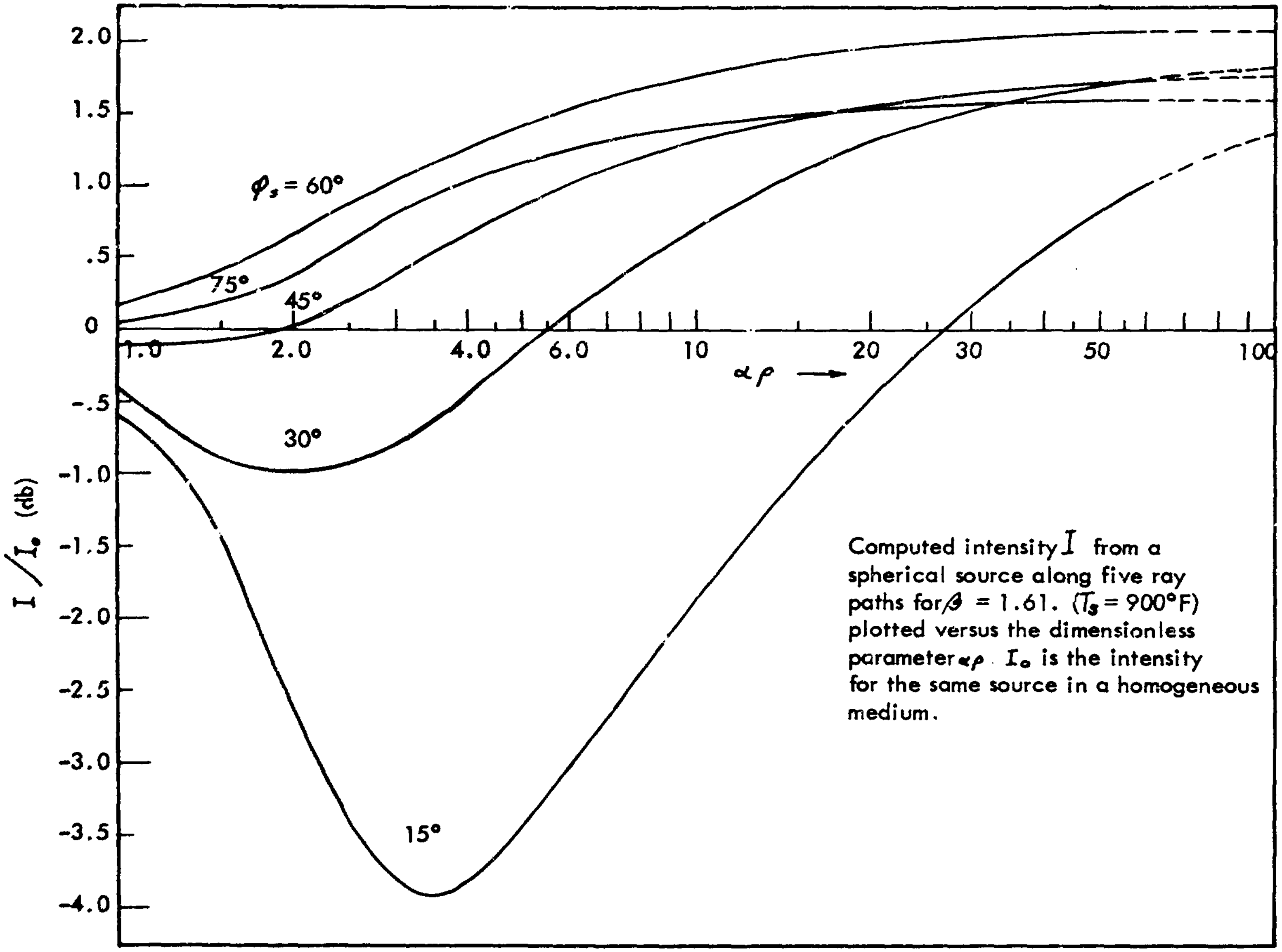

Computed intensity I from a spherical source along five ray paths for $\beta = 1.61$. ($T_s = 900°F$) plotted versus the dimensionless parameter $\alpha\rho$. I_o is the intensity for the same source in a homogeneous medium.

Figure 107.

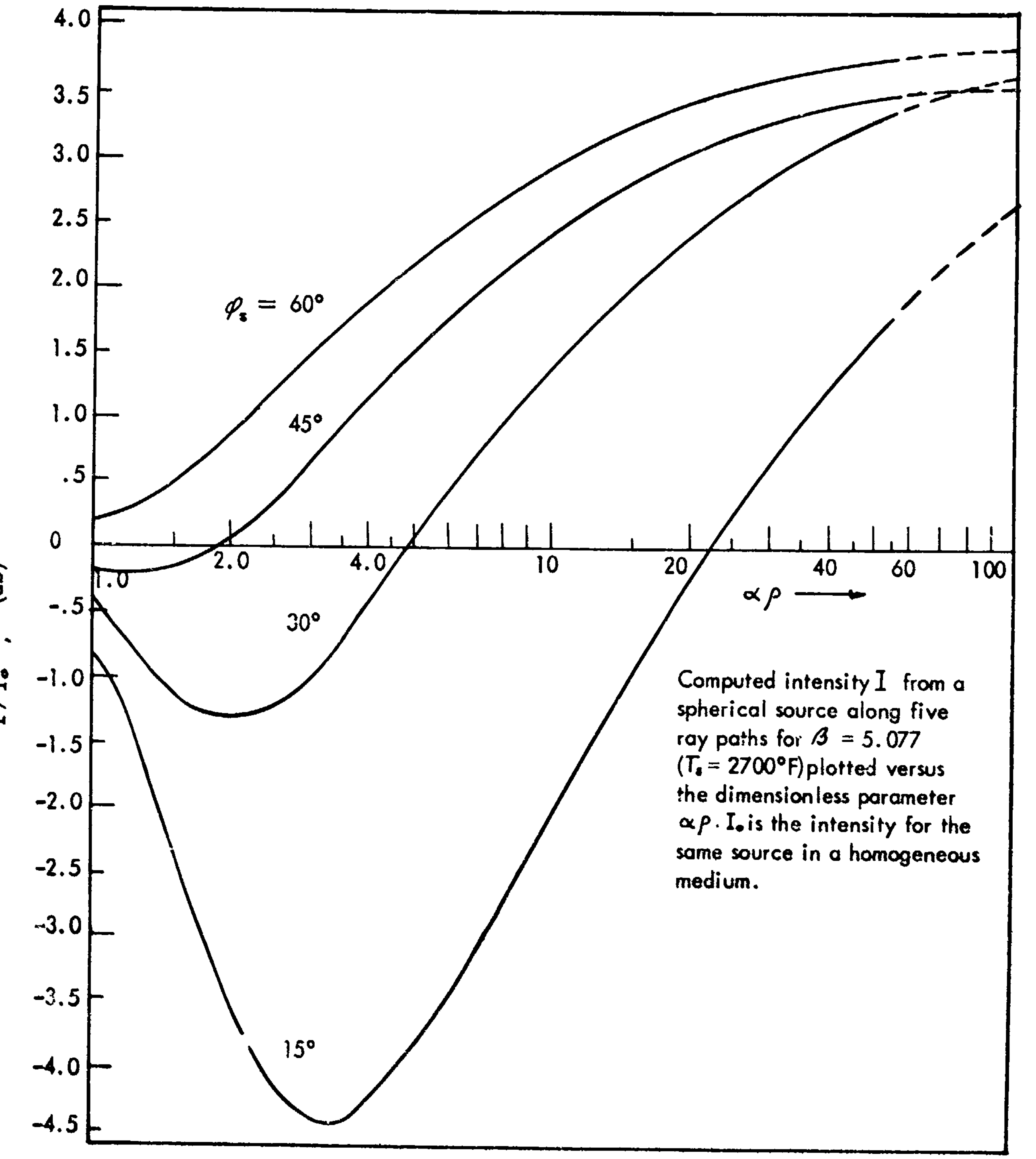

4.0
3.5
3.0
2.5
2.0
1.5
1.0
.5
0
-.5
-1.0
-1.5
-2.0
-2.5
-3.0
-3.5
-4.0
-4.5
I/I₀ , (db)
φ_s = 60°
45°
30°
15°
1.0
2.0
4.0
10
20
40
60
100
$\alpha\rho$
Computed intensity I from a spherical source along five ray paths for β = 5.077 (T_s = 2700°F) plotted versus the dimensionless parameter $\alpha\rho$. I_0 is the intensity for the same source in a homogeneous medium.

Figure 108.

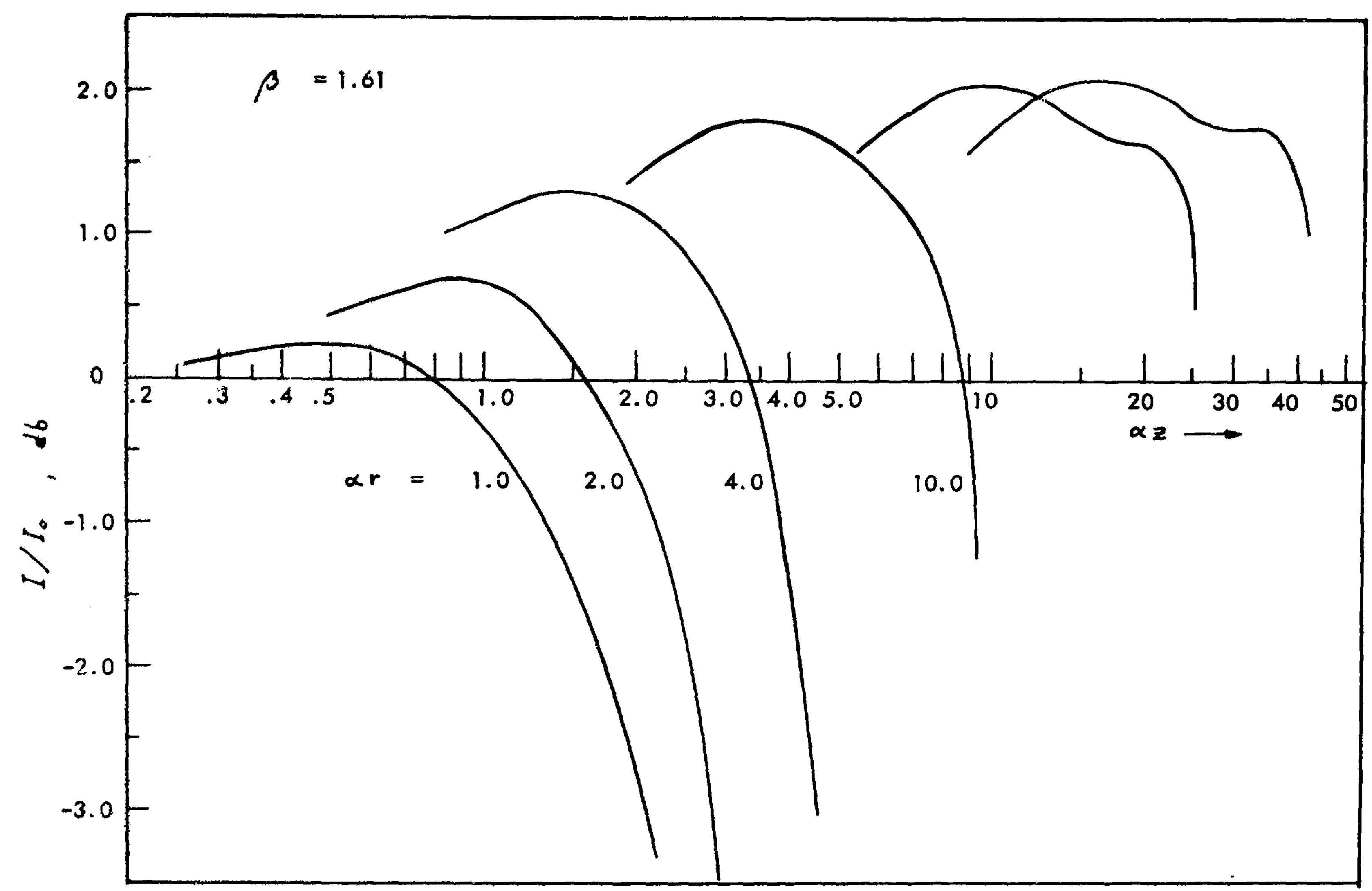

Figure 109. Intensity variation along lines parallel to the axis of symmetry of the temperature distribution (z - axis). T_s=900°F.

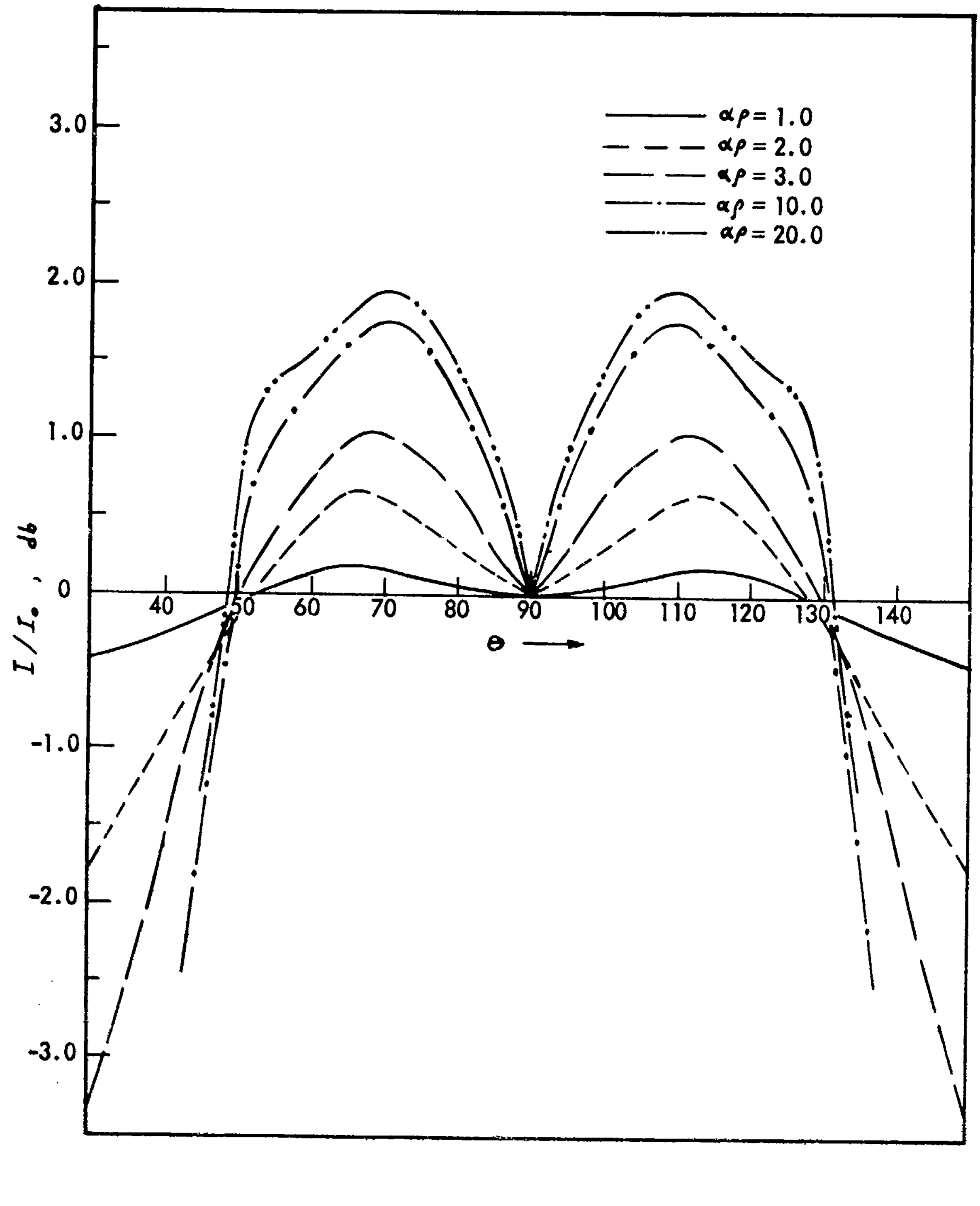

Figure 110. Polar distribution of the intensity in a z - r plane for β = 1.61(T_s = 900°F). θ is the angle which the axis of an observer makes with the z - axis.

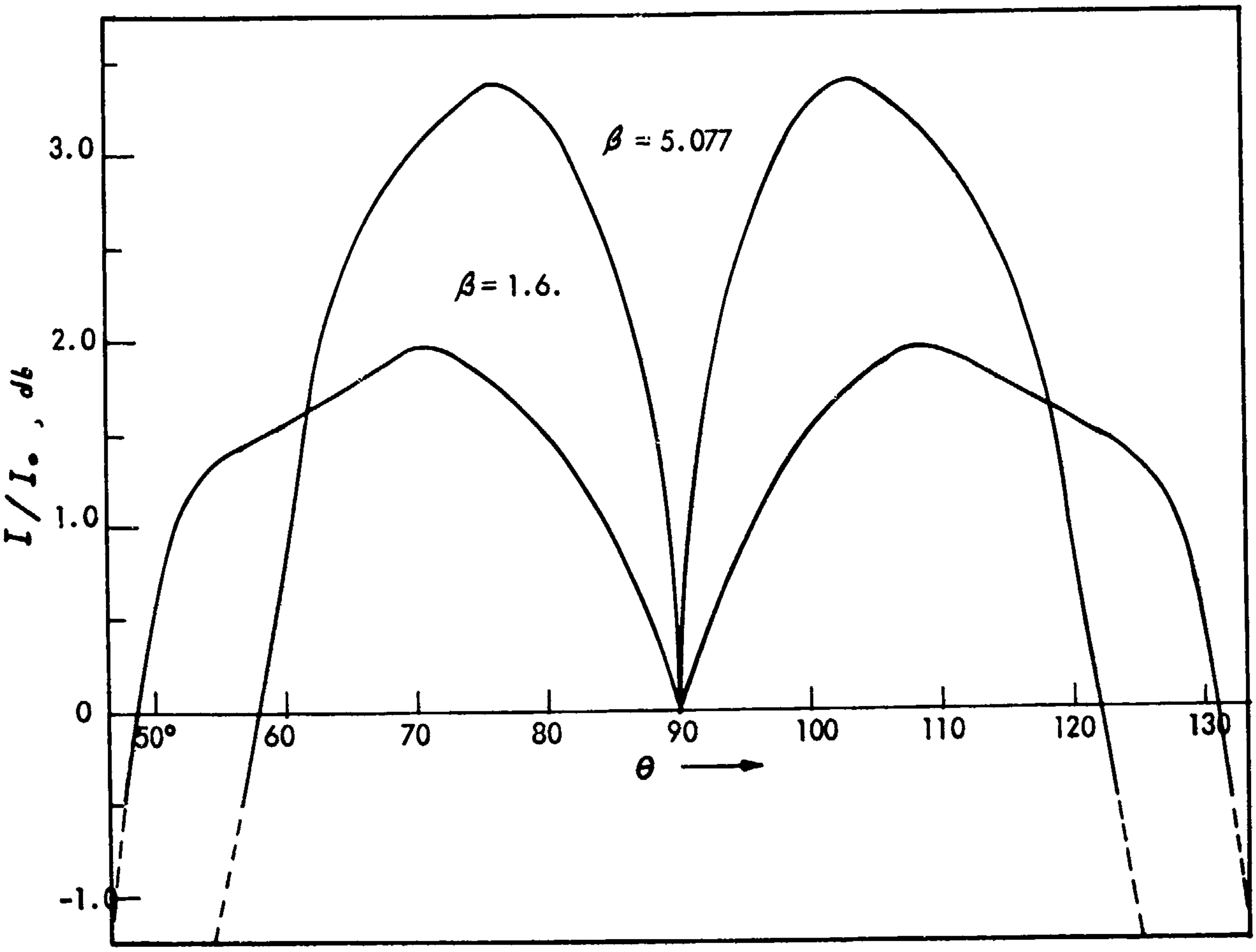

Figure 111. Comparison of the directivity patterns resulting from two different temperature distributions at $\alpha\rho = 20$. Θ is the angle which the axis of an observer makes with the z -axis.

The intensity variation along lines parallel to the z-axis (any r-z plane) or on the surface of cylindrical shells (three dimensions), the z-axis being their axis of symmetry, is shown in figure 109. Again, regions of relative increase are found in the intensity.

The polar distribution of the intensity is shown in figure 110, where the angle is that which the axis of an observer makes with the z-axis. A slight shift of the maxima toward $\phi = 90°$ is noted as an observer moves away from the source. Finally, a comparison of the directivity pattern at $\alpha\rho = 20$ for $\beta = 1.61$ and $\beta = 5.077$ indicates the increase in the directionality of the source for larger values of β (figure 111).

WAVE THEORY

The Formal Solution

In this section the solution to the wave equation will be sought in the form of a Green's function expressed as a series of normal modes. To do this, a plane boundary - acoustically described by a normal impedance Z independent of the angle of incidence - is introduced. The boundary is defined by y = constant or by $r = r_o / \sin\theta$ where r, θ are the cylindrical coordinates and r_o is the perpendicular distance from the origin (figure 112). $(0 < \theta < \pi)$

Consider a spherical source of sound located at the origin of coordinates and driven at a constant frequency $f = \omega / 2\pi$ The sound field at a point $P(r, \theta, z)$ may be derived from a velocity potential

$$\phi = \psi(r, z) e^{-i\omega t}$$

satisfying the wave equation

$$\nabla^2 \psi + \frac{\omega^2}{c^2(r)} \psi = 0 \qquad \text{(C-23)}$$

The use of this equation entails two inherent approximations, namely, the usual requirement of small amplitudes and that the fractional change in any property of the medium must be small within a distance of a wavelength. The latter condition restricts the solution to high frequencies but has not been found stringent even for very high temperature gradients (Ref. 7).

Assuming $\psi(r,z) = R(r) F(z)$ Eq. (C-23) can be separated in cylindrical coordinates, yielding

$$\frac{1}{F} \frac{d^2 F}{dz^2} = -k^2 \qquad \text{(C-24)}$$

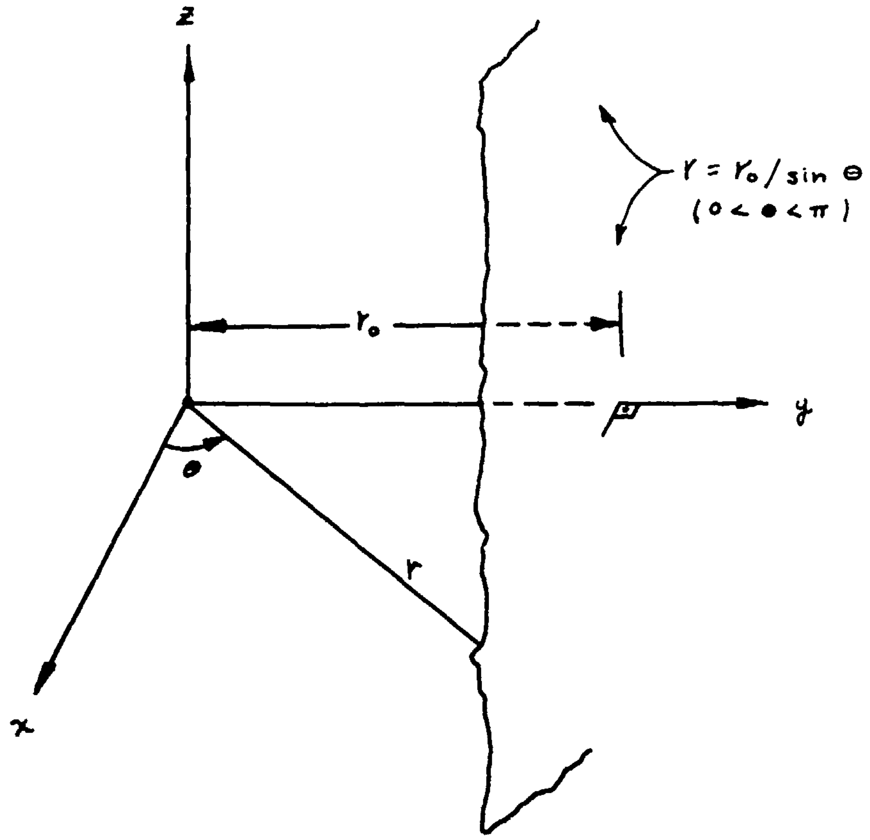

Figure 112. Definition of coordinate system and plane boundary used in the solution of the wave equation.

$$\frac{1}{r}\frac{d}{dr}\left(r\frac{dR}{dr}\right)+\left[\frac{\omega^2}{c^2(r)}-k^2\right]R=0 \qquad \text{(C-25)}$$

where k is the separation constant.

If

(i) R and its derivative are continuous (so that the normal model theory holds),

(ii) at the plane boundary the logarithmic derivative satisfies the condition

$$\frac{R}{\frac{dR}{dr}}=\frac{Z}{i\omega\rho}$$

(iii) $c(r)$ is a continuous monotonic function of r such that $c(o) = c_s$ and $c(r=-H/\sin\theta)=0$ where $r = -H/\sin\theta$ defines a "pressure release" boundary to the left of the source $(\pi < \theta < 2\pi)$

(iv) for large values of r the solution represents only outgoing waves,

a set of eigenfunctions $R_m(r)$ with corresponding eigenvalues k_m may be determined. The space part of the solution will then be

$$\psi(r,z)=\sum_m A_m e^{\pm i k_m z} R_m(r) \qquad \text{(C-26)}$$

where A_m are, as yet, undetermined coefficients, and where the solution to Eq. (C-24), $e^{\pm i k_m z}$ in conjunction with the time factor $e^{-i\omega t}$ represents outgoing waves, the positive or negative sign being used in the region $z > 0$ or $z < 0$ respectively.

To evaluate the coefficients A_m, substitute Eq. (C-25) into the inhomogeneous wave equation

$$\nabla^2\psi+\frac{\omega^2}{c^2(r)}\psi=-\frac{2}{r}\delta(r)\,\delta(z) \qquad \text{(C-27)}$$

where the right hand side corresponds to a point source located at the origin. Here δ denotes the Dirac delta function defined by:

$$\begin{aligned}\delta(x) &= 0 \;; \quad x \neq 0\\ &= \infty \;; \quad x = 0\end{aligned}$$

in such a way that $\int \delta(x)\,dx = 1$ where the region of integration includes the point x = 0.

Substituting Eq. (C-26) in Eq. (C-27) and using Eq. (C-25), we obtain

$$\left[\frac{d^2}{dz^2} e^{\pm i k_m z} + k_m^2 e^{\pm i k_m z} \right] A_m R_m = -\frac{2}{r} \delta(r) \delta(z)$$

Now, multiply both sides by R_m , integrate over a small cylinder enclosing the source and let $z \to 0$. Utilizing the orthoganality relation for the eigenfunctions, namely

$$\left(k_m^2 - k_n^2 \right) \int_{r = r_o/\sin\theta}^{r = -H/\sin\theta} r R_m(r) R_n(r) dr = 0$$

we can obtain the following expression:

$$\left[\frac{d}{dz} e^{\pm i k_m z} + k_m^2 z \right] A_m \int_{r_o/\sin\theta}^{-H/\sin\theta} r R_m^2(r) dr = -R_m(0)$$

$$\left[\pm i k_m e^{\pm i k_m z} + k_m^2 z \right] A_m \int_{r_o/\sin\theta}^{-H/\sin\theta} r R_m^2(r) dr = -R_m(0)$$

as $z \to 0$
$$\frac{-R_m(0)}{\int_{r_o/\sin\theta}^{-H/\sin\theta} r R_m^2(r) dr} \longrightarrow \pm i k_m A_m$$

or

$$A_m \longrightarrow \pm i R_m(0) \Big/ k_m \int_{r_o/\sin\theta}^{-H/\sin\theta} r R_m^2(r) dr$$

Thus, the complete solution is

$$\phi = \pm i e^{-i\omega t} \sum_m e^{\pm i k_m z} R_m(0) R_m(r) \Big/ k_m \int_{r_o/\sin\theta}^{-H/\sin\theta} r R_m^2(r) dr \qquad \text{(C-28)}$$

where the functions R_m depend on the velocity profile $c(r)$ and the boundary condition at the plane boundary.

The Radial Equation

With the particular choice of $C(r)$ given by Eq. (C-2), the radial equation (C-25) becomes:

$$\ddot{R} + \frac{1}{r}\dot{R} + \frac{\omega^2}{C_0^2}\left[\left(1 + \frac{\beta}{\cosh^2\alpha r}\right)^{-1} - \frac{k^2C_0^2}{\omega^2}\right]R = 0$$

or

$$\ddot{R} + \frac{1}{r}\dot{R} + \frac{\omega^2}{C_0^2}\left[\left(1 - \frac{k^2C_0^2}{\omega^2}\right) - \frac{\beta}{\cosh^2\alpha r}\right]R = 0$$

where the approximation

$$\left(1 + \frac{\beta}{\cosh^2\alpha r}\right)^{-1} \simeq 1 - \frac{\beta}{\cosh^2\alpha r}$$

will hold for $\beta \ll \cosh^2\alpha r$ which in general will be true.

Introducing a new dependent variable U related to R by

$$R = \frac{U}{\sqrt{r}} \tag{C-29}$$

one obtains the following equation in U:

$$\ddot{U} + \left\{\frac{\omega^2}{C_0^2}\left[\left(1 - \frac{k^2C_0^2}{\omega^2}\right) - \frac{\beta}{\cosh^2\alpha r}\right] + \frac{1}{4r^2}\right\}U = 0$$

At both asymptotic limits ($r \to 0$; $r \to \infty$) the term $\frac{1}{4r^2}$ will prevail and the pertrubation to the eigenfunctions and eigenvalues for a homogeneous medium which will result due to the $\beta/\cosh^2\alpha r$ term can be calculated with the use of variational methods or techniques of stationary pertrubation theory. However, depending on the choice of β and α, there will be an intermediate region where the $\beta/\cosh^2\alpha r$ term dominates and hence the $\frac{1}{4r^2}$ term can be treated as a pertrubation. The radial equation will then read

$$\ddot{U} + \frac{\omega^2}{C_0^2}\left[\left(1 - \frac{k^2C_0^2}{\omega^2}\right) - \frac{\beta}{\cosh^2\alpha r}\right]U = 0 \tag{C-30}$$

Eq. (C-30) is now in the form of the one-dimensional Schrödinger equation for a potential barrier $\beta/\cosh^2\alpha r$ and can be solved exactly (Ref. 8). The solution regular at the origin is

for $1 - (k^2C_0^2/\omega^2) < 0$:

$$U = \cosh^{-s}\alpha r\left\{C_1 F\left(-\frac{s}{2} + \frac{\epsilon}{2}, -\frac{s}{2} - \frac{\epsilon}{2}, \frac{1}{2}, -\sinh^2\alpha r\right) + C_2 \sinh\alpha r\, F\left(-\frac{s}{2} + \frac{\epsilon}{2} + \frac{1}{2}, -\frac{s}{2} - \frac{\epsilon}{2} + \frac{1}{2}, \frac{3}{2}, -\sinh^2\alpha r\right)\right\} \tag{C-31}$$

for $1-\left(k^2 C_0^2/\omega^2\right) > 0$

$$\mathcal{U} = \cosh^{-s}\alpha r\left\{C_1 F\left(-\frac{s}{2}+\frac{i\mathcal{K}}{2\alpha}, -\frac{s}{2}-\frac{i\mathcal{K}}{2\alpha}, \frac{1}{2}, -\sinh^2\alpha r\right)\right.$$
$$\left. + C_2 \sinh\alpha r\, F\left(-\frac{s}{2}+\frac{i\mathcal{K}}{2\alpha}+\frac{1}{2}, -\frac{s}{2}-\frac{i\mathcal{K}}{2\alpha}+\frac{1}{2}, \frac{3}{2}, -\sinh^2\alpha r\right)\right\} \tag{C-32}$$

where F stands for "hypergeometric function" and

$$\left.\begin{aligned} s &= \frac{1}{2}\left[-1+\left(1-\frac{4\omega^2 B}{C_0^2\alpha^2}\right)^{1/2}\right] \\ \epsilon &= \left[-\frac{\omega^2}{C_0^2\alpha^2}\left(1-\frac{k^2C_0^2}{\omega^2}\right)\right]^{1/2} \\ \mathcal{K} &= \left[\frac{\omega^2}{C_0^2}\left(1-\frac{k^2C_0^2}{\omega^2}\right)\right]^{1/2} \end{aligned}\right\} \tag{C-33}$$

C_1, C_2 = arbitrary constants.

The hypergeometric functions appearing in Eq. (C-31) and Eq. (C-32) are defined in the circle $\sinh^2\alpha r<1$ in which they converge. By analytic continuation, the solutions may be extended to the region of convergence $\sinh^2\alpha r>1$, thus:

$$R(r) = \frac{\cosh^{-s}\alpha r}{\sqrt{r}}\left\{C_1\left[\frac{\Gamma(\frac{1}{2})\Gamma(-\epsilon)}{\Gamma(-\frac{s}{2}-\frac{\epsilon}{2})\Gamma(\frac{1}{2}+\frac{s}{2}-\frac{\epsilon}{2})}\sinh^{s-\epsilon}\alpha r\right.\right.$$
$$\cdot F\left(-\frac{s}{2}+\frac{\epsilon}{2}, -\frac{s}{2}+\frac{\epsilon}{2}+\frac{1}{2}, \epsilon+1, \frac{1}{-\sinh^2\alpha r}\right)$$
$$\left. + \frac{\Gamma(\frac{1}{2})\Gamma(\epsilon)}{\Gamma(-\frac{s}{2}+\frac{\epsilon}{2})\Gamma(\frac{s}{2}+\frac{\epsilon}{2}+\frac{1}{2})}\sinh^{s+\epsilon}\alpha r\cdot F\left(-\frac{s}{2}-\frac{\epsilon}{2}, -\frac{s}{2}-\frac{\epsilon}{2}+\frac{1}{2}, -\epsilon+1, \frac{1}{-\sinh^2\alpha r}\right)\right]$$
$$+ C_2\sinh\alpha r\left[\frac{\Gamma(\frac{3}{2})\Gamma(-\epsilon)}{\Gamma(-\frac{s}{2}-\frac{\epsilon}{2}+\frac{1}{2})\Gamma(\frac{s}{2}-\frac{\epsilon}{2}+1)}\sinh^{s-\epsilon-1}\alpha r\right.$$
$$\cdot F\left(-\frac{s}{2}+\frac{\epsilon}{2}+\frac{1}{2}, -\frac{s}{2}+\frac{\epsilon}{2}, \epsilon+1, \frac{1}{-\sinh^2\alpha r}\right)$$
$$\left.\left. + \frac{\Gamma(\frac{3}{2})\Gamma(\epsilon)}{\Gamma(-\frac{s}{2}+\frac{\epsilon}{2}+\frac{1}{2})\Gamma(\frac{s}{2}+\frac{\epsilon}{2}+1)}\sinh^{s+\epsilon-1}\alpha r\cdot F\left(-\frac{s}{2}-\frac{\epsilon}{2}+\frac{1}{2}, -\frac{s}{2}-\frac{\epsilon}{2}, -\epsilon+1, \frac{1}{-\sinh^2\alpha r}\right)\right]\right\},$$

$$\left[1-\left(k^2C_0^2/\omega^2\right)<0\ ;\ \sinh^2\alpha r>1\right] \tag{C-34}$$

where we have used Eq. (C-29) and where Γ denotes "gamma function," s and ϵ are given by Eq. (C-33), and C_1 and C_2 are arbitrary constants. The solution for $1-(k^2c_0^2/\omega^2)>0$ is immediately found by replacing ϵ by $(i\kappa/\alpha)$ in Eq. (C-34) where κ is defined in Eq. (C-33).

The ratio C_1/C_2 can be determined by making use of the boundary condition at large values of r, namely that asymptotically only outgoing waves should exist. Noting that in this limit the hypergeometric functions appearing in Eq. (C-34) approach unity and that $\sinh x \to \cosh x \to \frac{e^x}{2}$ we obtain

$$R(r) \to r^{-1/2}\left\{C_1\left[\Gamma_1\left(\frac{e^{\alpha r}}{2}\right)^{-\epsilon}+\Gamma_2\left(\frac{e^{\alpha r}}{2}\right)^{\epsilon}\right]\right.$$
$$\left.+C_2\left[\Gamma_3\left(\frac{e^{\alpha r}}{2}\right)^{-\epsilon}+\Gamma_4\left(\frac{e^{\alpha r}}{2}\right)^{\epsilon}\right]\right\}$$

Write $\left(\frac{e^{\alpha r}}{2}\right)^{\pm\epsilon}=\left(\frac{e^{\alpha r}}{e^{\ln 2}}\right)^{\pm\epsilon}=e^{\pm(\alpha r-\ln 2)\epsilon}$ so that

$$R(r) \to r^{-1/2}\left[\left(C_1\Gamma_1+C_2\Gamma_3\right)e^{-(\alpha r-\ln 2)\epsilon}\right.$$
$$\left.+\left(C_1\Gamma_2+C_2\Gamma_4\right)e^{(\alpha r-\ln 2)\epsilon}\right] \tag{C-35}$$

where

$$\left.\begin{aligned}\Gamma_1&=\frac{\Gamma(\frac{1}{2})\,\Gamma(-\epsilon)}{\Gamma(-\frac{s}{2}-\frac{\epsilon}{2})\Gamma(\frac{s}{2}-\frac{\epsilon}{2}+\frac{1}{2})}\;;\;\Gamma_3=\frac{\Gamma(\frac{3}{2})\,\Gamma(-\epsilon)}{\Gamma(-\frac{s}{2}-\frac{\epsilon}{2}+\frac{1}{2})\Gamma(\frac{s}{2}-\frac{\epsilon}{2}+1)}\\ \Gamma_2&=\frac{\Gamma(\frac{1}{2})\,\Gamma(\epsilon)}{\Gamma(-\frac{s}{2}+\frac{\epsilon}{2})\,\Gamma(\frac{s}{2}+\frac{\epsilon}{2}+\frac{1}{2})}\;;\;\Gamma_4=\frac{\Gamma(\frac{3}{2})\,\Gamma(\epsilon)}{\Gamma(-\frac{s}{2}+\frac{\epsilon}{2}+\frac{1}{2})\Gamma(\frac{s}{2}+\frac{\epsilon}{2}+1)}\end{aligned}\right\} \tag{C-36}$$

For Eq. (C-35) to represent only outgoing waves, we must set the coefficient $(C_1\Gamma_1+C_2\Gamma_3)$ equal to zero. It follows that

$$\frac{C_1}{C_2}=-\frac{\Gamma_3}{\Gamma_1}=-\frac{\Gamma(-\frac{s}{2}-\frac{\epsilon}{2})\,\Gamma(\frac{s}{2}-\frac{\epsilon}{2}+\frac{1}{2})}{2\,\Gamma(-\frac{s}{2}-\frac{\epsilon}{2}+\frac{1}{2})\,\Gamma(\frac{s}{2}-\frac{\epsilon}{2}+1)} \tag{C-37}$$

Using the definition of ϵ and $\mathcal{K}$ we finally obtain the asymptotic solution to the radial equation in the form

$$R(r) \xrightarrow[r\to\infty]{} \Gamma C_2 e^{-\frac{\ln 2}{\alpha}\left(k^2-\frac{\omega^2}{C_0^2}\right)^{\frac{1}{2}}} \frac{e^{\left(k^2-\frac{\omega^2}{C_0^2}\right)^{\frac{1}{2}} r}}{\sqrt{r}} \quad ; \left(1-\frac{k^2C_0^2}{\omega^2}<0\right)$$

$$R(r) \xrightarrow[r\to\infty]{} \Gamma' C_2 e^{-i\frac{\ln 2}{\alpha}\left(k^2-\frac{\omega^2}{C_0^2}\right)^{\frac{1}{2}}} \frac{e^{i\left(k^2-\frac{\omega^2}{C_0^2}\right)^{\frac{1}{2}} r}}{\sqrt{r}} \quad ; \left(1-\frac{k^2C_0^2}{\omega^2}>0\right)$$

where $\Gamma=\Gamma_4-(\Gamma_3\Gamma_2/\Gamma_1)$ and where the prime (′) indicates substitution of ϵ by $i\mathcal{K}/\alpha$ in the definitions of Eq. (C-36). The constant C_2 can be evaluated from the boundary conditions at the source and will depend on the source strength.

The Eigenvalue Equation

The eigenvalues, k_m corresponding to the eigenfunctions $R_m(r)$ are determined from the condition at the plane boundary, namely that

$$\frac{dR_m/dr}{R_m} = \frac{i\omega\rho}{Z} \quad \text{at} \quad r = r_0/\sin\theta \tag{C-38}$$

in conjunction with the defining equations for ϵ or $\mathcal{K}$ (Eq. C-33). The eigenvalues resulting from the solution of Eq. (C-38) will, in general, differ depending on the region of convergence considered, i.e. on the choice of R_m to be used in Eq. (C-38), and can, in principle, be computed for a particular mode by retaining the appropriate number of terms in the hypergeometric series which appear in the solutions R_m.

Consider the region $\sinh \alpha r < 1$ and the case of $\left(1-\frac{k^2C_0^2}{\omega^2}\right)<0$, for which the appropriate eigenfunctions are given by Eq. (C-31).

With the use of Eq. (C-29) and the identification

$$\begin{aligned} \sinh^2\alpha r &\equiv \xi \\ -\frac{s}{2}+\frac{\epsilon}{2} &\equiv a \\ -\frac{s}{2}-\frac{\epsilon}{2} &\equiv b \\ \frac{1}{2} &\equiv c \end{aligned}$$

the solutions take the form

$$R(r) = r^{-\frac{1}{2}}\cosh^{-s}\alpha r\left\{C_1F(a,b,c,-\xi)+C_2\sqrt{\xi}\,F\left(a+\tfrac{1}{2},b+\tfrac{1}{2},c+1,-\xi\right)\right\}$$

which when substituted into Eq. (C-38) yield (for a perfect reflector) the following equation in ϵ :

$$
\begin{aligned}
&\left(S\alpha + \frac{1}{2r}\right)\left\{ \frac{C_1}{C_2} \frac{\Gamma(c)}{\Gamma(a)\Gamma(b)} \sum_n (-1)^n \frac{\Gamma(a+n)\Gamma(b+n)}{\Gamma(c+n)} \frac{\xi^n}{n!} \right. \\
&\qquad \left. + \sqrt{\xi}\ \frac{\Gamma(c+1)}{\Gamma(a+\frac{1}{2})\Gamma(b+\frac{1}{2})} \sum_n (-1)^n \frac{\Gamma(a+\frac{1}{2}+n)\Gamma(b+\frac{1}{2}+n)}{\Gamma(c+1)} \frac{\xi^n}{n!} \right\} \\
&= \frac{C_1}{C_2} \frac{d}{dr}(-\xi) \frac{\Gamma(c)}{\Gamma(a)\Gamma(b)} \sum_n (-1)^n \frac{(a+n)(b+n)}{(c+n)} \frac{\Gamma(a+n)\Gamma(b+n)}{\Gamma(c+n)} \frac{\xi^n}{n!} \\
&\quad + \frac{d}{dr}\sqrt{\xi}\ \frac{\Gamma(c+1)}{\Gamma(a+\frac{1}{2})\Gamma(b+\frac{1}{2})} \sum_n (-1)^n \frac{\Gamma(a+\frac{1}{2}+n)\Gamma(b+\frac{1}{2}+n)}{\Gamma(c+1)} \frac{\xi^n}{n!} \\
&\quad + \sqrt{\xi}\ \frac{d}{dr}(-\xi) \frac{\Gamma(c+1)}{\Gamma(a+\frac{1}{2})\Gamma(b+\frac{1}{2})} \sum_n (-1)^n \frac{(a+\frac{1}{2}+n)(b+\frac{1}{2}+n)}{c+1} \\
&\qquad\qquad \cdot \frac{\Gamma(a+\frac{1}{2}+n)\Gamma(b+\frac{1}{2}+n)}{\Gamma(c+1)} \frac{\xi^n}{n!} \qquad \text{(C-39)}
\end{aligned}
$$

where the ratio C_1/C_2 is given by Eq. (C-37) and where the relations

$$\frac{d}{dz} F(\alpha,\beta,\gamma,z) = \frac{\alpha\beta}{\gamma} F(\alpha+1,\beta+1,c+1,z)$$

$$z\,\Gamma(z) = \Gamma(z+1)$$

and the definition

$$F(\alpha,\beta,\gamma,z) = \frac{\Gamma(\gamma)}{\Gamma(\alpha)\Gamma(\beta)} \sum_n \frac{\Gamma(\alpha+n)\Gamma(\beta+n)}{\Gamma(\gamma+n)} \frac{z^n}{n!}$$

have been used. The evaluation of Eq. (C-39) is to be carried out at $r = k_0/\sin\theta$. A similar, yet more complicated, equation results if Eq. (C-34) is substituted in Eq. (C-38). In either case, a closed form solution in ϵ (and hence k) for any given mode cannot be easily obtained by ordinary means, except in limiting cases.

Such a case results if we consider distances from the source for which the asymptotic limit of the hypergeometric functions can be used to a fair approximation*. Consider, for example, the region $\sinh(\alpha r) > 1$. Substituting unity for the hypergeometric functions in Eq. (C-34) and using Eq. (C-37), the eigenfunctions take the simple form

$$R(r) = r^{-\frac{1}{2}} \cosh^{-s} \alpha r \ \sinh^{s+\epsilon} \alpha r \ (C_1 \Gamma_2 + C_2 \Gamma_4)$$

whence

$$\frac{dR}{dr} = R\left[(s+\epsilon)\alpha \coth \alpha r - s\alpha \tanh \alpha r - \frac{1}{2r}\right]$$

so that Eq. (C-38) yields

$$\frac{1}{R}\frac{dR}{dr} = (s+\epsilon)\alpha \coth u - s\alpha \tanh u - \frac{\alpha}{2u} = \frac{i\omega\rho}{Z}$$

or

$$\epsilon = \frac{\tanh u}{2u} - \frac{\operatorname{sech}^2 u}{2}\left[-1 + \left(1 - \frac{4\omega^2\beta}{C_0^2\alpha^2}\right)^{\frac{1}{2}} + \frac{i\omega\rho}{Z}\tanh u\right. \qquad \text{(C-40)}$$

where $u = \alpha r_0 / \sin\theta \quad (0 < \theta < \pi)$

Eq. (C-40) relates the eigenvalue k, appropriate for the assumed limiting case, to the temperature parameters α and β, the frequency $f = \omega/2\pi$, and the boundary impedance Z. A similar expression to the above is obtained in the case of $\left(1 - \frac{k^2 C_0^2}{\omega^2}\right) > 0$ by substituting iK/α for ϵ.

Thus far in this section the wave equation has been formally solved (Eq. C-28), and the solution to the radial equation has been obtained in a certain region. Its validity depends on the particular choice of α and β values for which the approximations evoked in solving the radial equation are valid. An equation satisfied by the eigenvalues k_m has also been obtained (Eq. C-39). However, before the above results can be put to practical use the eigenvalues appropriate for the region considered must be determined in a closed form, for it is precisely the knowledge of k_m which will indicate how the sound is propagated in the medium. This will not be carried out here. Instead, any qualitative conclusions which are to be drawn regarding the effect of the presence of the temperature distribution considered in this appendix are to be based on the results of the analysis presented in the section Geometrical Acoustics Approximation, and will, of course, be valid only in the high frequency range.

*This is an approximation one order higher than that in which only the first mode is assumed to survive.

LIST OF SYMBOLS USED IN APPENDIX C

A, α, β	Temperature distribution parameters (Eqs. C-1, C-2)
C	Speed of sound
$E(\psi, k)$	Elliptic integral of the second kind
$F(\psi, k)$	Elliptic integral of the first kind
$F(a,b,c,x)$	Hypergeometric function
I	Acoustic intensity
k	Modulus
Q	Acoustic power
r, θ, z	Radial, circumferential and axial coordinates, respectively, of polar, cylindrical coordinate system
T	Temperature
W, q,	Transformation variables (Eqs. C-5, C-8)
Z	Impedance
$\Gamma(x)$	Gamma function
δ	Variation of a functional; also, constant (Eq. C-7)
$\delta(x)$	Dirac's delta function (Eq. C-27)
	Parameter
$\Pi(\psi, \mu, k)$	Elliptic integral of third kind

Superscripts

*	Reciprocal
•	Time rate of change

Subscripts

o	Unperturbed or ambient
s	At the source

Definitions of other symbols used in algebraic manipulations may be found in the text.

APPENDIX C

References:

1. Laurence, J. C., "Intensity, Scale and Spectra of Turbulence in Mixing Region of Free Subsonic Jet," NACA Report 1292 (1956).

2. e.g., Copson, E. T., An Introduction to the Theory of Complex Variable, Oxford, 1957, pp 399 ff.

3. Hancock, H., Elliptic Integrals, Dover Publications, Inc., New York (1958)

4. Byrd, P. F., Friedman, M. D., Handbook of Elliptic Integrals for Engineers and Physicists, Springer, Berlin (1954).

5. Selfridge, R. G., Maxfield, J. E., A Table of the Incomplete Elliptic Integral of the Third Kind, Dover Publications, Inc., New York (1958).

6. Pekeris, C. L., "Theory of Propagation of Sound in a Half-Space of Variable Velocity Under Conditions of Formation of a Shadow Zone," Journal of Acoustical Society of America 18 (Oct. 1946), pp 295-315.

7. Pridmore-Brown, D., Ingard, U., "Sound Propagation into the Shadow Zone in a Temperature Stratified Atmosphere Above a Plane Boundary," NACA TN 3494 (Oct. 55).

8. Landau, L. D., Lifshitz, E. M., Quantum Mechanics: Non-Relativistic Theory, Addison-Wesley Publishing Co., Inc. (1958) pp 69, 76.